Measurement of Neutrino Oscillation in the T2K Experiment

Masashi Otani

January, 2012

Department of Physics, Graduate School of Science
Kyoto University

Measurement of Neutrino Oscillation in the T2K Experiment

A dissertation
submitted in partial fulfillment of the requirements
for the Degree of Doctor of Science
in the Graduate School of Science, Kyoto University

Masashi Otani

Department of Physics, Graduate School of Science
Kyoto University
January, 2012

Dissertation Committee:

Tsuyoshi Nakaya
Atsuko K. Ichikawa
Akihiro Minamino
Toru Tamimori
Tatsuo Kobayashi

Abstract

We present a measurement of neutrino oscillation in the T2K experiment. T2K is a long baseline neutrino oscillation experiment. The muon neutrino beam is generated at J-PARC and is detected with Super-Kamiokande which is 295 km away from J-PARC. T2K started physics data taking in January 2010. Data of 1.4×10^{20} protons on target were collected between January 2010 and March 2011. Analysis of neutrino oscillation in the muon neutrino disappearance mode ($\nu_\mu \to \nu_x$) is performed by comparing observations with the expectations at Super-Kamiokande for both the neutrino energy spectrum and the number of muon neutrino events. For the precise prediction of the expectations, the beam direction and the event rate of the neutrino events are measured by near detectors. The beam x direction and y direction are measured to be -0.014 ± 0.025(stat.)$\pm$0.33(syst.) mrad and -0.107 ± 0.025(stat.)$\pm$0.37(syst.) mrad, respectively. The neutrino event rate relative to the prediction is measured to be 1.06 ± 0.001(stat.)$\pm$0.037(syst.) for the on-axis near detector and $1.036 \pm 0.028(\text{stat.})^{+0.042}_{-0.036}$(syst.)$\pm$0.037 (phys.) for the off-axis near detector. In total, 31 muon neutrino events are observed at Super-Kamiokande, while the expectation without neutrino oscillation is $103.7^{+16.6}_{-16.2}$. The best fit oscillation parameters are obtained to be ($\sin^2 2\theta_{23}$, Δm^2_{32}) = (0.99, 2.6×10^{-3}[eV^2/c^4]). The 90% confidence interval is estimated to be $2.1 \times 10^{-3} < \Delta m^2_{32}$ [eV^2/c^4] $< 3.1 \times 10^{-3}$ at $\sin^2 2\theta_{23} = 1.0$, and $0.86 < \sin^2 2\theta_{23}$ at $\Delta m^2_{32} = 2.6 \times 10^{-3}$[eV^2/c^4]. We firmly confirm the neutrino oscillations in the muon neutrino disappearance mode and precisely measure the oscillation parameters. This result is one of the most precise measurements today and is consistent with other experiment. Finally it is shown that we have a potential sensitivity of $\delta(\sin^2 2\theta_{23}) = 0.01$ with final goal of statistics (8.0×10^{21} protons on target).

Acknowledgements

Fist of all, this thesis is an achievement not by me but by all the people supported me. I just did with their help for five years.

I would like to express my sincere gratitude to Prof. Tsuyoshi Nakaya, Prof. Atsuko Ichikawa, Dr. Akihiro Minamino and Prof. Masashi Yokoyama. My years are strongly supported by them. Prof. Tsuyoshi Nakaya, my supervisor, gave me advises with depthful insight of physics. The great-granddaddy of his greatness, however, is not his depthful insight but his energetic and positive attitude; he promoted (is promoting) our T2K experiment toward success with his great-granddaddy. Prof. Atsuko Ichikawa, she is also my supervisor, has depthful love and passion to physics and students. She checked my analysis results, suggested alternative methods, and even looked hard at my programming codes one by one. Dr. Akihiro Minamino helped me most closely. Without his strong leadership in the construction of the INGRID detector, this thesis could not be achieved at all. I don't have words to describe my appreciation for many given by Prof. Masashi Yokoyama; he gave me step-by-step how-to-do-it guides; he gave me a advise firstly almost always.

My first year is supported by Mr. H. Kawamuko and Mr. K. Nitta for the beam test at KEK FUJI test beamline. I also thank KEK FUJI test beam line group. I am thankful to Dr. A. Pla-dalmau in Fermilab who developed and mass-produced the INGRID scintillator bars. Many people helped me for the assembly of the INGRID scintillator planes in my second year. I'd like to thank Mr. A. Murakami, Ms. A. Ozaki, Ms. B. Magali, Mr. C. Bronner, Mr. D. Orme, Mr. IekikeI, Mr. K. Tashiro, Mr. K. Yamamoto, Prof. M. Gonin, Mr. N. Nagai, Prof. N. Tanimoto, Mr. O. Drapier, Mr. P. Dinh Tran, Mr. Y. Declais and Mr. Y.Shimizu. And the important thing to remember is the help by Taino family. My third and fourth year might be one of the most exciting period in my life. Many, many people were plunged into this exciting period and helped me. Daiichitekkou Company Dr. S. Tada supported for the construction and installation of the INGRID modules. The T2K electronics and DAQ group created the readout electronics and the DAQ system with sophisticated technology. Especially, Prof. A. Weber, Mr. C. Angelsen, Mr. C. Metelco, Prof. G. Barr, Prof. G. Pearce, Mr. Q. Weiming, Mr. S. Mohammed, Mr. T. Matt and Mr. T. Nicholls cooperated closely with us for the commissioning and operation of the systems. Mr. A. Murakami have devoted considerable efforts for building the INGRID Monte Carlo simulation. Ms. C. Matsumura helped the construction and the INGRID analysis. Mr. Y. Nakajima gave me many pieces of advice for the INGRID analysis software. Mr. T. Kikawa and Mr. K. Suzuki worked together for the additional INGRID modules. It was very exiting experience to measure the neutrino beam with close communication with MUMONers. Especially, Dr. K. Matsuoka and Mr. H. Kubo supported us with their excellent detector. Dr. T. Nakadaira and Dr. T. Nakadaira always kindly supported us for the neutrino beam commissioning and operation. My fifth year is supported by many people in the Super-Kamiokande experiment. Dr. J. Kameda closely helped me for the oscillation analysis. His sincere attitude to the analysis and physics are very respected for me. Prof. M. Shiozawa greatly supported my work with the Super-Kamiokande detector. Prof. M. Nakahata gave me many advises and carefully checked the oscillation analysis.

I am grateful to all the T2K collaborators, the Super-Kamiokande collaborators and the J-PARC accelerator teams. The data for my thesis is the products by all the members.

In addition, I would like to thank all members in the high energy physics group of Kyoto University: Prof. N. Sasao, Prof. T. Nomura, Dr. H. Nanjo, Dr. T. Sumida, Mr. H. Yokoyama, Dr. H. Morii, Dr. N. Taniguchi, Mr. Y. Kurosawa, Dr. M. Ikeda, Mr. K. Shiomi, Mr. T. Usuki, Mr. N. Kawasaki, Mr. T. Masuda, Mr. D. Naito, Mr. Y. Maeda, Mr. G. Takahashi, Mr. T. Yamauchi, Mr. T. Hiraki, Mr. K. Goda, Mr. S. Seki, Mr. T. Tashiro and Mr. T. Nagasaki. They have advised and encouraged me and I have enjoyed the laboratory life with them. I wish to acknowledge the secretaries' care of my business in Kyoto University, KEK, J-PARC and Kimioka Observatory.

Finally, I want thank to my families living in Osaka and Kagawa prefecture. They always believed me and supported me.

Masashi Otani
Kyoto, Japan
January, 2012

Contents

Chapter 1

Introduction

Neutrino is an elementary particle first postulated by W. Pauli [1]. Three flavors are found so far; ν_e [2], ν_μ [3], and ν_τ [4], associating with the three charged leptons. It has spin of 1/2 and no electric charge. Finite neutrino masses have been directly searched for [5–8] in a long time. The efforts set upper limit on these masses. The evidence of the finite neutrino mass, however, came from other phenomenon.

The discovery of neutrino oscillation in 1998 by Super-Kamiokande [9] revealed that the neutrinos have finite mass. Because the neutrinos have mass, the leptonic system can be in a situation quite analogous to the quark system. The weak eigenstates do not correspond to the mass eigenstates and the mixing is descried by a 3×3 unitary matrix. It makes possible to consider new CP violation in addition to that in quarks. Moreover, the measurement of neutrino oscillation shows large difference of the flavor mixing between quarks and leptons, suggesting a different flavor symmetry between them.

Thus the neutrino oscillation phenomenon took us to new horizon for understanding of nature. Now we face the new mysteries. This thesis opens a new era where the mysteries might be pull away.

In the following sections, we describe the physics of neutrino oscillation and the current knowledge. T2K (Tokai-to-Kamioka) is a long baseline neutrino oscillation experiment aimed for the precise measurement of ν_μ disappearance ($\nu_\mu \to \nu_x$) and the discovery of ν_e appearance ($\nu_\mu \to \nu_e$). We introduce the T2K long baseline neutrino oscillation experiment in Section 1.2. The outline of this thesis is shown in Section 1.3.

1.1 Physics of Neutrino Oscillation

1.1.1 Neutrino mixing

If a neutrino has mass, we expect that the weak eigenstate could be different from the mass eigenstate, as analogous to the quark system [10]. For simplicity, consider the two flavor case at first. The flavor eigenstates, ν_α and ν_β, is written by

$$\begin{pmatrix} \nu_\alpha \\ \nu_\beta \end{pmatrix} = \begin{pmatrix} \cos\theta & \sin\theta \\ \sin\theta & \cos\theta \end{pmatrix} \begin{pmatrix} \nu_1 \\ \nu_2 \end{pmatrix} \equiv U \begin{pmatrix} \nu_1 \\ \nu_2 \end{pmatrix} \tag{1.1}$$

where ν_1 and ν_2 are the mass eigenstates and θ is the mixing angle. After traveling with a certain time period t, each component of the mass eigenstate gets a different phase:

$$\begin{pmatrix} \nu_1(t) \\ \nu_2(t) \end{pmatrix} = \begin{pmatrix} e^{-iE_1 t} & 0 \\ 0 & e^{-iE_2 t} \end{pmatrix} \begin{pmatrix} \nu_1(0) \\ \nu_2(0) \end{pmatrix} \tag{1.2}$$

Detection of neutrinos by the charged current interaction projects these new states back onto the flavor eigenstates:

$$\begin{pmatrix}\nu_\alpha(t)\\ \nu_\beta(t)\end{pmatrix} = U\begin{pmatrix}e^{-iE_1t} & 0\\ 0 & e^{-iE_2t}\end{pmatrix}U^{-1}\begin{pmatrix}\nu_\alpha(0)\\ \nu_\beta(0)\end{pmatrix} \tag{1.3}$$

Supposing a neutrino is generated as ν_α (*i.e.* $\nu_\alpha(0) = 1$ and $\nu_\beta(0) = 0$), its surviving probability in the same flavor eigenstate after traveling a certain distance L is obtained as

$$P(\nu_\alpha \to \nu_\alpha) = |\nu_\alpha(t)|^2 = 1 - \sin^2 2\theta \cdot \sin^2\left(1.27\Delta m^2[\mathrm{eV}^2/\mathrm{c}^4]\frac{L[\mathrm{km}]}{E[\mathrm{GeV}]}\right) \tag{1.4}$$

when m_i is very small compared to E_i ($E_i \simeq p + m_i^2/2p$). Here $\Delta m^2 \equiv m_2^2 - m_1^2$. Thus the flavor of neutrinos oscillates as a function of L/E.

1.1.2 Three generation mixing

In the three generation framework ($\alpha = \mathrm{e}, \mu, \tau$), neutrino mixing is described by a 3×3 unitary matrix, called the Pontecorvo-Maki-Nakagawa-Sakata [11, 12] (PMNS) matrix. It is defined by a product of three rotation matrices with θ_{12}, θ_{13}, θ_{23} and CP phase δ.

$$\begin{pmatrix}\nu_e\\ \nu_\mu\\ \nu_\tau\end{pmatrix} = \begin{bmatrix}\\ U_{\alpha i}\\ \\ \end{bmatrix}\begin{pmatrix}\nu_1\\ \nu_2\\ \nu_3\end{pmatrix} \tag{1.5}$$

$$\begin{aligned} U &= \begin{pmatrix}1 & 0 & 0\\ 0 & c_{23} & s_{23}\\ 0 & -s_{23} & c_{23}\end{pmatrix}\begin{pmatrix}c_{13} & 0 & s_{13}e^{-i\delta}\\ 0 & 1 & 0\\ -s_{13}e^{i\delta} & 0 & c_{13}\end{pmatrix}\begin{pmatrix}c_{12} & s_{12} & 0\\ -s_{12} & c_{12} & 0\\ 0 & 0 & 1\end{pmatrix}\\ &= \begin{pmatrix}c_{12}c_{13} & s_{12}c_{13} & s_{13}e^{-i\delta}\\ -s_{12}c_{23} - c_{12}s_{23}s_{13}e^{i\delta} & c_{12}c_{23} - s_{12}s_{23}s_{13}e^{i\delta} & s_{23}c_{13}\\ s_{12}s_{23} - c_{12}c_{23}s_{13}e^{i\delta} & -c_{12}s_{23} - s_{12}c_{23}s_{13}e^{i\delta} & c_{23}c_{13}\end{pmatrix} \end{aligned} \tag{1.6}$$

where $\alpha = e, \mu, \tau$ are flavor indices, $i = 1, 2, 3$ are the indices of mass eigenstates, $s_{ij}(c_{ij})$ stands for $\sin\theta_{ij}(\cos\theta_{ij})$. The probability of the oscillation is given by the formula,

$$P(\nu_\alpha \to \nu_\beta) = \delta_{\alpha\beta} - 4\sum_{i>j} Re(U_{\alpha i}^* U_{\beta i} U_{\alpha j} U_{\beta j}^*)\cdot\sin^2\Phi_{ij} \pm 2\sum_{i>j} Im(U_{\alpha i}^* U_{\beta i} U_{\alpha j} U_{\beta j}^*)\cdot\sin 2\Phi_{ij} \tag{1.7}$$

where

$$\Phi_{ij} \equiv 1.27\frac{\Delta m_{ij}^2[\mathrm{eV}^2/\mathrm{c}^4]L[\mathrm{km}]}{E_\nu[\mathrm{GeV}]}, \tag{1.8}$$

$\Delta m_{ij}^2 \equiv m_i^2 - m_j^2$, L is the flight distance, and E_ν is the neutrino energy. The $\pm$ sign in the third term is the CP violation effect, + for neutrinos and − for anti-neutrinos. Here the matter effect is neglected.

Here some practical expressions of Eq. 1.7 are calculated. In the calculation, we take the oscillation parameters as the values suggested by atmospheric neutrino, solar neutrino and reactor neutrino; $\Delta m_{32}^2 \simeq \Delta m_{31}^2 = 1.9 \times 10^{-3} \sim 3.0 \times 10^{-3}$ [$\mathrm{eV}^2/\mathrm{c}^4$], $\Delta m_{21}^2 = 7.38 \times 10^{-5} \sim 7.79 \times 10^{-5}$ [$\mathrm{eV}^2/\mathrm{c}^4$], $\sin^2 2\theta_{23} > 0.90$, $\tan\theta_{12} = 0.428 \sim 0.497$ and $\sin^2 2\theta_{13} < 0.15$. For the oscillation measurement with $E_\nu \simeq \Delta m_{32}^2 \cdot L$, the contribution of Δm_{21}^2 term is small because $\Delta m_{32}^2 \gg \Delta m_{21}^2$. Since θ_{13} is small and θ_{23} is almost equal to $\pi/4$, the probability of $\nu_\mu \to \nu_\mu$ can be approximately calculated as

$$\begin{aligned} P(\nu_\mu \to \nu_\mu) &\simeq 1 - \sin^2 2\theta_{23}\cdot\sin^2\Phi_{32}\\ &= 1 - \sin^2 2\theta_{23}\cdot\sin^2(1.27\frac{\Delta m_{32}^2[\mathrm{eV}^2/\mathrm{c}^4]L[\mathrm{km}]}{E_\nu[\mathrm{GeV}]})\\ P(\nu_\mu \to \nu_x) &= 1 - P(\nu_\mu \to \nu_\mu) \end{aligned} \tag{1.9}$$

In this way, the mixing angle θ_{23} and the mass difference Δm^2_{32} are measured through ν_μ disappearance ($\nu_\mu \to \nu_x$). In the same way, the probability of ν_e appearance ($\nu_\mu \to \nu_e$) is also calculated as

$$P(\nu_\mu \to \nu_e) \simeq \sin^2 2\theta_{13} \cdot \sin^2 \theta_{23} \cdot \sin^2(1.27\frac{\Delta m^2_{32}[\mathrm{eV}^2/\mathrm{c}^4]L[\mathrm{km}]}{E_\nu[\mathrm{GeV}]}) \tag{1.10}$$

Hence θ_{13} is measured via ν_e appearance.

1.1.3 Current understanding

There are several neutrino sources in nature: cosmic-rays interacted in Earth's atmosphere, stars and so on. In addition to them, neutrino beam can be produced by accelerators and $\bar{\nu}_e$ is emitted from fusion in reactors. Through these sources, neutrino oscillation is investigated in several experiments. Past experiments deduced that $|\Delta m^2_{32}| \simeq |\Delta m^2_{31}| = 1.9 \times 10^{-3} \sim 3.0 \times 10^{-3}$ [eV^2/c^4], $\Delta m^2_{21} = 7.38 \times 10^{-5} \sim 7.79 \times 10^{-5}$ [eV^2/c^4], $32.7 < \theta_{12} < 36.0$ degrees [13], $36.8 < \theta_{23} < 53.2$ degrees [14] and $\theta_{13} < 11.4$ degrees [15]. Thus, the PMNS matrix is

$$\begin{aligned} U_{PMNS} &= \begin{pmatrix} c_{12}c_{13} & s_{12}c_{13} & s_{13}e^{-i\delta} \\ -s_{12}c_{23} - c_{12}s_{23}s_{13}e^{i\delta} & c_{12}c_{23} - s_{12}s_{23}s_{13}e^{i\delta} & s_{s3}c_{13} \\ s_{12}s_{23} - c_{12}c_{23}s_{13}e^{i\delta} & -c_{12}s_{23} - s_{12}c_{23}s_{13}e^{i\delta} & c_{23}c_{13} \end{pmatrix} \\ &= \begin{pmatrix} 0.79 \sim 0.84 & 0.53 \sim 0.59 & < 0.20 \\ -(0.57 \sim 0.19) & 0.39 \sim 0.74 & 0.59 \sim 0.80 \\ 0.19 \sim 0.57 & -(0.72 \sim 0.42) & 0.59 \sim 0.80 \end{pmatrix} \end{aligned} \tag{1.11}$$

The mixing in quarks is described in the same way by using a 3×3 unitary matrix, called the Cabibo-Kobayashi-Maskawa (CKM) matrix. The CKM matrix is measured to be [16]

$$U_{CKM} = \begin{pmatrix} 0.97428 \pm 0.00015 & 0.2253 \pm 0.0007 & 0.00347^{+0.00016}_{-0.00012} \\ 0.2252 \pm 0.0007 & 0.97345^{+0.00015}_{-0.00016} & 0.0410^{+0.0011}_{-0.0007} \\ 0.00862^{+0.00026}_{-0.00020} & 0.0403^{+0.0011}_{-0.0007} & 0.999152^{+0.000030}_{-0.000045} \end{pmatrix} \tag{1.12}$$

The difference between U_{PMNS} and U_{CKM} may indicate the difference of the generation symmetry between leptons and quarks.

1.1.4 Generation symmetry and mixing matrix

Here, the relation between the generation symmetry and the mixing matrix is shown. The mass matrices (and mass eigen values) are just parameters in Standard Model of the particle physics. However, it is shown that the form of the mass matrices is related to the mixing matrices.

First, let's consider the quark case as an example. The Lagrangian related to the quarks can be written as

$$\bar{\boldsymbol{u}}_L M_u \boldsymbol{u}_R + \bar{\boldsymbol{d}}_L M_d \boldsymbol{d}_R + \frac{g}{\sqrt{2}} W^+_\mu \bar{\boldsymbol{u}}_L \gamma^\mu \boldsymbol{d}_L + (\mathrm{h.c.}) \tag{1.13}$$

where $\boldsymbol{u} = {}^t(u, c, t)$, $\boldsymbol{d} = {}^t(d, s, b)$ and M_u (M_d) is a 3×3 mass matrix for the up (down) type quarks. Here the Lagrangian is diagonalized to the weak interaction. As one example, a cyclic permutation (C_3) symmetry of the generation is considered;

$$\begin{aligned} &X_{u_L 1} = X_{d_L 1} = X_{u_R 1} = X_{d_R 1} = \begin{pmatrix} 0 & 0 & 1 \\ 1 & 0 & 0 \\ 0 & 1 & 0 \end{pmatrix} \\ &X_{u_L 2} = X_{d_L 2} = X_{u_R 2} = X_{d_R 2} = \begin{pmatrix} 0 & 1 & 0 \\ 0 & 0 & 1 \\ 1 & 0 & 0 \end{pmatrix} \\ &\boldsymbol{u}_L \to X_{u_L} \boldsymbol{u}_L,\ \boldsymbol{u}_R \to X_{u_R} \boldsymbol{u}_R,\ \boldsymbol{d}_L \to X_{d_L} \boldsymbol{d}_L,\ \boldsymbol{d}_R \to X_{d_R} \boldsymbol{d}_R \end{aligned} \tag{1.14}$$

For the Lagrangian to be invariant under C_3 symmetry, the mass matrix must obey the restrictions

$$M_u = X_{u_L}^\dagger M_u X_{u_R},\ M_d = X_{d_L}^\dagger M_d X_{d_R} \tag{1.15}$$

So the mass matrix must have the form

$$M_u = \begin{pmatrix} a_u & b_u & c_u \\ c_u & a_u & b_u \\ b_u & c_u & a_u \end{pmatrix},\ M_d = \begin{pmatrix} a_d & b_d & c_d \\ c_d & a_d & b_d \\ b_d & c_d & a_d \end{pmatrix}. \tag{1.16}$$

These mass matrices are diagonalized by

$$\begin{aligned} &U_{u_L} = U_{u_R} = U_{d_L} = U_{d_R} = \frac{1}{\sqrt{3}} \begin{pmatrix} 1 & e^{-2\pi i/3} & e^{2\pi i/3} \\ 1 & 1 & 1 \\ 1 & e^{2\pi i/3} & e^{-2\pi i/3} \end{pmatrix} \\ &\boldsymbol{u}_L \to U_{u_L}\boldsymbol{u}, \boldsymbol{u}_R \to U_{u_R}\boldsymbol{u} \ \Rightarrow M_u \to U_{u_L}^\dagger M_u U_{u_R} \\ &\boldsymbol{d}_L \to U_{d_L}\boldsymbol{d}, \boldsymbol{d}_R \to U_{d_R}\boldsymbol{d} \ \Rightarrow M_d \to U_{d_L}^\dagger M_d U_{d_R} \end{aligned} \tag{1.17}$$

Then the mixing matrix is extracted to be

$$U_{CKM} = U_{uL}^\dagger U_{dL} = \begin{pmatrix} 1 & 0 & 0 \\ 0 & 1 & 0 \\ 0 & 0 & 1 \end{pmatrix} \tag{1.18}$$

Small symmetry breaking can be introduced to generate off-diagonal terms in the mixing matrix. In this way, the generation symmetry (C_3 in this example) is related to the mixing matrix (Eq. 1.18 in this example).

In the same fashion, let's consider the lepton case. This time, the C_3 symmetry is assumed for the charged leptons and a $S_2 \times S_2$ symmetry for the neutrinos as one possible example:

$$\begin{aligned} &X_{L1} = X_{R1} = \begin{pmatrix} 0 & 0 & 1 \\ 1 & 0 & 0 \\ 0 & 1 & 0 \end{pmatrix},\ X_{\nu 1} = \begin{pmatrix} 0 & 0 & 1 \\ 0 & 1 & 0 \\ 1 & 0 & 0 \end{pmatrix} \\ &X_{L2} = X_{R2} = \begin{pmatrix} 0 & 1 & 0 \\ 0 & 0 & 1 \\ 1 & 0 & 0 \end{pmatrix},\ X_{\nu 2} = \begin{pmatrix} 1 & 0 & 0 \\ 0 & -1 & 0 \\ 0 & 0 & 1 \end{pmatrix} \\ &\boldsymbol{\ell}_L \to X_L\boldsymbol{\ell}_L,\ \boldsymbol{\ell}_R \to X_R\boldsymbol{\ell}_R,\ \boldsymbol{\nu} \to X_\nu\boldsymbol{\nu} \end{aligned} \tag{1.19}$$

The mass matrix must have the form

$$M_\ell = \begin{pmatrix} a & b & c \\ c & a & b \\ b & c & a \end{pmatrix},\ M_\nu = \begin{pmatrix} x & 0 & y \\ 0 & z & 0 \\ y & 0 & x \end{pmatrix} \tag{1.20}$$

and the mass matrices are diagonalized by

$$\begin{aligned} &U_\ell \equiv U_L = U_R = \frac{1}{\sqrt{3}} \begin{pmatrix} 1 & e^{-2\pi i/3} & e^{2\pi i/3} \\ 1 & 1 & 1 \\ 1 & e^{2\pi i/3} & e^{-2\pi i/3} \end{pmatrix} \\ &U_\nu = \begin{pmatrix} 1/\sqrt{2} & 0 & -1/\sqrt{2} \\ 0 & 1 & 0 \\ 1/\sqrt{2} & 0 & 1/\sqrt{2} \end{pmatrix} \end{aligned} \tag{1.21}$$

This gives so-called tri-bimaximal mixing

$$U_{PMNS} = U_\ell^\dagger U_\nu = \begin{array}{c} \\ e \\ \mu \\ \tau \end{array} \begin{array}{c} \begin{array}{ccc} \nu_1 & \nu_2 & \nu_3 \end{array} \\ \begin{pmatrix} \sqrt{2/3} & 1/\sqrt{3} & 0 \\ -1/\sqrt{6} & 1/\sqrt{3} & 1/\sqrt{2} \\ 1/\sqrt{6} & -1/\sqrt{3} & 1/\sqrt{2} \end{pmatrix} \end{array} = \begin{array}{c} \\ e \\ \mu \\ \tau \end{array} \begin{array}{c} \begin{array}{ccc} \nu_1 & \nu_2 & \nu_3 \end{array} \\ \begin{pmatrix} 0.816 & 0.577 & 0 \\ -0.408 & 0.577 & 0.707 \\ 0.408 & -0.577 & 0.707 \end{pmatrix} \end{array} \tag{1.22}$$

in a particular phase convention ($\nu_3 \to i\nu_3$, $\tau \to (-1)\tau$). This form is pointed to by the current understanding (Eq. 1.11).

To proceed discussion more quantitatively, precise measurements of the mixing angles are necessary. The θ_{13} is only known as the upper limit of 11.4 degree and the uncertainty of θ_{23} has a large contribution to the error on the current understanding. If $\sin^2 2\theta_{23}$ is measured with a precision of $\delta(\sin^2 2\theta_{23}) \sim 0.01$, the range of (2, 3) element of U_{PMNS} is down to 0.66-0.74. The $\sin^2 2\theta_{23}$ can be measured via ν_μ disappearance as shown in Eq. 1.9 and $\sin^2 2\theta_{13}$ can be measured via ν_e appearance as shown in Eq. 1.10.

1.2 Introduction to the T2K experiment

1.2.1 Overview

T2K is a long baseline neutrino oscillation experiment. The ν_μ beam is produced at J-PARC (Japan Proton Accelerator Research Complex) and detected in Super-Kamiokande (SK) which is 295 km away from J-PARC. The location of J-PARC and SK are shown in Fig. 1.1. The peak of the beam neutrino energy is ~ 0.6 GeV. Thus the measurement of the ν_μ beam in SK is sensitive to the neutrino oscillation occurred at $\Delta m^2 \sim E_\nu[\mathrm{GeV}]/L[\mathrm{km}] \sim 10^{-3}\mathrm{eV}^2/\mathrm{c}^4$.

Figure 1.1: Bird's eye view of the T2K layout

1.2.2 Purpose

The T2K experiment is proposed to measure $\sin^2 2\theta_{23}$ and Δm^2_{32} precisely via ν_μ disappearance ($\nu_\mu \to \nu_x$) and to search for finite $\sin^2 2\theta_{13}$ via ν_e appearance ($\nu_\mu \to \nu_e$): the probability of ν_μ disappearance is described in Eq. 1.9 and the probability of ν_e appearance is described in Eq. 1.10. Our goals are

- to measure $\sin^2 2\theta_{23}$ and Δm^2_{32} with a precision of $\delta(\sin^2 2\theta_{23}) \simeq 0.01$ and $\delta(\Delta m^2_{32}) \simeq 10^{-4}$ eV^2/c^4. This is an order of magnitude improvement over the result of past experiments [17–19].
- to search for $\sin^2 2\theta_{13}$ down to 0.006 at 90% confidence level. This is an order of magnitude improvement over the result of the CHOOZ limit [15].

with $\sim 8\times10^{21}$ protons on target (POT) corresponding to (proton beam of 0.75 MW) $\times$ (5 years).

1.2.3 Neutrino oscillation signals

The probability of ν_μ disappearance in SK is described in Eq. 1.9. According to that equation, the neutrino energy (E_ν) spectrum is calculated as shown in Fig. 1.2. The signal of ν_μ disappearance has two features: the distortion of the E_ν spectrum and the deficit of the ν_μ flux.

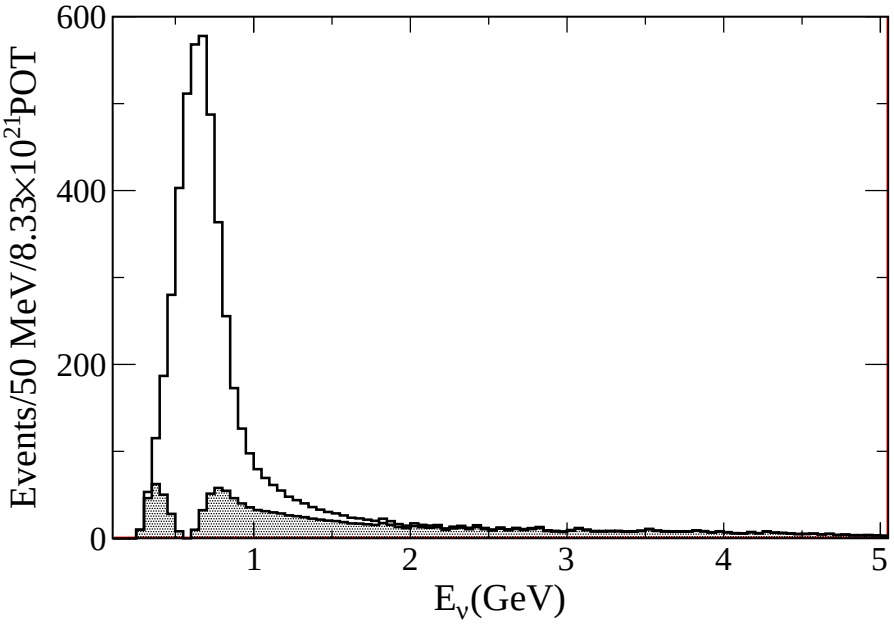

Figure 1.2: Expected neutrino energy spectrum for null oscillation (solid line) and the oscillation with $\sin^2 2\theta_{23} = 1.0$ and $\Delta m^2_{32} = 2.4 \times 10^{-3}$ eV^2/c^4 (hatched region).

The signal of ν_e appearance is the enhancement of ν_e compared to backgrounds as shown in Fig. 1.3. The main components of the background are intrinsic beam ν_e ($\sim 1\%$ in the total flux).

1.2.4 Features

To achieve the goals, T2K has several features: high intensity beam, off-axis beam, near detectors and the far detector.

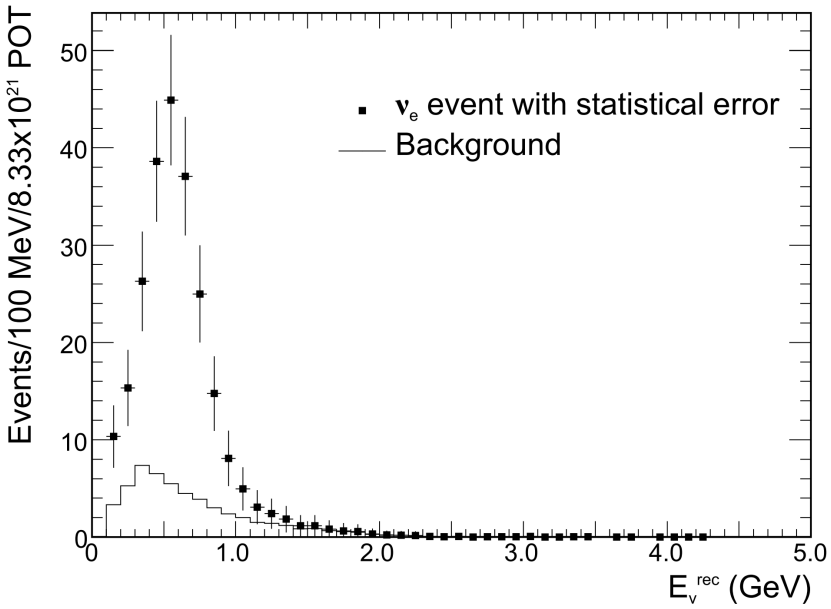

Figure 1.3: Expected number of ν_e events as a function of the reconstructed neutrino energy ($E_\nu^{\rm rec}$) for the oscillation with $\sin^2 2\theta_{13} = 0.1$, $\sin^2 2\theta_{23} = 1.0$ and $\Delta m^2_{32} = 2.4 \times 10^{-3}$ eV^2/c^4. The $E_\nu^{\rm rec}$ is calculated by the muon momentum and the angle respect to the neutrino beam direction assuming the interaction of $\nu_e + n \to e^- + p$. The solid line shows the background estimation.

High intensity beam

T2K utilizes the J-PARC 30-GeV proton beam to produce the ν_μ beam. The beam protons imping the production target and the charge pions are produced. The pions decay in flight into pairs of a muon and a muon neutrino. The muon neutrino files to SK.

J-PARC is designed to be the most powerful beam (design intensity is 750 kW) in the world. This feature is increasing the beam neutrino flux.

Off-axis beam

The second feature is the off-axis beam method; the beam axis is slightly shifted away from the direction of SK so that the muon neutrino beam has narrow energy peak. This increases the signal to the background ratio.

Here we give an explanation of the off-axis method [20]. The ν_μ beam is produced from the charged pion decay ($\pi \to \mu\nu_\mu$). The energy of the neutrino in the pion rest frame (in which quantities are labeled with the superscript $*$) is

$$E_\nu^* = \frac{m_\pi^2 - m_\mu^2}{2m_\pi} = 29.8 \text{ MeV} \tag{1.23}$$

The laboratory frame 4-momentum can be calculated by Lorentz transformation:

$$\begin{pmatrix} \\ p_\mu \\ \\ \end{pmatrix} \rightarrow \begin{bmatrix} \gamma_\pi & 0 & 0 & \gamma_\pi\beta_\pi \\ 0 & 1 & 0 & 0 \\ 0 & 0 & 1 & 0 \\ \gamma_\pi\beta_\pi & 0 & 0 & \gamma_\pi \end{bmatrix} \begin{pmatrix} \\ p_\mu \\ \\ \end{pmatrix} \tag{1.24}$$

$$\begin{aligned} &(E_\nu, E_\nu \sin\theta, 0, E_\nu \cos\theta) \\ \rightarrow &(E^*_\nu\gamma_\pi(1+\beta_\pi\cos\theta^*), E^*_\nu \sin\theta^*, 0, E^*_\nu\gamma_\pi(\beta_\pi+\cos\theta^*)) \end{aligned} \tag{1.25}$$

where θ is angle between the pion momentum and the neutrino momentum. The relation between the angle in the pion rest (θ^*) and that in the lab. frame (θ) is obtained from the 1st and 3rd components of Eq. 1.25:

$$\tan\theta = \frac{E^*_\nu \sin\theta^*}{E^*_\nu\gamma_\pi(\beta_\pi + \cos\theta^*)} \tag{1.26}$$

If $E_\nu, E_\pi \gg m_\pi$ and then $\beta_\pi \simeq 1$, we can re-write Eq. 1.26 to

$$\tan\theta \simeq \frac{E^*_\nu \sin\theta^*}{E_\nu} \tag{1.27}$$

using the 0th component of Eq. 1.25. This equation indicates that a maximum lab angle θ_{max} is obtained at $\theta^* = 90°$:

$$\tan\theta_{max} \simeq \frac{E^*_\nu}{E_\nu} \tag{1.28}$$

In other words, there is a maximum neutrino energy ($E_\nu^{max.}$) with fixed angle θ:

$$E_\nu^{max.} \simeq \frac{E^*_\nu}{\tan\theta} = \frac{29.8\text{MeV}}{\tan\theta} \tag{1.29}$$

The relation between E_ν, E_π and θ is obtained from the 0th component of Eq. 1.25:

$$E_\nu = \frac{\gamma_\pi + \gamma_\pi\beta_\pi\sqrt{1-\tan^2\theta}}{1+\gamma_\pi^2\beta_\pi^2}E^*_\nu \tag{1.30}$$

, and is shown in Fig. 1.4. As expected from Eq. 1.29, there is a maximum neutrino energy $E_\nu^{max.}$ with non-zero θ, and as the neutrino energy approaches this value, pions in large range of energies contribute to neutrinos in a small range of energy. Thus semi-monochromatic energy neutrino beam with the peak around $E_\nu^{max.}$ is achieved with the fixed angle θ which is called as the off-axis angle.

In T2K, the off-axis angle is set to be 2.5 degrees so that the ν_μ beam has a narrow energy peak at ~ 0.6 GeV as shown in Fig. 1.5 (top). This maximizes the effect of the neutrino oscillation at the far detector located at 295 km away from the beam origin because the oscillation probability has a peak around $E_\nu \sim 0.6$ GeV as shown in Fig. 1.5 (middle). In addition, this reduces background neutrino interactions as shown in Fig. 1.5 (bottom); our signal is Charged Current Quasi-Elastic (CCQE) interaction as explained in Section 1.2.5 and the background is Charged Current π production (CC1π) and Neutral Current π production (NC1π) interaction.

As shown in Fig. 1.5 top, the neutrino beam energy varies depending on the off-axis angle. Therefore, the beam direction measurement is directly connected to the precision of the neutrino oscillation measurement in T2K. Hence the measurement of the neutrino beam direction is very important. To achieve the precision of $\delta(\sin^2 2\theta_{23}) \sim 0.01$ at T2K, the beam direction is required to be measured with a precision better than 1 mrad [21].

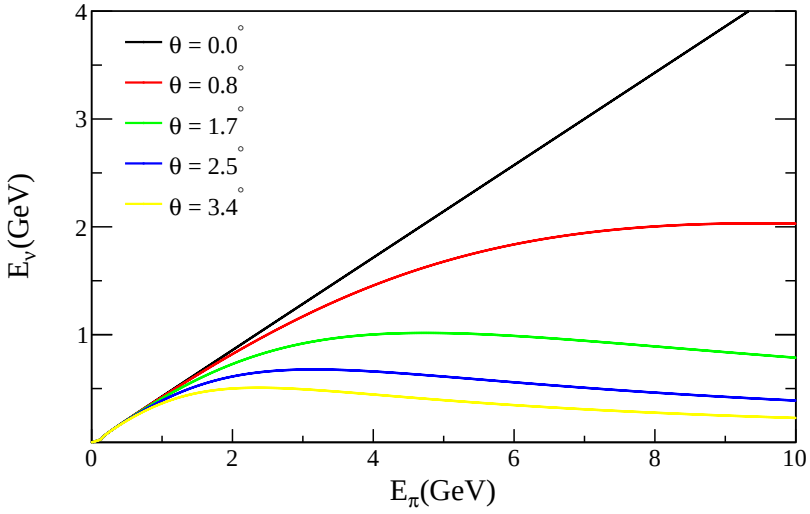

Figure 1.4: Relation between neutrino energy (E_ν) and pion energy (E_π) in the pion decay with several off-axis angles.

Near detector measurement

Third feature of T2K is sophisticatedly designed near detectors. We have two near detectors for different purposes; an on-axis near detector and an off-axis near detector. The on-axis near detector, INGRID (Interactive Neutrino GRID), measures the neutrino beam direction and the neutrino event rate. The beam direction measurement is necessary to precisely predict the neutrino energy spectrum in SK. INGRID is designed to have sufficient target mass to measure the beam direction on a day-by-day basis with the 0.75 MW proton beam operation. Since the neutrino oscillation analysis is performed on the assumption that the neutrino beam is stable, the confirmation of the beam stability is important. The off-axis near detector, ND280, measures the beam neutrino properties in the same direction to SK. In that position we can measure the beam properties corresponding to those expected at the far detector.

Far detector measurement

Fourth feature is the far detector, the Super-Kamiokande (SK) water Cherenkov detector. SK has sufficient mass of 50 kton to accumulate the beam neutrino events. By using Cherenkov ring pattern, SK has capability to catch the oscillation signals as described in Section 1.2.5. Water Cherenkov detectors promise us the high performance to identify the neutrino interaction type around sub-GeV energy region.

1.2.5 Analysis strategy

To catch the oscillation signals, we detect the beam neutrinos in SK which is 295 km away from J-PARC. Especially the neutrino charged current quasi-elastic (CCQE) interaction event,

$$\nu_\ell + n \to \ell^- + p \tag{1.31}$$

is selected because of following reasons.

- The CCQE interaction is a dominant interaction mode in the T2K neutrino energy region. About 40% interactions are expected to be the CCQE interactions in SK in case without neutrino oscillation.

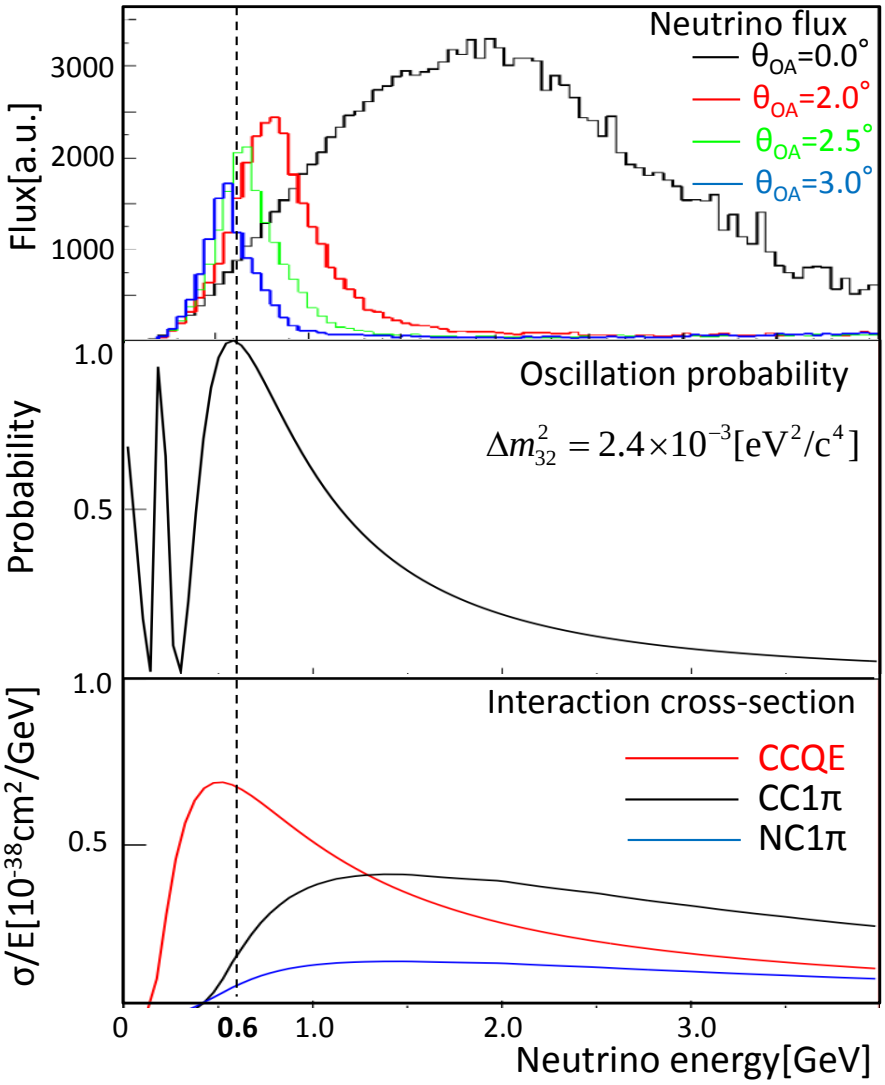

Figure 1.5: (Top) Neutrino energy spectra with several off-axis angles (θ_{OA}). (Middle) Oscillation probability as a function of the neutrino energy. (Bottom) Neutrino interaction cross-sections.

- The neutrino energy can be reconstructed ($E_\nu^{\rm rec}$) by measuring the lepton momentum (p_ℓ) and the angle with respect to the neutrino (θ_ℓ):

$$E_\nu^{\rm rec} = \frac{(m_n - V)E_\ell + (m_p^2 - m_\ell^2)/2 - (m_n - V)^2/2}{(m_n - V) - E_\ell + p_\ell \cos\theta_\ell} \tag{1.32}$$

  where m_n, m_p and m_ℓ are the mass of the neutron, proton and lepton, respectively. E_ℓ is the lepton energy and V is the nuclear potential of nucleus (it is 27 MeV for oxygen).

- Flavor of the neutrino can be determined by identifying the flavor of the lepton

In order to select the CCQE interaction event, we require only one Cherenkov ring in SK because the associated proton often does not emit Cherenkov light due to its high Cherenkov threshold in water ($\sim$ 1.1 GeV/c). The momentum of the muon or the electron can be reconstructed by observed number of Cherenkov photons. The direction of the muon or the electron is determined by the Cherenkov ring direction. The muon and electron can be distinguished because a muon makes a sharp edge ring and an electron makes a fuzzy one due to electromagnetic showers.

For an analysis of the neutrino oscillation in ν_μ disappearance, both the energy spectrum and the number of the muon neutrino events in SK are compared between expectation and observation. The energy spectrum at SK, $\Phi_{SK}(E_\nu)$, strongly depends on the off-axis angle as described in Section 1.2.4. Hence precise measurement of the beam direction is important for the $\Phi_{SK}(E_\nu)$ estimation. In this thesis, the expected number of events at SK ($N_{\rm SK}^{\rm exp.}$) is calculated by using the number of events measured in the near detector ($N_{\rm ND}^{\rm obs}$):

$$\begin{aligned} N_{\rm SK}^{\rm exp} &= N_{\rm ND}^{\rm obs} \cdot \frac{N_{\rm SK}^{\rm MC}}{N_{\rm ND}^{\rm MC}} \\ &= N_{\rm ND}^{\rm obs} \cdot \frac{\int dE_\nu \Phi_{SK} \cdot \sigma_{SK} \cdot \epsilon_{SK} \cdot P(E_\nu; \sin^2 2\theta_{23}, \Delta m^2_{32})}{\int dE_\nu \Phi_{ND} \cdot \sigma_{ND} \cdot \epsilon_{ND}} \end{aligned} \tag{1.33}$$

where σ_{SK} (σ_{ND}) is the neutrino cross-section of the target material of SK (ND), ϵ_{SK} (ϵ_{ND}) is the detection efficiency of SK (ND), and P is the oscillation probability as described in Eq. 1.9. One of the characteristic of Eq. 1.33 is the error cancellation between ND and SK. For example, Φ_{ND} and Φ_{SK} have a common uncertainty of the production rate of the parent pions. Because the uncertainty is included in both the numerator and the denominator, the uncertainty in Φ_{SK}/Φ_{ND} is canceled even if Φ_{SK} or Φ_{ND} itself has ambiguities. Thus the event rate measurement at the near detectors is important for the $N_{\rm SK}^{\rm exp.}$ estimation.

An analysis of the neutrino oscillation in ν_e appearance is performed with almost same procedure; the beam direction measurement is also important for this analysis.

1.2.6 Experimental setup

Here, overview of the T2K experiment setup is described. More details are describe in Chapter 2.

Neutrino beamline

Figure 1.6 shows a schematic of the way to produce the ν_μ beam in T2K. The 30 GeV protons are hit on a graphite target to produce charged pions. The pions are focused by three magnetic horns and decay in flight into pairs of a muon and a muon neutrino. The muons are stopped by the beam dump and subsequent soil.

To confirm the stable beam neutrino production, it is important to monitor the beam neutrino directly by the near detector.

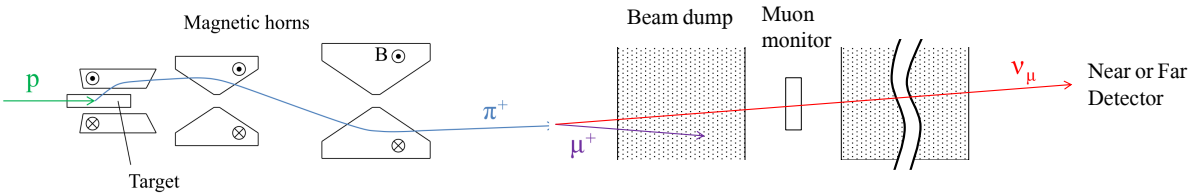

Figure 1.6: Schematic of the way to produce the muon neutrino beam at T2K.

Near detectors

We have two near detectors; INGRID and ND280. These are located $\sim$ 280 m away from the graphite target. To confirm the stable beam neutrino production, we measure the neutrino event rate and the beam direction by using INGRID. These measurements are also necessary to precisely estimate both the expected number of events and the expected energy spectrum in SK. We also measure the neutrino event rate by using ND280. Because neutrino properties at ND280 are close to that at the far detector, we can reduce the uncertainty on $N_{\mathrm{SK}}^{\mathrm{exp.}}$ thanks to the error cancellation between $N_{\mathrm{SK}}^{\mathrm{MC}}$ and $N_{\mathrm{ND}}^{\mathrm{MC}}$.

Super-Kamiokande

We employ Super-Kamiokande (SK) as the far detector of T2K. As described in Section 1.2.5, SK is able to measure the number of neutrino events and the neutrino energy by detecting the single Cherenkov ring event. In addition, SK is suitable as the far detector because SK has large mass to accumulate neutrino events; about two events are expected to be observed in a day with the 0.75 MW proton beam operation. Because ambiguities of the SK measurements are directly connected to the ambiguities of the oscillation signals, it is important to estimate the systematic uncertainties of the SK measurement.

1.3 Outline of this thesis

This thesis first describes the measurement of the neutrino beam direction and the event rate by using the INGRID detector. Both measurements are needed for the oscillation analysis as described. Then this thesis focuses on an analysis of the neutrino oscillation in ν_μ disappearance with the first T2K physics data set, corresponding to 1.43×10^{20} protons on target.

The outline is as follows. Chapter 2 introduces the T2K experimental setup. INGRID and its basic performance are subsequently described in Chapter 3. The MC simulations are explained in Chapter 4. Chapter 5 gives an introduction of the analysis. The measurement of the beam neutrino event rate and the beam direction by using INGRID, and the event rate measurement by using ND280 are described in Chapter 6. The analysis of Super-Kamiokande is described in Chapter 7 together with the estimation of the systematic uncertainties, and the neutrino oscillation analysis is performed in Chapter 8. Finally, the conclusion is summarized in Chapter 9.

Chapter 2

T2K Experiment

This chapter gives an overview of the experimental setup of the T2K experiment [22]. It consists of the proton accelerator (Section 2.1), the neutrino beamline (Section 2.2), the near detectors (Section 2.3) and Super-Kamiokande (Section 2.4).

2.1 Proton accelerator

The primary proton beam is provided by the 30-GeV proton synchrotron at J-PARC (Japan Proton Accelerator Research Complex). J-PARC consists of three accelerators as shown in Fig. 2.1: a linear accelerator (LINAC), a Rapid-Cycling Synchrotron (RCS) and the Main Ring (MR). A H^- beam is accelerated up to 181 MeV (400 MeV in future) by LINAC, and is converted to an H^+ beam at the RCS injection. Then the beam is accelerated up to 3 GeV by RCS, injected to MR, and accelerated to 30 GeV. The eight of nine bunches in MR are filled by the beam and extracted to the T2K neutrino beamline in one turn. The bunch spacing is 581 nsec and the spill spacing is 3.52 sec up to June 2010, 3.2 sec during November 2010 to March 7th 2011, and 3.04 sec during March 8th to 11th. The parameters of the extracted proton beam are listed in Tab. 2.1.

Table 2.1: Parameters of the extracted proton beam to the T2K neutrino beamline

Kinetic energy	30 GeV
Number of bunches	6 /spill (up to June 2010) 8 /spill (from November 2010 to March 2011)
Number of protons	$6 \times 10^{12} \sim 9 \times 10^{13}$ /spill (corresponding to 8∼145 kW)
Bunch interval	581 nsec
Bunch width	58 nsec
Spill interval	3.52 sec (up to June 2010) 3.2 sec (November 2010 ∼ March 7th 2011) 3.04 sec (March 7th 2011 ∼ March 11th 2011)

2.2 Neutrino beamline

The 30-GeV proton beam is extracted from MR to the T2K neutrino beamline. The neutrino beamline is composed of two sections: the primary and secondary beamlines. In the primary beamline, the extracted proton beam is bent to proper direction against Super-Kamiokande and

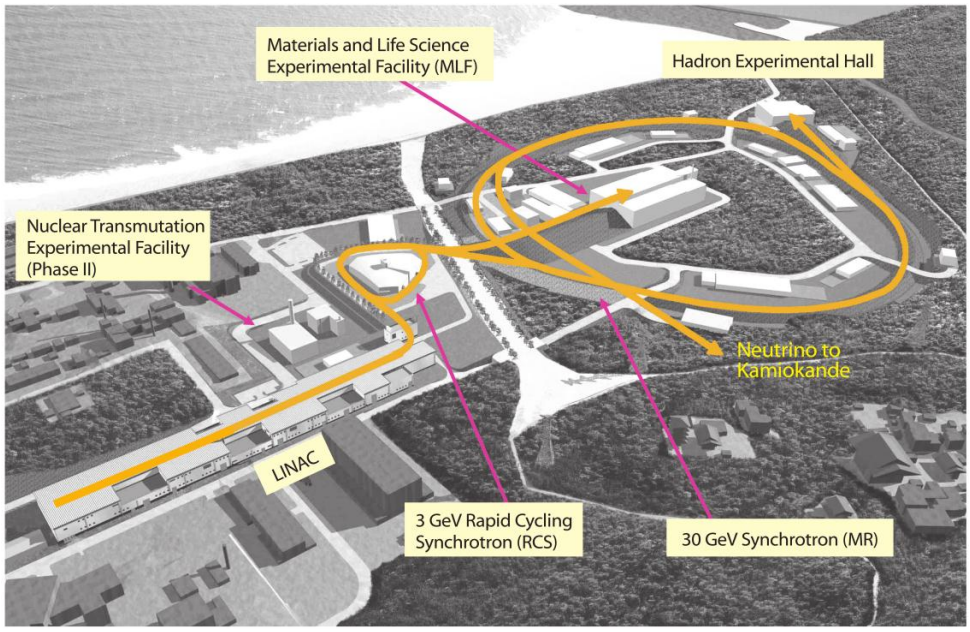

Figure 2.1: Bird eye's view of the J-PARC site.

transported to the neutrino production target. In the secondary beamline, the proton beam impinges on the target to produce secondary pions. Those pions are focused by magnetic horns and decay into neutrinos.

2.2.1 Primary beamline

Figure 2.2 shows a schematic view of the primary beamline. The proton beam is extracted to the preparation section ($\sim$ 50 m) and bent by 80.7 degrees in the arc section ($\sim$150 m). The beam is finally directed downward by 3.636 degrees and focused to the target in the final focusing section ($\sim$ 40 m).

There are several beam monitors in the primary beamline to monitor the proton beam intensity, timing, position, profile and beam loss. The location of each monitor is shown in Fig. 2.2.

The beam intensity and timing is monitored by current transformers (CT). The CT is a toroidal coil which picks up the induced magnetic field by the proton beam. The precision of the absolute intensity, relative intensity and beam timing are 2%, 0.5% and 5 nsec, respectively.

The beam position is monitored by electro statics beam position monitors (ESM). The ESM has four round-rectangular electrodes surrounding the proton beam and measures top-bottom and left-right asymmetry of the induced electric field by the proton beam to monitor the beam position (Fig. 2.3). The precision of the beam center position is estimated to be less than 0.45 mm, while the required precision is 0.50 mm.

The beam profile is monitored by segmented secondary emission profile monitors (SSEM). The SSEM has two thin titanium foils stripped horizontally and vertically to the beam orbit. The beam profile is reconstructed by measuring charges induced by the emission of the secondary electrons (Fig. 2.4). The precision of the beam center position and the beam width are estimated to be less than 0.45 mm and 0.20 mm, respectively.

The beam loss is monitored by wire proportional chamber filled with Ar-CO_2 mixture. The signal is integrated during each spill, and if it exceeds a threshold, a beam abort signal is fired.

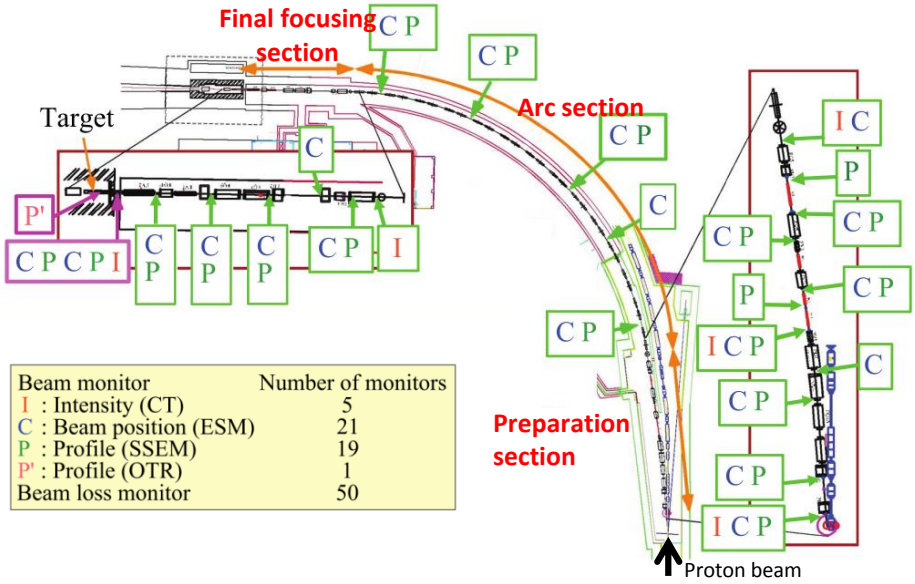

Figure 2.2: Top view of the primary beamline. I, C, P and P' show location of the CT, ESM, SSEM and OTR, respectively.

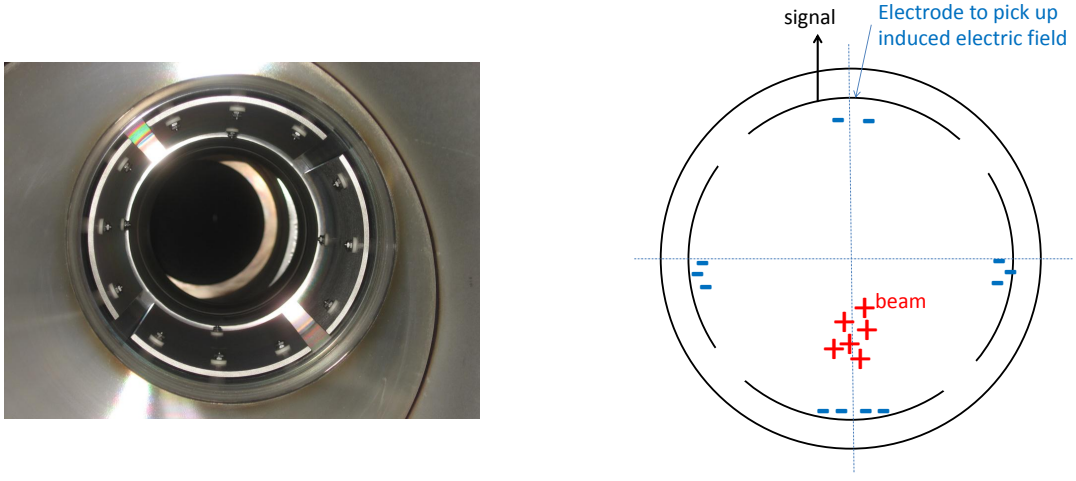

Figure 2.3: Left: The ESM viewed from inside the beampipe. right: schematic of how to measure the beam position by the ESM.

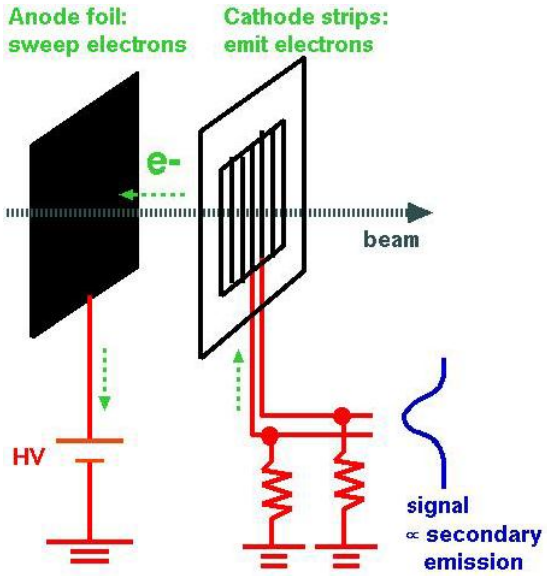

Figure 2.4: Schematic of how to measure the beam profile by the SSEM.

2.2.2 Secondary beamline

Figure 2.5 shows the side view of the secondary beamline. The proton beam goes through the baffle, which is a graphite block with a beam hole of 30 mm in a diameter, and impinges the production target.

The optical transition radiation (OTR) monitor is installed between the baffle and the target to monitor the beam profile and center. The OTR monitor uses optical transition radiation, the emission of visible photons when energetic charged particles traverse a boundary between media with different dielectric constants. A titanium alloy foil is placed at 45 degrees to the proton beam, so that backward going OTR light from the foil is reflected at 90 degrees to the beam. The light is transported by mirrors and collected by a CCD camera. The precision of the beam center and width measurement is estimated to be 0.4 mm and 0.3 mm, respectively.

Production target and magnetic horns

The production target is a 2.6 cm diametral, 91.4 cm long graphite rod, which corresponds to 1.9 interaction length. The target is inserted in the first horn.

T2K uses three horns. Each magnetic horn consists of two coaxial (inner and outer) conductors. The conductors encompass a closed volume in which a toroidal magnetic field is generated [23]. The maximum field is 2.1 T for the current at 320 kA (250 kA for the data set used in this thesis). Positive pions are focused by the horns, and negative ones are defocused.

Decay volume and beam dump

The pions decay to muon neutrinos and muons in the decay volume. The decay volume is a 96 m long steel tunnel. The cross section is 1.4 m wide and 1.7 m high at the entrance, and 3.0 m wide and 5.0 m high at the end.

At the end of the decay volume, there is a beam dump composed of 3.174 m long, 1.94 m wide and 4.69 m high graphite blocks. The beam dump stops all the particles except for neutrinos and high energy muons.

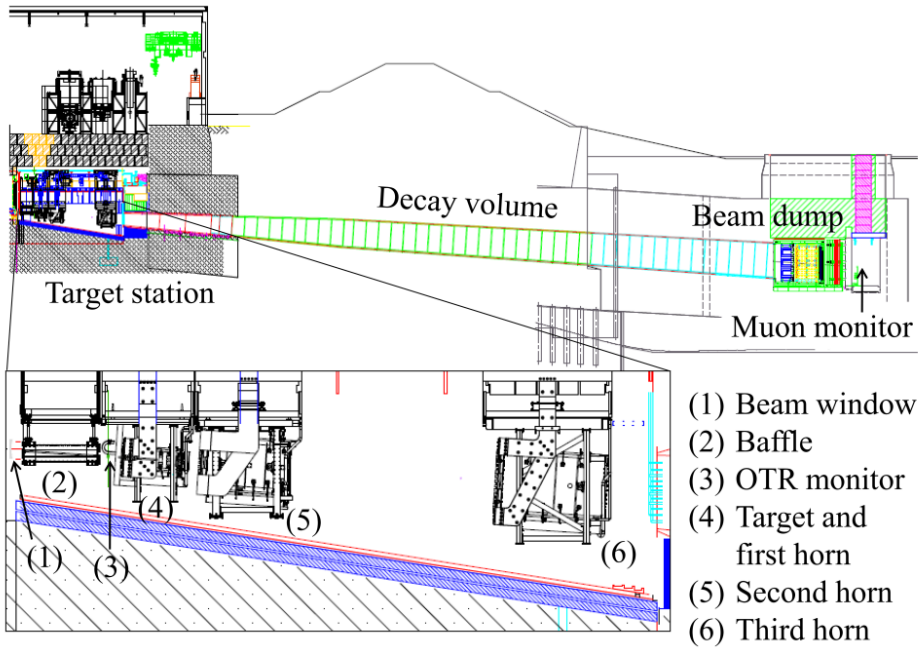

Figure 2.5: Side view of the secondary beamline.

Muon monitor

The muon monitor located just after the beam dump ($\sim$ 118 m downstream from the target) measures the muon intensity and profile. The muon monitor consists of two types of detector arrays: ionization chambers and silicon PIN photodiodes as shown in Fig. 2.6. Each array holds 49 sensors at 25 cm $\times$ 25 cm intervals and covers a 150×150 cm^2 area. The two-dimensional muon profile is reconstructed in each array for each spill. The precision of the muon intensity and direction are estimated to be $\sim 0.1\%$ and 0.2 mrad, respectively. The details of the muon monitor are described in [24].

Data acquisition and event synchronization

The data of the neutrino beam lines are taken on a spill by spill basis. The data acquisition system is triggered by a signal synchronized with the MR extraction. The local time clock (LTC) module receives the timing signal and sends the trigger signal to the beamline monitors.

The LTC modules is a heart of the event synchronization between J-PARC and Super-Kamiokande. It records time based on 1 pps (pulse per second) signals from two independent GPS receivers, 1 pss from the Rb clock, and 100 MHz internal clock. When the MR synchronized signal is received, the LTC module counts the accumulated number of received signals as the spill number and sends its spill number and its time to Super-Kamiokande which has the same LTC system. The Super-Kamiokande LTC module immediately sends back the spill number and its time for consistency check. This system provides $O(50$ nsec) scale synchronization between the neutrino beamline and Super-Kamiokande [*]. The LTC module also provides the trigger for near detectors.

[*]It is expected to be improved because of the GPS common-view system operating from RUN-II.

Figure 2.6: Photograph of the muon monitor inside the support enclosure. The silicon PIN photodiode array is on the right side and the ionization chamber array is on the left side. The muon beam enters from the right side.

2.3 Near detectors

The near detectors are located approximately 280 m away from the production target. There are two detectors (Fig. 2.7); one is an on-axis near detector, INGRID (Interactive Neutrino GRID), to measure the neutrino beam direction and intensity, and the other is an off-axis near detector, ND280, to measure the beam neutrino properties in the same direction as the far detector. Details of INGRID are described in Chapter 3.

Figure 2.8 shows an exploded view of ND280. The ND280 elements are contained inside the UA1 magnet [25]. The magnet consists of aluminum coils, which create the dipole field oriented horizontally to the beam, and a flux return yoke, which is eight C-shaped yokes made of low-carbon steel plates. The inner dimensions of the magnet are $3.5 \times 3.6 \times 7.0$ m^3. The magnet is operated with a horizontal uniform magnetic field of 0.188 T during RUN-I and 2.02 T during RUN-II. The ND280 elements are aligned along the beam direction; from the upstream of the beam, there is a Pi-Zero Detector [26] (P0D), three Time Projection Chambers [27] (TPCs) interleaved with two Fine Grained Detectors [28] (FGDs) and the DownStream Electromagnetic Calorimeter (DSECal). The P0D, TPCs, and FGDs are surrounded on all four sides by Electromagnetic Calorimeter (ECal). All sides of the magnet are instrumented with the Side Muon Range Detector [29]. Because the neutrino event rate is measured by using FGDs and TPCs in this thesis, these detectors are described below.

Two FGDs serves as neutrino interaction target and detects the charged particles coming from the interaction vertex. The FGDs are constructed from 9.61 mm×9.61 mm×1864.3 mm bars of extruded polystyrene scintillator, which are oriented perpendicular to the beam in either horizontal and vertical direction. Total volume of each FGD is 2300 mm×2400 mm×365 mm and the mass is 1.1 tons. The scintillator bar has a hole in its center in which a wave length

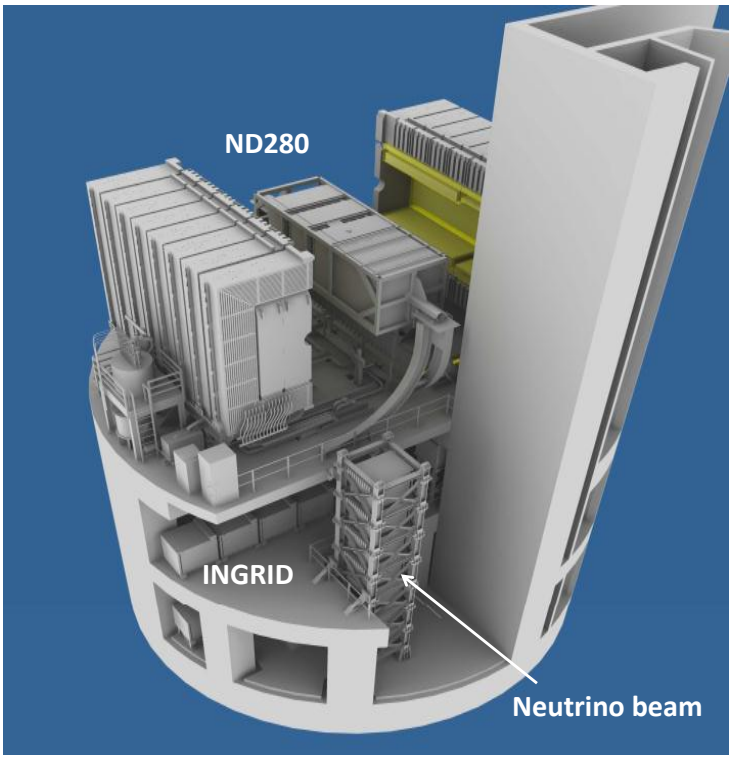

Figure 2.7: T2K near detectors. The ND280 detector and the magnet are located at the upper level, and the vertical and horizontal INGRID modules are located at the middle and bottom levels. The magnet is opened in this figure, though it is operated with its close position.

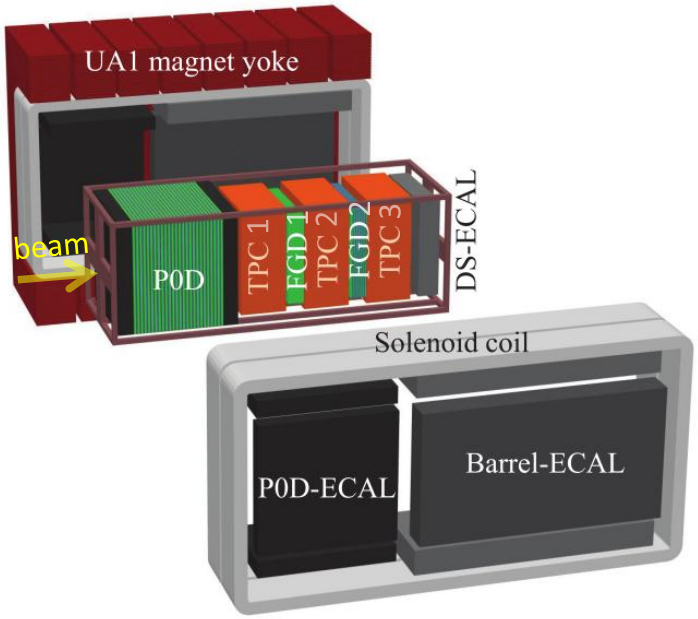

Figure 2.8: Exploded view of ND280. The neutrino beam enters from the left side. The magnet is shown in its open position, though it is operated with its close position.

shifting (WLS) fiber is inserted. The scintillation light is collected and transported via the WLS fiber to the photosensor attached at one end of the fiber.

The TPCs perform three functions: tracking of the particles coming from FGD's or P0D, measurement of momentum with the magnetic field, and measurement of the ionization loss for particle-identification. The TPCs use a gas mixture Ar:CF4:iC$_4$H$_{10}$ (95:3:2) and MicroMegas detectors [30]. The point spatial resolution is estimated to be 0.7 mm. The resolution of deposited energy is estimated to be 7.8% for minimum ionization particles.

2.4 Super-Kamiokande detector

Super-Kamiokande serves as the far detector in T2K. It is in operation also to study the atmospheric and solar neutrinos, to watch cosmic neutrinos from supernova explosions, to search for proton decay, and more. Super-Kamiokande is located 295 km west of J-PARC and is in the Kamioka mine, 1 km deep inside a mountain. It is a cylindrical cavern, 39 m in diameter and 41 m in height (Fig. 2.9), filled with 50 kton of pure water and has a 22.5 kton fiducial volume. It is mainly comprised of two segments: the inner detectors (ID) and outer detectors (OD). ID is completely surrounded by OD. The size of ID is 36.2 m in height and 33.8 m in diameter, containing 32 ktons of water (Fig. 2.10). ID (OD) holds 11129 (1885) inward-facing (outward-facing) 20-inch (8-inch) diameter photomultiplier tubes (PMTs) on its cylindrical wall. Neutrinos are detected with these PMTs by measuring Cherenkov lights emitted by charged particles from neutrino interactions in water. The Cherenkov lights are fitted to rings, from which the particle's vertex, energies, directions and species are reconstructed. Neutrino interactions are distinguished from the other activities like cosmic muons by selecting events in which the vertex exists inside the fiducial volume. Details of Super-Kamiokande are described in [22, 31].

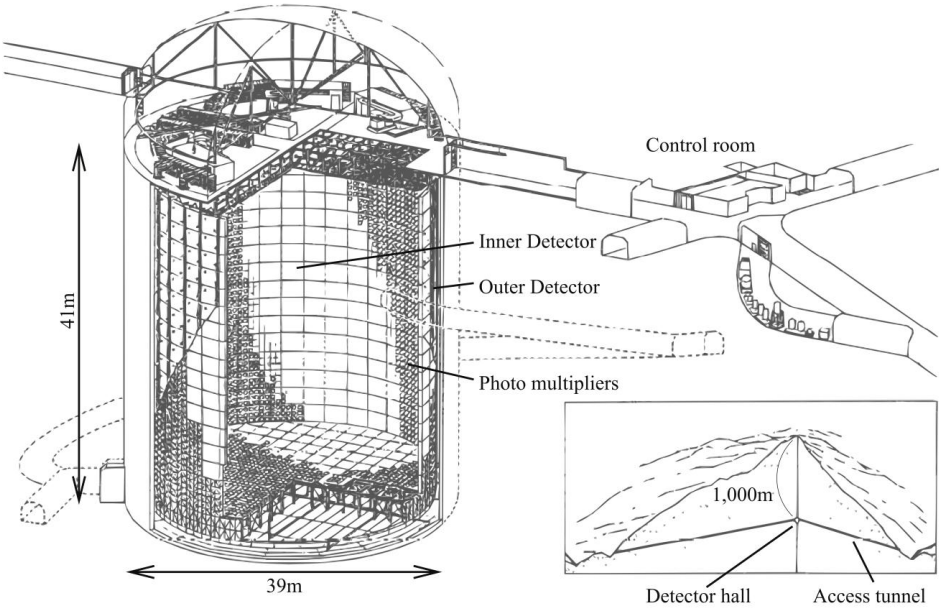

Figure 2.9: Schematic overview of Super-Kamiokande. This figure comes from [32]

T2K beam data

The charge and timing of all the hit PMTs (hit threshold is $\sim$ 0.25 PE) within 500 μsec from the beam arrival time (Fig. 2.11) are written to disk. The hits are fed into the offline processing

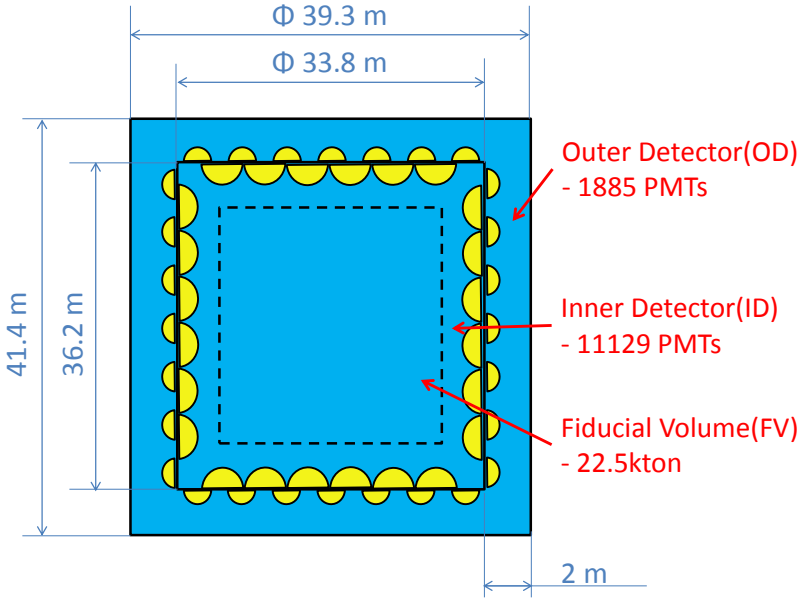

Figure 2.10: Cross section view of the SK water tank.

and the neutrino event selection as described in Section 7.2.

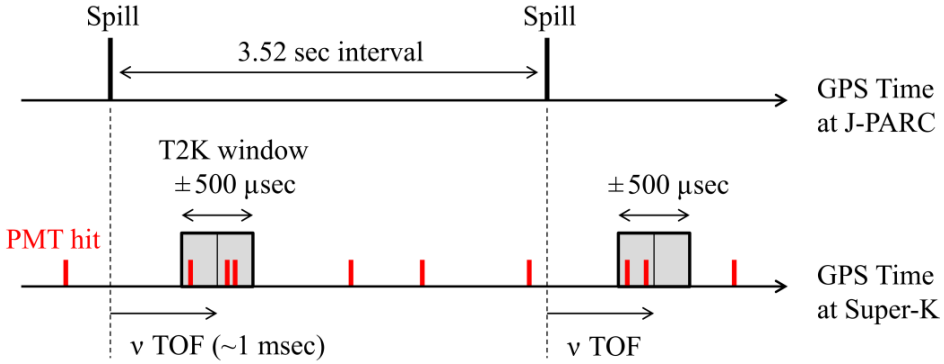

Figure 2.11: Illustration of the timing of the data taking at Super-Kamiokande. The T2K time window for ± 500 μsec is set at the beam arrival time which is aproximately 1 msec of the neutrino time of flight after each spill.

Chapter 3

INGRID Detector

The INGRID (Interactive Neutrino GRID) detector is an on-axis neutrino near detector located at 280 m downstream from the proton target. This chapter describes the detector configuration, the details of each component, and the basic performance of INGRID.

3.1 Detector configuration

The main purpose of the INGRID detector is to monitor the neutrino beam profile center with a precision better than 28 cm; 28 cm corresponds to 1 mrad of the beam direction at the INGRID location (280 m $\times$ 1 mrad). The spatial width (1σ) of the neutrino beam at the INGRID location is about five meters as shown in Fig. 3.1. Because the decay volume has the rectangular cross-section (See Section 2.2.2), the spatial width is different in the x direction and the y direction. To cover the sufficient region of the beam profile, INGRID is designed to sample the beam in a transverse section of 10 m $\times$ 10 m with 14 identical modules arranged as a two identical groups along the horizontal axis and vertical axis, as shown in Fig. 3.2. Two separate modules, called as shoulder modules, are placed at off-axis positions off the main cross to monitor the asymmetry of the beam. The measurements using the shoulder modules is not covered in this thesis and INGRID means the horizontal seven modules and the vertical seven modules here.

Each of the module consists of nine iron target plates and eleven tracking scintillator planes as shown in Fig. 3.3 left. They are surrounded by veto scintillator planes (Fig. 3.3 right) to reject charged particles coming from outside the modules. The dimensions of the iron target plates are 124×124 cm^2 in the horizontal and vertical directions and 6.5 cm along the beam direction. The total iron mass serving as a neutrino interaction target is 7.1 tons per module. The tracking scintillator plane consists of two scintillator layers: the layers arranged in the horizontal and vertical directions. Each layer has 24 scintillator bars, constructing a plane of 120×120cm^2 in the horizontal and vertical directions and 1.0 cm along the beam direction. The veto scintillator plane consists of one scintillator layer which is made by 22 scintillator bars segmented along the beam direction in order to identify the coming charged particles produced by neutrino interactions in upstream wall of the detector hole.

Figure 3.4 shows an example of neutrino event candidates in one module. Neutrino interaction events are selected by reconstructing the track of charged particles generated in neutrino interactions in the iron target. The horizontal and vertical neutrino beam profiles are reconstructed from the number of observed events in each module.

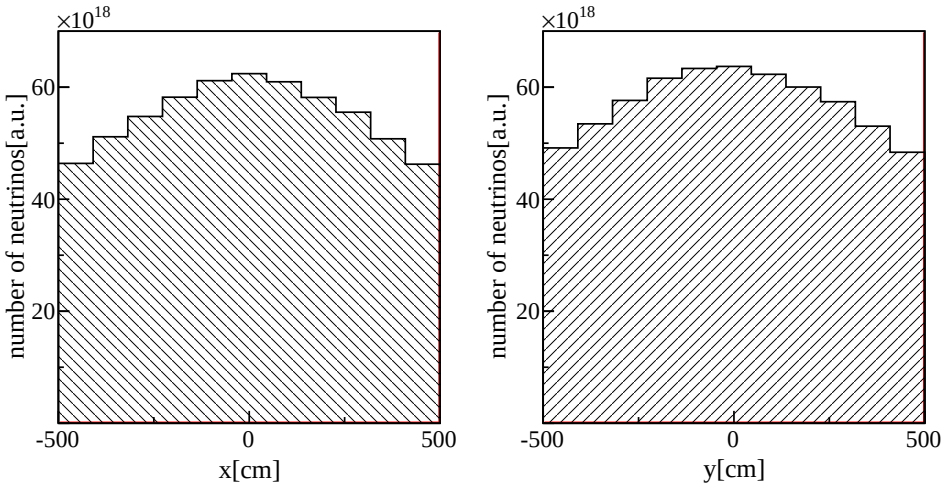

Figure 3.1: Expected neutrino beam profile at the INGRID location (280 m downstream from the primary proton beam target). Left distribution is the horizontal profile and right distribution is the vertical profile. The spatial width (1σ) of both profiles is about five meters.

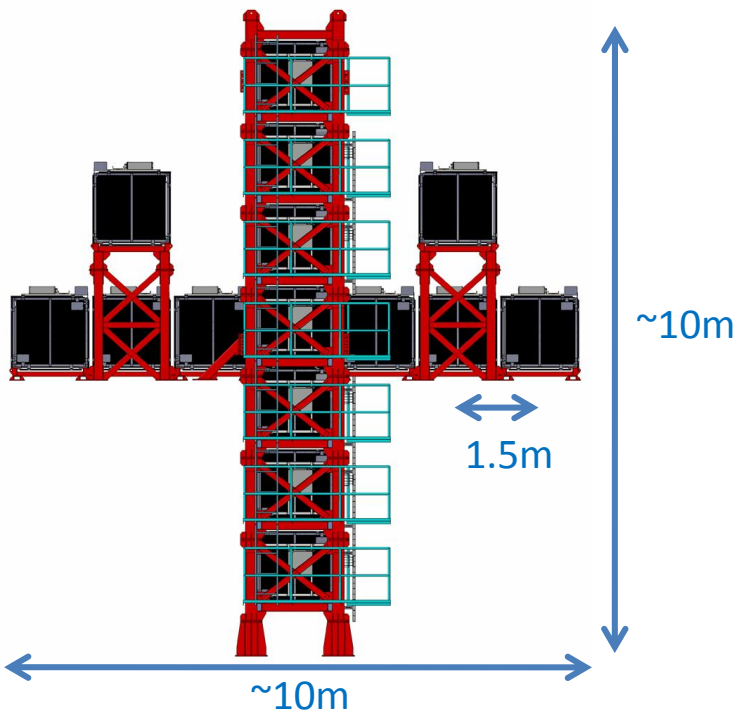

Figure 3.2: Overview of the INGRID detector.

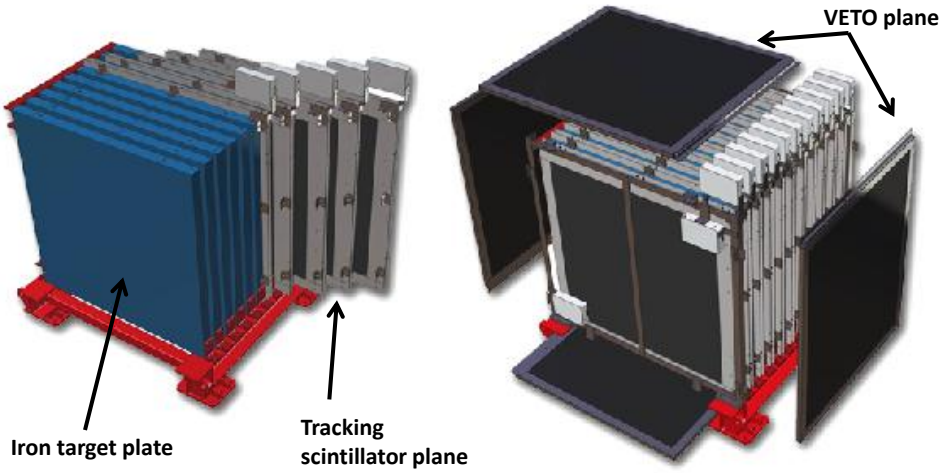

Figure 3.3: Exploded view of the INGRID module. It consists of nine iron target plates and eleven scintillator trackers (left), and it is surrounded by the scintillator VETO planes (right).

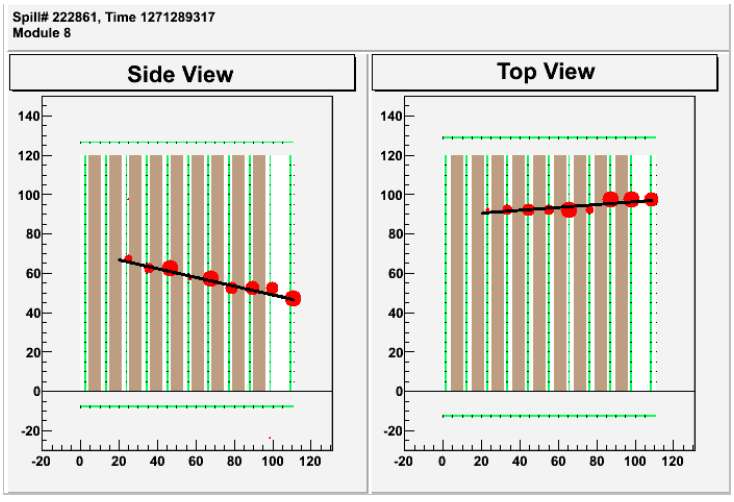

Figure 3.4: Typical neutrino interaction event candidate in one module in the real data. A beam neutrino enters from the left and interacted in the 2nd iron target plate. The size of the circles is proportional to the observed number of photo-electrons at each scintillator bar, and black lines show the reconstructed tracks in the side and top views.

3.2 Detector elements

3.2.1 Extruded scintillator

All the INGRID scintillator bars were produced at Fermilab [33]. The scintillator bars are made of polystyrene, infused with PPO (1%) and POPOP (0.03%), and are produced by extrusion in the shape of rectangular (1.0 cm × 5.0 cm) bar with white reflective coating composed of TiO_2 infused in polystyrene (15% by weight). The wavelength of the scintillation light at the emission peak is 420 nm. One side of the rectangular face, far from light readout, is painted with white reflective coating (ELJEN® EJ-510). The length of the scintillator bars is 120.3 cm, 111.9 cm and 129.9 cm for the tracking, top/bottom-veto and right/left-veto planes, respectively. A hole of about 3 mm in diameter at the center of the scintillator bar allows the insertion of a wavelength shifting (WLS) fiber for light collection. INGRID has 8360 scintillator bars in total.

In order to build a scintillator tracking plane, a vertical and a horizontal layers are glued together using epoxy resin (Cemedine PM-200) with aluminum (A6063) frames and black plastic (ABS) plates surrounding the layers (Fig. 3.5). In addition, rubber (EPDM) strips are attached between the aluminum frames and the plastic plate to prevent light leak.

During assembly, one scintillator bar per every one layer was sampled and its dimension and weight were measured. The mean value and root-mean-square (RMS) of the measurement are summarized in Tab. 3.1.

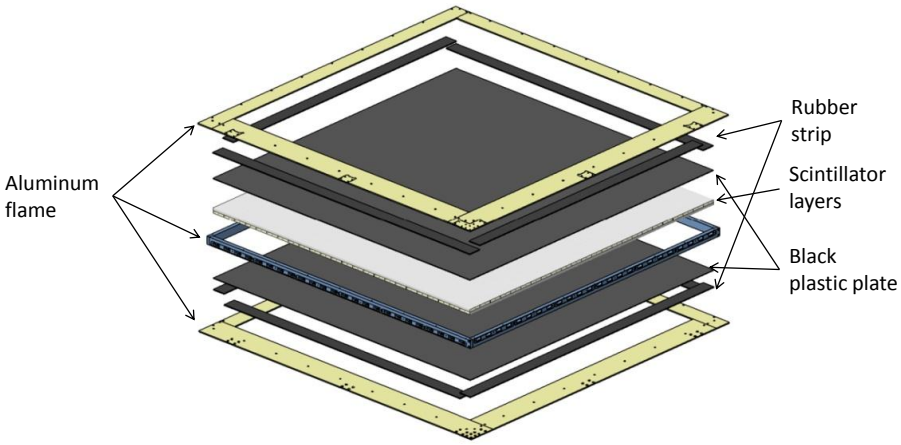

Figure 3.5: Exploded view of the scintillator plane.

Table 3.1: Mean value and RMS of the measured dimensions and weight of the scintillator bars. In total, 349 bars were measured.

	unit	mean	RMS
width	mm	50.01	0.062
thickness	mm	9.921	0.094
length	mm	1203	0.42
weight	g	602.1	2.8

3.2.2 Wave length shifting fiber

The WLS fiber, Y11(200)M by Kuraray, is used for the light collection. The diameter of the fibers is 1.0 mm and fits the active region of the photo-detector (1.3×1.3 mm^2). The scintillation photons are absorbed by the Y-11 fluor and re-emitted. As shown in Fig. 3.6, the absorption spectrum, centered at the wavelength of 430 nm, has only a little overlap with the emission spectrum, centered at 476 nm, so that self-absorption in the fiber is small.

The fiber is a double-clad type; the inner core containing the WLS fluor (200 ppm) is polystyrene (refractive index $n_1 = 1.59$), the thin intermediate layer is acrylic ($n_2 = 1.49$), and the thin outer cladding is a polyfluor ($n_3 = 1.42$). The light whose angle with respect to the fiber axis is less than 26.7 degree is trapped and transported along the fiber.

The fiber is non-S type; the core of non-S type is of almost no oriented polystyrene chain and is optically isotropic and very transparent. The 1/e attenuation length is 242 cm, which was measured at KEK FUJI test beam line [34]. We also measured the attenuation length of each fiber after assembly of the scintillator plane and the result is consistent with 242 cm.

The fibers are cut to the lengths of the scintillators. The cut surfaces of the fibers were polished with diamond blades (Fiberfing Inc. FiberFin 4). The fiber is attached to the Multi-Pixel Photon Counter (MPPC) through the specially developed connector [35]. The connector consists of two parts as shown in Fig. 3.7: one part holds the MPPC at the bottom of the funnel, and the other part holds the fiber by gluing with optical cement (ELJEN® EJ-500). The other side of the fiber is painted with the reflective coating (ELJEN® EJ-510) to increase the light yield at the far side. After cutting, we sampled 204 fibers and measured their mean light yields at a test-bench using LED light. The RMS of the mean light yields is 10%.

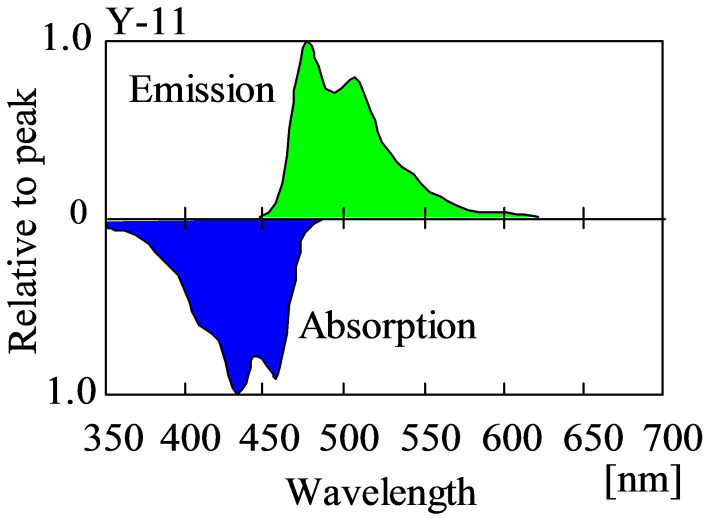

Figure 3.6: Absorption and emission spectra of Y-11 WLS fiber.

3.2.3 Multi-Pixel photon counter

INGRID uses a Multi-Pixel Photon Counter (MPPC, Hamamatsu S10362-13-050C) [36] manufactured by Hamamatsu Photonics as the photo-sensor. Figure 3.8 shows a photo of MPPC. MPPC is a newly developed photon sensor. It is an electrically parallel array of avalanche photodiodes (APDs) which operates in Geiger-mode at above the breakdown voltage. It is able to count the photons as the number of fired pixels. INGRID is the first large application of MPPC.

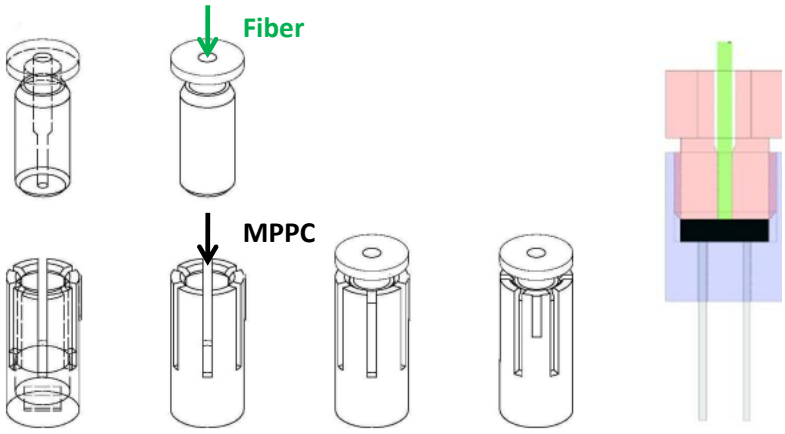

Figure 3.7: Optical connector between the WLS fiber and the photo-sensor.

MPPC has great features such as high photon detection efficiency (40% at 500 nm) and the capability of photon counting. Its basic parameters such as a gain and dark noise rate depend on the overvoltage, ΔV, which is the difference between the applied voltage and its breakdown voltage.

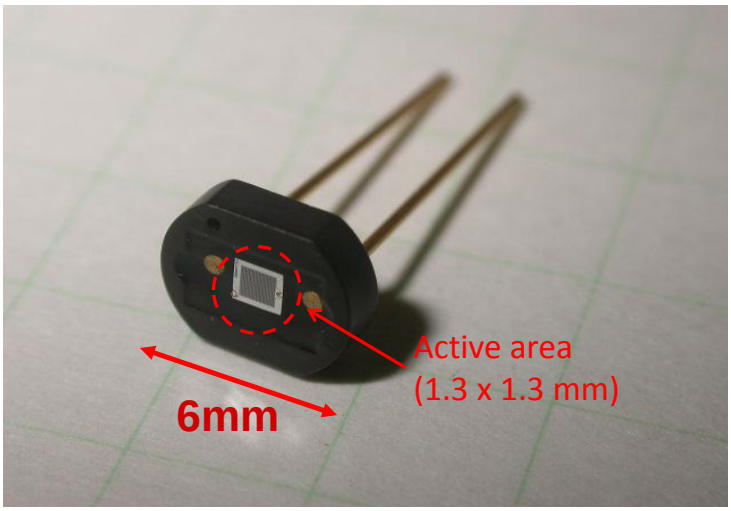

Figure 3.8: Photo of the Multi-Pixel Photon Counter (MPPC).

The gain is defined as the charge of a fired single pixel divided by the charge of an electron. Because the capacitance C of a single pixel is on the order of 10 $\sim$ 100 fF and ΔV is a few volts, the gain ($= C \times \Delta V/e$) is order of $10^5 \sim 10^6$. There are a few bad features in MPPC. MPPC has dark noise of few hundreds Hz due to the thermal generation of carries. Afterpulse occurs following the true signal with some probability. It is generated by the primary carries trapped by crystal defects. Photons emitted during avalanche multiplication at the firing pixel propagate inside the lattice and could create another electron-hole pairs at neighboring pixels and these free carriers can trigger another pulses there. This phenomenon is so-called crosstalk. The probability of afterpulse and cross-talk is typically ~ 0.1.

Before the installation, the basic parameters together with their dependence on ΔV and the temperature are measured for all the MPPCs [37] as summarized in Tab. 3.2. Using this

result, the applied voltage to each MPPC in INGRID is determined and controlled at front-end electronics with an accuracy of 0.02 V. The ΔV of the INGRID MPPC is 1.1 V. At this operation voltage, the gain is $\sim 5.0 \times 10^5$. The dark noise rate is $\sim 5.0 \times 10^5$ Hz and average number of the noise hits (threshold = 2.5 PE) at one of the module (number of channels = 616) during the integration window (530 nsec) is five (Fig. 3.9).

Table 3.2: Mean value and RMS of gain, dark noise, after pulsing and cross-talk probability and photo detection efficiency (PDE) for 17686 MPPCs at 15, 20, 25°C and $\Delta V = 1.0\ V$, quoted from [37].

Parameter	Temperature	Measured values	RMS
Gain	15°C	4.91×10^5	0.26×10^5
	20°C	4.85×10^5	0.26×10^5
	25°C	4.75×10^5	0.24×10^5
Breakdown voltage (V)	15°C	68.05	0.73
	20°C	68.29	0.73
	25°C	68.53	0.73
Dark noise rate (Hz)	15°C	3.37×10^5	0.85×10^5
	20°C	4.47×10^5	1.02×10^5
	25°C	6.03×10^5	1.21×10^5
After pulsing and cross-talk probability	15°C	0.073	0.039
	20°C	0.070	0.036
	25°C	0.066	0.031
PDE (×PMT of Hamamatsu R1818)	15°C	1.45	0.32
	20°C	1.53	0.33
	25°C	1.62	0.34

3.2.4 Readout electronics

Readout electronics of INGRID consist of Trip-t front-end Boards (TFBs) and three kinds of back-end boards (BEBs): Readout Merger Module (RMM), Master Clock Module (MCM) and cosmic-ray trigger Module (CTM), as shown in Fig. 3.10.

TFB (Fig. 3.11) has four Trip-t chips, two 10-bit dual channel ADC chips (AD9201), eight 8-channel 8-bit DACs (AD5308), a FPGA (Xillinx Spartan 3) and so on. Details of Trip-t and TFB can be found in [38, 39]. Each TFB reads out MPPCs in one tracking plane or MPPCs in two veto planes: INGRID has 182 TFBs in total. The MPPC signals are capacitively split (low gain and high gain outputs) and routed to two separate channels of Trip-t. Trip-t integrates the charge and stores the result of 23 integration cycles. The data is multiplexed onto AD9201 which digitize the data. The dynamic range of high (low) gain output is up to $\sim$ 100 (1000) PE. Signals from the high gain channel are routed to a discriminator, which is a part of Trip-t to provide timing information. TDC data is recored with a time resolution of 2.5 nsec (least significant bit). TDC data is also used to calculate a cosmic-ray trigger primitive signal, which is sent to CTM. AD5308 provides the 0 to 5 V programmable trim voltage to each MPPC. The TFB operation is controlled by FPGA. TFB needs four low voltage levels (1.7 V, 3.1 V, 3.8 V and 5.5 V), which are provided together with the MPPC high voltage by a power supply (TDK Lambda ZUP6-33) installed on each INGRID module.

All BEBs are developed on the same hardware platform with a high-end Vertex II Pro FPGA from Xillinx (Fig. 3.12). RMM is connected to TFB via Cat 5e cables and all BEBs are connected to each other via their RocketIOs. RMM transmits parameters to TFB for the

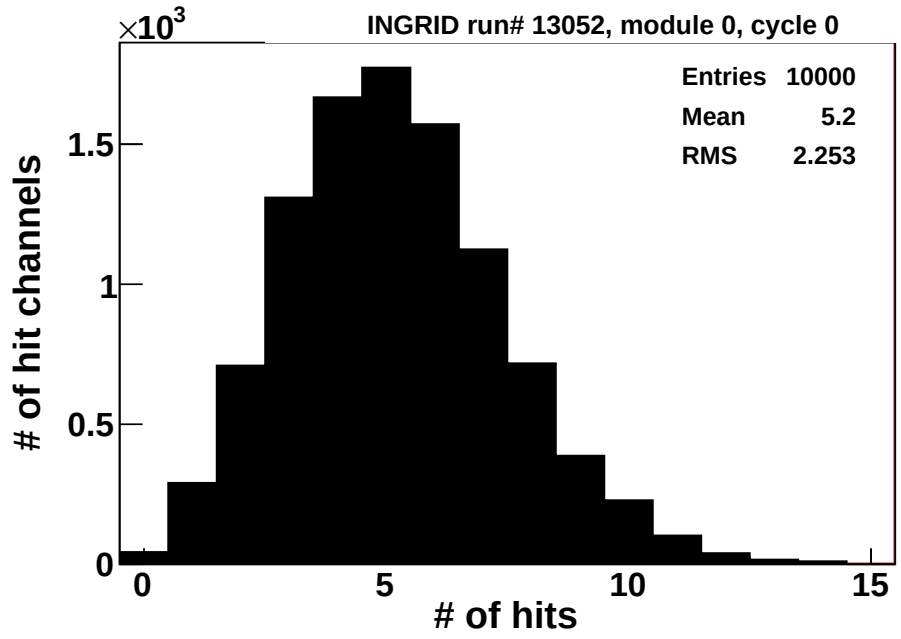

Figure 3.9: Number of the MPPC dark noise hits during a integration window (530 nsec).

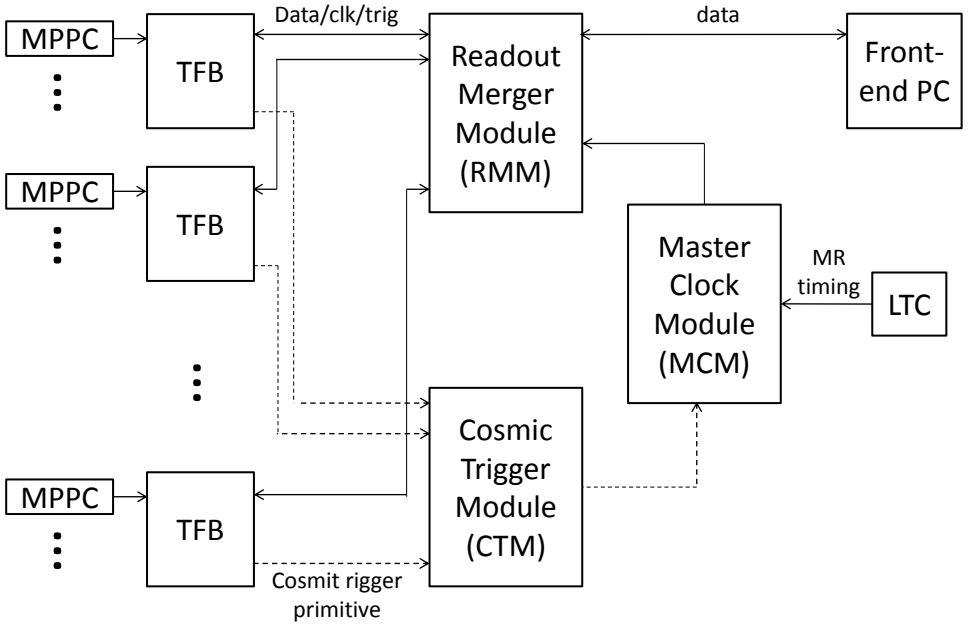

Figure 3.10: Overview of the INGRID readout electronics system.

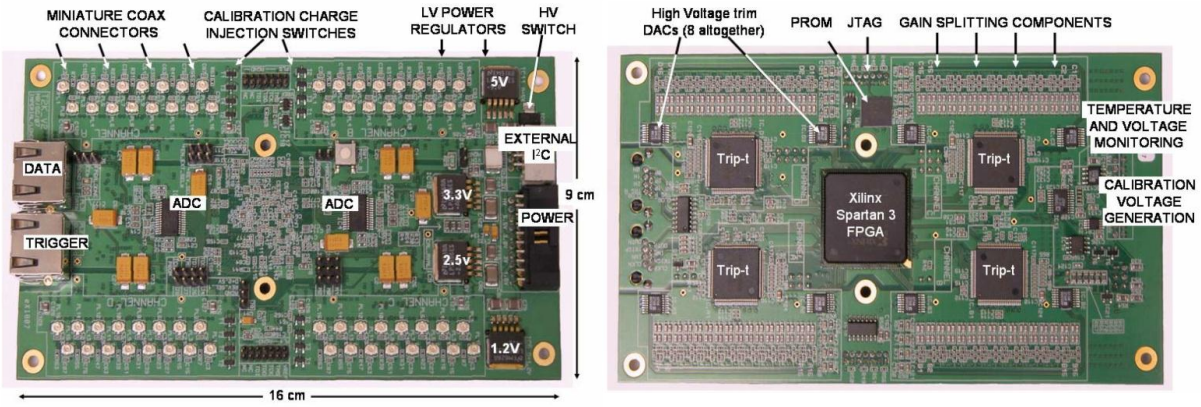

Figure 3.11: Photograph of the TFB top surface (left) and its bottom surface (right).

set-up and running. MCM distributes the beam trigger to TFB via RMM. It also distributes the cosmic-ray trigger signal generated by CTM. CTM generates the cosmic-ray trigger from the primitive signal from TFBs.

Figure 3.12: Photograph of the back-end board.

BEBs are connected to the DAQ PCs by optical Gigabit Ethernet links. The DAQ architecture is based on the MIDAS framework [40] and details can be found in [41].

3.2.5 Connection between MPPC and TFB

Each MPPC is connected to TFB via co-axial cable (Hirose U.FL-2LP-068) of 150 cm. There are several components around the MPPC and TFB as a guide of the cable.

Figure 3.13 shows a Printed Circuit Board (PCB) connector attached to the MPPC. The MPPC is electrically connected to the co-axial cable via this PCB. Figure 3.14 left shows components around the MPPC and the PCB. There are two parts, a cover attached to the aluminum frame and a cap attached to the cover. Figure 3.14 right shows the photo of the cover. To prevent the light leak from the cable hole, the black rubber is installed inside of the cover and the cover and cap are coated with black anodizing.

Each TFB is contained inside a box made by aluminum (Fig. 3.15 left). Between TFB and bottom of the box, a rubber is inserted as a heat conductor. The TFB boxes are attached to the top side of the module (Fig. 3.15 right).

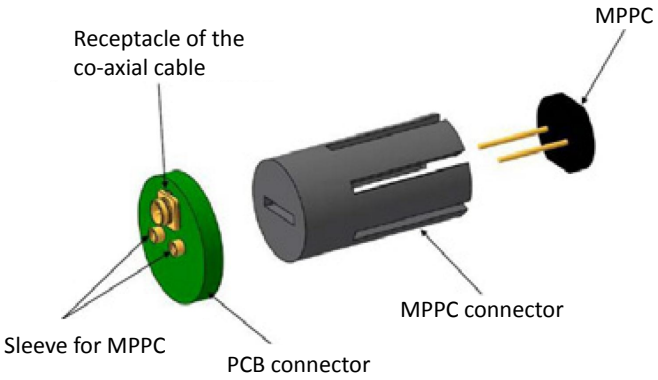

Figure 3.13: Printed Circuit Board (PCB) connector. The MPPC is electrically connected to the cable via PCB.

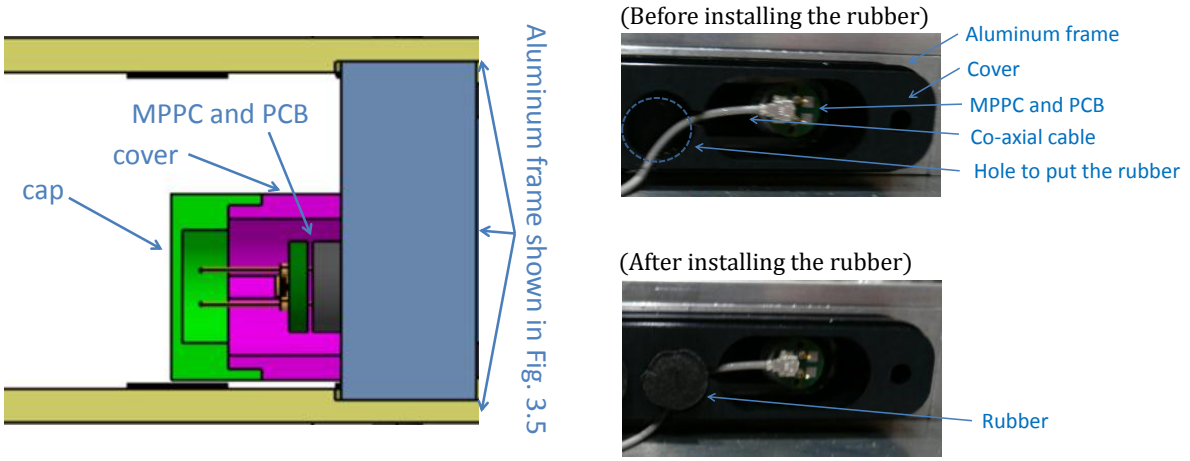

Figure 3.14: (Left) Components around the MPPC and the PCB. (Right) Photo of the cover. There is a hole on the cover in which the black rubber is put to prevent the light leak and hold the cable. The cap is not shown in this photo.

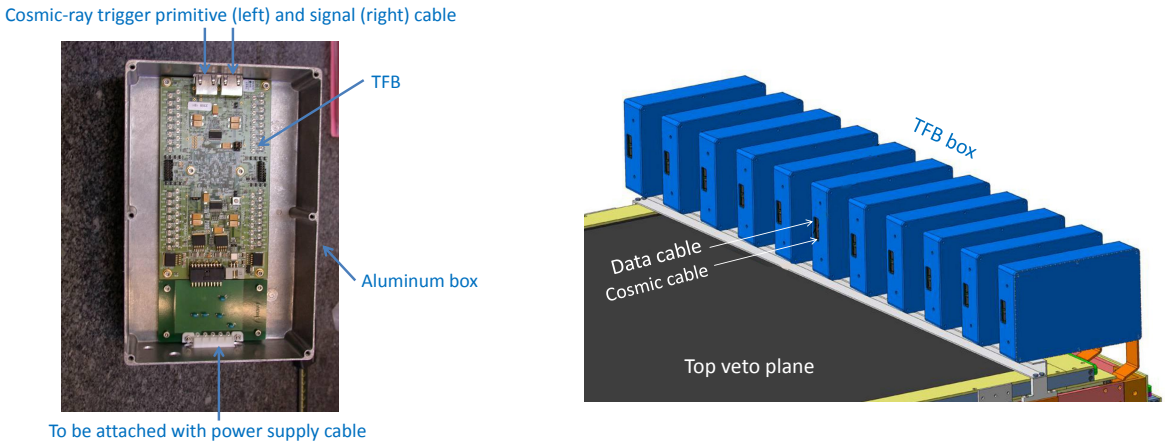

Figure 3.15: (Left)TFB mounted in the aluminum box. (Right)TFB boxes attached to the top side of the module.

3.2.6 Iron and module support structure

The iron plates and the module support structures were fabricated in France. After fabrication of the iron plates, the mass of each plate was measured within a precision of 1 kg, whereas designed mass is 785 kg. Table 3.3 shows measured mass of nine iron plates installed in each module. The difference between measured and designed value is taken into account to correct observed number of neutrino interaction events as described in Section 6.2.4.

Table 3.3: Mass of each module iron plates. The design value is 7065 kg (785 kg×9 plates).

module	0	1	2	3	4	5	6	7	8	9	10	11	12	13
weight[kg]	7124	7081	7065	7076	7059	7094	7114	7041	7063	7094	6987	7079	6979	6988

The support structures of the module are made of welded steel beams onto which the target plates are bolted. For the horizontal modules, the mechanical structure is a simple frame with base plates to interface the module to the concrete floor (Fig. 3.16). The structure of the vertical modules is more complex with columns and bracing (Fig. 3.17) that serves to build the twelve meter high tower of the detector by stacking and bolting together the modules. An aluminum frame, mounted around the target plates and tracking planes, provides the mechanical support for the VETO planes, the power supply units and the cable trays.

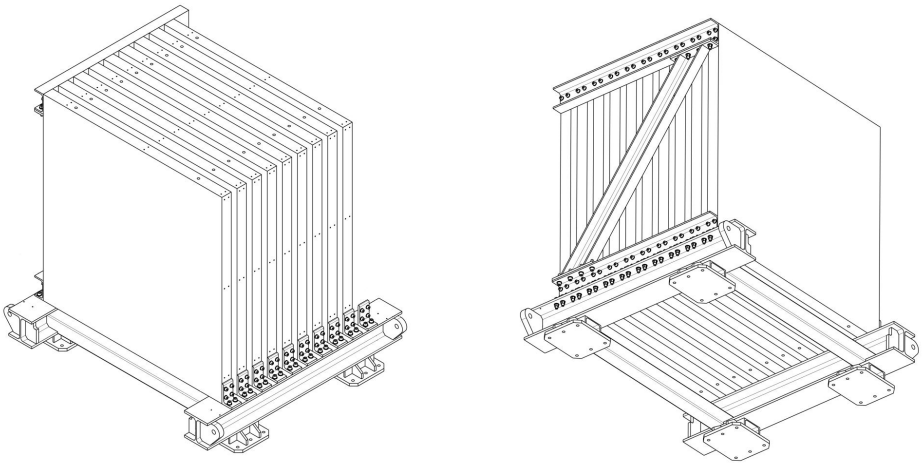

Figure 3.16: Support structure of the horizontal module. The nine iron plates are attached in this figure. The eleven scintillator tracking planes are inserted between iron plates.

3.3 Data acquisition

The timing diagram of the INGRID data acquisition (DAQ) is shown in Fig. 3.18. There are two triggers: beam trigger and cosmic-ray trigger.

The beam trigger is provided from the accelerator via the LTC module as described in Section 2.2. After getting the beam trigger signal and waiting 2.5 μsec so that the first bunch timing is in the middle of fifth cycle, the INGRID DAQ starts to take data and record the data of 23 cycles. The time window of the integration and the reset is 530 nsec and 50 nsec, respectively, whereas the spill spacing is 581 nsec. Before 0.1 sec of the beam trigger, there is a

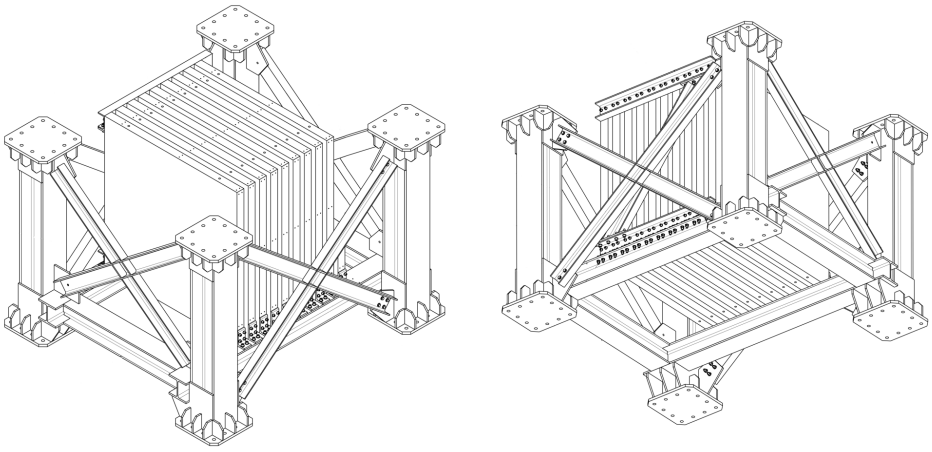

Figure 3.17: Support structure of the vertical module. The nine iron plates are attached in this figure. The eleven scintillator tracking planes are inserted between iron plates.

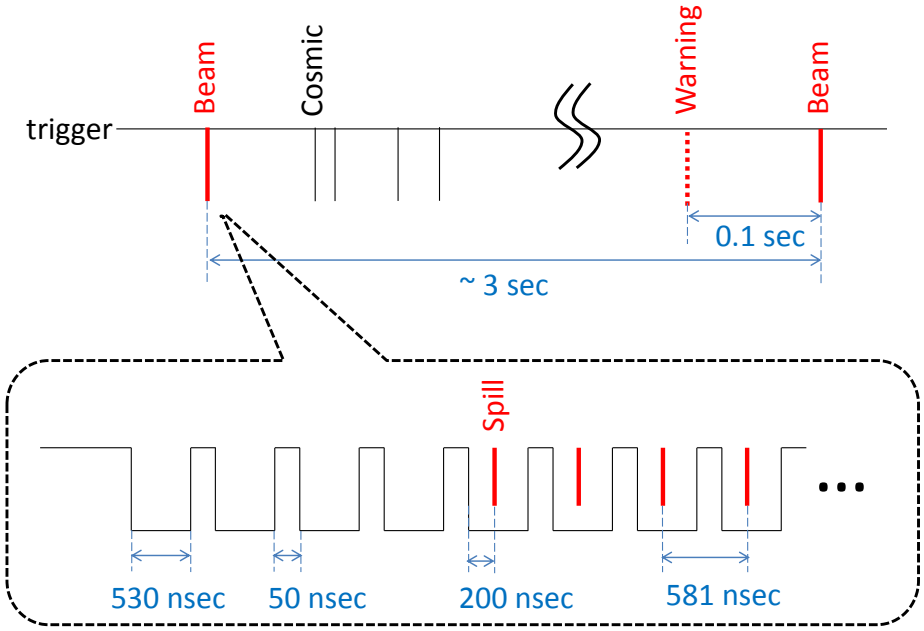

Figure 3.18: Timing diagram of the data acquisition.

beam warning trigger with which the INGRID DAQ aborts taking the data to be ready for the beam trigger.

The cosmic-ray trigger is enabled between the beam triggers. During this period, the INGRID DAQ takes the data continuously and records the data of last 23 cycles only when the cosmic-ray trigger is fired. The cosmic-ray trigger is generated by CTM when the one of the module satisfies a cosmic-ray trigger algorithm. The algorithm is shown in Fig. 3.19; the cosmic-ray trigger primitive signal at each TFB is generated with two hits and the cosmic-ray trigger is generated with four primitive signals from one of the combination in Fig. 3.19. To suppress the data size, only the data of the channels with 2.5 photo-electrons or more are recorded in the cosmic-ray trigger events.

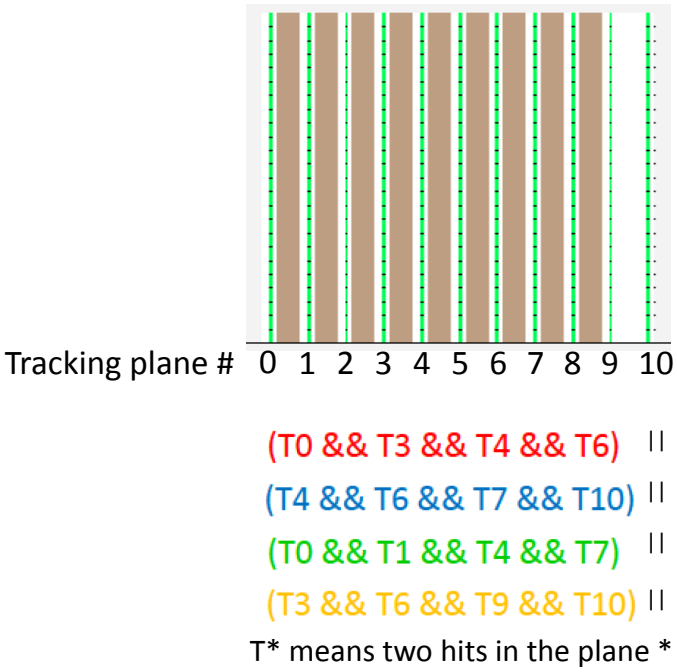

Figure 3.19: Algorithm of the cosmic-ray trigger.

3.4 Coordinate system

INGRID uses the right-handed Cartesian coordinate system in which the z axis is the beam direction and the y axis is the vertical upward direction. The origin is located on the most upstream surface of each module in the z dimension and the edge of the tracking plane in the x and y dimensions. Each module has an independent origin and the neutrino event selection at each module are described based on the this coordinate system. The numbering of scintillators in a tracking plane is done from -x to +x (0 to 23) and -y to +y (0 to 23). Similarly the numbering of the tracking plane is done from -z to +z (0 to 10). In both cases the counting starts from zero. Usually the event selection is explained by the scintillator number and the scintillator tracker number. Since each module is read out both vertically and horizontally, two views are defined: x-z projection (top) and y-z projection (side).

3.5 Basic performance of INGRID

3.5.1 Dead channel fraction

Because MPPC has the capability of single photon counting and high dark noise rate, the peaks corresponding to zero photo-electron (pedestal) and one photo-electron can be observed without light source, as shown in Fig. 3.20. By checking these two peaks, we found 14 (0.17%) dead channels out of 8360 channels.

Following three problems caused dead channels. First one is damage to the co-axial cable between the MPPC and the TFB: 10 of 14 channels. Second one is trouble with the chip on the TFB which controls the voltages applied to the MPPCs: 3 of 14 channels. Third one is trouble with an electrical circuit; the pedestal of these channel are not stable 1 of 14 channels.

3.5.2 Gain

As described in 3.5.1, the zero photo-electron and one photo-electron can be observed without any light source. The MPPC gain is measured using these two peaks. Figure 3.21 shows the MPPC gain for all the channels. Figure 3.22 shows the MPPC gain for all the channels as a function of time. Because of the variation of temperature, the MPPC gain varied slightly. Especially, the temperature is different for the horizontal seven modules and the vertical seven modules. The voltage applied to the MPPCs is tuned at the start of the MR run. The gain is stable within 10% level.

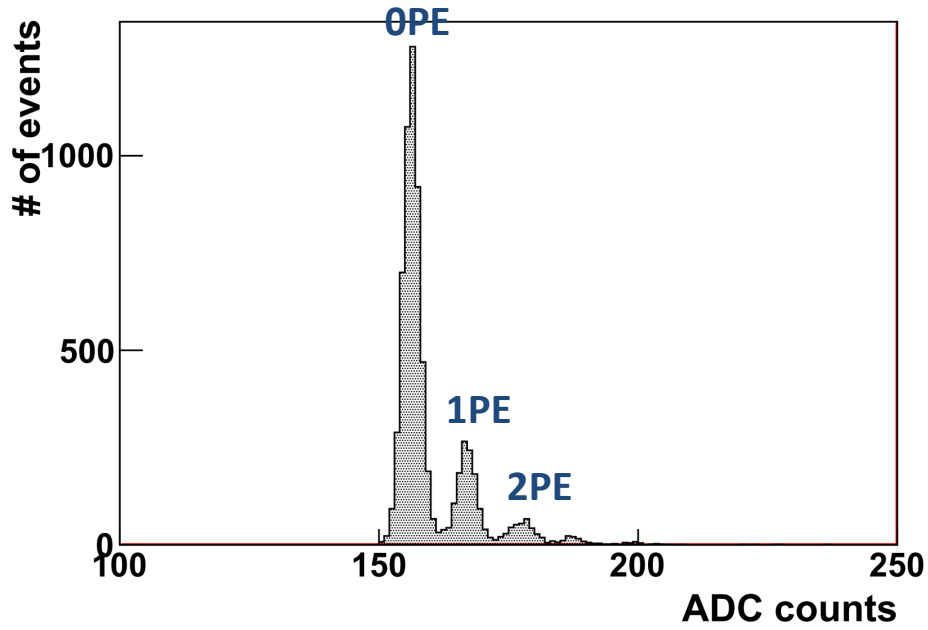

Figure 3.20: Typical ADC distribution of MPPC dark noise.

3.5.3 Light yield

The light yield per 1cm of a muon track is monitored with inter-spill cosmic-ray data for each channel. A typical light yield distribution of one channel is shown in Fig. 3.23. The distribution

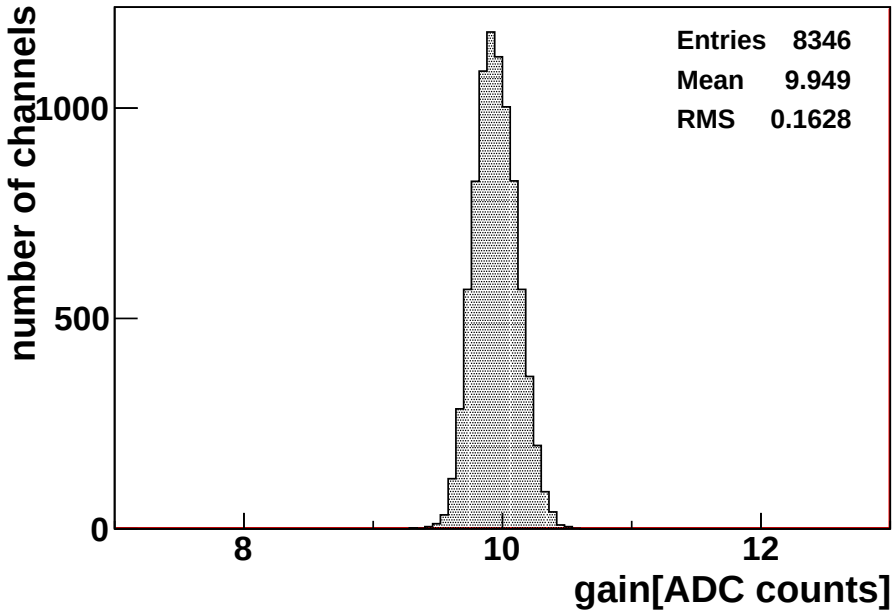

Figure 3.21: MPPC gain for all the channels.

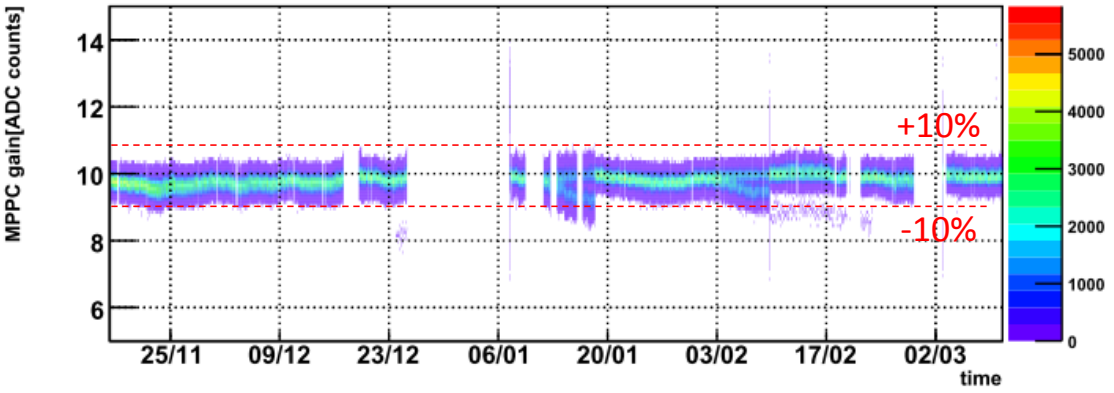

Figure 3.22: Stability of the MPPC gain for all channels.

is consistent with the Landau distribution. The mean light yield of all the channels are shown in Fig. 3.24.

Table 3.4 shows the average and RMS of the mean light yields for each month. The average become larger slightly and RMS become smaller between Jun. 2010 and Dec. 2011, because a fine tuning for the MPPC voltage was done. There is no light yield measurement between Jan. 2010 and Feb. 2010 because cosmic-ray trigger module was not available. During that period, hit efficiency described in Section 3.5.4 was measured with the beam induced muons and the result shows that the efficiency is high enough.

From these measurements, we concludes that the light yields of all the channels are sufficiently high and stable during all the measurement periods.

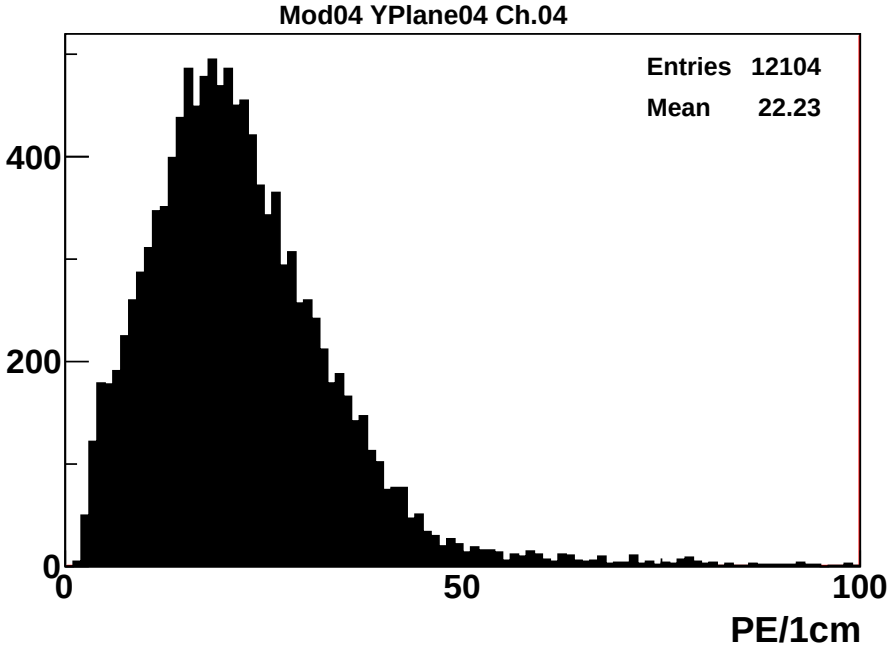

Figure 3.23: Typical light yield distribution. Light yield is normalized by the pass length (1 cm).

Table 3.4: Average and RMS of mean light yields

period	Average[PE/1cm]	r.m.s.[PE]
Mar. 2010	23.8	2.4
Apr. 2010	23.1	2.3
May 2010	23.5	2.4
Jun. 2010	23.2	2.4
Dec. 2010	24.3	1.6
Feb. 2011	24.6	1.6
Mar. 2011	24.8	1.7

3.5.4 Hit efficiency

The hit efficiency is evaluated by using beam induced muon tracks with the following procedure; a muon track is reconstructed without using the hit information in the scintillator plane being

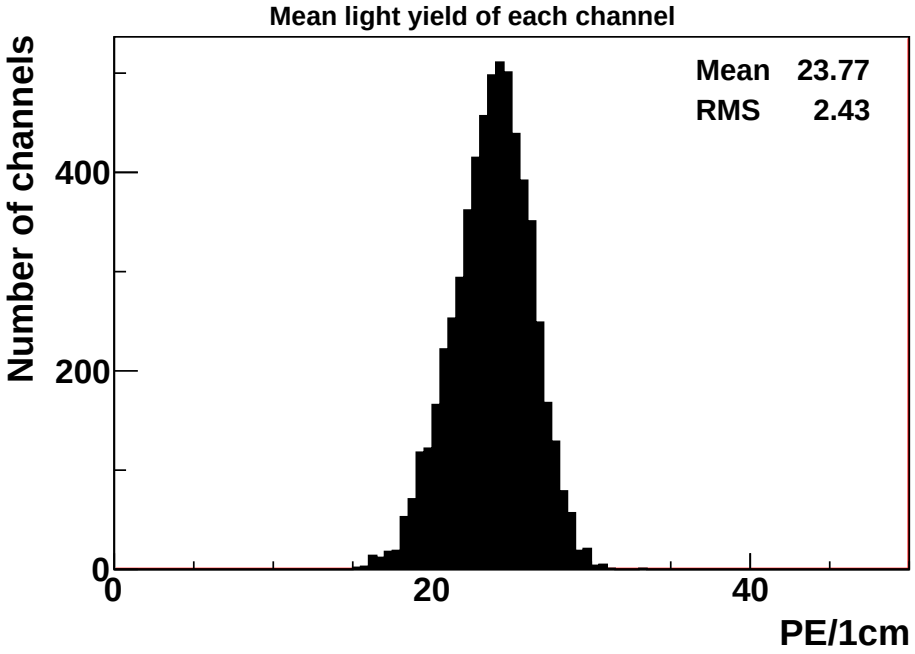

Figure 3.24: Mean light yields of all the channels.

evaluated, and then in that plane, channels expected to have hits from the track trajectory are checked whether they have hit or not.

Figure 3.25 shows the result of the hit efficiency measurement with the beam induced muons. Figure 3.26 shows the efficiency as a function of the track angle measured by using the beam induced muons. The track angle is defined as the angle between the beam direction and the reconstructed track. Because the main origin of the inefficiency comes from the gap between scintillators, the efficiency depends on the track angle: a particle with small angle has a higher probability to go through the gap. As a result, the efficiency is smaller than that expected from photo-electron statistics with measured light yield described in 3.5.3.

3.5.5 Hit timing resolution

Hit timing resolution is estimated by measuring the time difference among hit channels for cosmic-ray tracks. Figure 3.27 shows the time differences of each hit channel from the average of all channels after the correction for differences in the readout cable length and the light propagation time through the fiber. The RMS is 0.9 nsec, which corresponds to the timing resolution if all the channels have the same resolution. The width of the primary proton beam bunch was about 30 nsec during RUN-I and RUN-II, so this resolution is sufficient for selecting the beam events.

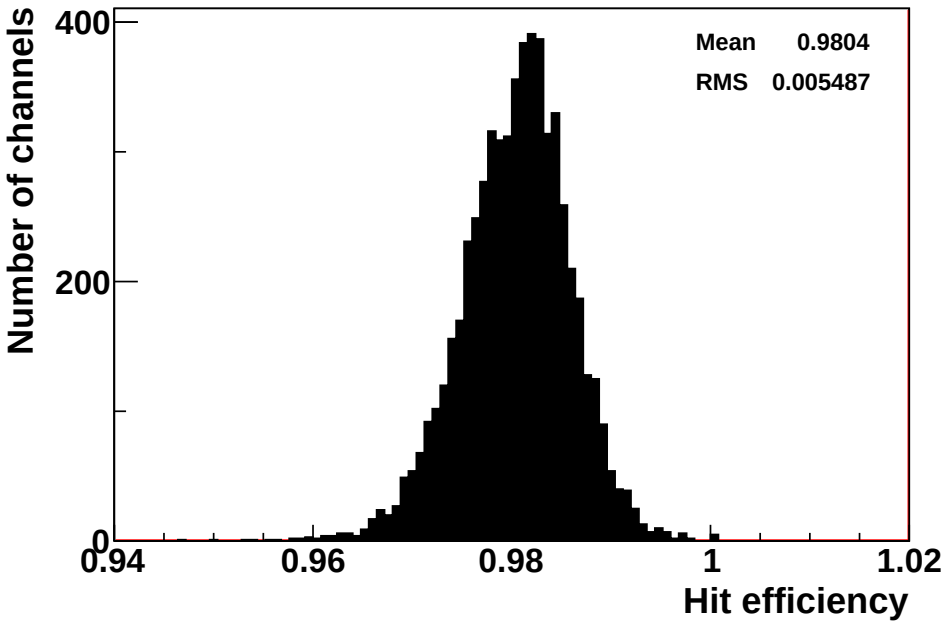

Figure 3.25: Hit efficiencies of all the channel measured with the beam induced muons.

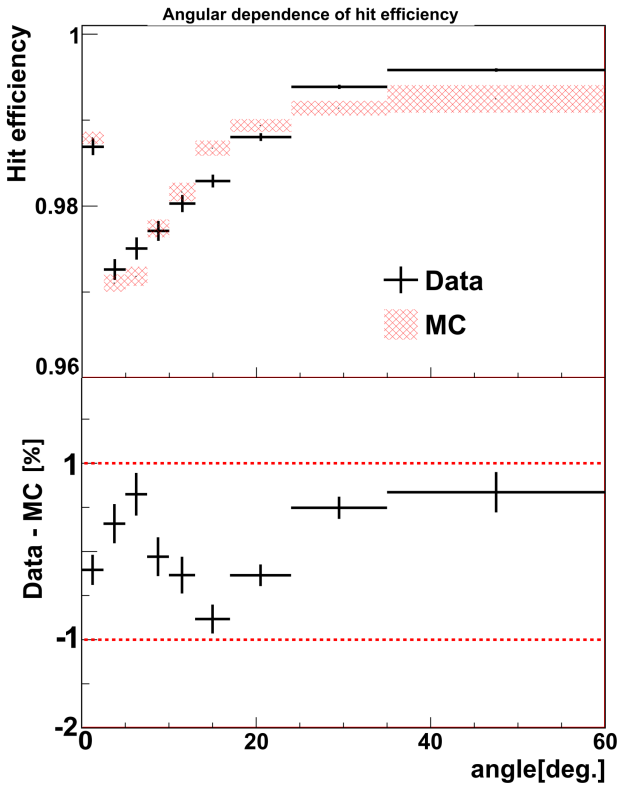

Figure 3.26: Hit efficiency as a function of reconstructed track angle measured with beam induced muons.

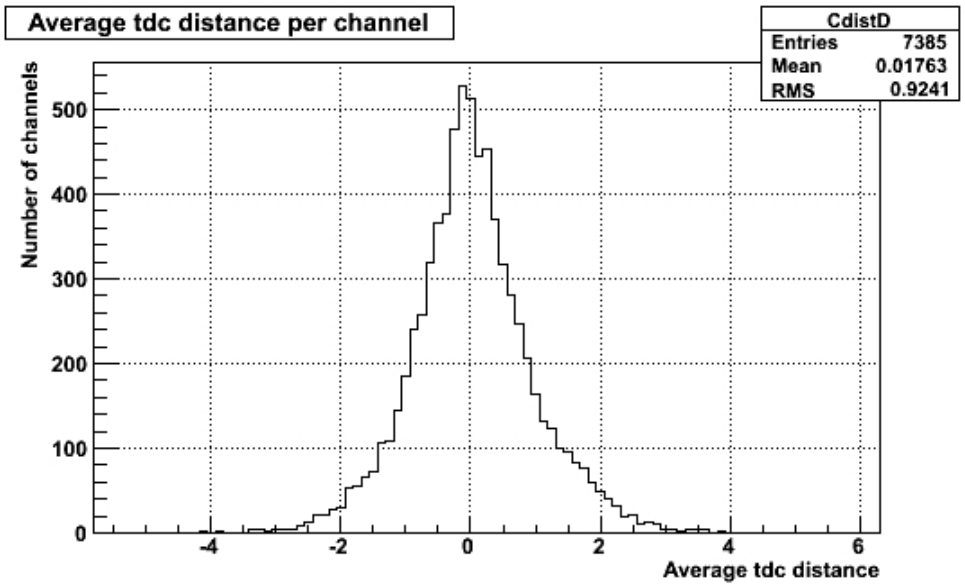

Figure 3.27: Time difference of hit channels from the average hit times for cosmic-ray tracks. Timing is corrected taking cable length and the light propagation through the fiber int account.

Chapter 4

Monte Carlo Simulation

The T2K Monte Carlo (MC) simulations are processed in three steps:

- Simulation of the neutrino beam. It gives the neutrino flux and energy spectra at the near detectors (ND) and Super-Kamiokande (SK).
- Simulation of the neutrino interaction. It generates final state particles with their kinematics in the neutrino-nucleus interaction.
- Simulation of the detector response. It simulates the passage of particles in a material and the response of detector components.

They are described one by one in the following sections.

4.1 Neutrino beam simulation

In order to predict the neutrino flux and energy spectrum at each detecor location, a neutrino beam Monte Carlo simulation, called JNUBEAM, has been developed. JNUBEAM is based on the GEANT3 [42] simulation tool. The secondary beamline geometry is implemented in the simulation and particles are tracked in materials until they decay into neutrinos or are absorbed in the material. The tracks of neutrinos are extrapolated to the ND and SK location. Then the flux and the energy spectrum at each location are provided.

In JNUBEAM, protons with a kinetic energy of 30 GeV are injected into the production target. The beam optics such as spatial distribution are reproduced according to the beam monitor measurements.

The proton interaction inside the target is simulated by the FULUKA hadron interaction model [43,44]. The differential cross section and production rate for the secondary charged pions production are tuned using the NA61 measurement [45]. This measurement covers 92% (98%) of the T2K phase space for π^+'s (π^-'s). The systematic errors are typically 5 $\sim$ 10% for the differential cross section and 2.3% for the production rate. These errors are propagated to the error of the neutrino flux prediction. The pion production by the secondary proton is tuned by the NA61 data after they are scaled to that momentum by the Feynman scaling [46, 47]. For productions of pions at the phase space uncovered by the NA61 measurement and the productions of other hadrons, the FLUKA hadron interaction model [43, 44] is used because FLUKA shows better agreement with the NA61 result than GEANT3 hadron interaction model.

Hadron interactions outside the target are simulated by the GCALOR [48] hadron interaction model. The particles are traced through the magnetic horns and the decay volume until they decay into neutrinos or are absorbed in the material. In JNUBEAM, $\pi^{\pm}$, $K^{\pm}$, K^0_L and $\mu^{\pm}$ decays listed in Tab. 4.1 are neutrino sources.

In order to save CPU time, whenever a particle decays into a neutrino, the flavor and energy of the neutrino as well as the ancestors' information are stored with a probability that the neutrino is produced in the direction of ND or SK.

Table 4.1: Neutrino-producing decay modes in JNUBEAM and their branching ratio in percentage. Decay modes for $\bar{\nu}_\mu$ and $\bar{\nu}_e$ are omitted in this table. The π^- (K^-) mode is charge conjugate of the π^+ (K^+) mode.

	Parent particle				
	π^+	K^+	K^0_L	μ^+	μ^-
ν_μ	$\mu^+\nu_\mu$	$\mu^+\nu_\mu$, $\pi^0\mu^+\nu_\mu$	$\pi^-\mu^+\nu_\mu$		$e^-\nu_\mu\ \bar{\nu}_e$
	99.9877	63.55, 3.353	27.04		≈100
ν_e	$e^+\nu_e$	$\pi^0 e^+\nu_e$	$\pi^- e^+\nu_e$	$e^+\bar{\nu}_\mu\ \nu_e$	
	1.23×10^{-4}	5.07	40.55	≈100	

The composition of the neutrino beam is dominated by muon neutrinos since the horn magnets mainly focus the positive mesons. Figure 4.1 shows the energy spectrum of ν_μ, ν_e, $\bar{\nu}_\mu$ and $\bar{\nu}_e$ at SK with showing the contribution from different neutrino parents.

Energy spectra at the INGRID center and end of the horizontal modules are shown in Fig. 4.2. Because each module covers different off-axis angle, the neutrino energy spectrum at different location is different. The difference of the average neutrino energy between the center module and the end modules is about 0.2 GeV.

4.2 Neutrino interaction simulation (NEUT)

Neutrino interactions with nuclear targets are simulated with the NEUT program library [49,50]. Nuclear targets handled in NEUT are hydrogen, oxygen, carbon, and iron. The energy of neutrinos handled in NEUT ranges from 100 MeV to 100 TeV. The following neutrino interactions in both the charged current (CC) ($\nu_\ell + N \to \ell + X$) and neutral current (NC) ($\nu_\ell + N \to \nu_\ell + X$) are considered:

- quasi-elastic scattering (QE), $\nu_\ell + N \to \ell(\nu_\ell) + N'$;
- resonant single π production, $\nu_\ell + N \to \ell(\nu_\ell) + N' + \pi$;
  resonant single γ production, $\nu_\ell + N \to \ell(\nu_\ell) + N' + \gamma$;
  resonant single K production, $\nu_\ell + N \to \ell(\nu_\ell) + N' + K$;
  resonant single η production, $\nu_\ell + N \to \ell(\nu_\ell) + N' + \eta$;
- coherent π production, $\nu_\ell + {}^{16}O \to l(\nu_\ell) + X + \pi$
- deep inelastic scattering (DIS), $\nu_\ell + N \to l(\nu_\ell) + N' + hadrons$

where N and N' are nucleons and ℓ is a charged lepton. The neutrino-nucleus cross-sections in NEUT for these interactions are shown in Fig. 4.3.

Quasi-elastic (QE) scattering

The CCQE interaction is implemented with the Smith and Moniz model [51]. The vector mass M_V and axial vector mass M_A are set to be 1.21 ($\pm$0.2) GeV/c^2 and 0.84 ($\pm$0.1)GeV/c^2, respectively. For the neutrino-nucleon interaction, Fermi motion of the nucleon and Pauli blocking effect are taken into account. The Fermi surface momentum (the nuclear potential) for oxygen,

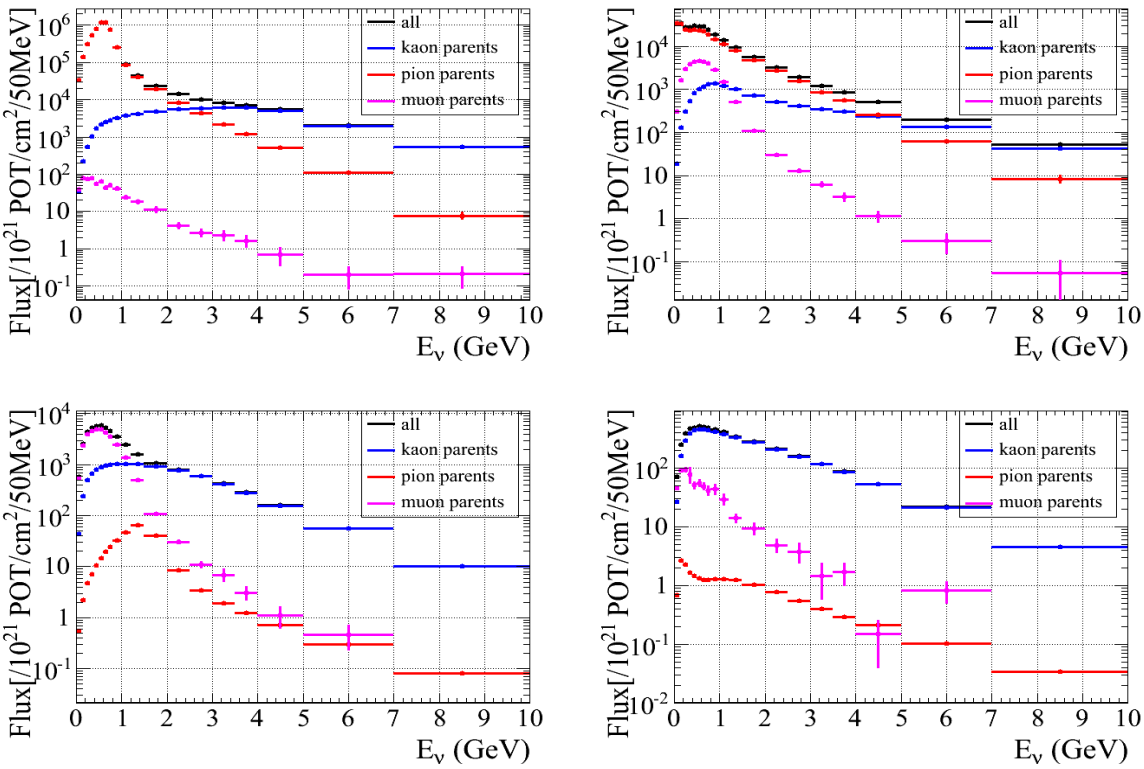

Figure 4.1: Neutrino energy spectrum predicted by JNUBEAM at SK for ν_μ (upper left), $\bar{\nu}_\mu$ (upper right), ν_e (lower left) and $\bar{\nu}_e$ (lower right). Each color shows a contribution of each parent particles. The error bars are the MC statistical errors.

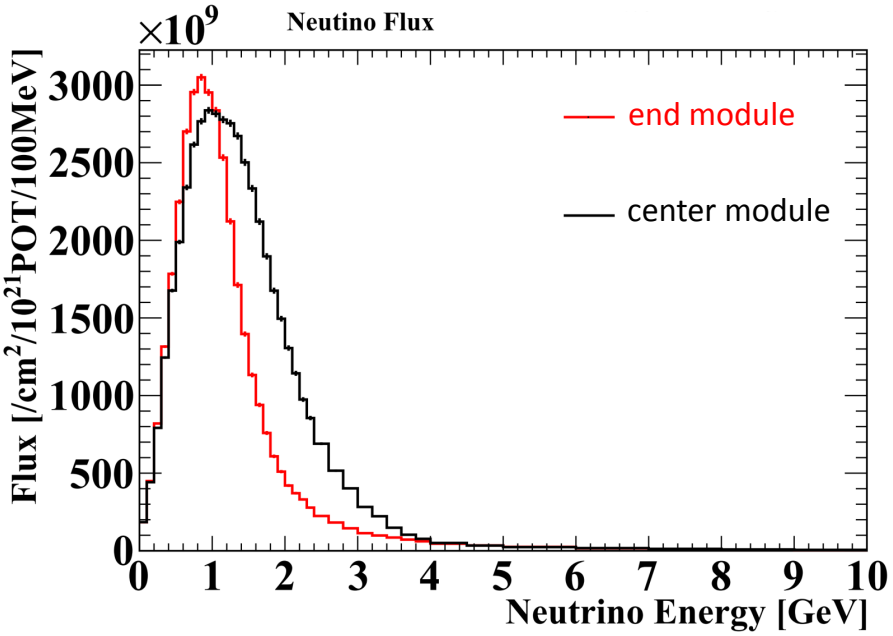

Figure 4.2: Neutrino energy spectrum predicted by JNUBEAM at the INGRID center and end modules. The error bars are the MC statistical errors.

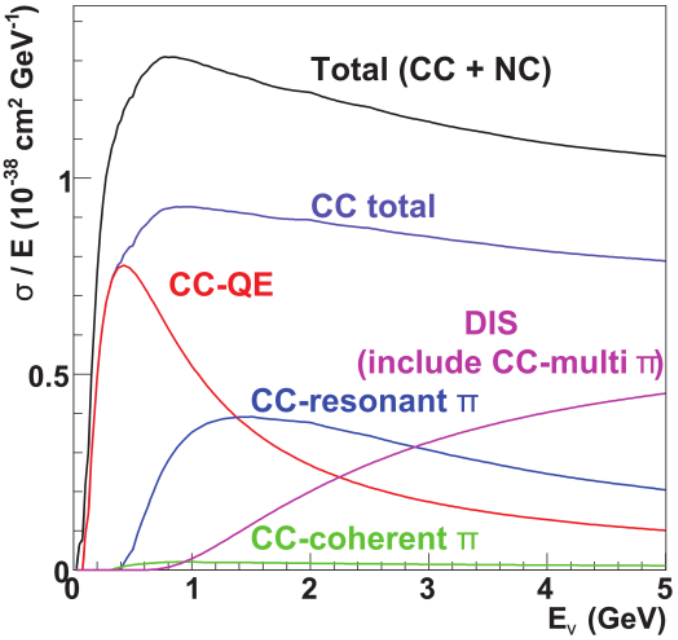

Figure 4.3: Neutrino-nucleus cross-sections per nucleon divided by the neutrino energy in NEUT.

iron and carbon is set to 225 MeV (27 MeV), 237 MeV (32 MeV), and 217 MeV (27 MeV), respectively, as extracted from electron scattering data [52].

The cross-sections of the neutral current elastic interaction are calculated by using the following relations [53, 54]:

$$\sigma(\nu p \to \nu p) = 0.153 \times \sigma(\nu n \to \mu^- p) \quad (4.1)$$
$$\sigma(\bar{\nu} p \to \bar{\nu} p) = 0.218 \times \sigma(\bar{\nu} n \to \mu^+ n) \quad (4.2)$$
$$\sigma(\nu n \to \nu n) = 1.5 \times \sigma(\nu p \to \nu p) \quad (4.3)$$
$$\sigma(\bar{\nu} n \to \bar{\nu} n) = 1.0 \times \sigma(\bar{\nu} p \to \bar{\nu} p) \quad (4.4)$$

Resonant single π, γ, K and η production

The resonant single π production is implemented with the Rein-Sehgal's model [55, 56]. The interaction is separated into

$$\begin{aligned} \nu_\ell + N &\to \ell + N^* \\ N^* &\to \pi + N', \end{aligned} \quad (4.5)$$

where N is the nucleons, and N^* is the baryon resonance. To obtain net cross sections, we calculate the amplitude of each resonance production and then multiply the probability of decay into one pion and nucleon for each resonance. The resonances below 2 GeV/c^2 are considered and the resonances over 2 GeV/c^2 are simulated as the deep inelastic interaction. In the calculation of the angular distribution of pion in the final state, we use the Rein-Sehgal's method for the $P_{33}(1232)$ resonance. For other resonances, directional distribution of the generated pion is set to be isotropic in the resonance rest frame.

The cross-section of single γ, K and η production is implemented with same way: the amplitude of each resonance production is multiplied with the probabilities of decay into γ, K or η for each resonance.

Coherent pion production

The coherent pion production is implemented with the model of D. Rein and L.M. Sehgal [57,58]. The model is based on Adlers PCAC theorem [59, 60].

Deep inelastic scattering

Cross-section of deep inelastic scattering (DIS) is calculated as the neutrino-quark scattering. The nucleon structure functions are taken from the parton distribution function GRV98 [61] with corrections proposed by Bodek and Yang [62].

For the cross-sections for multi-pion production induced by the neutral current, we use the following relations:

$$\begin{aligned}
\frac{\sigma(\nu N \to \nu X)}{\sigma(\nu N \to \mu^- X)} &= \begin{cases} 0.26 & (E_\nu \leq 3\text{GeV}) \\ 0.26 + 0.04 \times \left\{(E_\nu - 3)/3\right\} & (3\text{ GeV} < E_\nu < 6\text{GeV}) \\ 0.30 & (E_\nu \geq 6\text{GeV}) \end{cases} \\
\frac{\sigma(\bar{\nu} N \to \bar{\nu} X)}{\sigma(\bar{\nu} N \to \mu^+ X)} &= \begin{cases} 0.39 & (E_\nu \leq 3\text{GeV}) \\ 0.39 - 0.02 \times \left\{(E_\nu - 3)/3\right\} & (3\text{ GeV} < E_\nu < 6\text{GeV}) \\ 0.37 & (E_\nu \geq 6\text{GeV}) \end{cases}
\end{aligned} \tag{4.6}$$

These values are estimated from the experimental results [63, 64].

4.2.1 Final state interaction (FSI)

The interactions of the mesons, especially of pions, which are generated by the neutrino interactions, is important to estimate background events in Super-Kamiokande. Especially interaction inside the nucleus in which neutrino interaction occurred is important and called as final state interaction (FSI). FSI is simulated as follows. When a pion is created by the neutrino interactions, the production point of a pion inside the nucleus is set according to the Woods-Saxon type density distribution. Then the following pion interactions are considered: inelastic scattering, charge exchange and absorption. Each cross section is calculated based on the Oset model [65], which agrees well with the past experimental data [66]. In the simulation, Fermi motion of nucleus and Pauli blocking effect are taken into account.

4.3 Detector response simulations

4.3.1 Near detectors

The INGRID detector response simulation code was developed with the Geant4 framework [67]. The simulation includes the detailed geometry of the experimental hall in addition to the detector itself. The energy deposit in each scintillator bar is simulated by Geant4 library and is converted to the number of photo-electrons at each MPPC. The conversion factor from the energy deposit to a number of photo-electrons is determined based on the measured light yields with cosmic-rays. Because the main origin of the hit inefficiency comes from the gap between scintillator bars as described in Section 3.5.4, the shape of the scintillator bar is important to reproduce the detector response. The cross-section of the scintillator bar (Fig. 4.4) is tuned to reproduce the hit efficiency as a function of the track angle as shown in Fig. 3.26. Scintillator quenching effect is simulated by using the Birk's law with the value measured in [68]. Attenuation in the fiber is taken into account based on the measured attenuation length [34]. The response of MPPC, such as linearity of observed photo-electrons to injected photo-electrons, is modeled based on the test bench measurements [69].

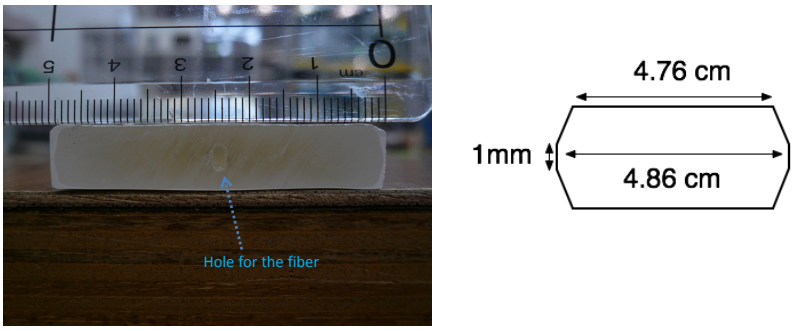

Figure 4.4: Cross-section of the INGRID scintillator bar. (right) the photo of the scintillator bar. (left) the shape implemented in the INGRID simulation.

Geant4 is also used to simulate the response of the ND280 detectors. The geometry of the detectors is constructed in Geant4 code. The energy deposits from the final state particles that pass through the detector is simulated. The response of the active detectors (scintillator bars, fibers, MPPCs and electronics, and TPC electron drift and electronics) is simulated through custom-written code [22, 70].

4.3.2 Super-Kamiokande

The Super-Kamiokande detector response to the particle generated in the neutrino interaction is simulated by SKDETSIM [22], a program library based on GEANT3 [42]. SKDETSIM simulates the particle propagation across the detector, Cherenkov photon propagation, photo-electron production at PMT and response of the electronics.

For the propagation of the Cherenkov photos in water, the absorption, Raleigh scattering and Mie scattering are considered. The parameters of the scatterings are tuned based on measurements with calibration sources. In addition to the propagation in water, the reflection, refraction and absorption at the detector components such as the PMT surface are also implemented.

The absolute quantum efficiency for the photo-electron production at PMT refers to the measurement by Hamamatsu Photonics K.K. The relative efficiency of the PMTs are calibrated by the measurement with the Ni calibration source.

The energy scale for SKDETSIM is checked by using cosmic data as described in Section 7.3. For all samples, the agreement of the energy scale between data and SKDETSIM is within a few percent.

Chapter 5

Analysis Overview

This chapter introduces the outline of the neutrino oscillation analysis. Section 5.2 summarizes the neutrino beam data set used for the analysis.

5.1 Outline of the analysis

Figure 5.1 shows the block diagram of the analysis flow. The analysis strategy is already described in Section 1.2.5; the analysis is performed by comparing observations with the expectations at Super-Kamiokande for both the neutrino energy spectrum and the number of ν_μ events. The expected neutrino energy spectrum, $\Phi_{\mathrm{SK}}^{\mathrm{exp}}$, is obtained by the neutrino beam MC prediction multiplied by the oscillation probability. To precisely predict $\Phi_{\mathrm{SK}}^{\mathrm{exp}}$, the measurement of the beam direction is important because we use the off-axis method. The expected number of events, $N_{\mathrm{SK}}^{\mathrm{exp.}}$, is estimated by using the number of events in the near detector as described by Eq.1.33.

To perform the oscillation analysis, we measure the following quantities:

(1) neutrino beam direction

(2) number of events in the near detectors

(3) energy spectrum and the number of events at SK

Chapter 6 describes the measurement (1) and (2). The measurement (3) is subsequently described in Chapter 7. Finally, we perform the neutrino oscillation analysis in Chapter 8. These measurements and analyses are introduced below.

5.1.1 Neutrino beam direction

We measure the beam direction using INGRID. The beam neutrino events are counted in each INGRID module and the beam profile is reconstruct. The beam center is measured as the peak of the profile. Then the beam direction is reconstructed as the direction from the neutrino production target to the measured INGRID center.

5.1.2 Number of neutrino events in the near site

The neutrino event rate is measured by using both INGRID and ND280. For the INGRID measurement, the number of neutrino events is counted by using all the INGRID modules. For the ND280 measurement, FGDs and TPCs are used to reconstruct ν_μ CC inclusive event.

5.1.3 Super-Kamiokande analysis

Neutrino events in SK are selected by using the beam timing, information of the reconstructed Cherenkov ring, and the delayed activities due to decay electrons. We select the single μ-like ring events for the analysis of neutrino oscillation in ν_μ disappearance, and the single e-like ring events for ν_e appearance. Because this thesis focuses on the oscillation in ν_μ disappearance, Chapter 7 describes the selection of the single μ-like ring events and the systematic uncertainties.

5.1.4 Neutrino oscillation analysis

The analysis is performed to get both the best fit value and the confidence region of ($\sin^2 2\theta_{23}$, Δm^2_{32}). The best fit value is determined with the method of maximum likelihood. The confidence region is constructed by using the method based on Feldman and Cousins [71]. Section 8 describes the method and result of the analysis.

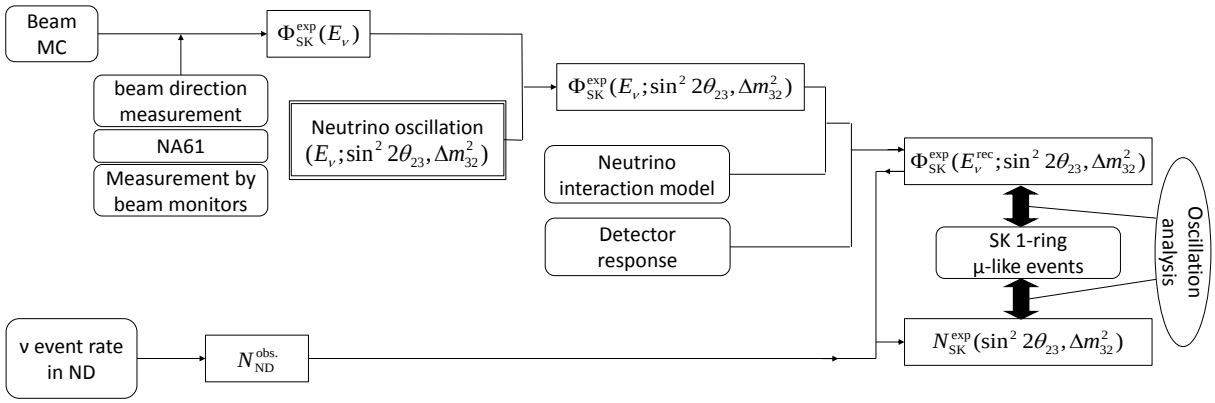

Figure 5.1: Block diagram of the ν_μ disappearance analysis.

5.2 Data set

T2K started taking neutrino beam data from January 2010. The analysis in this thesis is based on a data set collected from January to June 2010 (RUN-I), and from November 2010 to March 2011 (RUN-II). There are nine physics run periods according to the MR run number: run 29 to 34 (RUN-I) and 36 to 38 (RUN-II). The history of number of protons on target (POT) and accumulated POT are shown in Fig. 5.2. The collected data set corresponds to an accumulated POT of 1.44×10^{20}.

In order to guarantee good beam conditions, following selections are applied offline.

1. "Physics run": Spills during the physics run are selected. Before this selection, spills for the beam line DAQ test, the beam tuning and the beam study are included.

2. "Beam trigger": Spills with the beam trigger, which is synchronized with the MR extraction, are selected.

3. "Good GPS status": The time difference between the two GPSs (GPS1 and GPS2) at the J-PARC site has to be less than 200 nsec to guarantee the good status of the GPS system.

4. "Spill flag": The number of protons per spill at the most downstream CT is required to be more than 1×10^{11} to exclude spills which do not contain the beam.

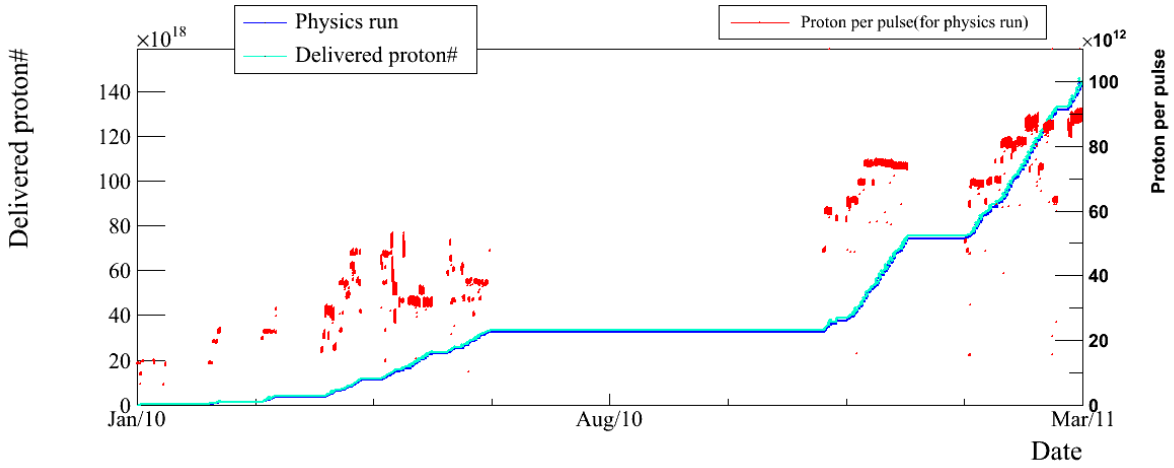

Figure 5.2: History of proton per spill and accumulated POT.

5. "Normal beam condition": Every component in the beam line has to be under the normal condition.

6. "Horn current cut": Variations of every horn current have to be within ±5 kA from the nominal value.

7. "Muon center and yield cut": The muon profile center and variation of the muon yield normalized by the number of protons per spill have to be within ±10 cm and ±5%, respectively.

The number of spills and accumulated POT after each selection are listed in Tab. 5.1. The fraction of the POT loss due to the good beam spill selections was less than 1%. The total POT after all selections is 1.446×10^{20} which is 2% of the T2K goal.

Table 5.1: Number of spills and POT after each good beam spill selection.

Selection	Number of spills	Number of POT
All	3046839	1.458×10^{20}
1. Physics run	2529368	1.449×10^{20}
2. Beam trigger	2512746	1.449×10^{20}
3. Good GPS status	2512746	1.449×10^{20}
4. Spill flag	2508871	1.449×10^{20}
5. Normal beam condition	2500184	1.446×10^{20}
6. Horn current cut	2499409	1.446×10^{20}
7. Muon center and yield cut	2499013	1.446×10^{20}

Chapter 6

Neutrino Beam Measurements using Near Detectors

This chapter describes the measurements by using INGRID and ND280; Section 6.1 $\sim$ 6.3 describe the INGRID measurements and Section 6.4 describes the ND280 measurement. Section 6.5 summarizes the results.

6.1 Data set for the INGRID measurements

INGRID has been taking data from the beginning of T2K RUN-I. The results presented here is based on the data set of RUN-I and RUN-II. Good beam spills are selected as described in Section 5.2. Table 6.1 shows the summary of the neutrino beam data taking in INGRID. INGRID took more than 99% of all the good beam spills. The reasons of the missing beam spill are as following:

- dead time during switching of a INGRID data acquisition (DAQ) run (404 spills, 6% of missing spills).
- trouble of the INGRID DAQ system (712 spills, 11% of missing spills).
- data corruption due to the INGRID DAQ trouble (5328 spills, 80% of missing spills).
- mis-configuration of slow control system (185 Spills, 3% of missing spills).

Table 6.1: Summary of neutrino beam data taken at INGRID.

MR run	period	delivered spills	collected spills	delivered POT	collected POT
29	Jan. 2010	26813	26813	0.32×10^{18}	0.32×10^{18}
30	Feb. 2010	59256	59070	1.13×10^{18}	1.12×10^{18}
31	Mar. 2010	86980	86935	1.97×10^{18}	1.97×10^{18}
32	Apr. 2010	237350	236647	7.65×10^{18}	7.64×10^{18}
33	May. 2010	350079	350012	1.22×10^{19}	1.22×10^{19}
34	Jun. 2010	246504	246410	9.30×10^{18}	9.30×10^{18}
36	Nov. 2010	601344	601294	4.19×10^{19}	4.19×10^{19}
37	Jan. 2011	747993	742606	5.75×10^{19}	5.70×10^{19}
38	Mar. 2011	142694	142597	1.26×10^{19}	1.26×10^{19}
Total		2499013	2492384	1.44×10^{20}	1.44×10^{20}

The generate MC data used for the analysis corresponds to 1×10^{23} POT equivalent. In addition to the neutrino interactions inside the INGRID module, we also simulate interactions inside the upstream wall of the experimental hall.

6.2 Neutrino event selection

The neutrino beam profile is reconstructed based on the observed number of neutrino events at each module.

6.2.1 Selection criteria

Overview

A neutrino event is identified by a long track of the charged particle generated in the neutrino interaction. First, pre-selections are applied to reject events due to the MPPC dark noise hit. Then, tracks are reconstructed by using hit information. After that, charged particles from outside of the module are rejected by using the veto planes. In addition, the start point of the track is required to be inside the fiducial volume (FV) to reject remaining background events. In these selections, each module is treated separately. The details of selection criteria are described as follows.

Event definition

An event is composed of hit (hit threshold = 2.5 photo-electrons) clusters within $\pm$50 nsec. It is required that the number of hits is four or more.

Pre-selections

A tracking plane with at least one hit in both x and y layers is defined as an "active" plane. Events with three or more active planes are selected as shown in Fig. 6.1. There is a discrepancy in the number of events with no active plane between the data and the MC simulation. Figure 6.2 shows a MC event display of a typical event with no active plane. The first tracking plane is not counted as the active plane, but is used for the veto plane. Most of the events originate in low energy particles produced in the neutrino interactions inside the wall of the experimental hall. We consider that the discrepancy is caused by uncertainty on the production rate of these low energy particles.

After the selection with the number of active planes, light yields averaged over x or y layers of the active planes are required to be larger than 6.5 photo-electrons (PE) for both x layers and y layers as shown in Fig. 6.3; inefficiency due to this selection is negligible for muon tracks because the mean light yield is measured to be 24 photo-electrons with the cosmic-ray muons (Section 3.5.3).

Tracking

After the previous selections, tracks in x-z and y-z projection are reconstructed independently with a simple algorithm; first, hits in the most downstream active layer are adopted as the end point of the track. Then the track is linearly extrapolated to upstream layers by checking the upstream hits. A hit is included in the track if the hit position is within two scintillator bars from the straight line extrapolated from the downstream hits. Figure 6.4 shows an example of a reconstructed track. Tracking efficiency is checked with cosmic-ray data and the efficiency is $\sim 95\%$ for cosmic-rays passing three scintillator planes.

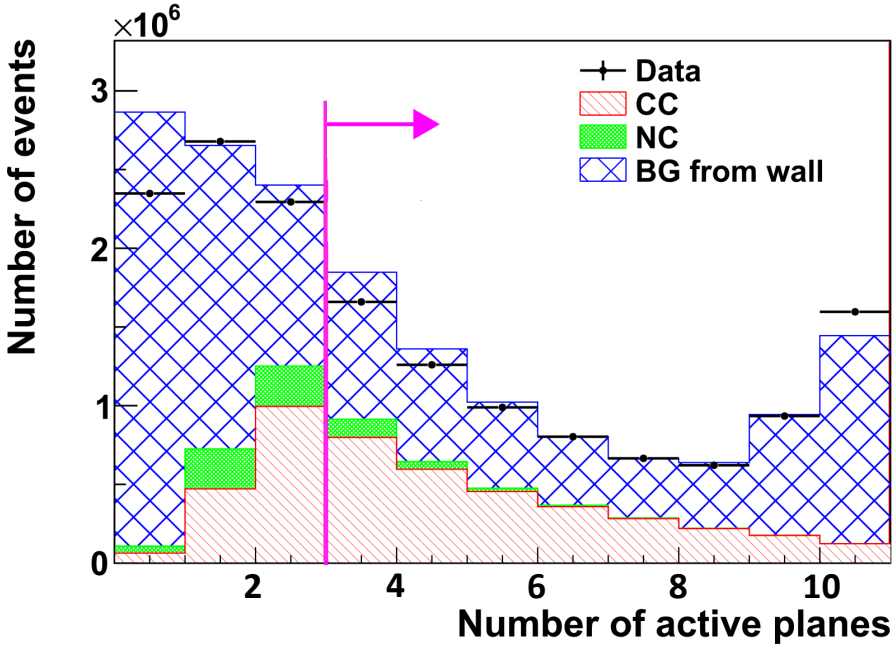

Figure 6.1: Number of active planes. Events with three or more active planes are selected. BG from wall is normalized with the number of beam induced muon events, as described in Section 6.2.2.

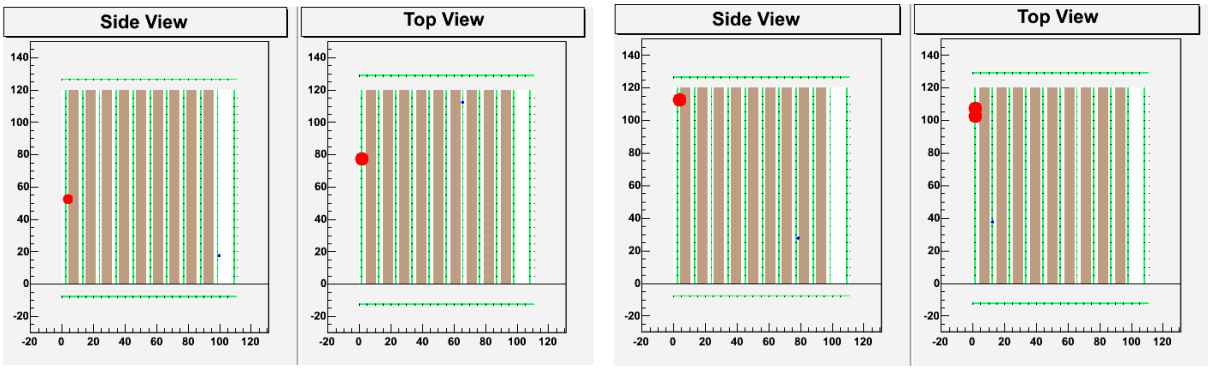

Figure 6.2: Examples of the MC event with no active plane. The red circle shows a hit by the particle and the blue circle shows the hit by the MPPC dark noise.

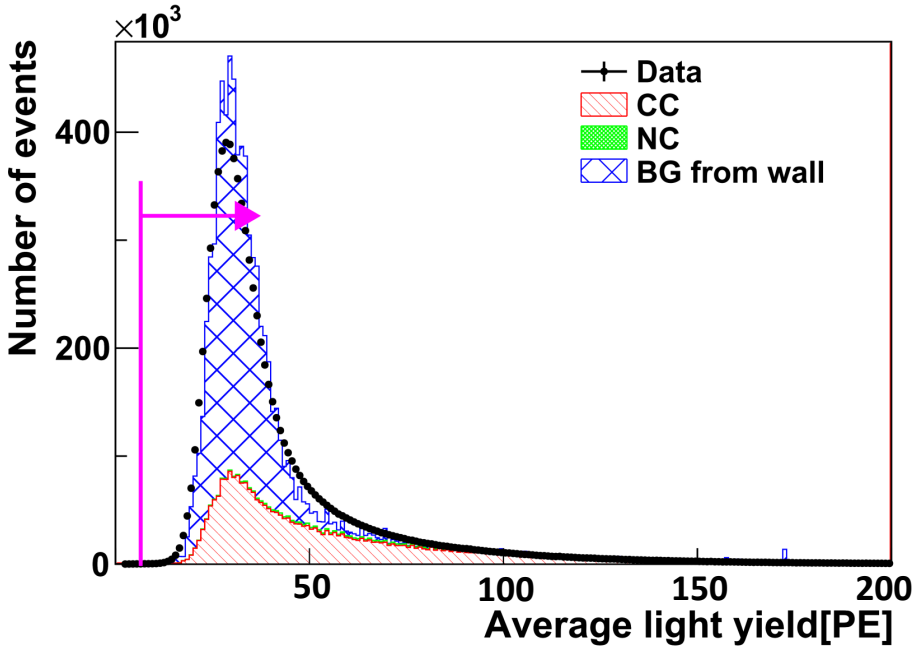

Figure 6.3: Light yield averaged over active layers. Events with more than 6.5 photo-electrons are selected. BG from wall is normalized with the number of beam induced muon events, as described in Section 6.2.2.

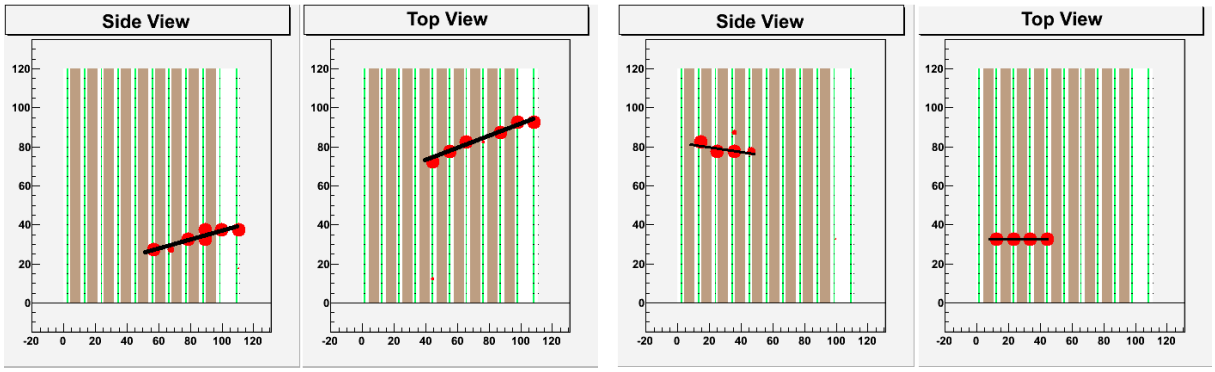

Figure 6.4: Examples of the reconstructed tracks. The size of the circles shows the observed number of photo-electrons at scintillator bars, and black lines show the reconstructed tracks.

The vertex position is reconstructed as the most upstream point of the track for each projection. The track angle is obtained by fitting the hits composing the track with a straight line. Figure 6.5 and 6.6 show differences between true and reconstructed x and z vertex positions, respectively, for MC events. The RMS for the x vertices is 2.7 cm. Figure 6.7 shows the distribution of 3D angle between true and reconstructed muon tracks for MC events. The RMS is 3.8 degrees.

After the tracking, some badly fitted tracks are rejected by using the position difference of the vertex z between x-z and y-z projections. The difference is required to be within ± 1 plane, as shown in Fig. 6.8.

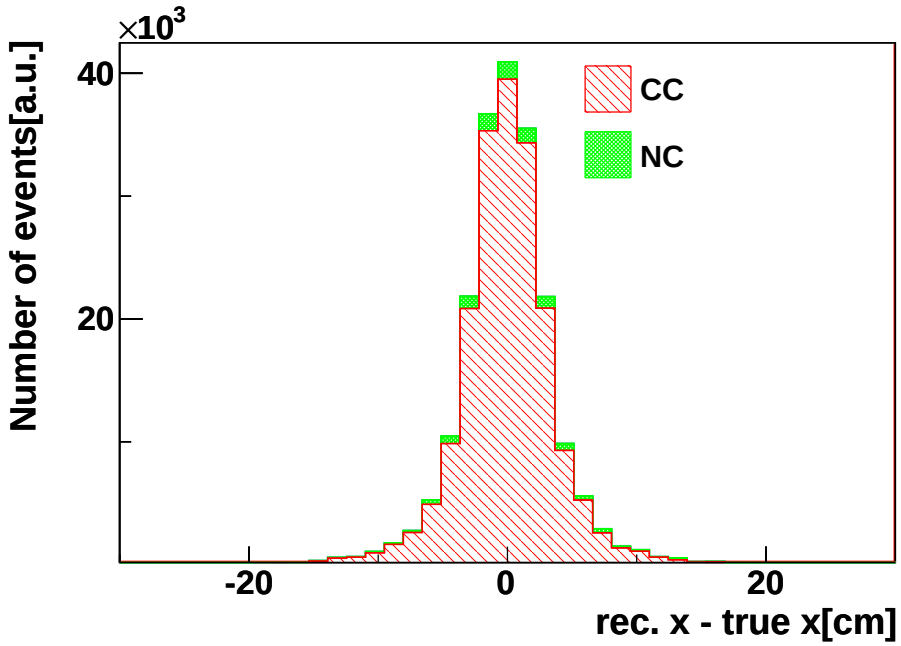

Figure 6.5: Differences between true and reconstructed vertex position in the x direction for MC events.

Timing cut

Figure 6.9 shows the event timing distribution. The six or eight bunch structure is clearly seen. Here the event timing is defined by the hit at the start point of the track. To reject off-timing events such as cosmic-ray events, only events of ± 100 nsec from the expected neutrino event timing are selected as shown in Fig. 6.10. The expected timing is evaluated for each bunch with the primary proton beam timing measured by CT, the time of flight of the particles from the proton target to INGRID, and the delay of the electronics and cables. Both CT and INGRID use the MR timing for the data taking trigger.

Veto and fiducial volume (FV) cuts

Two selections are applied to reject incoming particles from outside, which are produced by neutrino interactions in the upstream material, such as the wall of the experimental hall. First, events which have a hit in a veto plane or the first tracker plane at the upstream position extrapolated from the reconstructed track are rejected. The displays of events rejected by the veto cut are shown in Fig. 6.11. After the veto cut, the fiducial volume (FV) cut is applied. The

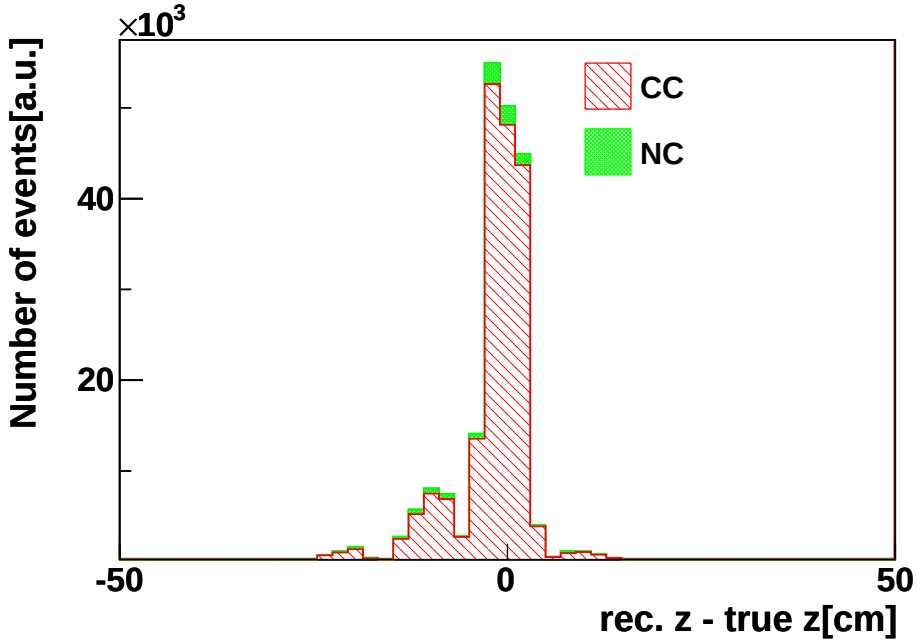

Figure 6.6: Differences between true and reconstructed vertex position in the z direction for MC events.

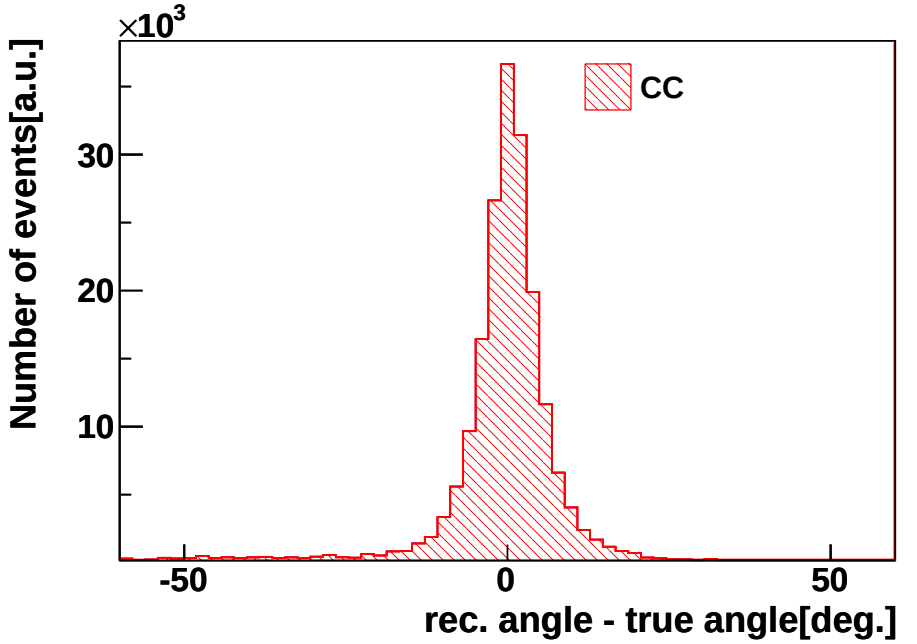

Figure 6.7: Angles between true and reconstructed tracks.

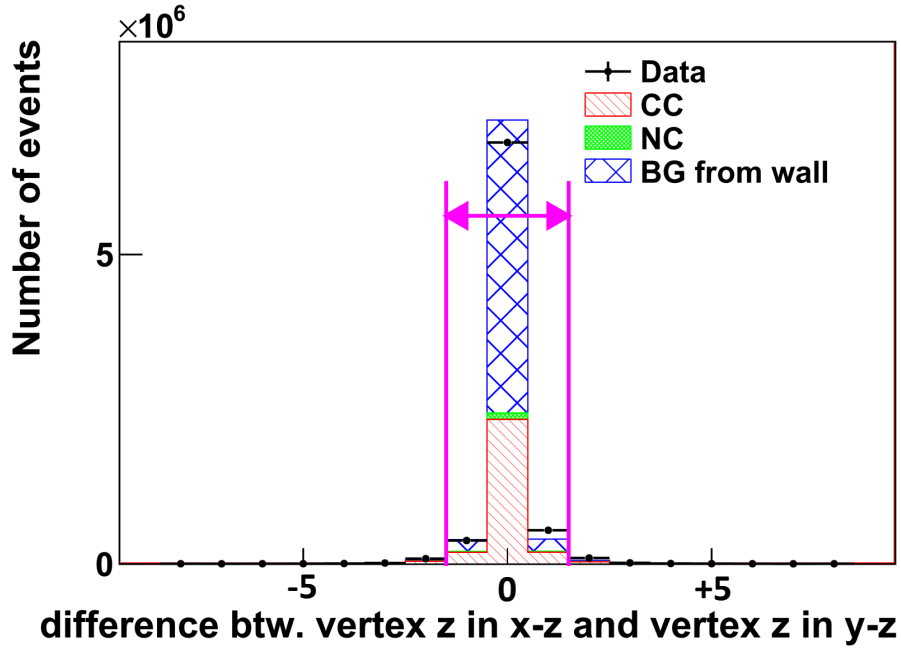

Figure 6.8: Difference of the z vertex positions between x-z and y-z projections. BG from wall is normalized with the number of beam induced muon events, as described in Section 6.2.2.

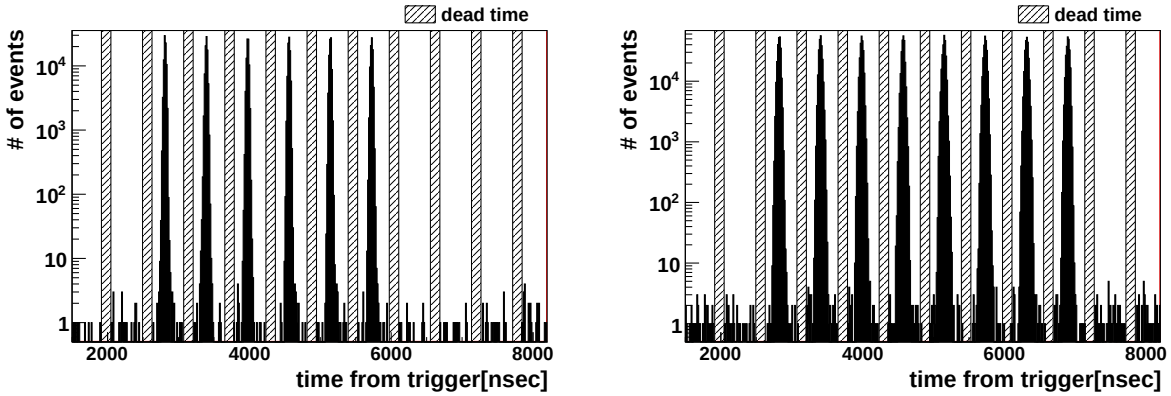

Figure 6.9: Event timing distributions after reconstructing the track with RUN-I (left) and RUN-II (right) data. The number of beam bunches is six and eight during RUN-I and RUN-II, respectively.

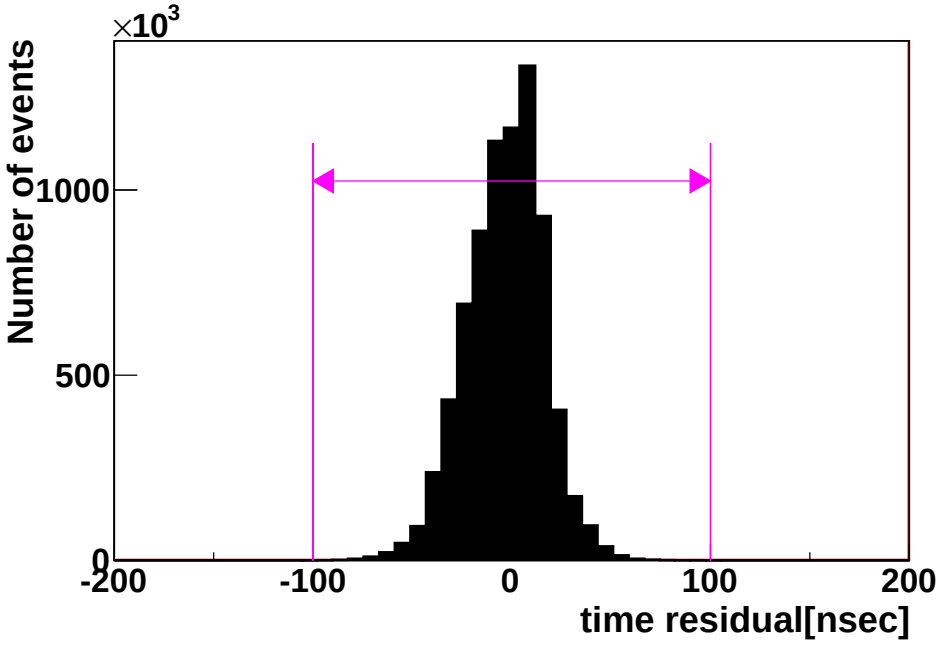

Figure 6.10: Time difference between the measured event timing and the expected neutrino arrival timing. Events within ±100 nsec are selected.

FV of each module is defined as a volume composed of the 3rd to 22nd of the 24 scintillator bars in the x and y directions, and from the second to the ninth tracker plane in the z direction. Events having a vertex inside the FV are selected as shown in Fig. 6.12. The events rejected by these selections are identified as "beam induced muon" events.

Figure 6.13 shows the vertex distributions in the x and y directions after all cuts.

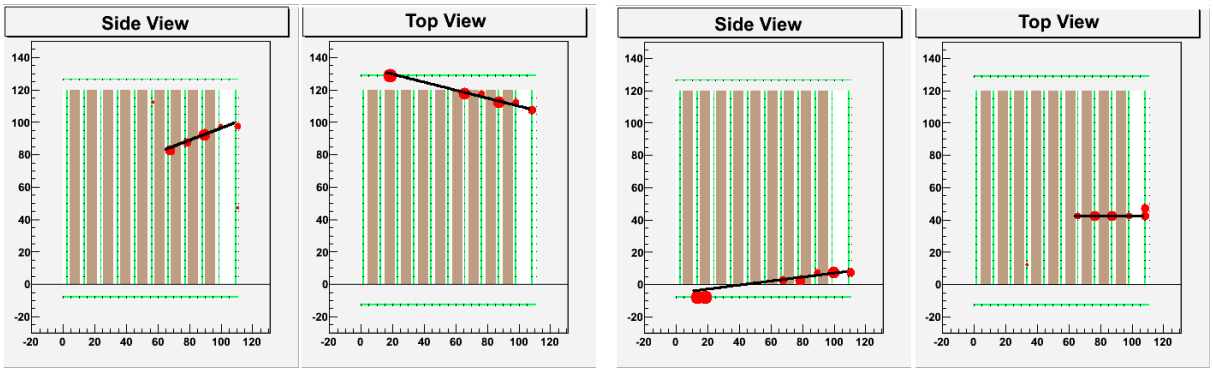

Figure 6.11: Event displays of rejected events by the veto cut.

6.2.2 Event selection summary

The result of the event selection is summarized in Table 6.2. The MC simulation reproduces the reduction in the data well.

The MC simulation includes neutrino interactions inside the upstream wall of the experimental hall. The MC prediction of the beam induced muon events is 35% smaller than the observation. It is considered to be caused from the uncertainties of the density of wall, the neutrino flux and the neutrino interaction model. When we compare the data and MC, the

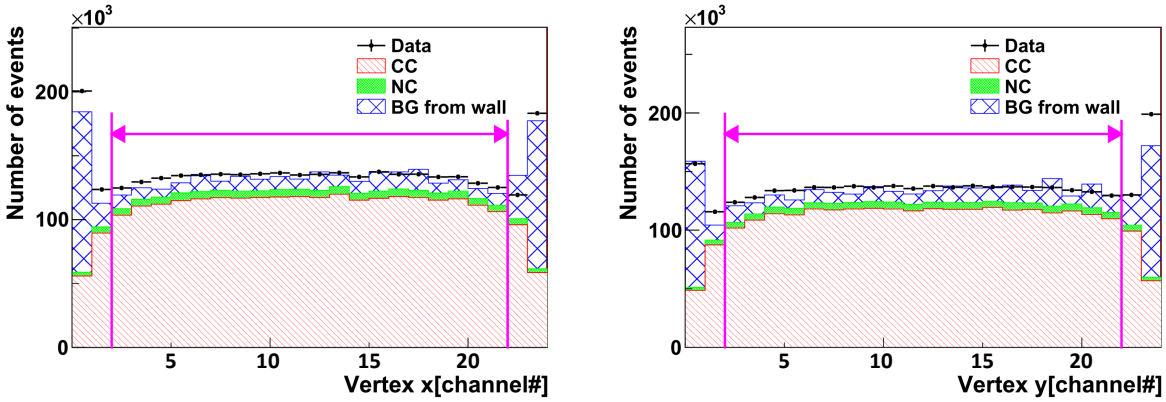

Figure 6.12: Vertex x and y distributions. A volume composed of the 3rd to 22nd scintillator bars in the x and y directions is defined as Fiducial Volume (FV). BG from wall is normalized with the number of beam induced muon events, as described in Section 6.2.2.

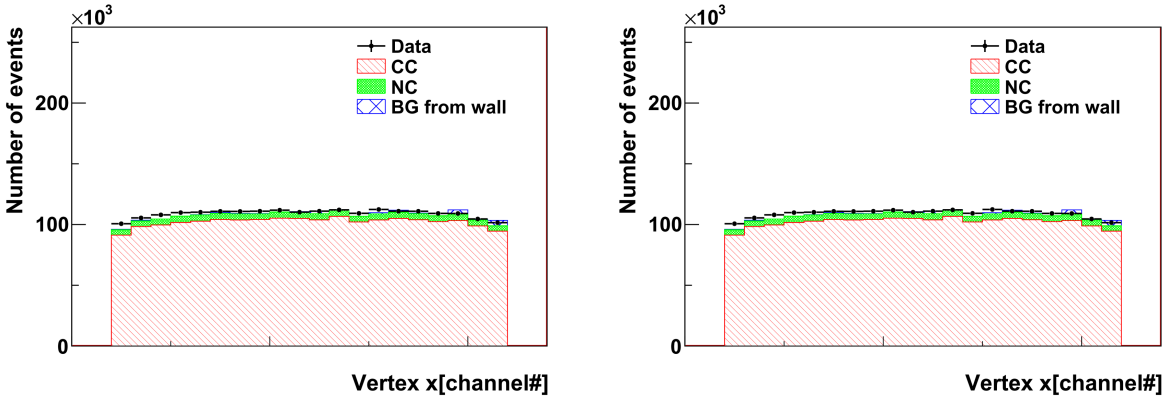

Figure 6.13: Vertex x and y distributions after all the event selections. BG from wall is normalized with the number of beam induced muon events, as described in Section 6.2.2.

number of neutrino interactions inside the wall in the MC simulation is normalized by the observed number of the beam induced muons. The 35% discrepancy is assigned as the systematic uncertainty of the background contamination fraction.

A fraction of the background contamination is estimated to be 0.4% by the MC simulation and the data. The uncertainty is estimated to be 0.2% (=0.4% × 35%).

Table 6.2: Event selection summary for the RUN-I and RUN-II data. The MC number is normalized by POT. The MC simulation includes neutrino interactions in the wall of the experimental hall.

	selection	Data	(%)	MC	(%)
1	# of active planes > 2	8.53×10^6	100	9.02×10^6	100
2	PE / active layers > 6.5	8.53×10^6	99.9	9.02×10^6	99.9
3	Tracking	8.01×10^6	94	8.40×10^6	93
4	Track matching	7.74×10^6	91	8.10×10^6	90
5	Beam timing	7.73×10^6	91	8.10×10^6	90
6	veto cut	3.30×10^6	39	3.30×10^6	37
7	FV cut	2.18×10^6	26	2.17×10^6	24

6.2.3 Selection efficiency

Figure 6.14 shows estimated selection efficiency as a function of true neutrino energy in the MC simulation after several selection criterion: after # of active planes > 2, after tracking, and after all FV cut. The efficiency for each neutrino interaction is shown in Fig. 6.15. The efficiency around 0.6 GeV is about 40% for neutrino CC interaction. The ∼20% inefficiency at high energy for the CC interaction is due to the events in which muons are produced with rather large angle: for such events, the muon escapes from the module before it penetrates two iron plates.

6.2.4 Correction factors

Two corrections are applied to the number of selected neutrino events. The correction factors are for the iron target mass and accidental MPPC noise.

The neutrino interactions in the MC simulation are generated with the design mass of iron target plates, so correction is applied to the neutrino interaction rate in each module individually based on the difference of the design mass to the measured mass of the module (Tab. 3.3): $-1 \sim +1\%$ for each module.

Accidental MPPC noise hits sometimes results in mis-identification of the vertex. The dependence of the selection efficiency on the MPPC noise rate is estimated by MC simulation where the ADC distribution and hit timing distribution are varied to reproduce measured noise rate. According to estimated dependence on the MPPC noise rate and measured noise rate, the number of selected events is decreased by 3% with the existence of MPPC noise. The number of events in the MC simulation is corrected to account this effect.

6.2.5 Systematic errors

Table 6.3 shows the summary of the systematic errors. Total error is calculated as quadratic sum of the errors and it is 3.7%. The each error is explained as follows.

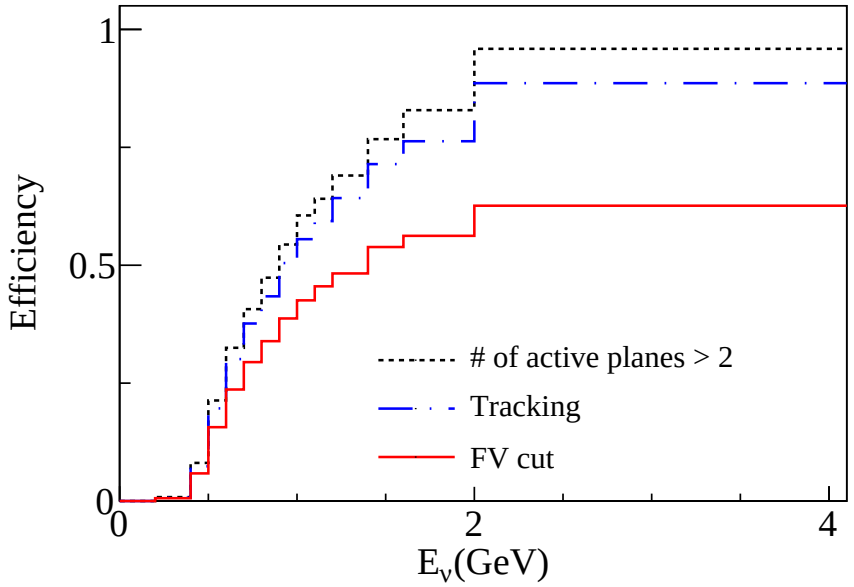

Figure 6.14: Neutrino event selection efficiency as a function of true neutrino energy after # of active planes > 2 (black dashed), after tracking (blue chain) and after FV cut (red solid)

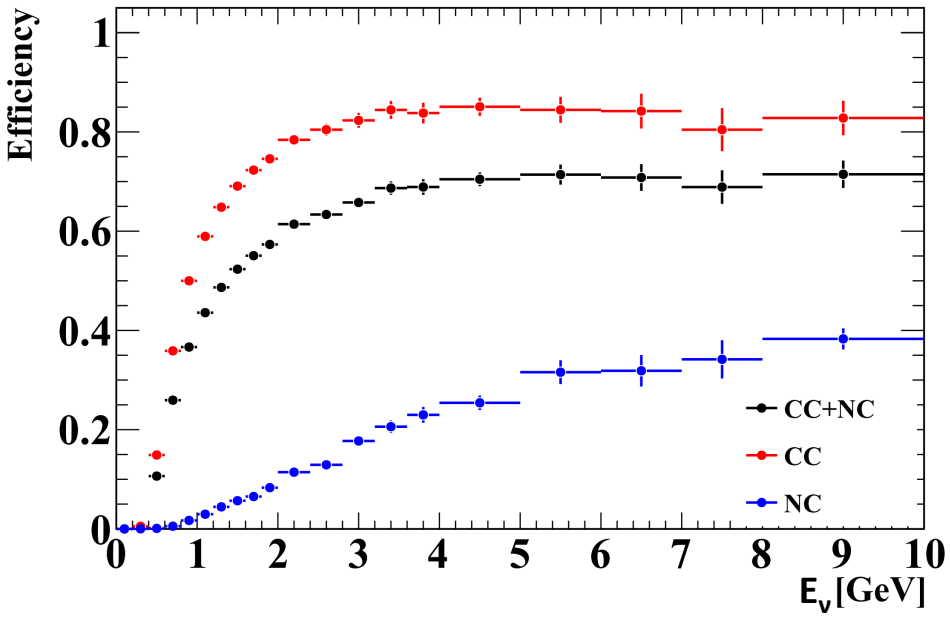

Figure 6.15: Neutrino event selection efficiency as a function of true neutrino energy.

Table 6.3: Systematic error table

Item	Error[%]
Vertex z matching	2.7
Channel hit efficiency	1.8
Tracking efficiency	1.4
FV cut	1.1
Accidental MPPC noise	0.7
Beam-related background	0.2
Iron mass	0.1
Average light yield per active layer	<0.1
Out-of-beam events	<0.1
Beam timing selection	<0.1
Total	3.7

Vertex z matching

In the neutrino event selection, the position difference of the vertex z between the x-z and y-z projections is required to be within one plane. There is an error of the MPPC dark noise hit and the optical cross-talk among the scintillator bars of the x-z and y-z layer. These errors cause the migration between the position difference of the vertex z. To estimate the event migration effects, we compare the ratio of the number of selected events to the number of events selected with different cut value for the vertex z matching selection. Table 6.4 shows the result. The maximum difference, 2.7%, is taken as the systematic error.

Table 6.4: Ratio of the number of events with the nominal selection to the number of events selected with several cut values of track matching.

(vertex z of x-z track) - (vertex z of y-z track) [plane]	Data[%]	MC[%]	diff.[%]
-1, 0, +1 (nominal selection)	100.0	100.0	0.0
0	83.0 ±0.2	85.7	2.7
-2, -1, 0, +1, +2	104.0±0.2	103.0	1.0

Channel hit efficiency

Because a missing hit at the scintillator bar results in miss-reconstruction of tracks, the number of selected events varies with the hit efficiency of each channel.
The relation between the hit efficiency and the number of selected events is estimated with the MC simulation in which the hit efficiency is changed. The result shows that the decrease of the hit efficiency by 1% corresponds to the decrease of the number of selected events of 1.6%.

The channel hit efficiency is measured by using the beam induced muons as shown in Fig. 3.25. The RMS (0.5%) is assigned as one of the uncertainties of the channel hit efficiency. The MC simulation reproduces the hit efficiency of the data by tuning the cross-section of the scintillator bar. The discrepancy after the tuning is within 1% across the entire track angle as shown in Fig. 3.26. From these two uncertainties, the error of the hit efficiency is estimated to be $\sqrt{1.0^2 + 0.5^2} = 1.1\%$. It corresponds to 1.8% error of the number of the selected events.

Tracking efficiency

The tracking efficiency is compared between the data and the MC simulation with two methods.

The first method is a re-tracking test. This test is schematically explained in Fig. 6.16. The event sample used in this test is the event after the neutrino event selections. The tracking efficiency is defined as the ratio of the number of tracks which pass the re-track test to the number of original tracks. The result is shown in Tab. 6.5. The maximum difference between the data and the MC simulation is 1.3%.

The second method is to count the number of events before and after tracking for some samples having different number of active planes. In this method, the efficiency is defined as the ratio of the number of events after tracking to that before tracking. Using the beam events after the pre-selections, the efficiency is estimated as shown in Tab. 6.6. The maximum difference between data and the MC simulation is 1.4%. The discrepancy comes from the difference of the hit efficiency and the uncertainties of the neutrino interaction model which results in the uncertainty of the hits by the final state particles.

The maximum difference among two methods, 1.4%, is taken as the systematic error of the tracking efficiency.

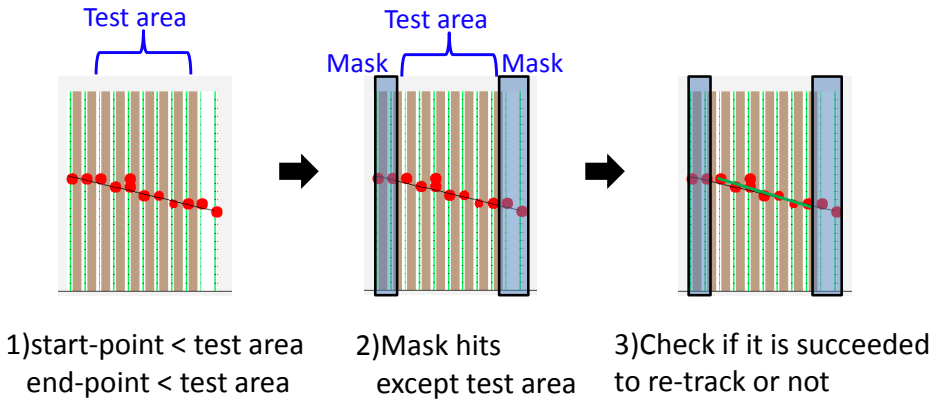

Figure 6.16: Method of the re-tracking test.

Table 6.5: Tracking efficiency estimated by the re-tracking test.

Test area	Data[%]	MC[%]	diff.[%]
$2 \sim 5$ (in x-z)	95.0±0.3	94.0	1.0
$2 \sim 5$ (in y-z)	95.3±0.3	94.0	1.3
$2 \sim 6$ (in x-z)	96.9±0.2	96.3	0.6
$2 \sim 6$ (in y-z)	96.9±0.2	96.2	0.7
$2 \sim 7$ (in x-z)	97.5±0.2	97.8	0.3
$2 \sim 7$ (in y-z)	97.8±0.2	97.7	0.1
$3 \sim 8$ (in x-z)	98.1±0.1	98.0	0.1
$3 \sim 8$ (in y-z)	97.9±0.1	98.2	0.3

Table 6.6: Ratio of the number of events before and after tracking. The events after pre-selections are divided into sub-samples according to the number of active planes.

Number of active planes	Data[%]	MC[%]	diff.[%]
3	87.6±0.2	86.9	0.7
4	93.2±0.2	91.8	1.4
5	94.7±0.2	94.3	0.5
6	95.6±0.2	96.2	0.6
7	96.2±0.2	96.6	0.4
8	96.7±0.2	96.8	0.1
9	98.7±0.2	97.9	0.8
10	99.1±0.1	99.0	0.1

FV cut

Different fiducial volumes are defined and the number of selected events with each fiducial volume is compared between the real data and the MC simulation. Here, the different volumes are set in the center, middle and edge region in order to check the contamination fraction of the beam induced muon backgrounds which are expected to distribute more in the edge region. Table 6.7 shows the result. The maximum difference, 1.1%, is taken as the systematic error.

Table 6.7: Ratio of the number of events selected with nominal FV and the number of events selected with several tried fiducial volumes.

x-y dimension of FV	Data[%]	MC[%]	diff.[%]
<50 cm from center(nominal selection)	100.0	100.0	0.0
<25 cm	25.6 ±0.2	25.2	0.4
25 ∼ 40 cm	39.9 ±0.2	39.3	0.6
40 ∼ 50 cm	34.4 ±0.3	35.5	1.1

Accidental MPPC noise

The effect of the accidental MPPC noise on the number of selected events is studied by using the MC simulation. The correction on it is applied on the data as described in Section 6.2.4. The systematic error on the accidental MPPC noise is estimated to be 0.7% based on the errors on the correction and the time variation of the MPPC noise rate.

Beam-related background

The contamination fraction of the beam-related background is 0.4% and the uncertainty is 0.2% as described in Section 6.2.2.

Iron mass

As described in Section 6.2.4, the mass of each iron plate was measured with a precision of 0.1%, which is taken as the systematic error.

Average light yield per active layer

The cut value is changed from nominal value (6.5 PE/active layer) and the number of events with several cut values are compared to that with the nominal cut. Because the nominal cut value is much smaller than the mean light yield measured with cosmic-ray (Fig. 3.24), the difference between each cut value is very small (0.01%). Thus the error of this selection is negligible.

Non beam-related backgrounds

To estimate the contamination fraction of non beam-related backgrounds, the data of the off-beam integration cycles (18th cycle to 23rd cycle, whereas the on-beam integration cycles are from 5th to 10th (RUN-I) or from 5th to 12th (RUN-II)) is analyzed with the same event selections for the neutrino event. Figure 6.17 shows the examples of the selected events. They are considered as the cosmic-ray stopped within one of the modules. The fraction of the non beam-related backgrounds in the on-beam integration cycles is estimated to be 0.02 % and it is negligible, where the number of off-beam events is normalized by the ratio of the number of on-beam cycles to that of off-beam cycles.

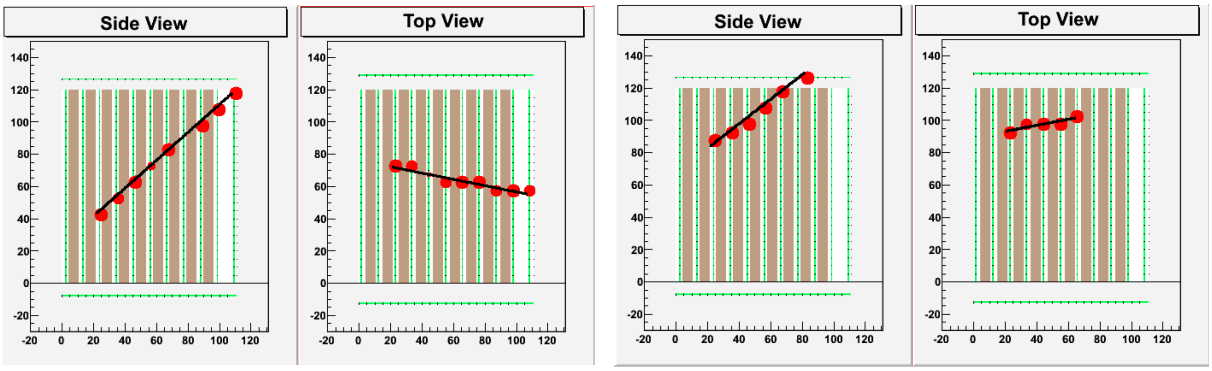

Figure 6.17: Examples of the non beam-related backgrounds. They are considered as the cosmic-ray stopped event within one of the modules.

Beam timing selection

Because of the finite timing resolution of INGRID and time stretch of the proton beam, there is a probability that some neutrino events are lost in the timing selection. To estimate the uncertainty, the cut value is changed from nominal value (±100 nsec) and the number of selected events with several cut values are compared to that with the nominal cut. The result is shown in Tab. 6.8. Because non beam-related background rate is negligible and the nominal time window for the selection is taken as much wider than the detector resolution and the time stretch of the primary proton beam, the differences between the cut values are very small (0.01%). In conclusion, the error of this selection is negligible.

Table 6.8: The number of the selected events with three cut values for the event timing

Cut value[nsec]	number of selected events	ratio[%]
±100	2179674	100.0
±90	2179570	99.995
±110	2179895	100.001

6.3 Results of the measurement

6.3.1 Event rate

Stability

Figures 6.18 and 6.19 show the daily rates of the neutrino events and the beam induced muon events normalized by protons on target (POT). The beam induced muon events are defined as the events rejected by the veto cut or the FV cut in Section 6.2. The average rate, typical statistical error and χ^2 from the average rate are summarized in Tab. 6.9. The relatively large χ^2 values (226.9/158 for neutrino event rate and 286.0/158 for beam induced muon events) come from the decrease of the event rate after February 4th, 2011. It is considered to be caused by a change in the primary beamline condition because the muon yield measured by the muon monitor showed a consistent tendency. The average rate, typical statistical error and χ^2 from the average rate before and after February 4th are summarized in Tab. 6.9. The χ^2 values are almost equal to the degree of freedom (ndf) and it is concluded that the event rate is stable within the statistical error. The decrease of 0.9% in the neutrino event rate is sufficiently small compared to assigned systematic error and the statistical error of ν_μ event in SK (17%).

We concluded that the beam neutrino production rate is stable. It confirms that the neutrino flux in Super-Kamiokande is stable.

Table 6.9: Average rate, typical statistical error and χ^2 from the average rate.

		average rate (events/10^{14} POT)	typical statistical error	χ^2/ndf
neutrino	(whole period)	1.512 ± 0.001		226.9/158
event	(before Feb. 4th 2011)	1.518 ± 0.001	1.7%	111.5/125
	(after Feb. 4th 2011)	1.504 ± 0.002		26.4/ 32
beam	(whole period)	3.851 ± 0.002		286.0/158
induced	(before Feb. 4th 2011)	3.859 ± 0.003	1.1%	122.1/125
muon	(after Feb. 4th 2011)	3.841 ± 0.004		25.6/ 32

Data over MC

The data to MC ratio of the neutrino event rate is measured to be

$$[N_{\mathrm{ND}}^{\mathrm{obs}}/N_{\mathrm{ND}}^{\mathrm{MC}}]_{(\mathrm{on-axis})} = 1.06 \pm 0.001(\mathrm{stat.}) \pm 0.037(\mathrm{syst.}) \tag{6.1}$$

after the correction. The uncertainties from the neutrino flux prediction and neutrino interaction model are not included in this systematic error. Agreement between the data and the MC simulation is very good.

6.3.2 Beam direction

The profile of the beam in the x and y directions are reconstructed with the number of neutrino events in seven horizontal and seven vertical modules, respectively. The observed profiles are fitted with a Gaussian function. The profile center is defined as the peak position of the fit. Finally, the beam direction is reconstructed as the direction from the proton beam target position to the measured center at INGRID.

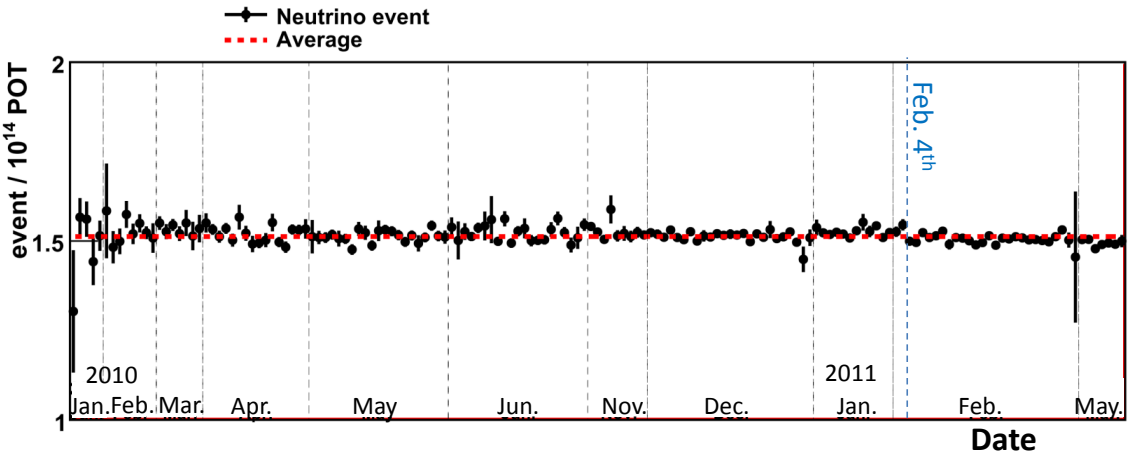

Figure 6.18: Daily event rate of the neutrino events normalized by protons on target.

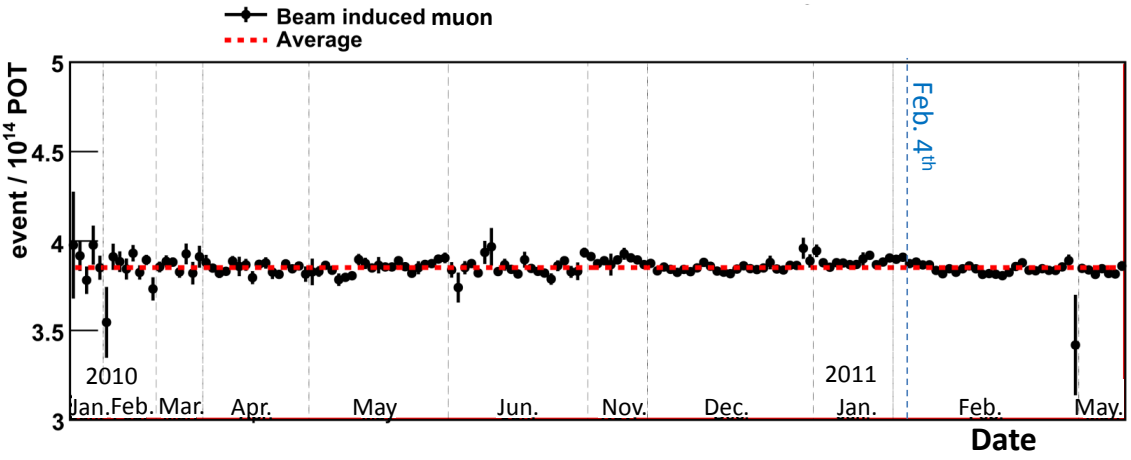

Figure 6.19: Daily event rate of the beam induced muon events normalized by protons on target.

Stability

In order to monitor the stability of the beam direction, the number of neutrino events is accumulated on a monthly basis. Figure 6.20 shows the observed profiles in April 2010. The black point in this figure shows the number of neutrino events in each module and the red dashed line shows the fitted Gaussian.

Black and blue points in Fig. 6.21 show the history of the beam centers in the x and y directions. All the points were stable well within 28 cm, which corresponds to the requirement of 1 mrad for the beam direction. Because the beam direction was adjusted in November 2010, the beam centers in the y direction after November 2010 are slightly shifted toward the center.

The beam direction is stable well within our requirement of 1 mrad. It confirms that the neutrino energy spectrum in Super-Kamiokande is stable.

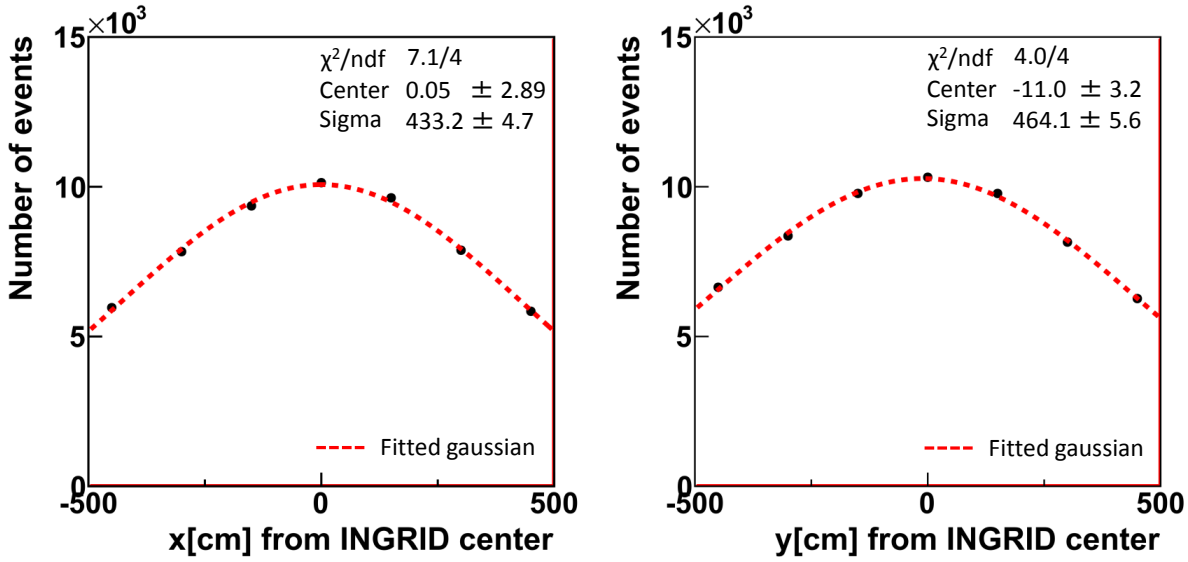

Figure 6.20: Neutrino beam profiles for horizontal (left) and vertical (right) directions measured in April 2010.

Systematic error and average beam direction

The systematic error on the profile center measurement was estimated by a toy MC simulation. In the simulation, the number of events at each module is changed within the range of the total detector systematic error of 3.7%. Here the error between each module is assumed to have no correlation. The 100,000 profiles are generated and the distribution of reconstructed beam centers are shown in Fig. 6.22. RMSs of the reconstructed center values are taken as the systematic errors; 9.2 cm and 10.4 cm for the x and y center, respectively. Because the width of the y profile is wider than that of the x profile as described in Section 3.1, the error of the y center is bigger than that of the x center.

From the beam center measurement and the survey between the proton target and the INGRID detectors, the average beam direction in x and y direction are measured to be

$$\begin{aligned} \text{x direction} &= -0.014 \pm 0.025(\text{stat.}) \pm 0.33(\text{syst.}) \text{ [mrad]} \\ \text{y direction} &= -0.107 \pm 0.025(\text{stat.}) \pm 0.37(\text{syst.}) \text{ [mrad]} \end{aligned} \tag{6.2}$$

We succeeded to measure the beam direction with a precision better than the requirement of

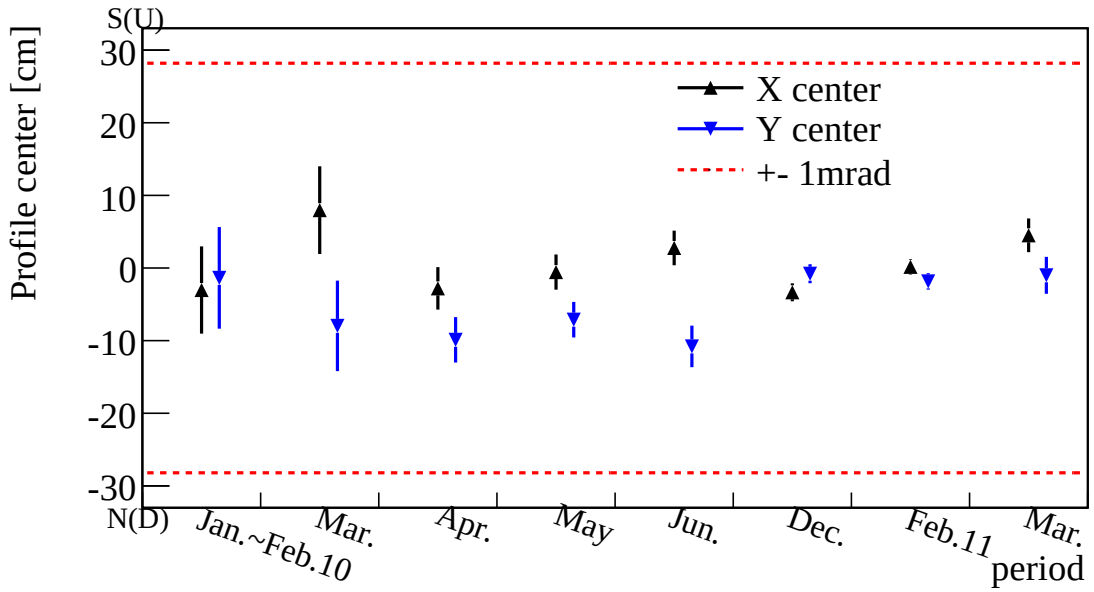

Figure 6.21: History of the neutrino beam centers.

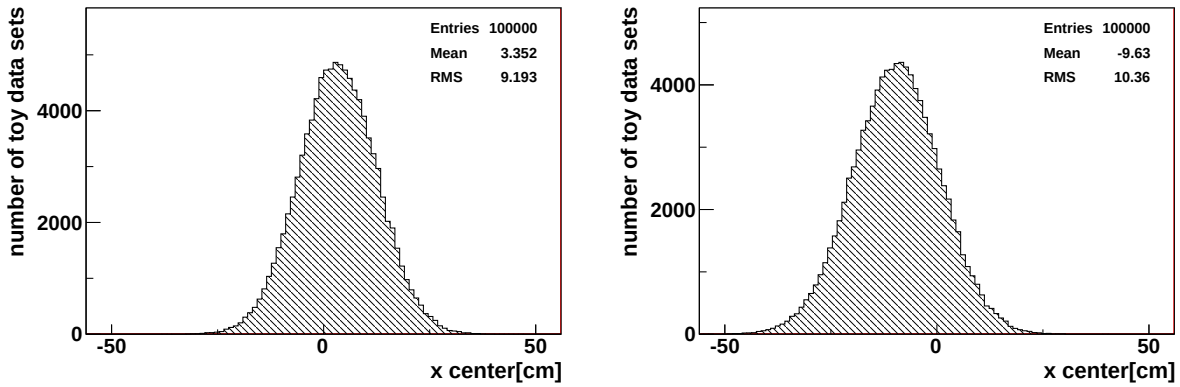

Figure 6.22: The reconstructed beam center distributions for x (left) and y (right) directions of the 100'000 profiles made by the toy MC simulation.

1 mrad. It ensures that the beam direction uncertainty on the $\sin^2 2\theta_{23}$ measurement does not effect on achieving the precision of $\delta(\sin^2 2\theta_{23}) \sim 0.01$.

6.4 Measurement by ND280

The number of neutrino events in the ND280 detector is measured with FGDs and TPCs; FGDs serve as the neutrino interaction target and identifies the interaction point, and TPCs measure charged particles generated in the interaction. Combining the momentum measurements and the ionization loss of the charged particles, TPCs identify muons and select the charged current (CC) interactions.

The overview of the event selection criteria is following:

1. Require no track in TPC1 to veto the through-going muons.
2. Require that there is at least one track reconstructed in TPC2, the associated hits in FGD1 start in the FGD1 fiducial volume, and the momentum of the track is larger than 50 MeV/c
3. Select the track with the highest momentum among the negative tracks reconstructed in TPC2 as a lepton track
4. Apply a PID cut to this track based on the TPC information about the energy deposit versus momentum, to select a muon and to reject a low energy electron/position
5. Repeat the steps 2-4 for TPC3 and FGD2 when there is no track in TPC2
6. To suppress miss-identified particle coming from outside of FGDs, reject a single track event in which track angle is $\cos\theta$ <0.9, momentum < 500 MeV/c and the TPC extrapolated track is close to FGD hits lying outside the fiducial volume.

The data set used for this analysis corresponds to 2.88×10^{19} POT in T2K RUN-I. We took the data during the T2K RUN-II period but don't use it because the data process and quality checks require a long time. Figure 6.23 shows the distribution of $E_\nu^{\rm rec}$ calculated by Eq. 1.32. After subtracting the background interactions outside the FGDs, we obtained 1456 neutrino events. As a result, the ratio of data over the MC simulation is 1.036 ± 0.028 (stat.).

The systematic error related to the detector response is estimated by using the beam data, the cosmic-ray data and the MC simulation. The total error is (+4.2, -3.6)%. The main sources are TPC-FGD track matching (±2.1%) and PID efficiency (+3.0%). The first one comes from the uncertainties of alignment between TPC and FGD. The error of the background interactions outside of the FGDs is estimated with a positive track sample; the sample is defined by changing the selection step (3) to select the positive charge track. In this sample, we can eliminate the main components of muons and obtain a background-enriched sample. The number of events in this sample are consistent within 0.9% between the data and the MC simulation. The 0.9% is assigned as the systematic error of the background contamination. In addition to the detector systematic error, the error due to the neutrino interaction model is estimated to be ±3.7%.

In conclusion, the ratio of data over the MC simulation is measured to be

$$[N_{\rm ND}^{\rm obs}/N_{\rm ND}^{\rm MC}]_{(\rm off-axis)} = 1.036 \pm 0.028(\rm stat.)\ ^{+0.042}_{-0.036}(\rm syst.) \pm 0.037(\rm phys.) \tag{6.3}$$

6.5 Summary of the measurements using near detectors

For the neutrino oscillation analysis, we need followings as described in Section 1.2.5:

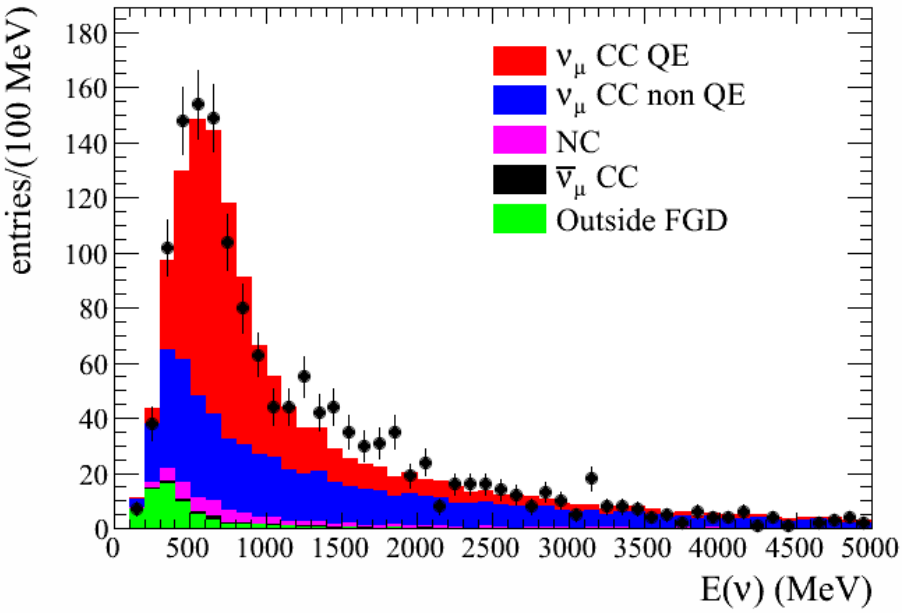

Figure 6.23: Distribution of the $E_\nu^{\rm rec}$ calculated by Eq. 1.32

(1) confirmation of the stable neutrino beam production

(2) measurement of the neutrino event rate in the near site

(3) measurement of the beam direction

INGRID measurement

We measured (1), (2) and (3) by using INGRID. We took more than 99% of all good beam spills.

The day-by-day neutrino event rates normalized by POT were stable within statistical error (it is typically 1.7%). The moth-by-month beam directions were stable well within our requirement of 1 mrad. From these measurements, we confirmed the stable neutrino beam production.

The data to MC ratio of the neutrino event rate was measured to be

$$[N_{\rm ND}^{\rm obs}/N_{\rm ND}^{\rm MC}]_{\rm (on-axis)} = 1.06 \pm 0.001({\rm stat.}) \pm 0.037({\rm syst.})$$

The beam x direction and y direction were measured to be

$$\begin{aligned} &\text{x direction} = -0.014 \pm 0.025(\text{stat.}) \pm 0.33(\text{syst.}) \ [\text{mrad}] \\ &\text{y direction} = -0.107 \pm 0.025(\text{stat.}) \pm 0.37(\text{syst.}) \ [\text{mrad}] \end{aligned} \tag{6.4}$$

We succeeded to measure the beam direction with a prediction better than our requirement of 1 mrad. It ensures that the beam direction uncertainty on the $\sin^2 2\theta_{23}$ measurement is negligible.

ND280 measurement

We measured (2) by using ND280. ND280 analysis is performed with RUN-1 data after a quality cut, corresponding to 2.88×10^{19} protons on target. The data to MC ratio of the neutrino event rate was measured to be

$$[N_{\rm ND}^{\rm obs}/N_{\rm ND}^{\rm MC}]_{\rm (off-axis)} = 1.036 \pm 0.028({\rm stat.}) \ ^{+0.042}_{-0.036}({\rm syst.}) \pm 0.037({\rm phys.})$$

Application of $N_{\mathrm{ND}}^{\mathrm{obs}}/N_{\mathrm{ND}}^{\mathrm{MC}}$ on the neutrino oscillation analysis

As described in Eq. 1.33, the expected number of events in SK ($N_{\mathrm{SK}}^{\mathrm{exp.}}$) is obtained by using $N_{\mathrm{ND}}^{\mathrm{obs}}/N_{\mathrm{ND}}^{\mathrm{MC}}$. With this method, the error on $N_{\mathrm{SK}}^{\mathrm{exp.}}$ can be reduced because of the error cancellation between ND and SK. As a typical example, Tab. 6.10 shows the estimated beam flux error size on $N_{\mathrm{SK}}^{\mathrm{MC}}$ and $N_{\mathrm{SK}}^{\mathrm{exp.}}$ with two cases: using INGRID and using ND280. Thanks to the error cancellation, the error size on $N_{\mathrm{SK}}^{\mathrm{exp.}}$ is smaller than that on $N_{\mathrm{SK}}^{\mathrm{MC}}$. Because ND280 measures the neutrinos in the same direction to SK, the error size on $N_{\mathrm{SK}}^{\mathrm{exp.}}$ by using ND280 is smaller than that by using INGRID. Hence we use the ND280 measurement for the neutrino oscillation analysis.

In this analysis the ND280 measurement with only the RUN-I data set is available because it takes too much time to process the data. Because the stability of the neutrino beam production between RUN-I and RUN-II is confirmed by the INGRID measurements, we can use RUN-I and RUN-II data for the oscillation analysis by scaling the RUN-I ND280 measurements according to POT.

Table 6.10: Uncertainties of $N_{\mathrm{SK}}^{\mathrm{MC}}$ and $[N_{\mathrm{SK}}^{\mathrm{MC}}/N_{\mathrm{ND}}^{\mathrm{MC}}\ ]$ from the beam flux prediction, two cases (normalized with INGRID and ND280) are shown.

	INGRID	ND280
Error on $N_{\mathrm{SK}}^{\mathrm{MC}}$	$\sim 15\%$	
Error on $[N_{\mathrm{SK}}^{\mathrm{MC}}/N_{\mathrm{ND}}^{\mathrm{MC}}\ ]$ (no oscillation)	11.2%	6.4%

Chapter 7

Far Detector Analysis

The number of ν_μ events and their energy spectrum are measured with Super-Kamiokande (SK) which is 295 km away from J-PARC. This chapter describes the data set used for the analysis, the ν_μ event selection, and the systematic uncertainties.

7.1 Data set

All the data during RUN-I and RUN-II are used for this analysis. The good beam spills are selected as described in Section 6.1. After the good beam spill selections, following selections are applied to the SK data in order to ensure the SK data quality.

(1) SK DAQ alive
The dead time fraction is 0.1%.

(2) Bad subrun cut
A "Subrun" is a unit of SK data corresponding to approximately one minute of observation. Each subrun is judged to be suitable for the analysis or not. The primary cause of the bad subruns is PMT flasher (the flasher events are described in Section 7.2). Other reasons are DAQ trouble and so on. The dead time fraction by this cut is 0.5%. The good/bad subrun list is also defined for the SK atmospheric neutrino analyses [72].

(3) DAQ/GPS error cut
DAQ status is checked by the number of hits (hit threshold is ~ 0.25 PE) in a ± 500 μsec T2K window; because most of the hits are due to the PMTs' dark noise and dark noise rate is almost constant, the number of hits of ID-PMT and OD-PMT are required to be above 48000 and 6000, respectively. The threshold values, 48000 and 6000, are determined by the study with the data without the beam. In addition, if both the GPS1 data and the GPS2 data have error flags, the spill is classified as a bad spill. No spill has been rejected by DAQ/GPS error cut so far.

(4) Special data block cut
The SK electronics system records all the hit signals in units of the 17 μsec data block. Two types of special blocks are rejected. One is "pedestal block" for taking pedestal data every 65536 blocks. The other is "TDC reset block" for resetting some counters every 4096 blocks. The reduction inefficiency caused by this cut is 0.08%.

(5) Pre-activity cut
In order to remove an accidental contamination of a decay-electron from cosmic-ray muons stopped inside the detector tank, events which have another event in the 100 μsec before the original event are rejected. The spill loss by this cut is 0.3%.

The number of spills after each cut is summarized in Tab. 7.1. A total of 2474419 spills are selected and inefficiency is 1.0%. Figure 7.1 shows the accumulated number of POT as a function of date. The total POT after the SK quality cut is 1.43×10^{20}.

Table 7.1: Number of spills after each SK quality cut.

Selection	Number of spills	Inefficiency
Beam good spills	2499013	
(1) SK DAQ alive	2495955	0.1%
(2) Bad subrun cut	2484348	0.5%
(3) DAQ/GPS error cut	2484348	no
(4) Special data block cut	2482298	0.08%
(5) Pre-activity cut	2474419	0.3%

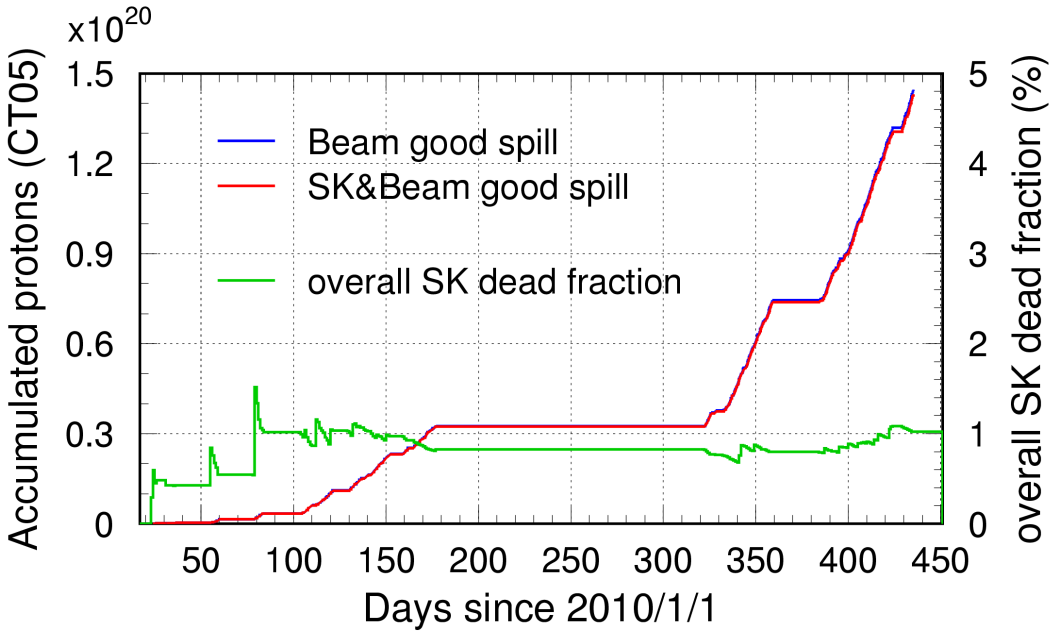

Figure 7.1: Accumulated number of POT after the beam good selections (blue) and the SK data quality selections (red), together with a change in the SK dead fraction.

7.2 Event selection

Overview

To measure the neutrino flux and the energy spectrum, we select the muon neutrino CCQE interaction events. The neutrino energy is reconstructed by the muon momentum and the angle against the neutrino direction as described in Eq. 1.32. Figure 7.2 shows the classification of the neutrino event in SK. As the first step, the outer detector (OD, see Fig. 2.10) and partially contained (PC) events are rejected using the OD PMTs activities. After that the muon neutrino CCQE interaction events are selected from the information of the reconstructed Cherenkov rings

and the delayed activities due to decay electrons. Details are described below. The selection criterion are established through the atmospheric neutrino analysis [73] before the T2K neutrino analysis.

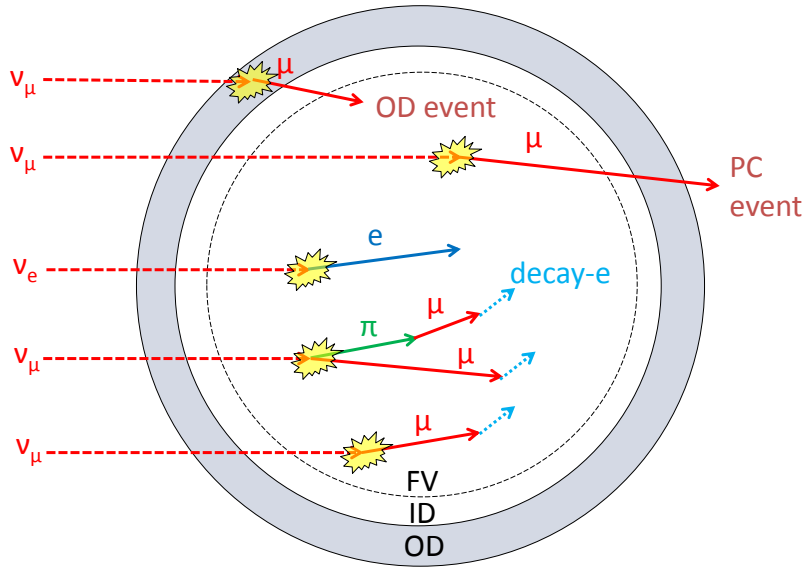

Figure 7.2: Illustration of the event classification at SK.

FC event reduction

As described in Section 2.4, the charge and timing of all the hit PMTs (hit threshold is ~ 0.25 PE) within 500 μsec from the beam arrival time are written to disk. Then an event is extracted as the clustered hits within $-5 \sim +35$ μsec from the timing of the trigger which is fired by 47 ID-PMT hits in a 200 nsec time window (corresponding to a 5 MeV electron) or by 22 OD-PMT hits in a 200 nsec time window.

In the following the events in the T2K beam window are called as the beam events. All the beam events are then classified into 5 categories as shown in Fig. 7.3:

1. Calibration events
   Events with a flag for identifying detector calibration

2. OD candidates
   Events in which the number of PMT hits in the largest OD hit cluster is larger than 15 are selected, where the OD hit cluster is searched by sliding 200 nsec time window in the event.

3. Low energy (LE) candidates
   Events in which the total charge of the inner detector (ID, see Fig. 2.10) PMT hits in a 300 nsec window is less than 200 PE are selected. Events in which the maximum charge in a single ID-PMT is more than half of the total charge are also selected as low energy events mainly caused by radioactivity near the PMT.

4. Flasher events
   The flusher events are spurious events due to a sudden "flashing" PMT that emit light

from internal corona discharges. Because the flusher events have a broader hit timing distribution than the neutrino events (Fig. 7.4), the flusher events are removed by checking the timing distribution. In addition, because the flusher events have a tendency to be repeated with similar spatial hit pattern, the pattern information of the candidate event is compared with one of the flasher event in the database to cut the flasher event. The parameter used for the cut is evaluated with the charge observed in ID-PMTs of 2 m×2 m square patch and a charge pattern between the patches. Figure 7.5 shows the flasher cut parameter for the atmospheric neutrino samples and the flasher events. The inefficiency to the neutrino events due to this cut is estimated to be $\sim 1\%$.

5. FC candidates
   Events which survive all criterion.

The FC events then go to following selections.

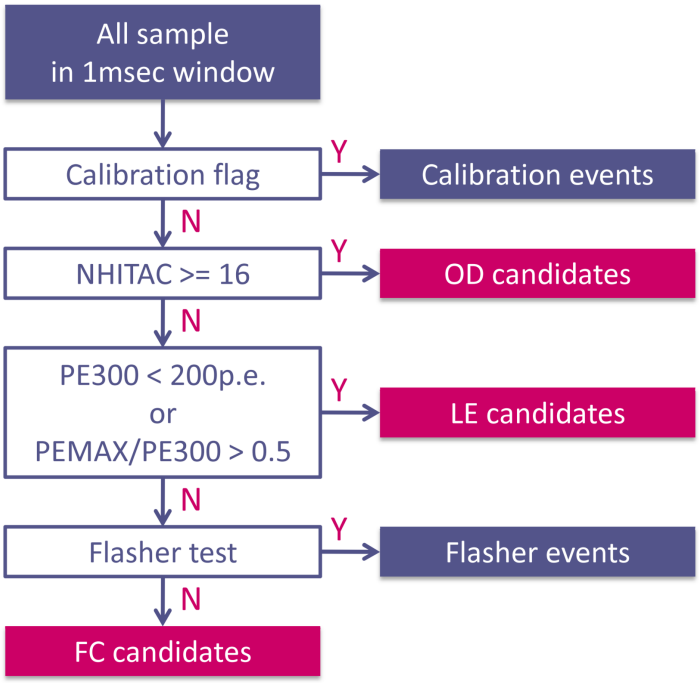

Figure 7.3: Flowchart of the FC event reduction.

Visible energy > 30 MeV

The visible energy (E_{vis}) is defined as the sum of the energy of all rings on an assumption that all rings are produced by electrons. In order to eliminate low energy events such as NC background events, events with $E_{vis} > 30$ MeV are selected as shown in Fig. 7.6.

Distance from the reconstructed vertex to the nearest ID wall > 200 cm (Fiducial volume)

The vertex is reconstructed by using two algorithm: "TDCfit" for all the events and "MSfit" for only single ring events. In TDCfit, the vertex position is estimated by finding the position at which the timing residual ((photon arrival time) - (time of flight)) distribution is mostly

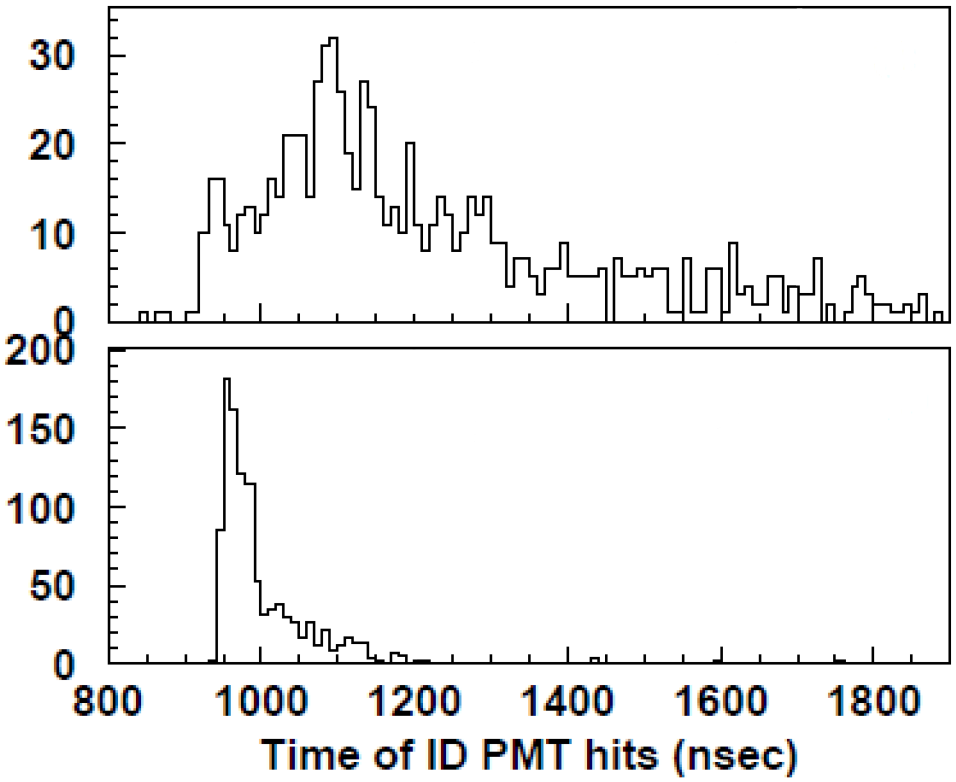

Figure 7.4: Timing distribution of the flasher event (top) and the neutrino event (bottom).

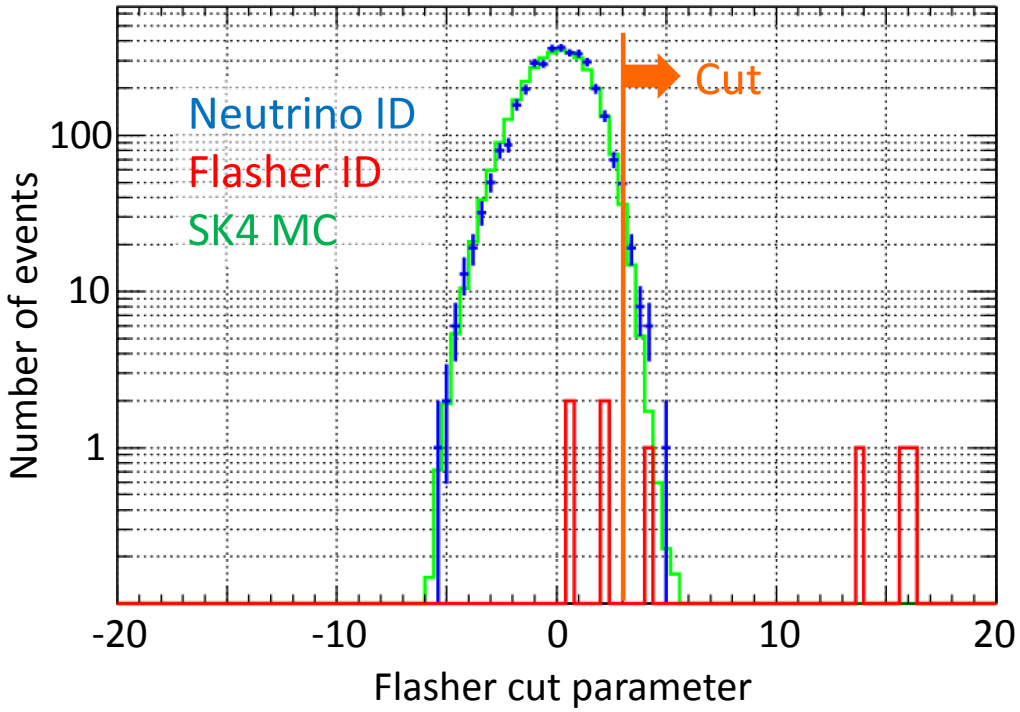

Figure 7.5: Flasher cut parameter distribution for atmospheric neutrino data (blue dots), atmospheric neutrino MC simulation (green) and flasher events (red) identified by eye-scan.

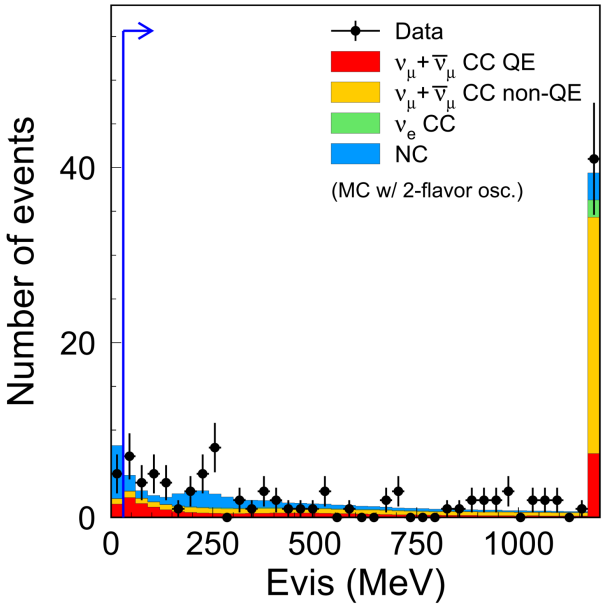

Figure 7.6: Distribution of the visible energy for the T2K beam data and its MC simulation. The MC sample is broken down into ν_μ and $\bar{\nu}_\mu$ CCQE interaction (red), ν_μ and $\bar{\nu}_\mu$ CC non-QE interaction sample (yellow), the ν_e CC interaction sample (green), and NC interaction sample (blue). The MC includes $\nu_\mu \to \nu_x$ oscillations with $\Delta m^2 = 2.4 \times 10^{-3}\mathrm{eV}^2/\mathrm{c}^4$ and $\sin^2 2\theta_{23} = 1.0$.

peaked. The MS vertex fitter uses not only the timing information but also the Cherenkov ring pattern information and improves the vertex resolution in the longitudinal direction. The vertex resolution is estimated to be 25 cm for 1 ring μ-like events in the MC simulation. Because the detection efficiency is slightly decreased near the edge region of the ID wall, events with the distance from the ID wall $>$ 200 cm are selected as shown in Fig. 7.7.

single ring

The ring counting algorithm consists of two steps. The first step is searching for second ring candidate using Hough transformation [74]. In the second step, likelihood is calculated by comparing the observed PMT hit map and one expected by the ring candidate. If the second ring is determined to be exiting, the two steps are repeated to find other possible rings up to five. An example of the ring finding for ν_μ CC1π event is shown in Fig. 7.8. The muon ring and charged pion ring are well fitted by the algorithm. The efficiency of single ring identification for CCQE event is estimated to be $\sim$ 96% in the MC simulation. Figure 7.9 shows the ring counting likelihood distribution for the beam events. Events with negative (positive) likelihood are recognized as single ring (multi-ring) events. In order to select ν_μ CCQE event, single ring events are selected.

μ-like ring

Each ring is classified as a showering particle (e-like) or a nonshowering particle (μ-like). Figure 7.10 shows the distribution of likelihood constructed with the Cherenkov ring pattern and opening angle for the beam events. Events with negative (positive) likelihood are recognized as e-like (μ-like) ring events. The μ-like events are selected.

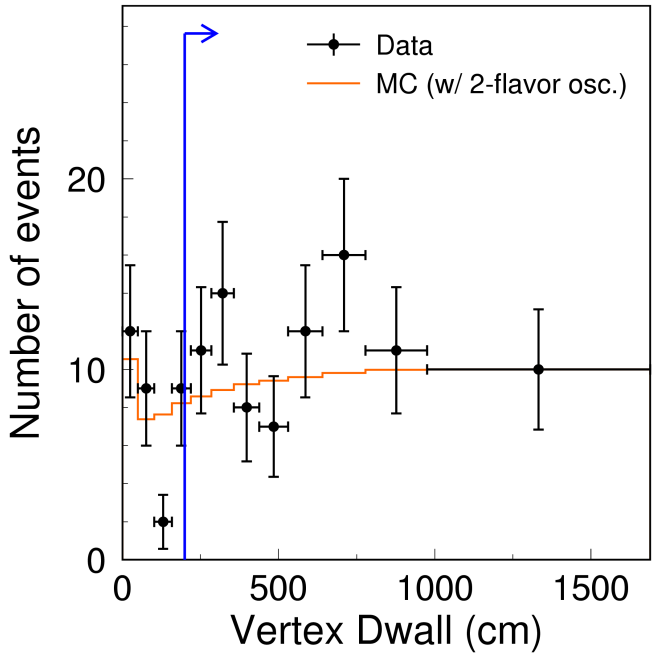

Figure 7.7: Distribution of the distance from the reconstructed vertex to the nearest ID wall for the T2K beam data and its MC simulation.

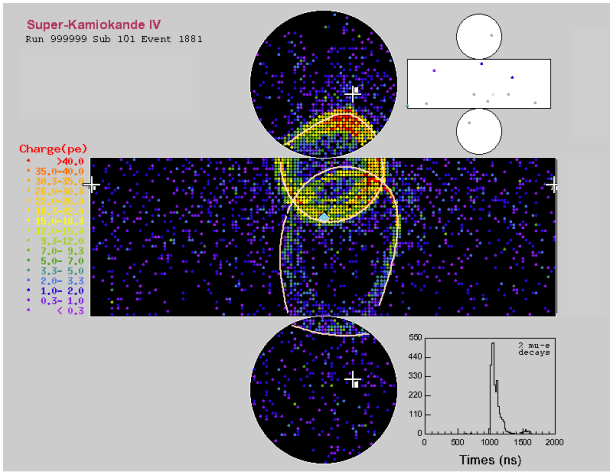

Figure 7.8: A result of the ring fitter. A ν_μ CC1π Monte Carlo event is reconstructed as a two ring event. The reconstructed Cherenkov rings are drawn by flesh color.

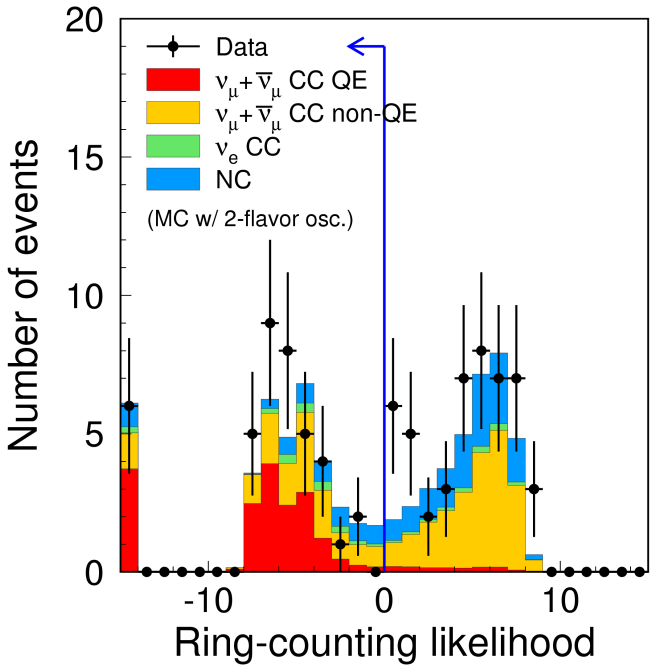

Figure 7.9: Ring counting likelihood for the T2K beam data.

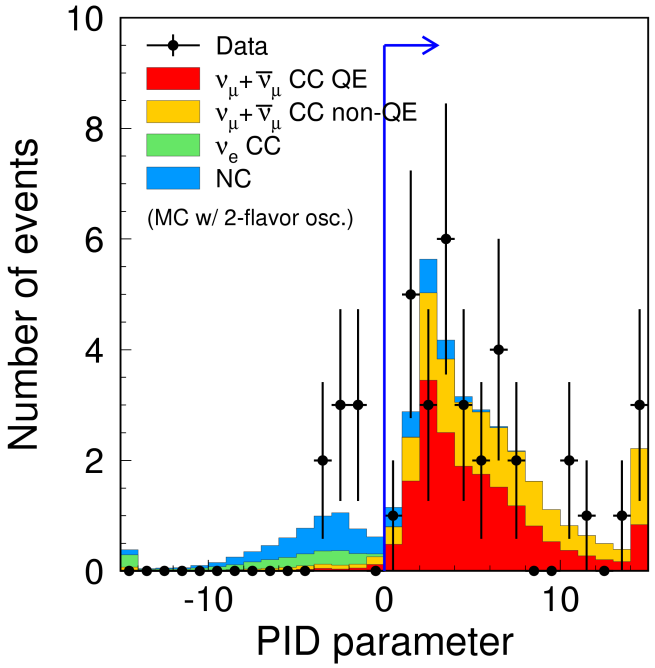

Figure 7.10: PID likelihood for the T2K beam data.

muon momentum > 200 MeV

The momentum is estimated from the total number of photo-electrons detected within a 70° half opening angle towards the reconstructed ring direction. The number of photo-electrons is corrected for light attenuation in water, PMT angular acceptance and PMT coverage. The reconstructed momentum resolution is estimated to be $\sim 3\%$ for the single ring muons. In order to keep the PID performance, events with the muon momentum > 200 MeV are selected as shown in Fig. 7.11.

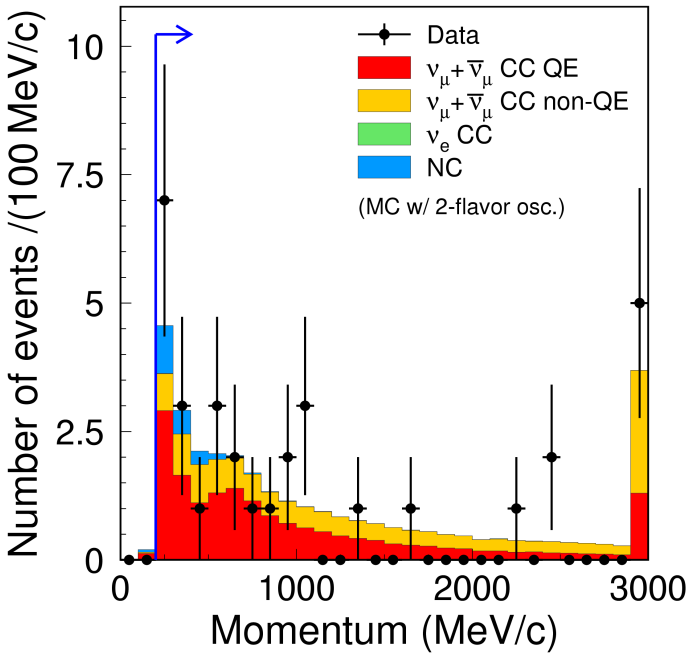

Figure 7.11: Distribution of the reconstructed muon momentum.

Number of decay electrons < 2

Decay electrons are tagged by searching for hit clusters after the primary event. The tagging efficiency is estimated to be $\sim 90\%$ with the cosmic-ray stopped muon in the tank. In order to eliminate the events with charged pions not reconstructed, events with the number of decay electrons < 2 are selected as shown in Fig. 7.12.

Event selection summary

Table 7.2 shows the number of selected events at each selection step. The number of selected events is 31. The distribution of the reconstructed neutrino energy is shown in Fig. 7.13.

Figure 7.14 shows the accumulated number of selected events as a function of POT. The hypothesis that the event rate is constant was examined by using the Kolmogorov-Smirnov (KS) test. Translated to the plot, this hypothesis is represented by the straight line between (0, 0) and (1.43×10^{20}POT, 31). Then the largest vertical distance $D_{\max}$ between the observation and the hypothesis was searched for. $D_{\max}$ was found to be 0.16 and the KS probability to obtain the values larger than 0.16 by statistical fluctuations was calculated to be 34%. The event rate is concluded to be stable.

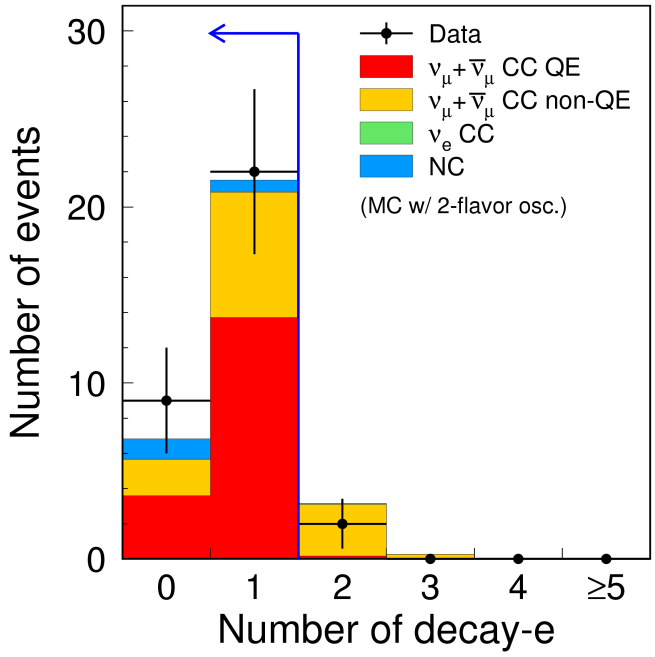

Figure 7.12: Distribution of the number of decay electrons.

Table 7.2: Number of events after each selection.

Selection	Data	Non-oscillated MC	Oscillated MC $\sin^2 2\theta = 1.0$ $\Delta m^2 = 2.4 \times 10^{-3}\text{eV}^2$
FC event	121	246	109
FV	88	166	74.1
single ring	41	120	38.7
μ-like	33	112	32.0
$p_\mu > 200$ MeV/c	33	111	31.8
# of decay electrons < 2	31	104	28.4

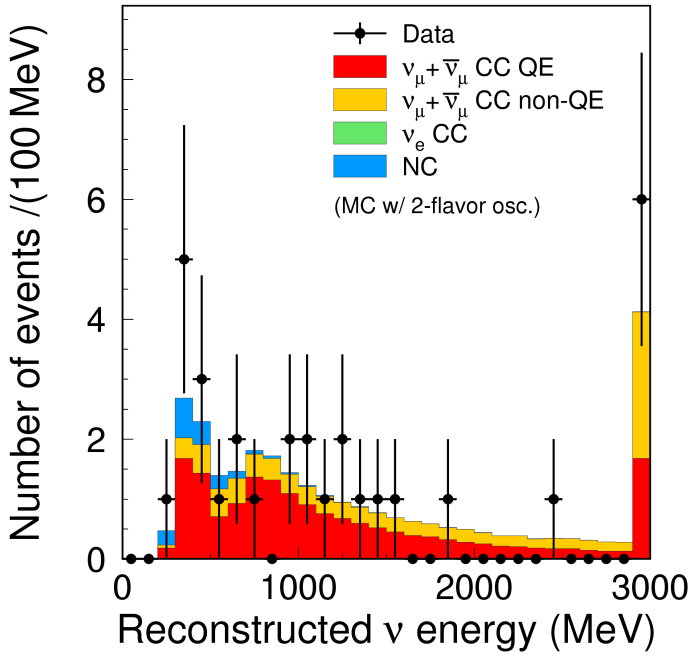

Figure 7.13: Reconstructed neutrino energy ($E_\nu^{\rm rec}$) distribution for the selected 31 events.

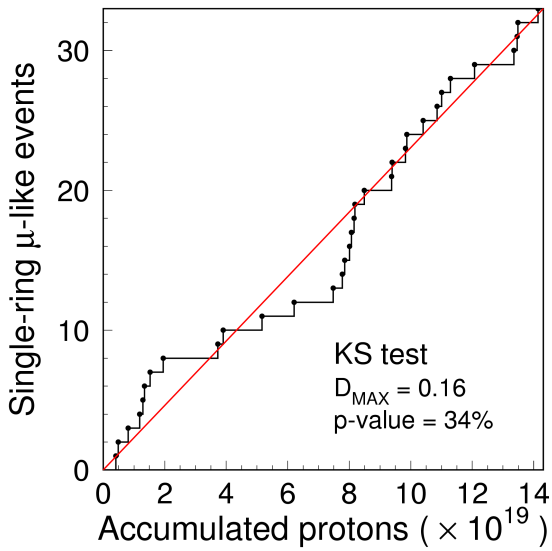

Figure 7.14: Accumulated number of 1 ring μ-like events as a function of POT.

7.3 Systematic error of the event selection

Table 7.3 shows the summary of the systematic errors. In this table, CCnonQE is defined as the CC interactions other than CCQE interaction. For the particle ID error for the NC interaction mode, 100% error is assigned because there is no estimation on it now. Other errors are explained as follows.

Table 7.3: Summary of the systematic error on the number of events in SK and the systematic error on $E_\nu^{\rm rec}$.

Systematic error on the number of events			
	ν_μ CCQE	ν_μ CC non-QE	NC
Ring Counting	1.7%, 3.5%, 9.3% with error matrix Eq.7.1	19.9%	48.2%
Flasher cut	1.0%		
Fiducial volume	1.0%		
Decay electron	1.0%		
Particle ID	$\ll$1%		100%
Momentum cut	$\ll$1%		
OD cut	$\ll$1%		

Systematic error on the reconstructed neutrino energy	
Energy scale	2.3%

7.3.1 Ring counting (RC)

Because the ring counting (RC) systematic error is the most dominant error of SK, details are described here. Before explaining the method, the result is shown in Tab. 7.4 in advance. We estimated the energy dependent error on the number of ν_μ CCQE events, the error on the number of the ν_μ CC non-QE events, and the error on the number of the NC interaction events by using the atmospheric neutrino data. For the CCQE interaction, the energy dependence of the error is estimated along with the correlation between them as shown in Eq.7.1.

Table 7.4: RC systematic error

Interaction mode	Error
CCQE ($E_{rec} < 0.4$ GeV)	1.7%
CCQE ($E_{rec} = 0.4 \sim 1.1$ GeV)	3.5%
CCQE ($E_{rec} > 1.1$ GeV)	9.3%
CC non-QE	19.9%
NC	48.2%

$$
\begin{array}{ccc}
\mathrm{E_{rec}} < 0.4\mathrm{GeV} & \mathrm{E_{rec}} = 0.4 \sim 1.1\mathrm{GeV} & \mathrm{E_{rec}} > 1.1\mathrm{GeV} \\
\left(\begin{array}{ccc}
\sigma_1^2 & 0.59\sigma_1\sigma_2 & 0.33\sigma_1\sigma_3 \\
 & \sigma_2^2 & 0.61\sigma_2\sigma_3 \\
 & & \sigma_3^2
\end{array} \right) &
\end{array}
\tag{7.1}
$$

$$\sigma_1 = 1.7\%, \sigma_2 = 3.5\%, \sigma_3 = 9.3\%$$

Overview of the method to estimate the error is as follows:

(1) Control samples are defined with atmospheric neutrino events; the enriched samples of ν_μ CCQE, ν_μ CC non-QE, and Neutral Current (NC) are defined to estimate the error for each neutrino interaction. In addition, the ν_μ CCQE enriched sample is divided with the visible energy ($E_{\rm vis}$) to estimate the energy dependence of the RC error.

(2) The number of events of each sample is compared between the data and the MC simulation. The RC error is estimated as the difference between the data and the MC prediction.

(3) For ν_μ CCQE interaction, the estimated errors as a function of $E_{\rm vis}$ are translated to the errors as a function of $E_{\rm rec}$ by the MC simulation.

Step(1), (2) and (3) are explained in following sub-section I, II and III, respectively. Finally the estimated errors are summarized in sub-section IV.

I. Control samples

Control samples among the fully contained fiducial volume events of atmospheric neutrinos as shown in Tab. 7.5. Each control sample enhances ν_μ CCQE, ν_μ CC non-QE, and NC interaction events. The ν_μ CCQE samples are divided with $E_{\rm vis}$ to estimate the energy dependent error. In addition, a ν_e CC enriched sample is defined to give a constraint on the uncertainty of that event rate in the other samples. Then each sample is divided into single-ring or multi-ring sample; there are twelve samples in total.

Table 7.5: Definition of the control samples.

Notation	Explanation	selection criteria
CCQE1	ν_μ CCQE enriched sample 1	Number of decay electrons = 1 Distance from the muon stopped point to decay electron < 80 cm $E_{\rm vis} < 0.13$GeV
CCQE2	ν_μ CCQE enriched sample 2	Number of decay electrons = 1 Distance from the muon stopped point to decay electron < 80 cm $E_{\rm vis} = 0.13 \sim 0.7$GeV
CCQE3	ν_μ CCQE enriched sample 3	Number of decay electrons = 1 Distance from the muon stopped point to decay electron < 80 cm $E_{\rm vis} > 0.7$GeV
CCnQE	ν_μ CC non-QE enriched sample	Number of decay electrons > 1 Distance from the muon stopped point to nearest decay electron < 160 cm
NC	NC enriched sample	Number of decay electrons = 0 not ν_e sample
nue	ν_e CC enriched sample	Brightest ring is e-like $E_{\rm vis} > 100$MeV π^0 assuming mass < 105 MeV

The data set is the SK-IV atmospheric neutrino data till March 2011 (live time = 762.2 days). The MC simulation is equivalent to 500 years statistics.

Table 7.6 shows the breakdown of the number of events of each control sample. The number of events are almost consistent between the data and the MC prediction. A large discrepancy of the CCnQE 1R sample is considered to be caused from the uncertainty of the atmospheric neutrino flux and the neutrino cross-section.

Table 7.6: Summary of number of events of ν_μ CCQE enriched sample (CCQE1,2,3), ν_μ CC non-QE enriched sample (CCnQE), NC enriched sample (NC), and ν_e CC enriched sample (nue). Samples are separated to single-ring sample (1R) and multi-ring sample (mR).

Sample	Data	MC total	ν_μ CCQE	ν_μ CC non-QE	NC	ν_e CC	(data-MC) /data[%]
CCQE1 1R	173	169.5	142.9	19.6	5.3	1.7	2.0 ± 7.6
CCQE1 mR	14	15.7	4.6	5.5	4.6	1.0	-12.1 ± 26.7
CCQE2 1R	400	378.2	312.8	59.7	4.9	0.8	5.5 ± 5.0
CCQE2 mR	60	59.3	12.1	30.6	12.1	4.4	1.2 ± 12.9
CCQE3 1R	250	258.4	183.3	74.9	0.2	0.02	-3.4 ± 6.3
CCQE3 mR	53	62.2	4.2	54.8	2.1	1.2	-17.4 ± 13.7
CCnQE 1R	115	80.4	4.4	73.9	1.5	0.5	30.1 ± 9.3
CCnQE mR	120	114.8	2.2	95.8	13.2	3.6	4.3 ± 9.1
NC 1R	751	781.6	227.8	72.1	154.8	326.9	-4.1 ± 3.7
NC mR	836	827.9	21.1	81.9	420.6	304.3	1.0 ± 3.5
nue 1R	1621	1440.0	5.3	5.0	40.1	1389.5	11.2 ± 2.5
nue mR	194	176.2	4.3	27.4	36.6	107.9	9.2 ± 7.2

II. Error estimation by comparing between the data and the MC prediction

To evaluate the RC error by comparing the data and the MC prediction while taking into account the uncertainty of the atmospheric neutrino flux and the neutrino cross-section, we define a χ^2 as

$$\begin{aligned}\chi^2 =& \sum_{i=1}^{6}\left[2\Big\{N_{i,1R}^{exp}(\boldsymbol{f},\boldsymbol{\alpha}) - N_{i,1R}^{Data}\Big\} + 2N_{i,1R}^{Data}\ln\big(\frac{N_{i,1R}^{Data}}{N_{i,1R}^{exp}(\boldsymbol{f},\boldsymbol{\alpha})}\big)\right] \\ &+ \sum_{i=1}^{6}\left[2\Big\{N_{i,mR}^{exp}(\boldsymbol{f},\boldsymbol{\alpha}) - N_{i,mR}^{Data}\Big\} + 2N_{i,mR}^{Data}\ln\big(\frac{N_{i,mR}^{Data}}{N_{i,mR}^{exp}(\boldsymbol{f},\boldsymbol{\alpha})}\big)\right] + \sum_{k=1}^{6}(\frac{\alpha_k}{\sigma_k})^2\end{aligned} \tag{7.2}$$

where the index i denotes the control samples (ν_μ CCQE1, 2, 3, ν_μ CCnQE, NC, and nue), $N_{i,1R}^{Data}$ ($N_{i,mR}^{Data}$) is the number of single-ring (multi-ring) events of sample i in the data, and $N_{i,1R}^{exp}$ ($N_{i,mR}^{exp}$) is the expected number of single ring (multi-ring) events in the MC simulation. The MC predictions are changed according to the systematic error parameters, $\boldsymbol{f}$ and $\boldsymbol{\alpha}$. $\boldsymbol{f}$ represents the RC efficiency for the each interaction mode: $\boldsymbol{f} = {}^t(f_{CCQE1}, f_{CCQE2}, f_{CCQE3}, f_{CCnQE}, f_{NC}, f_{nue})$. The nominal value of the RC efficiency is shown in Tab. 7.7. $\boldsymbol{\alpha}$ is the parameter for the physics uncertainties: the uncertainty of the atmospheric neutrino flux and the neutrino cross-section. The uncertainties considered in the atmospheric neutrino oscillation analysis are shown in Tab. 7.8 and Fig. 7.15 [73].

Table 7.7: RC efficiency predicted by the MC simulation.

Description	Prediction
RC efficiency for ν_μ CCQE $E_{vis} < 0.13$	0.969
RC efficiency for ν_μ CCQE $E_{vis} = 0.4 \sim 0.7$GeV	0.963
RC efficiency for ν_μ CCQE $E_{vis} > 0.7$GeV	0.978
RC efficiency for ν_μ CCnonQE	0.435
RC efficiency for NC	0.269
RC efficiency for ν_e CC	0.928

Table 7.8: Nuisance parameters for the physics uncertainties.

Notation	Description	Assigned error(σ)
σ_1	Atmospheric neutrino flux normalization ($E_\nu < 1$GeV)	$\pm$25%
σ_2	Atmospheric neutrino flux normalization ($E_\nu > 1$GeV)	$\pm$15%
σ_3	CCQE cross section energy dependent error	energy-dependent ($\pm$7% at 500 MeV)
σ_4	CCnQE/CCQE cross section ratio error	$\pm$20%
σ_5	NC/CCQE cross section ratio error	$\pm$20%
σ_6	ν_e/ν_μ flux ratio error	$\pm$5%

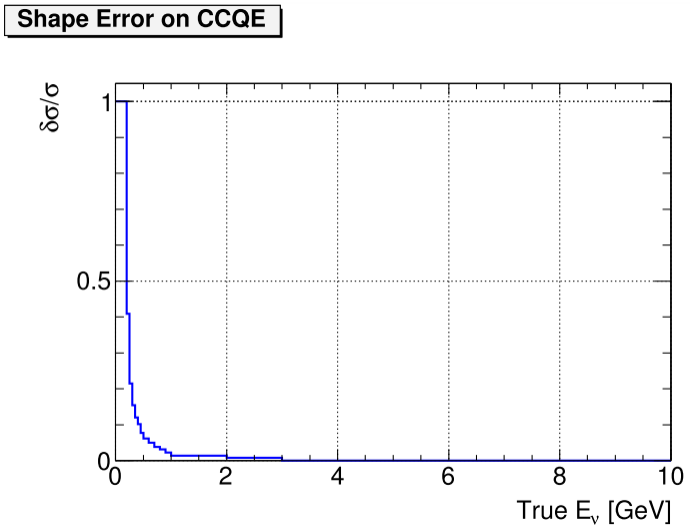

Figure 7.15: CCQE cross section shape error.

The χ^2 is minimized by changing the nuisance parameters ($\boldsymbol{f}$ and $\boldsymbol{\alpha}$) with MINUIT algorithm [75]. Table 7.9 shows the breakdown of the number of events at the χ^2 minimum point. The data and the MC prediction are consistent within the statistical error. The χ^2 minimum point is obtained within $\pm 1\sigma$ of the physics uncertainties (Tab. 7.10) and basic distribution such as reconstructed momentum is also in a good agreement between the data and the MC simulation.

Table 7.9: Breakdown of the number of 1 ring events and multi-ring events at the χ^2 minimum point.

enrich sample	Data	MC total	ν_μ CCQE	ν_μ CCnQE	NC	ν_e CC	(data-MC) /data[%]
CCQE1 1R	173	187.2	156.8	23.8	4.7	1.9	-8.2±7.6%
CCQE1 mR	14	15.2	3.4	6.6	4.0	1.1	-8.5±26.7%
CCQE2 1R	400	410.9	337.1	68.5	4.3	1.0	-2.7±5.0%
CCQE2 mR	60	61.6	11.3	35.0	10.5	4.8	-2.7±12.9%
CCQE3 1R	250	266.5	184.8	81.5	0.2	0.02	-6.6±6.3%
CCQE3 mR	53	56.6	0.0	53.6	1.8	1.2	-6.2±13.7%
CCnQE 1R	115	104.8	4.3	98.6	1.3	0.6	8.8±9.3%
CCnQE mR	120	109.1	2.0	92.0	11.3	3.8	9.0±9.1%
NC 1R	751	756.0	233.8	80.1	96.1	346.0	-0.7±3.7%
NC mR	836	841.5	21.9	90.2	415.5	313.9	-0.7±3.5%
nue 1R	1621	1588.5	5.5	5.7	35.5	1541.8	2.0±2.5%
nue mR	194	190.2	4.5	30.6	32.3	122.8	2.0±7.2%

Table 7.10: Nuisance parameter at best fit point.

Notation	Assigned error(σ)	Best fit value
α_1	±25%	+2.4%
α_2	±15%	-7.4%
α_3	energy-dependent (±7% at 500 MeV)	$+0.5\sigma$
α_4	±20%	+18.5%
α_5	±20%	-9.0%
α_6	±5%	+5.6%

The size of the RC error is estimated by the difference between nominal values of $\boldsymbol{f}$ and the values at the χ^2 minimum point. This difference is denoted as $\sigma_{\mathrm{best-def.}}$. To take into account the physics uncertainties $\boldsymbol{\alpha}$, the interval of the parameter $\boldsymbol{f}$ where $\Delta\chi^2 \leq 1$ are estimated by changing $\boldsymbol{\alpha}$. This interval is denoted as σ_{fit}. Finally the RC error is assigned as $\sqrt{\sigma^2_{\mathrm{best-def.}} + \sigma^2_{\mathrm{fit}}}$. The result for each sample is shown in Tab. 7.11. For CCQE samples, the energy dependent error is estimated with correlation as described in sub-section III.

III. Estimation of the energy dependent error for ν_μ CCQE

For the estimation of the energy dependent error of ν_μ CCQE, the bin-by-bin correlation is introduced by a covariance matrix. For $\sigma_{\mathrm{best-def.}}$, the bin-by-bin correlation is assumed as full correlation because this error denotes the difference between the data and the MC simulation of each sample and all the samples are fitted at the same time. Therefore, the covariance matrix

Table 7.11: Estimated error

	$\sigma_{\text{best-def.}}$	σ_{fit}	$\sqrt{\sigma^2_{\text{best-def.}} + \sigma^2_{\text{fit}}}$
CCQE1	+0.5%	±2.9%	-
CCQE2	+1.0%	±2.3%	-
CCQE3	+9.7%	±4.4%	-
CCnonQE	+18.0%	±8.4%	19.9%
NC	-41.6%	±24.4%	48.2%

$\text{V}_{\text{best-def.}}$ is expressed by

$$V_{best-def.} = \begin{array}{c} \begin{array}{ccc} \text{E}_{\text{vis}} & < 0.13\text{GeV} & 0.13 \sim 0.7\text{GeV} \quad > 0.7\text{GeV} \end{array} \\ \begin{pmatrix} \Delta f_1^2 & \Delta f_1 \Delta f_2 & \Delta f_1 \Delta f_3 \\ & \Delta f_2^2 & \Delta f_2 \Delta f_3 \\ & & \Delta f_3^2 \end{pmatrix} \end{array} \tag{7.3}$$

$\Delta f_1 = \sigma_{\sigma_{\text{best-def.}}}$ of CCQE1 sample (+0.5%),
$\Delta f_2 = \sigma_{\sigma_{\text{best-def.}}}$ of CCQE2 sample (+1.0%),
$\Delta f_3 = \sigma_{\sigma_{\text{best-def.}}}$ of CCQE3 sample (+9.7%)

For σ_{fit}, the bin-by-bin correlation is assumed as no correlation because the error size is consistent within the statistical error of the data. Therefore, the covariance matrix V_{fit} is expressed as Eq.7.4

$$V_{fit} = \begin{array}{c} \begin{array}{ccc} \text{E}_{\text{vis}} & < 0.13\text{GeV} & 0.13 \sim 0.7\text{GeV} \quad > 0.7\text{GeV} \end{array} \\ \begin{pmatrix} \sigma_1^2 & 0 & 0 \\ & \sigma_2^2 & 0 \\ & & \sigma_3^2 \end{pmatrix} \end{array} \tag{7.4}$$

$\sigma_1 = 2.9\%, \sigma_2 = 2.3\%, \sigma_3 = 4.4\%$

The covariance for the total RC error, V, is sum of the covariance matrices;

$$V = V_{best-def.} + V_{fit} \tag{7.5}$$

By using the MC simulation, the conversion matrix of RC efficiency for E_{rec} to RC efficiency for E_{vis} is estimated. With the conversion matrix A_{ij}, efficiency for i-th E_{vis} bin (ϵ_i) can be expressed by that for j-th E_{rec} bin (ϵ'_j):

$$\begin{aligned} \epsilon_i &= \sum_j^3 A_{ij} \epsilon'_j \\ A_{ij} &= \frac{N^{MC}_{i,j,1R} + N^{MC}_{i,j,mR}}{\sum_k^3 (N^{MC}_{i,k,1R} + N^{MC}_{i,k,mR})} \end{aligned} \tag{7.6}$$

where $N^{MC}_{i,j}$ denotes the number of events in which the visible energy equals to that of i-th E_{vis} bin and the reconstructed neutrino energy equals to that of j-th E_{rec} bin. The conversion matrix A_{ij} estimated by the MC simulation is shown in Eq.7.7

$$A = \begin{array}{c} \\ \text{E}_{\text{rec}} < 0.4\text{GeV} \\ \text{E}_{\text{rec}} = 0.4 \sim 1.1\text{GeV} \\ \text{E}_{\text{rec}} > 1.1\text{GeV} \end{array} \begin{array}{c} \begin{array}{ccc} \text{E}_{\text{vis}} < 0.13\text{GeV} & \text{E}_{\text{vis}} = 0.13 \sim 0.7\text{GeV} & \text{E}_{\text{vis}} > 0.7\text{GeV} \end{array} \\ \begin{pmatrix} 0.56 & 0.44 & 0.00 \\ 0.02 & 0.86 & 0.12 \\ 0.00 & 0.14 & 0.86 \end{pmatrix} \end{array} \tag{7.7}$$

The systematic term of log-likelihood for the oscillation analysis can be describe as follows.

$$\begin{aligned} -2\mathrm{Log}(\mathrm{L}_{\mathrm{sys.}}) &= {}^t(\Delta \boldsymbol{f}) V (\Delta \boldsymbol{f}) + \text{ (other error term)} \\ &= {}^t(\Delta \boldsymbol{f'}) {}^t A V A (\Delta \boldsymbol{f'}) + \text{ (other error term)} \end{aligned} \tag{7.8}$$

Here $\Delta \boldsymbol{f} = {}^t(\Delta f_1, \Delta f_2, \Delta f_3)$ means the difference of RC efficiency from the nominal value. From this equation, the covariance matrix for E_{rec} can be described as ${}^t AVA$. Finally, we obtained the covariance matrix for reconstructed energy dependent ν_μ CCQE RC error as in Eq. 7.1.

IV. Summary of the RC error estimation

Table 7.4 shows the estimated errors. In the selected ν_μ events in SK, the fraction of the CC non-QE interaction is about 15%; the error on the number of events due to the RC CC non-QE error is 3%. The fraction of the NC interaction is about 2%; the error on the number of events due to the RC NC error is 1%.

7.3.2 Flasher cut

As described in Section 7.2, the flasher events are rejected by using the spatial pattern and the timing distribution of the PMT hits. For the atmospheric neutrino events, the average value of flasher cut parameter (Fig. 7.5) for the MC simulation is smaller by 0.10 than that for the observed data, which is considered as a systematic difference of the flasher cut. If the likelihood distribution for the T2K neutrino MC simulation is shifted by 0.10, the FCFV selection efficiency changes by 1%. Therefore, the systematic error of the flasher cut is assigned to be 1%.

7.3.3 Fiducial volume

The vertex in the z (r) direction is checked with the cosmic-ray muons entering from the top (side). Figure 7.16 left (right) shows the reconstructed z (r) distribution of the cosmic-rays entering from the top (side). There is a good agreement between the data and the MC simulation. The systematic error is estimated by the difference of the peak between data and the MC simulation. The difference of the peak is within 5 cm in both z and r distribution. When the boundary of the FV is changed by 5 cm in z and r direction, the deviation of the FV is 1%. Therefore, the systematic error is estimated to be 1.0%.

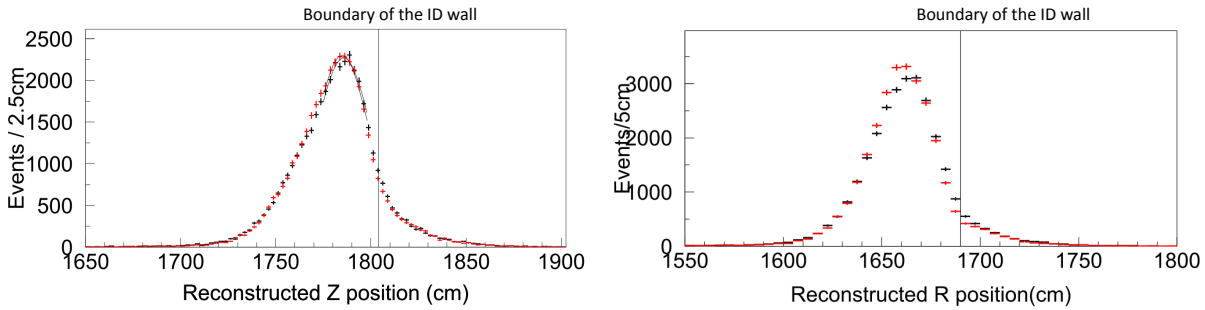

Figure 7.16: Reconstructed z distribution of cosmic-rays entering from the top (left) and reconstructed r distribution of the cosmic-ray entering from the side (right).

7.3.4 Decay electron cut

The decay electron tagging efficiency is compared between data and the MC simulation with cosmic-ray stopped muons. In the MC simulation, the expected μ^+/μ^- ratio (=1.37) and the probability of μ^- capture on the ^{16}O nucleus are accounted for. Figure 7.17 shows the tagging efficiency as a function of the decay time. The overall tagging efficiencies are $88.4 \pm 0.2\%$ in the data and $89.1 \pm 0.2\%$ in the MC simulation, respectively. This $\sim$1% difference is taken as the systematic error.

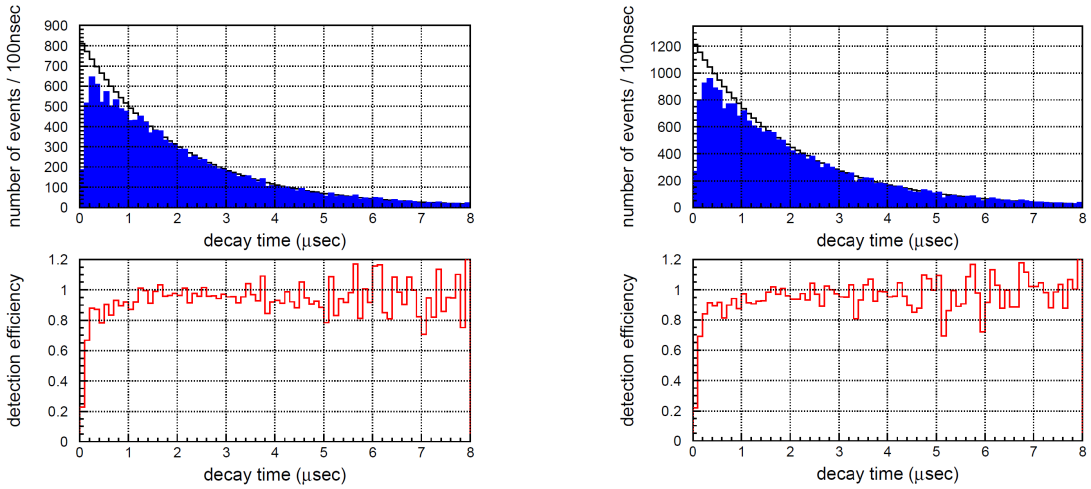

Figure 7.17: Decay electron distributions for cosmic-ray stopping muons. Top left and top right show the decay time distributions for data and MC, respectively. Black lines in each plot are the expected decay time curves and the blue histograms time distributions of tagged electrons. The bottom two figures show the tagging efficiencies as a function of the decay time.

7.3.5 Particle ID

The PID performance was checked with cosmic-ray muons which were selected by requiring the existence of a decay-electron. Figure 7.18 shows the probability of muon identification as a function of the reconstructed momentum. The differences of the PID probability between the data and the MC simulation are within 0.3% across the entire momentum range.

Atmospheric neutrino data is used for a cross check. For this study, following three criterion are applied to single ring events; there is a decay-electron; the distance between the reconstructed muon stopped point and decay-electron is less than 60 cm: the opening angle (θ) between the muon direction reconstructed by the Cherenkov ring and that reconstructed by the muon vertex and the decay-electron vertex is required to be $\cos\theta > 0.9$. Figure 7.19 shows the PID likelihood distribution of this sample. The PID likelihood distribution of the data is well reproduced by the MC simulation. The fraction of mis-identified events is $0.54 \pm 0.39\%$ and 0.20% in the data and the MC, respectively. The mis-ID fraction is consistent between data and the MC simulation within 0.3%.

Based on this study, the 0.3% is assigned as the systematic error.

7.3.6 OD cut

In the FC event reduction, the number of hit PMTs in the largest OD cluster, N_{hitac}, is used to reject cosmic-ray background events and so on. In order to estimate the systematic error of this

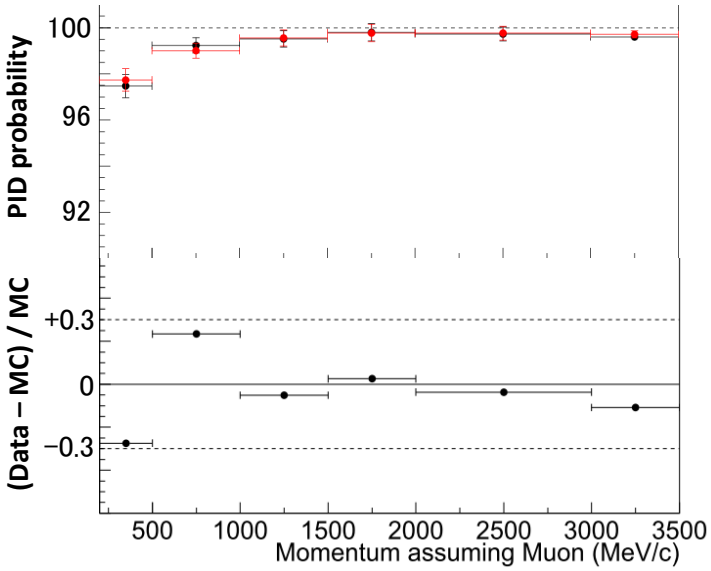

Figure 7.18: (Top) muon identification probability of cosmic-ray muons as a functino of muon momentum. Black is the probability of the data and red is the probability of the MC simulation. (bottom) the ratio of the difference between the data and the MC simulation divided by the MC simulation.

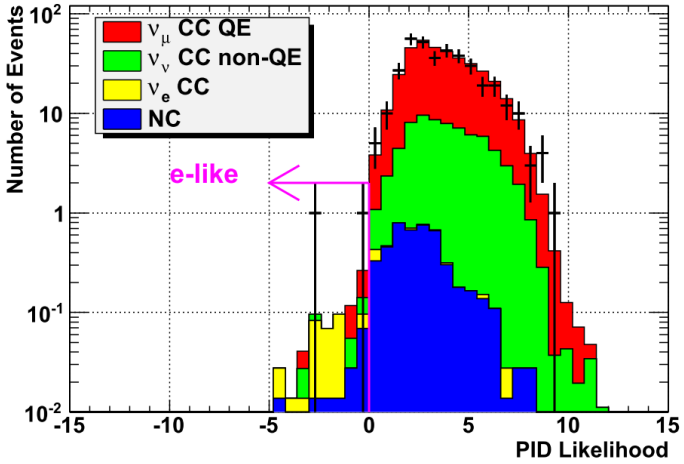

Figure 7.19: PID likelihood distribution of the ν_μ enriched sample of atmospheric neutrino data.

selection, the SK-IV * Partially-Contained (PC) atmospheric neutrino event sample was used. Figure 7.20 shows the N_{hitac} distribution of the data and the MC simulation. The peak position differs by 5.9% between data and the MC simulation. The 5.9% difference induces a shift of ± 0.89 hits at ν_μ selection threshold, $N_{hitac} = 15$. This ± 0.89 shift induces a $\pm 0.06\%$ change in the number of T2K FC events. This systematic error is negligible.

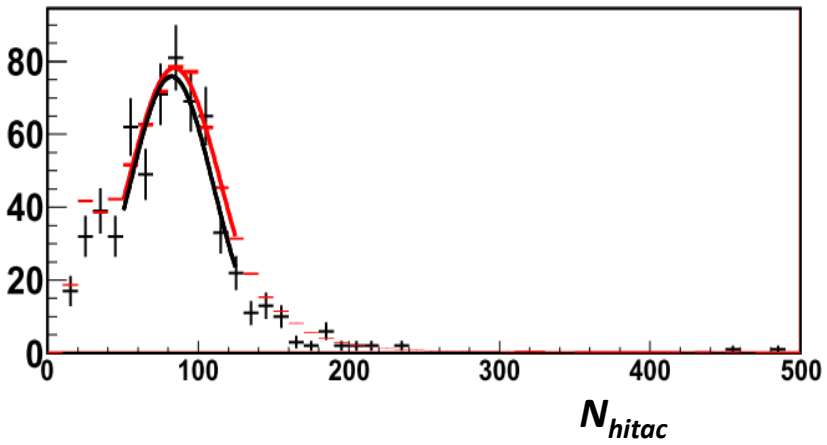

Figure 7.20: N_{hitac} distribution of the SK-IV PC atmospheric event sample. Black histogram shows the data and red shows the MC simulation.

7.3.7 Energy scale

The energy scale error is estimated with uncertainty of the absolute energy scale and stability of the energy scale. The absolute energy scale is compared between data and the MC simulation ranging from 10 MeV to 10 GeV. The stability is checked by using cosmic-ray over the entire period of the T2K RUN-I and RUN-II.

Absolute scale

The reconstructed momentum is compared between the data and the MC simulation in some samples in which the event energy is well known; for example, the energy spectrum of the decay-electron associated with cosmic-ray muon is used. The comparison is performed in following four samples ranging from 10 MeV to 10 GeV.

1. Decay-electron associated with stopping cosmic-ray muon (mean of 37 MeV)
   This sample is selected by searching for the delayed activities after a stopping muon. The reconstructed momentum distribution is compared between the data and the MC simulation. The shape of the distribution is consistent between them and the mean of ~ 37 MeV/c is consistent within -1.6%.

2. Neutral pion mass (peak of 135 MeV)
   This sample is selected using atmospheric neutrino data by requiring two showering Cherenkov

*Super-Kamiokande has been running since 1996. Over this time there have been four running periods: SK-I, SK-II, SK-III and SK-IV. The latest period, SK-IV, is still continuing with upgraded PMT readout electronics.

rings and no decay-electron. The reconstructed invariant mass of π^0 is compared between the data and the MC simulation. The shape of the reconstructed invariant mass distribution is consistent between them and the peak of $\sim$ 135 MeV/c^2 is consistent within +1.7%.

3. Stopping cosmic-ray muon (sub-GeV)
   This sample is selected by requiring OD activities, one decay-electron and the total charge is less than 1500 photo-electrons corresponding to the muon of $\sim$ 400 MeV/c. The momentum is reconstructed from the Cherenkov opening angle (p_θ) and from the observed photo-electrons (p). A difference between p_θ and p is checked over 200 MeV to 450 MeV. The differences are consistent within $-0.6 \sim 2.19\%$ between the data and the MC simulation.

4. Stopping cosmic-ray muon (multi-GeV)
   This sample is selected by requiring that the reconstructed track length is greater than 7 m and that there is one decay-electron. The momentum is reconstructed from the muon range ($p_{\rm range}$) and from the observed photo-electrons (p). A difference between ($p_{\rm range}$) and p is checked over 1 GeV to 10 GeV. The difference is consistent within $-1.4 \sim 0.3\%$ between the data and the MC simulation.

In summary, these four samples cover the energy of 10 MeV$\sim$ 10 GeV and the data and the MC simulation are consistent within 2.19% as shown in Fig. 7.21. The 2.19% is assigned as the systematic uncertainty of the absolute energy scale.

Stability

The stability of energy scale is measured by cosmic-ray stopping muons and associated decay electrons as shown in Fig. 7.22. It is stable within 0.4% statistical error and it is assigned as systematic uncertainty of the stability of the energy scale.

Summary of the systematic uncertainty on the energy scale

We estimate the systematic error on the energy scale as quadratic sum of the uncertainty of the absolute scale (2.19%) and the uncertainty of the stability (0.4%); the error is estimated to be $\sqrt{2.19^2 + 0.4^2} \sim 2.3\%$.

7.3.8 Momentum cut

The energy scale error of 2.3% induces a shift of 4.6 MeV/c at the selection threshold (200 MeV/c). Accordingly, it induces a less than 0.1% change in the number of selected events and systematic error is negligible.

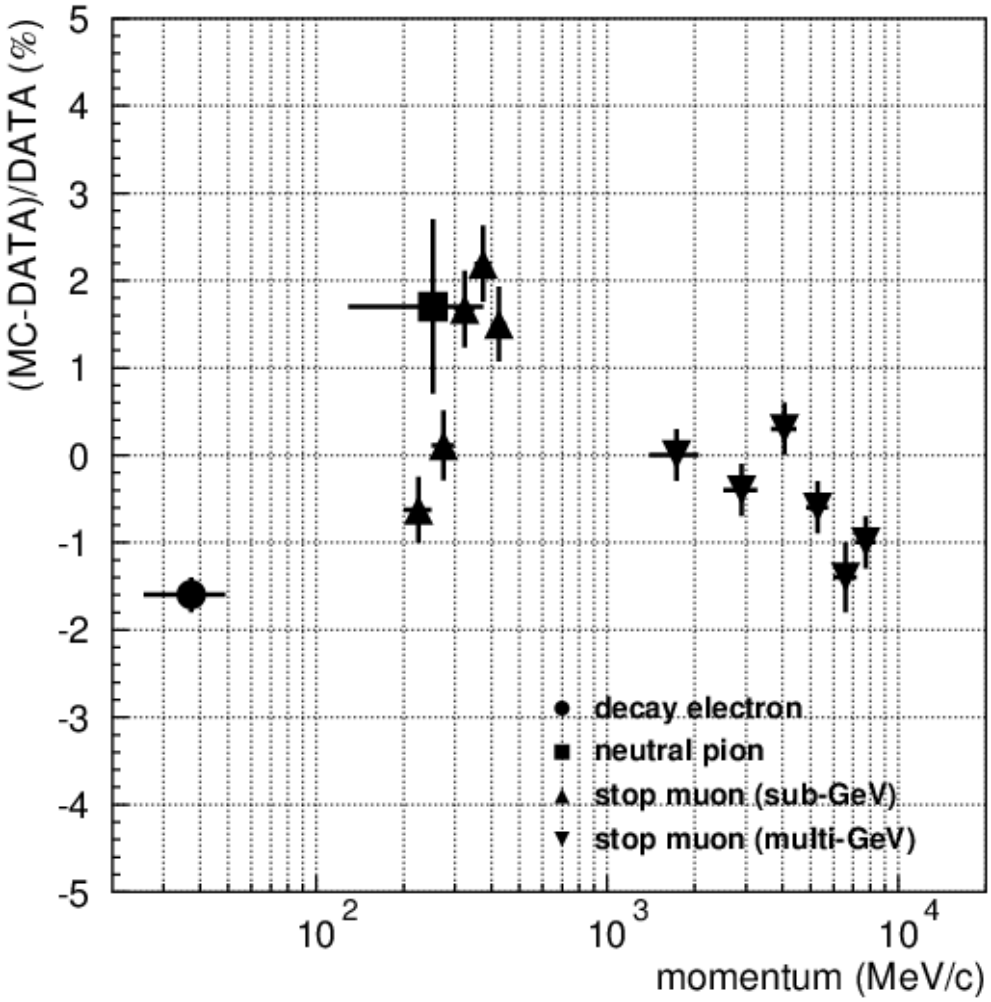

Figure 7.21: Difference of the energy scale between the data and the MC simulation with several samples.

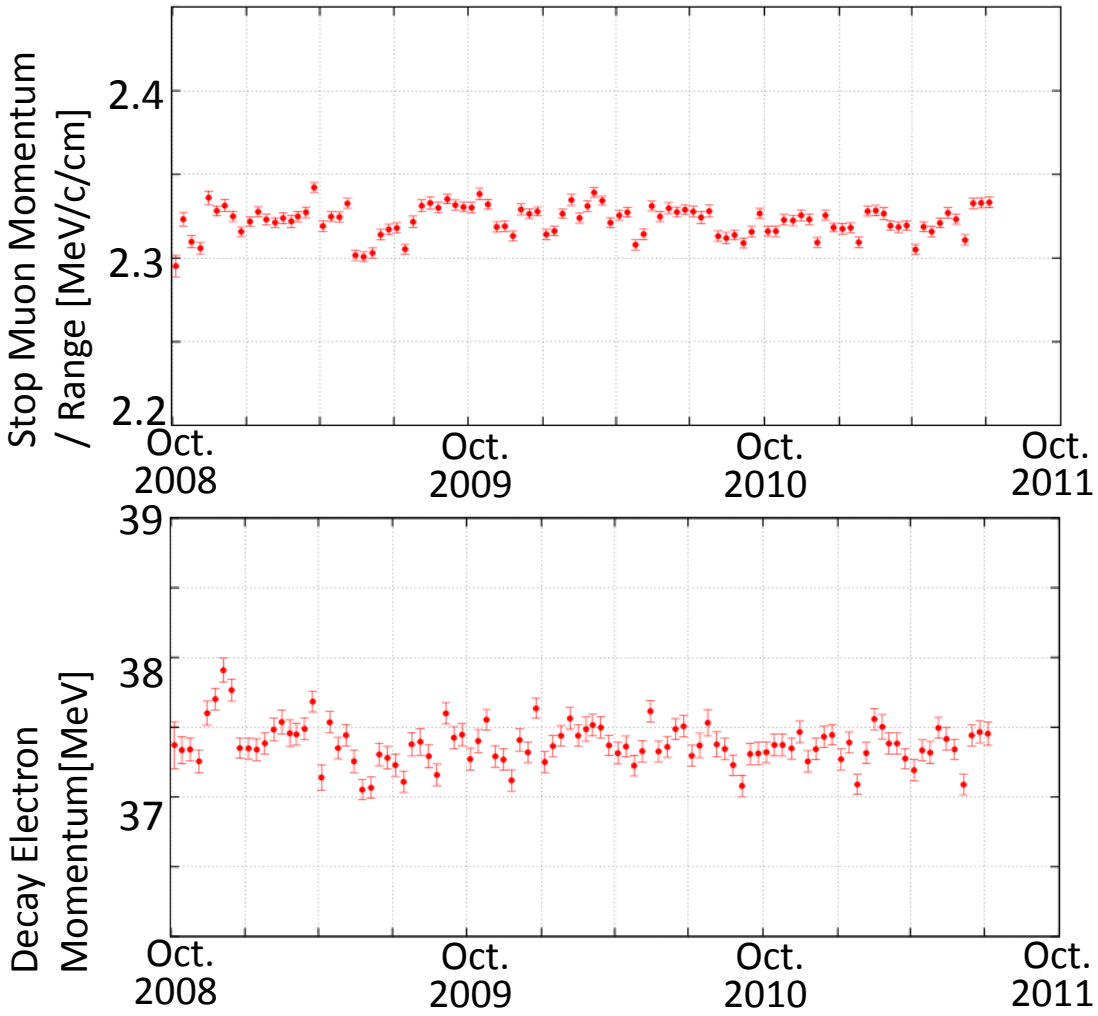

Figure 7.22: Stability of the energy scale measured with cosmic-ray stopping muons and associated decay-electrons.

Chapter 8

Neutrino Oscillation Analysis

This chapter describes the neutrino oscillation analysis in ν_μ disappearance with the T2K RUN-I and RUN-II data.

8.1 Expectation in Super-Kamiokande

The neutrino oscillation analysis in ν_μ disappearance is performed by comparing expectations and observations at Super-Kamiokande (SK) for both the number of events and the neutrino energy spectrum. The number of events and energy spectrum are estimated separately. For the estimation of the number of events, we consider both the spectrum shape and flux. For the estimation of the energy spectrum, we consider only the spectrum shape normalized to same number. This section shows how to calculate the the expectations with the systematic uncertainties.

8.1.1 Expected number of events

The expected number of events in SK ($N_{\rm SK}^{\rm exp.}$) is obtained by using the number of events in the near detector ($N_{\rm ND}^{\rm obs}$). In this analysis we use the number of events in ND280 as described in Section 6.5. $N_{\rm SK}^{\rm exp.}$ is calculated as

$$N_{\rm SK}^{\rm exp}(\sin^2 2\theta_{23}, \Delta m^2_{32}) = N_{\rm ND}^{\rm obs} \cdot \left[\frac{N_{\rm SK}^{\rm MC}}{N_{\rm ND}^{\rm MC}}\right](\sin^2 2\theta_{23}, \Delta m^2_{32}) \cdot \frac{M_{\rm SK}}{M_{\rm ND}} \cdot \frac{{\rm POT}_{\rm SK}}{{\rm POT}_{\rm ND}} \tag{8.1}$$

$M_{\rm SK}$	: fiducial mass of SK, which is 22.5 kton
$M_{\rm ND}$	: fiducial mass of ND280, which is 1.58 kton
${\rm POT}_{\rm SK}$	: number of protons on target for SK, which is 1.43×10^{20}
${\rm POT}_{\rm ND}$	: number of protons on target for ND280, which is 2.88×10^{19}

The $[N_{\rm SK}^{\rm MC}/N_{\rm ND}^{\rm MC}\,](\sin^2 2\theta_{23},\, \Delta m^2_{32})$ is expressed as

$$\left[\frac{N_{\rm SK}^{\rm MC}}{N_{\rm ND}^{\rm MC}}\right](\sin^2 2\theta_{23}, \Delta m^2_{32}) = \frac{N_{\rm SK}^{\rm MC}(\sin^2 2\theta_{23}, \Delta m^2_{32})}{N_{\rm ND}^{\rm MC}} \tag{8.2}$$

$$N_{\rm SK}^{\rm MC}(\sin^2 2\theta_{23}, \Delta m^2_{32}) \tag{8.3}$$
$$= \int dE_\nu \cdot \Phi_{\rm SK}(E_\nu) \cdot P(E_\nu; \sin^2 2\theta_{23}, \Delta m^2_{32}) \cdot \sum_I \sigma^I_{\rm SK}(E_\nu) \cdot \epsilon^I_{\rm SK}(E_\nu)$$

$$N_{\rm ND}^{\rm MC} \tag{8.4}$$
$$= \int dE_\nu \cdot \Phi_{\rm ND}(E_\nu) \cdot \sum_I \sigma^I_{\rm ND}(E_\nu) \cdot \epsilon^I_{\rm ND}(E_\nu)$$

$\Phi_{\rm SK}(\Phi_{\rm ND})$	: expected energy spectrum in SK (ND)
P	: oscillation probability in ν_μ disappearance as described in Eq. 1.9
$\sigma^I_{\rm SK}(\sigma_{\rm ND})$	: neutrino cross-section of the target material of SK (ND) for each interaction mode (I)
$\epsilon^I_{\rm SK}(\epsilon_{\rm ND})$	: efficiency in SK (ND) for each interaction mode (I)

The ν_μ CCQE, ν_μ CC1π production, ν_μ CC coherent π production, ν_μ CC other interactions, NC and ν_e CC interactions are considered as the possible interaction modes.

In the $\Phi_{\rm SK}$ estimation, the beam direction is important because we use the off-axis method. Because the measured deviation from the designed beam direction is well within our requirement (1 mrad), $\Phi_{\rm SK}$ is estimated with the beam MC simulation in which the the beam direction is set to the designed direction. The measured deviation of the beam direction is taken into account as one of the systematic errors in the beam MC prediction. The $\Phi_{\rm SK}$ prediction is shown in Fig. 4.1.

Figure 8.1 shows $N_{\rm SK}^{\rm exp.}$ as a function of $\sin^2 2\theta_{23}$ and Δm^2_{32}. The $N_{\rm SK}^{\rm exp.}$ is 103.7 in the case of null oscillation and is 28.3 in the case of $\sin^2 2\theta_{23}$ =1.0 and Δm^2_{32} =2.4×10^{-3} eV^2/c^4.

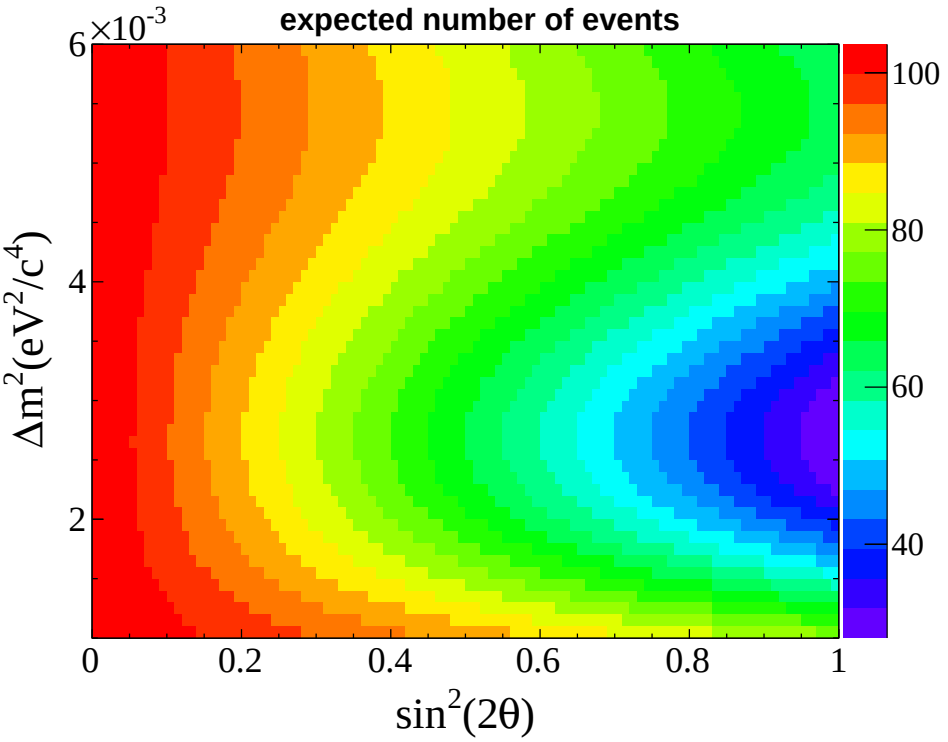

Figure 8.1: Expected number of events in SK for various values of Δm^2_{32} and $\sin^2 2\theta_{23}$.

8.1.2 Uncertainties of the number of events

The uncertainties come from the beam MC prediction, the neutrino interaction cross-section, the SK efficiency and the ND280 measurement.

Beam MC prediction

The uncertainty of the beam MC prediction on $[N_{\mathrm{SK}}^{\mathrm{MC}}/N_{\mathrm{ND}}^{\mathrm{MC}}]$ is estimated by propagating the uncertainties of the NA61 measurement and uncertainties of actual experimental condition such as the beam direction.

The uncertainty on $[N_{\mathrm{SK}}^{\mathrm{MC}}/N_{\mathrm{ND}}^{\mathrm{MC}}]$ is implemented as

$$\left[\frac{N_{\mathrm{SK}}^{\mathrm{MC}}}{N_{\mathrm{ND}}^{\mathrm{MC}}}\right](\sin^2 2\theta_{23}, \Delta m^2_{32}) \rightarrow f^{\Phi}_{\mathrm{SK/ND}} \left[\frac{N_{\mathrm{SK}}^{\mathrm{MC}}}{N_{\mathrm{ND}}^{\mathrm{MC}}}\right](\sin^2 2\theta_{23}, \Delta m^2_{32}) \tag{8.5}$$

where $f^{\Phi}_{\mathrm{SK/ND}}$ represents the systematic parameter defined as the relative value to the prediction. The error size is summarized in Fig 8.2 and in the first row of Tab. A.4.

Table 8.2 shows the break down of the $[N_{\mathrm{SK}}^{\mathrm{MC}}/N_{\mathrm{ND}}^{\mathrm{MC}}]$ uncertainty sources. Most dominant uncertainty comes from the "Kaon multiplicity" (it is 4.29%). The error size of the beam direction uncertainty (it is 0.52%) is negligible for the oscillation analysis thanks to the precise measurement with INGRID.

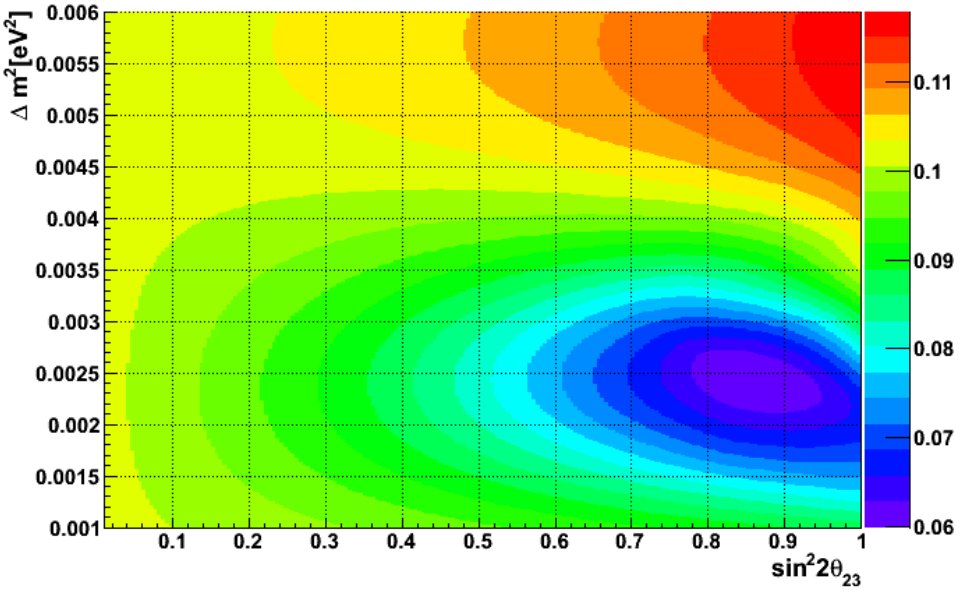

Figure 8.2: Estimated fractional error size of $[N_{\mathrm{SK}}^{\mathrm{MC}}/N_{\mathrm{ND}}^{\mathrm{MC}}]$ as a function of Δm^2_{32} and $\sin^2 2\theta_{23}$.

Neutrino interaction cross-section

The uncertainty of the cross-sections is estimated by comparison with recent measurements from the SciBooNE [76], MiniBooNE [77, 78], and K2K [79, 80] experiments, comparisons with the GENIE [81] and NuWro [82] neutrino interaction generators and recent theoretical work [83]. The error of the cross-section for interaction other than CCQE is estimated as the error on the ratio of that cross-section to the CCQE cross-section. For CCQE interaction, the systematic error of

Table 8.1: Summary of the systematic parameters and its errors. If a parameter is correlated with another, the square root of the diagonal element is written as the error.

$f^{\Phi}_{\mathrm{SK/ND}}$	$\sin^2 2\theta_{23}$ and Δm^2_{32} dependent ($\pm 4.8\%$ at $\sin^2 2\theta_{23} = 1.0$, $\Delta m^2_{32} = 2.4 \times 10^{-3}\mathrm{eV}^2/\mathrm{c}^4$)			
$f^{\Phi}_{\mathrm{shape1}}$	($E_\nu = 0.0$∼0.1 GeV)	$\pm 16.7\%$	f^{σ}_{CCQE}	energy-dependent ($\pm 7\%$ at 500 MeV)
$f^{\Phi}_{\mathrm{shape2}}$	($E_\nu = 0.1$∼0.2 GeV)	$\pm 15.0\%$	$f^{\sigma}_{CC1\pi}$	$\pm 30\%$ ($E_\nu < 2$GeV) $\sim \pm 25\%$ ($E_\nu > 2$GeV)
$f^{\Phi}_{\mathrm{shape3}}$	($E_\nu = 0.2$∼0.3 GeV)	$\pm 11.6\%$	$f^{\sigma}_{CCothers}$	$\pm 30\%$ ($E_\nu < 2$GeV) $\sim \pm 20$ %($E_\nu > 2$GeV)
$f^{\Phi}_{\mathrm{shape4}}$	($E_\nu = 0.3$∼0.4 GeV)	$\pm 9.7\%$	f^{σ}_{NC}	$\pm 36\%$
$f^{\Phi}_{\mathrm{shape5}}$	($E_\nu = 0.4$∼0.5 GeV)	$\pm 8.4\%$	$f^{\sigma}_{\nu_e/\nu_\mu}$	$\pm 6\%$
$f^{\Phi}_{\mathrm{shape6}}$	($E_\nu = 0.5$∼0.6 GeV)	$\pm 7.6\%$	f^{FSI}	energy-dependent ($\pm 10\%$ at 500 MeV)
$f^{\Phi}_{\mathrm{shape7}}$	($E_\nu = 0.6$∼0.7 GeV)	$\pm 6.5\%$	$f^{\mathrm{SK}}_{\mathrm{shape1}}$	$\pm 1.7\%$
$f^{\Phi}_{\mathrm{shape8}}$	($E_\nu = 0.7$∼0.8 GeV)	$\pm 10.5\%$	$f^{\mathrm{SK}}_{\mathrm{shape2}}$	$\pm 3.5\%$
$f^{\Phi}_{\mathrm{shape9}}$	($E_\nu = 0.8$∼1.0 GeV)	$\pm 14.0\%$	$f^{\mathrm{SK}}_{\mathrm{shape3}}$	$\pm 9.3\%$
$f^{\Phi}_{\mathrm{shape10}}$	($E_\nu = 1.0$∼1.2 GeV)	$\pm 14.0\%$	$f^{\mathrm{SK}}_{\mathrm{CCQE}}$	$\pm 1.8\%$
$f^{\Phi}_{\mathrm{shape11}}$	($E_\nu = 1.2$∼1.5 GeV)	$\pm 14.5\%$	f^{SK}_{CnCQE}	$\pm 20.0\%$
$f^{\Phi}_{\mathrm{shape12}}$	($E_\nu = 1.5$∼2.0 GeV)	$\pm 14.9\%$	f^{SK}_{NC}	$\pm 111.0\%$
$f^{\Phi}_{\mathrm{shape13}}$	($E_\nu = 2.0$∼2.5 GeV)	$\pm 13.8\%$	$f^{\mathrm{SK}}_{CC\nu_e}$	$\pm 100\%$
$f^{\Phi}_{\mathrm{shape14}}$	($E_\nu = 2.5$∼3.0 GeV)	$\pm 12.1\%$	$f^{\mathrm{SK}}_{E-scale}$	$\pm 2.3\%$
$f^{\Phi}_{\mathrm{shape15}}$	($E_\nu = 3.0$∼3.5 GeV)	$\pm 9.3\%$	f^{ND}	$^{+6.2}_{-5.9}\%$
$f^{\Phi}_{\mathrm{shape16}}$	($E_\nu = 3.5$∼4.0 GeV)	$\pm 8.9\%$		
$f^{\Phi}_{\mathrm{shape17}}$	($E_\nu = 4.0$∼5.0 GeV)	$\pm 11.3\%$		
$f^{\Phi}_{\mathrm{shape18}}$	($E_\nu = 5.0$∼7.0 GeV)	$\pm 16.5\%$		
$f^{\Phi}_{\mathrm{shape19}}$	($E_\nu = 7.0$∼10.0 GeV)	$\pm 23.3\%$		

Table 8.2: Breakdown of $f^{\Phi}_{\mathrm{SK/ND}}$ uncertainty

Source	Error size [%]
Beam direction	0.52
pion multiplicity	1.88
Tertiary pion scaling	0.37
Kaon multiplicity	4.29
Production cross-section	0.50
Secondary nucleon multiplicity	0.55
Proton beam	0.43
Target alignment	0.08
Horn alignment	0.05
Horn absolute current	0.39
Total	4.82

the absolute cross-section is not considered since the absolute normalization is determined by the number of events in the near detector. However, the systematic error due to the different nuclear targets in the near detector and far detector is considered as the CCQE energy dependent error. Because this CCQE energy dependent error is the relative uncertainty between interaction targets, the error is considered only for the SK expectation.

The estimated uncertainty is implemented as

$$\sigma^I_{\rm SK}(E_\nu) \rightarrow f^\sigma_I \cdot \sigma^I_{\rm SK}(E_\nu) \tag{8.6}$$

$$\sigma^I_{\rm ND}(E_\nu) \rightarrow \begin{cases} \sigma^I_{\rm ND}(E_\nu) & I = \text{CCQE} \\ f^\sigma_I \cdot \sigma^I_{\rm ND}(E_\nu) & I = \text{others} \end{cases} \tag{8.7}$$

where f^σ_I represents the systematic parameter for each interaction. The error size of each interaction is summarized in Tab. A.4 and Fig A.18.

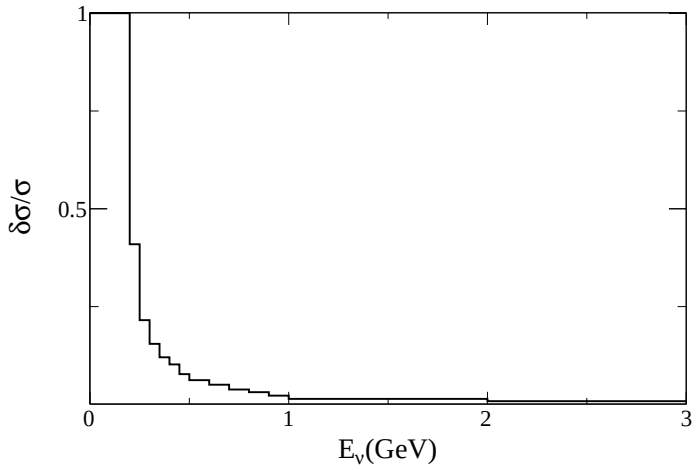

Figure 8.3: Energy dependent error on CCQE cross-section error. The error size at 0.5 GeV is ±7% and that above 3 GeV is zero.

SK efficiency

The uncertainties of the SK efficiency related to the detector uncertainty are described in Section 7.3. In addition to the detector uncertainty, the uncertainty related to the final state interaction (FSI) is estimated by using the external pion scattering data [84].

The estimated uncertainty is implemented as

$$\epsilon_{\rm SK}(E_\nu) \rightarrow f^{FSI} \times \begin{cases} f^{\rm SK}_{\rm CCQE} \cdot f^{\rm SK}_{\rm shape1} \cdot \epsilon_{\rm SK}(E_\nu) & I = \nu_\mu \text{ CCQE}, E^{\rm rec}_\nu < 0.4 GeV \\ f^{\rm SK}_{\rm CCQE} \cdot f^{\rm SK}_{\rm shape2} \cdot \epsilon_{\rm SK}(E_\nu) & I = \nu_\mu \text{ CCQE}, E^{\rm rec}_\nu = 0.4 \sim 1.1 GeV \\ f^{\rm SK}_{\rm CCQE} \cdot f^{\rm SK}_{\rm shape3} \cdot \epsilon_{\rm SK}(E_\nu) & I = \nu_\mu \text{ CCQE}, E^{\rm rec}_\nu > 1.1 GeV \\ f^{\rm SK}_{\rm CC\ other} \cdot \epsilon_{\rm SK}(E_\nu) & I = \nu_\mu \text{ CC other interactions} \\ f^{\rm SK}_{\rm NC} \cdot \epsilon_{\rm SK}(E_\nu) & I = \nu_\mu \text{ NC} \\ f^{\rm SK}_{\nu e} \cdot \epsilon_{\rm SK}(E_\nu) & I = \nu_e \text{ CC} \end{cases} \tag{8.8}$$

where f^{FSI} represents the systematic parameter of FSI, $f^{\rm SK}_{\rm shape}$ represents the energy dependent error on CCQE interaction mode (it comes from ring-counting systematic error), $f^{\rm SK}_I$ represents

the normalization error for each interaction mode. The error size of the SK detector uncertainties is summarized in Tab. 7.3. The error size of the uncertainty of FSI is shown in Fig. 8.4. Table A.4 shows the summary of the error size.

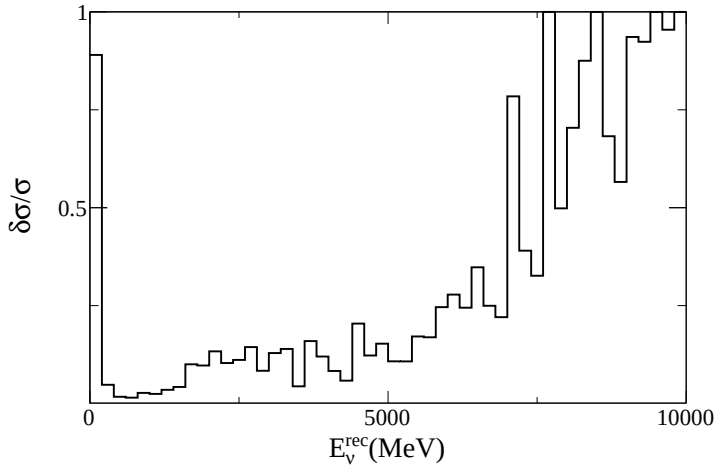

Figure 8.4: Energy dependent error on the SK efficiency from the final state interaction uncertainty.

ND measurement

The uncertainty of the number of events at ND280 is described in Section 6.4. This uncertainty is implemented as

$$N_{\mathrm{ND}}^{\mathrm{obs}} \rightarrow f^{\mathrm{ND}} \cdot N_{\mathrm{ND}}^{\mathrm{obs}} \tag{8.9}$$

where f^{ND} represents the systematic parameter defined as the relative value to the measured number of events. The error size is (+6.2%, -5.9%).

Error size on $N_{\mathrm{SK}}^{\mathrm{exp.}}$

The systematic error on $N_{\mathrm{SK}}^{\mathrm{exp.}}$ is broken down to each systematic error source in Tab. 8.3. The error cancellation of the beam prediction uncertainty is already described in Section 6.5. Furthermore, the cancellation of the cross-section uncertainty is also achieved; the error of CC1π production cross-section on $[N_{\mathrm{SK}}^{\mathrm{MC}}/N_{\mathrm{ND}}^{\mathrm{MC}}]$, for example, is less than (+2.2%, -1.9%) whereas the error on $N_{\mathrm{SK}}^{\mathrm{MC}}$ itself is $\sim 4\%$.

8.1.3 Expected energy spectrum shape

For the comparison of the energy spectrum, the reconstructed neutrino energy spectrum shape distribution $\rho(E_\nu^{\mathrm{rec}}; \sin^2 2\theta_{23}, \Delta m^2_{32})$ is calculated as

$$\begin{aligned}
&\rho(E_\nu^{\mathrm{rec}}; \sin^2 2\theta_{23}, \Delta m^2_{32}) \\
&= \frac{1}{A} \int dE_\nu \cdot \Phi_{\mathrm{SK}}(E_\nu) \cdot P(E_\nu; \sin^2 2\theta_{23}, \Delta m^2_{32}) \times \\
&\quad \sum_I \sigma^I_{\mathrm{SK}}(E_\nu) \cdot \epsilon^I_{\mathrm{SK}}(E_\nu) \cdot M^I(E_\nu \rightarrow E_\nu^{\mathrm{rec}})
\end{aligned} \tag{8.10}$$

Table 8.3: Summary of the systematic error on $N_{\mathrm{SK}}^{\mathrm{exp.}}$

Source of systematic errors	change of N_{exp}^{SK} ($\sin^2 2\theta = 1.0, \Delta m^2 = 2.4$)	change of N_{exp}^{SK} (Null Osc.)
$f_{\mathrm{SK/ND}}^{\Phi}$	+4.8% -4.8%	+6.9% -6.9%
f_{CCQE}^{σ}	+2.5% -2.5%	+4.1% -4.1%
$f_{CC1\pi}^{\sigma}$	+0.4% -0.5%	+2.2% -1.9%
$f_{CCothers}^{\sigma}$	+4.1% -3.6%	+5.3% -4.7%
f_{NC}^{σ}	+0.9% -0.9%	+0.8% -0.8%
$f_{\nu_e/\nu_\mu}^{\sigma}$	+0.0% -0.0%	+0.0% -0.0%
f^{FSI}	+6.7% -6.7%	+3.2% -3.2%
$\boldsymbol{f}_{\mathrm{shape}}^{\mathrm{SK}}$	+3.2% -3.2%	+3.1% -3.1%
$f_{\mathrm{CCQE}}^{\mathrm{SK}}$	+1.0% -1.0%	+1.4% -1.4%
$f_{CCothers}^{\mathrm{SK}}$	+6.5% -6.5%	+3.3% -3.3%
f_{NC}^{SK}	+7.2% -7.2%	+2.0% -2.0%
$f_{CC\nu_e}^{\mathrm{SK}}$	+0.0% -0.0%	+0.0% -0.0%
f^{ND}	+6.2% -5.9%	+6.2% -5.9%
Total	+15.4% -15.1%	+13.2% -12.7%

where $M(E_\nu \to E_\nu^{\mathrm{rec}})$ is the detector response function representing the probability to observe the event with true energy of E_ν as E_ν^{rec} for each interaction mode (I). A is a normalization factor,

$$A = \int dE \cdot \rho(E; \sin^2 2\theta_{23}, \Delta m^2_{32}) \tag{8.11}$$

so that $\int dE \cdot \rho$ is always normalized to one.

Figure 8.5 shows the estimated $\rho(E; \sin^2 2\theta_{23}, \Delta m^2_{32})$ with several ($\sin^2 2\theta_{23}$, Δm^2_{32}) sets.

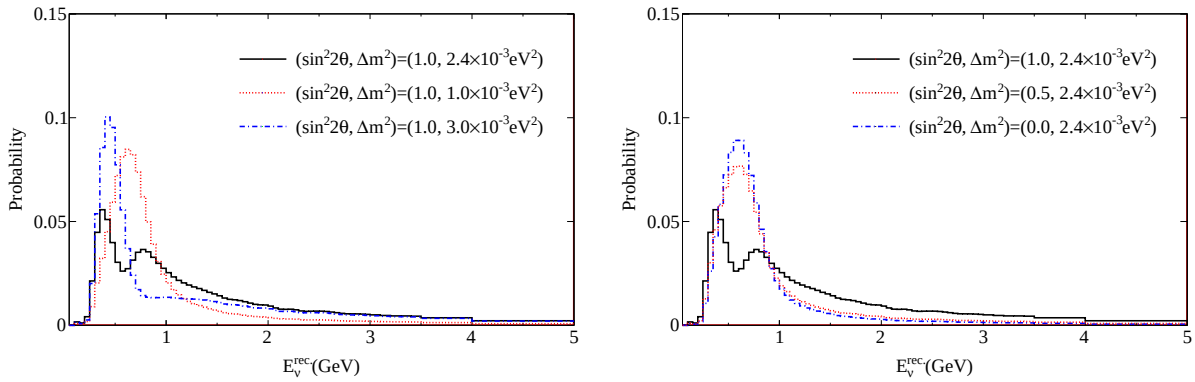

Figure 8.5: Expected shape of the reconstructed neutrino energy with several ($\sin^2 2\theta_{23}$, Δm^2_{32}) sets. (left) the expected shape by fixing $\sin^2 2\theta_{23} = 1.0$ while changing Δm^2_{32}. (right) the expected shape by fixing $\Delta m^2_{32} = 2.4 \times 10^{-3}\mathrm{eV}^2/\mathrm{c}^4$ while changing $\sin^2 2\theta_{23}$.

8.1.4 Uncertainties of the energy spectrum shape

The uncertainty comes from Φ_{SK}, σ_{SK}^I, ϵ_{SK}^I and $M(E_\nu \to E_\nu^{\mathrm{rec}})$. The uncertainty of σ_{SK}^I and ϵ_{SK}^I is already described in Section 8.1.2.

Uncertainty on $\Phi_{\rm SK}$

The uncertainty on $\Phi_{\rm SK}$ is estimated by propagating uncertainties of the NA61 measurement and uncertainties of actual experimental condition such as the beam direction. The estimated uncertainty is implemented as

$$\Phi_{\rm SK}(E_\nu) \to f^{\Phi}_{\text{shape } i} \cdot \Phi_{\rm SK}(E_\nu) \tag{8.12}$$

where $f^{\Phi}_{\text{shape } i}$ represents the systematic parameter defined as the relative value to the prediction at the i-th energy bin. The binning used is shown in Tab. 8.4. The error size is summarized in Tab. A.4 and Fig 8.6.

Table 8.4: Binning of energy used for the energy shape error of the neutrino beam prediction.

Energy [GeV]	$0 \sim 0.8$	$0.8 \sim 1.2$	$1.2 \sim 1.5$	$1.5 \sim 4.0$	$4.0 \sim 5.0$	$5.0 \sim 7.0$	$7.0 \sim 10.0$
Bin width [GeV]	0.1	0.3	0.3	0.5	1.0	2.0	3.0
Bin number	$1 \sim 8$	$9 \sim 10$	11	$12 \sim 16$	17	18	19

Uncertainty on $M(E_\nu \to E_\nu^{\rm rec})$

The uncertainty of the SK energy scale is described in Section 7.3. The estimated error is implemented by scaling $E_\nu^{\rm rec}$ by systematic parameter $f^{SK}_{E-scale}$:

$$M(E_\nu \to E_\nu^{\rm rec}) \to M(E_\nu \to E_\nu^{\rm rec} \cdot (1 + f^{SK}_{E-scale})) \tag{8.13}$$

Total error size

Figure 8.7 shows $\rho(E; \sin^2 2\theta_{23}, \Delta m^2_{32}, \boldsymbol{f})$ in the case of $(\sin^2 2\theta, \Delta m^2) = (1.0,\ 2.4 \times 10^{-3}\ eV^2)$. The systematic parameter $\boldsymbol{f}$ is randomly generated according to its error many times, and the mean and the standard deviation of each bin of $\rho(E)$ are plotted in this figure. Figure 8.8 shows the contribution of each systematic error source to $\rho(E)$. The error is dominated by the SK error in the low energy region and by the flux shape error in the high energy region. The SK error is dominated by the NC interaction event error because the NC interaction event is misidentified to low energy neutrino as shown in Fig. 7.13 so that the reconstructed energy shape is distorted.

8.2 Analysis method

The goals of the analysis are getting the best fit value and the confidence region of $(\sin^2 2\theta_{23}, \Delta m^2_{32})$. For the search of the best fit value, we employ the maximum likelihood method. The likelihood function is defined as the product of the likelihood for the number of events ($\mathcal{L}_{\rm norm}$), one for the shape of the reconstructed neutrino energy spectrum ($\mathcal{L}_{\rm shape}$) and one for the systematic uncertainty ($\mathcal{L}_{\rm syst}$):

$$\mathcal{L}(\sin^2 2\theta_{23}, \Delta m^2_{32}, \boldsymbol{f}) = \mathcal{L}_{\rm norm}(\sin^2 2\theta_{23}, \Delta m^2_{32}, \boldsymbol{f}) \times \mathcal{L}_{\rm shape}(\sin^2 2\theta_{23}, \Delta m^2_{32}, \boldsymbol{f}) \times \mathcal{L}_{\rm syst}(\boldsymbol{f}) \tag{8.14}$$

The best fit value is obtained by maximizing the likelihood function. For the confidence region, the method of Feldman and Cousin [71] is used with the same likelihood function; points close to the physical region occasionally have best fits in the unphysical region though the best fit is

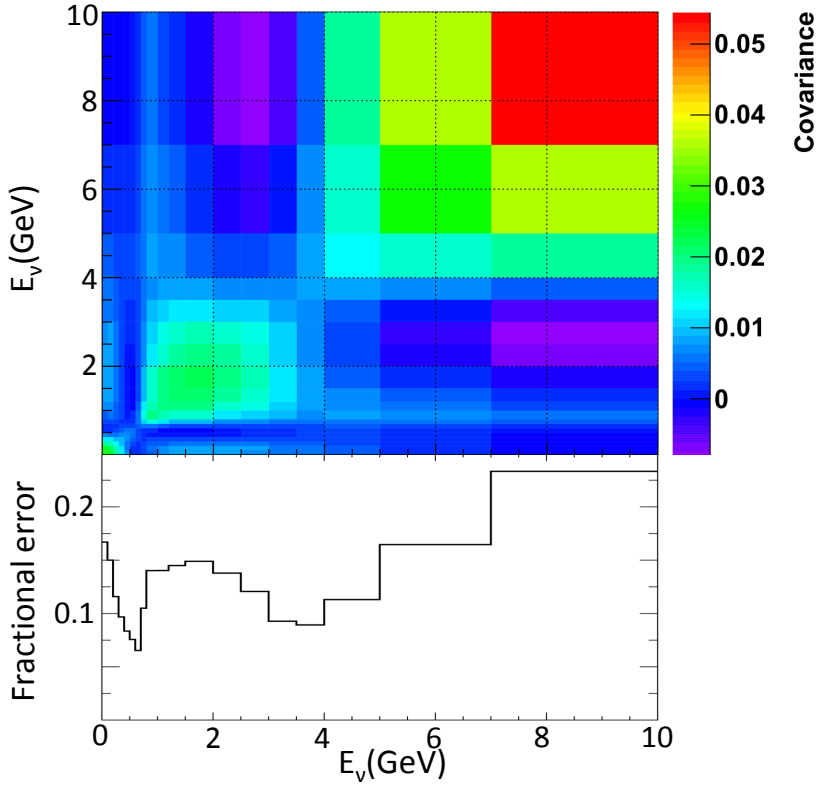

Figure 8.6: Error matrix (top) and fractional error (bottom) for the expected energy spectrum from the beam MC simulation. The fractional error (bottom) is defined as the square root of the diagonal element.

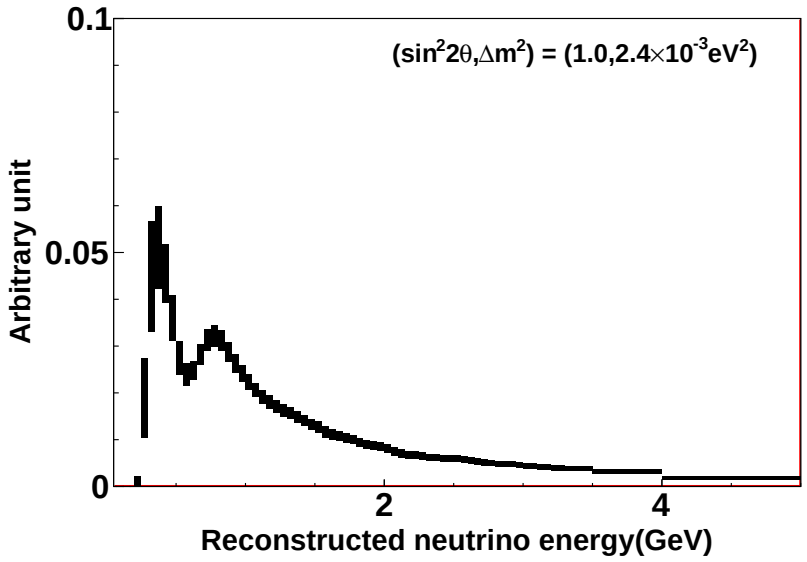

Figure 8.7: Reconstructed neutrino energy shape in the case of $(\sin^2 2\theta, \Delta m^2) = (1.0,\ 2.4 \times 10^{-3} eV^2)$. Each bar shows the standard deviation of each bin, if each systematic parameter is varied within its error.

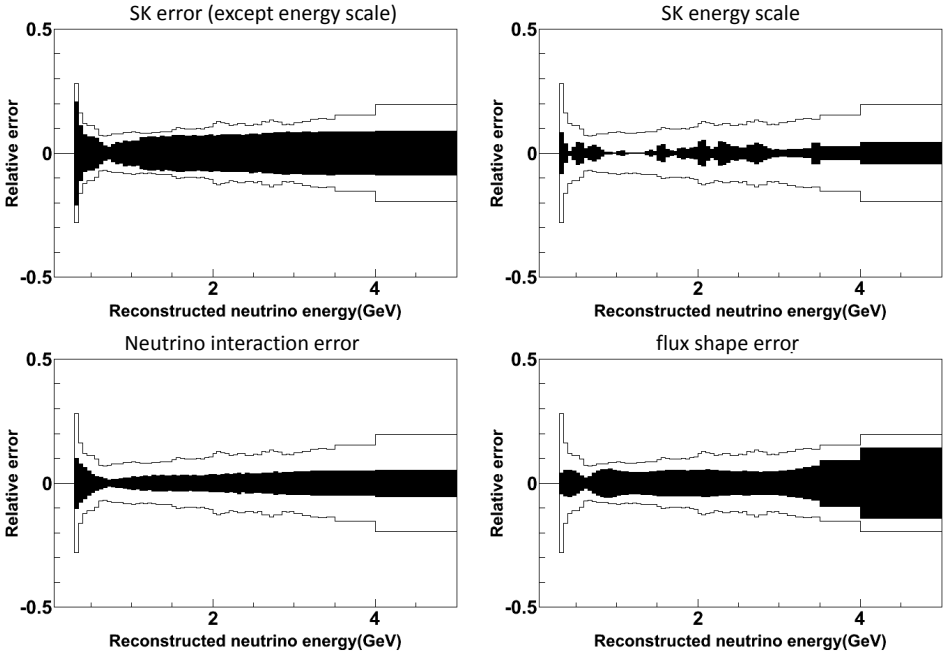

Figure 8.8: Contribution of each systematic error to ρ. Filled boxes are systematic errors from a specified error source, and open boxes are the total errors. The vertical axis shows the relative error to $\rho(E)$.

searched for within physics region. To estimate this effect on the confidence region construction, the toy MC data sets are generated.

The normalization term, $\mathcal{L}_{\rm norm}$ can be written by Poisson probability to observe $N_{\rm SK}^{\rm obs}$ when the expectation is $N_{\rm SK}^{\rm exp.}$:

$$\mathcal{L}_{\rm norm} = \frac{\exp(-N_{\rm SK}^{\rm exp}) \cdot (N_{\rm SK}^{\rm obs})^{N_{\rm SK}^{\rm exp}}}{N_{\rm SK}^{\rm obs}!} \tag{8.15}$$

where $N_{\rm SK}^{\rm exp.}$ is calculated as described in Section 8.1.1∼8.1.2 and $N_{\rm SK}^{\rm obs}$ equals 31 as shown in Tab. 7.2. We adopted the unbinned maximum likelihood for the neutrino energy spectrum:

$$\mathcal{L}_{\rm shape} = \prod_{i=1}^{N_{\rm SK}^{\rm obs}} \rho(E_i; \sin^2 2\theta_{23}, \Delta m^2_{32}, \boldsymbol{f}) \tag{8.16}$$

where ρ is calculated as described in Section 8.1.3∼8.1.4 and the reconstructed neutrino energy of each event (E_i, $i = 1 \sim 31$) are shown in Fig. 7.13.

The systematic parameters $\boldsymbol{f} =^t (\boldsymbol{f}^{\Phi}_{\rm shape}, f^{\Phi}_{\rm SK/ND}, f^{\sigma}_{I}, f^{FSI}, \boldsymbol{f}^{\rm SK}_{\rm shape}, f^{\rm SK}_{I}, f^{\rm SK}_{E-scale}, f^{\rm ND})$ are as-

sumed to follow the correlated Gaussian distribution:

$$\begin{aligned}\mathcal{L}_{\rm syst} \equiv & \exp\left[-{}^t\Delta\boldsymbol{f}^{\Phi}_{\rm shape}(M^{\Phi}_{\rm shape})^{-1}\Delta\boldsymbol{f}^{\Phi}_{\rm shape} - \frac{(\Delta f^{\Phi}_{\rm SK/ND})^2}{2(\sigma^{\Phi}_{\rm SK/ND})^2}\right] \\ & \times \exp\left[-\sum_I \frac{(\Delta f^{\sigma}_I)^2}{2(\sigma^{\sigma}_I)^2} - \frac{(\Delta f^{FSI})^2}{2(\sigma^{FSI})^2}\right] \\ & \times \exp\left[-{}^t\Delta\boldsymbol{f}^{\rm SK}_{\rm shape}(M^{\rm SK}_{\rm shape})^{-1}\Delta\boldsymbol{f}^{\rm SK}_{\rm shape} - \sum_I \frac{(\Delta f^{\rm SK}_I)^2}{2(\sigma^{\rm SK}_I)^2} - \frac{(\Delta f^{\rm SK}_{E-scale})^2}{2(\sigma^{\rm SK}_{E-scale})^2}\right] \\ & \times \exp\left[-\frac{(\Delta f^{\rm ND})^2}{2(\sigma^{\rm ND})^2}\right]\end{aligned} \tag{8.17}$$

where Δf is the difference of the parameters from their nominal value ($\Delta f = f - 1$), $M^{\Phi}_{\rm shape}$ is the error matrix for the spectrum shape as shown in Fig. 8.6, σ is the error size of each source as summarized in Tab. A.4 and $M^{SK}_{\rm shape}$ is the error matrix for the energy dependent error of the ring counting as shown in Eq. 7.1. When $\mathcal{L}$ is maximized, the $\boldsymbol{f}$ is also fitted to marginalize the effect of the systematic errors.

In the actual calculation, the integral over the neutrino energy is performed as sum over the energy bins. The definition of the energy bins is summarized in Tab. 8.5. The maximization of $\mathcal{L}(\sin^2 2\theta_{23}, \Delta m^2_{32}, \boldsymbol{f})$ by changing $(\sin^2 2\theta_{23}, \Delta m^2_{32}, \boldsymbol{f})$ is performed as the minimization of χ^2 defined by

$$\chi^2(\sin^2 2\theta_{23}, \Delta m^2_{32}, \boldsymbol{f}) \equiv -2\log\mathcal{L}(\sin^2 2\theta_{23}, \Delta m^2_{32}, \boldsymbol{f}) \tag{8.18}$$

with the MINUIT program [75].

Table 8.5: Binning of energy used for the analysis.

Energy [GeV]	$0 \sim 3.00$	$3.00 \sim 3.50$	$3.50 \sim 4.00$	$4.00 \sim 5.00$	$5.00 \sim 7.00$	$7.00 \sim 10.00$
Bin width [GeV]	0.05	0.10	0.50	1.00	2.00	3.00
Bin number	$1 \sim 60$	$61 \sim 65$	66	67	68	69

8.3 Analysis result

8.3.1 Best fit value of the oscillation parameters

The obtained best fit value of $(\sin^2 2\theta_{23},\ \Delta m^2_{32})$ is $(0.99,\ 2.6 \times 10^{-3}\mathrm{eV}^2/\mathrm{c}^4)$. This result is consistent with the current understandings as described in Section 1.1.3.

Number of events and energy spectrum

The number of events at the best fit point is 29.3 whereas the observed number is 31. The number of events is consistent between the observation and the expectation within the statistical error. Figure 8.9 shows the reconstructed neutrino energy of the observation and the expectation. There is a good agreement between the observation and the expectation with the best fit oscillation parameters.

Systematic error parameters at the best fit point

The systematic error parameters $\boldsymbol{f}$ at the best fit point are summarized in Fig. 8.10. This shows that the best fit is obtained with $\boldsymbol{f}$ within $\pm 1\sigma$ of the error size. This means that the data

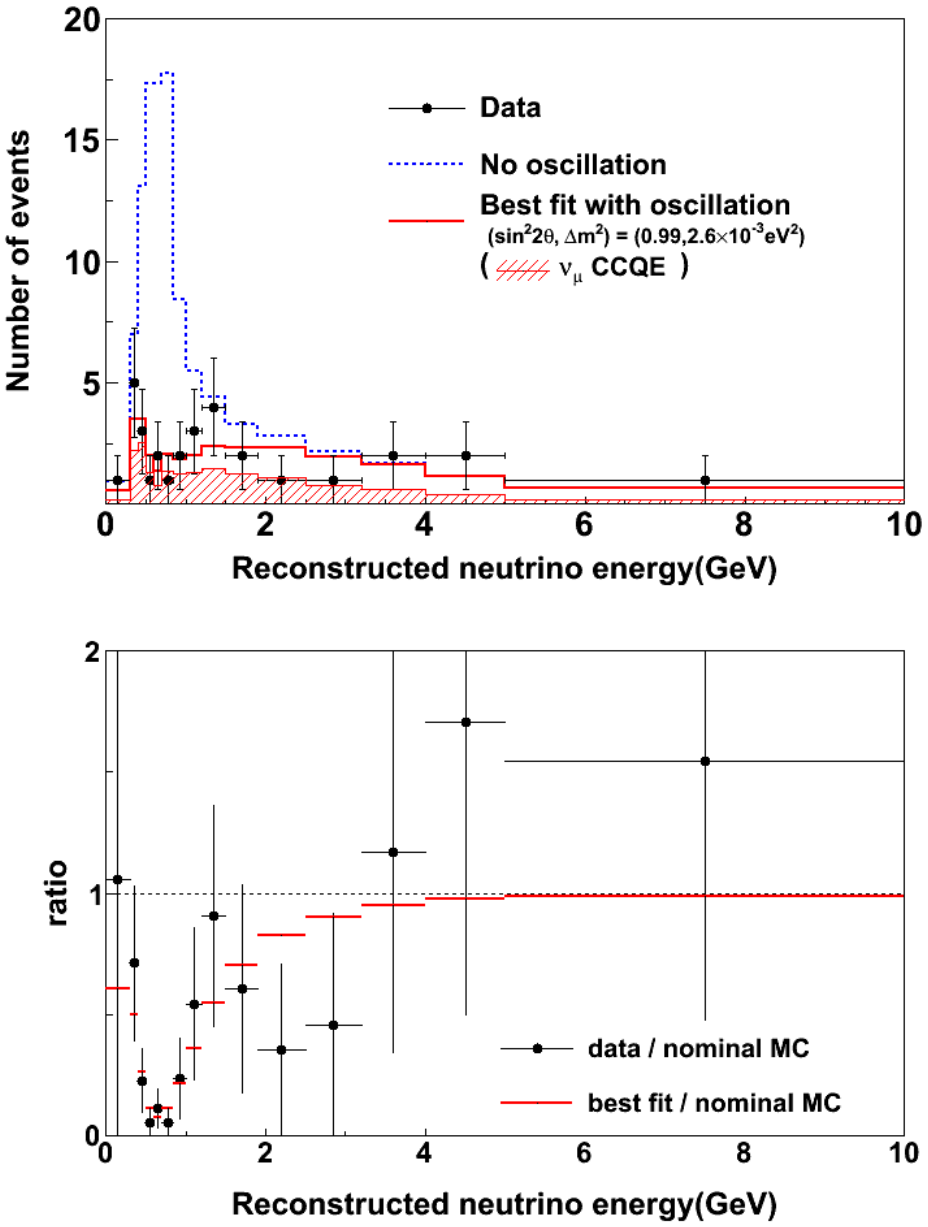

Figure 8.9: E_{rec} distribution of data (black) and expectation without oscillation (blue dashed) and with oscillation at the best fit point (red line). CCQE components is shown in the red hatched region.

agree well with the expectation with the best fit oscillation parameters and nominal systematic parameters.

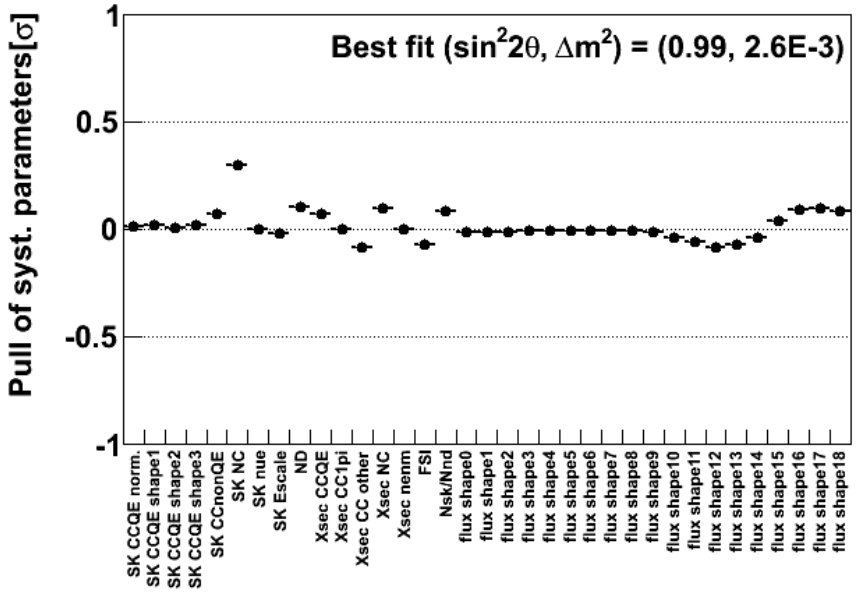

Figure 8.10: Pull of systematic parameters at the best fit point.

Goodness-of-fit

The minimum of χ^2 is 261.4. To evaluate the goodness-of-fit, the expected χ^2 distribution is calculated with toy MC data sets with $(\sin^2 2\theta, \Delta m^2)$=(0.99, 2.6×10^{-3}). In the toy MC simulation, number of events and reconstructed neutrino energy of each event are generated taking into account the statistical error and systematic error. For each data set, χ^2 is minimized by changing $\boldsymbol{f}$ while fixing the oscillation parameters to the input values :(0.99, 2.6×10^{-3}). Figure 8.11 shows the minimum χ^2 distribution. The p-value is calculated as the fraction of the number of MC data sets in which the minimum χ^2 is larger than that of the real data to total MC data sets (10000). As a result, the p-value is calculated to be 37%. It is concluded that the χ^2 of the real data is reasonable.

8.3.2 Null oscillation probability

The χ^2 in case of the null oscillation ($\sin^2 2\theta_{23} = 0$) is obtained to be 317.3. The χ^2 difference ($\Delta\chi^2$) between the null oscillation and the best fit is 55.9, and the probability that $\Delta\chi^2 > 55.9$ is calculated to be 7.3×10^{-11} assuming that $\Delta\chi^2$ obeys the χ^2 distribution of two degrees of freedom. Hence the null oscillation is strongly disfavored and we firmly confirm the neutrino oscillation in ν_μ disappearance.

8.3.3 Confidence region

To construct the allowed region of the oscillation parameters, the Feldman & Cousins method [71] is employed. In this method, the critical $\Delta\chi^2$ is calculated based on toy MC experiments for each set of neutrino oscillation parameters with a given confidence level. Comparing the estimated

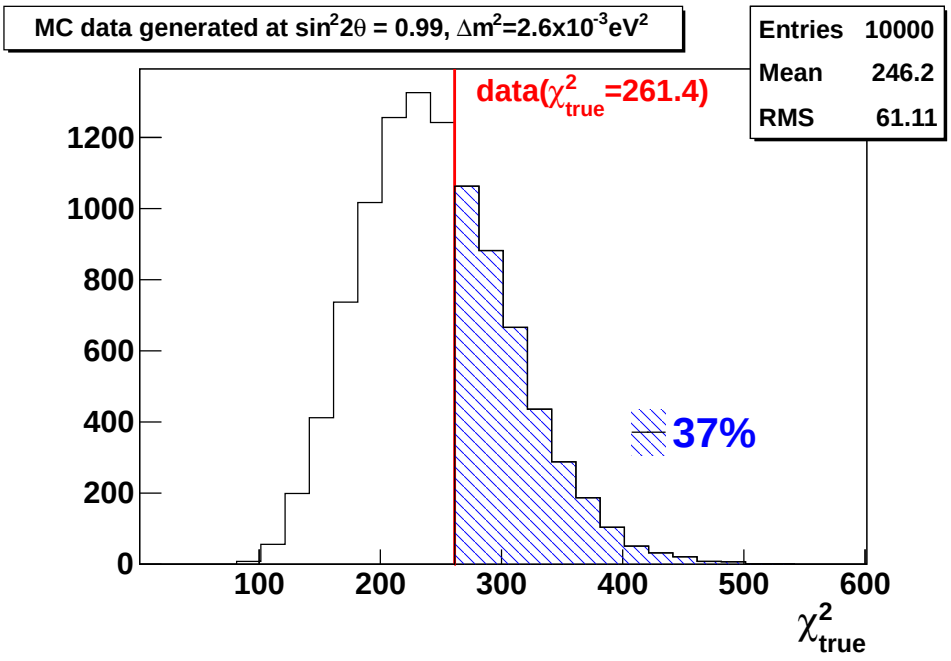

Figure 8.11: Minimum χ^2 distribution with toy MC experiments. The vertical red line indicates the value of the data.

critical $\Delta\chi^2$ and $\Delta\chi^2$ of the real data, the confidence regions are obtained. The actual procedure is as follows:

(1) A toy MC data set is generated for given $(\sin^2 2\theta, \Delta m^2)$. The statistical fluctuation and systematic uncertainties are included in the toy MC simulation.

(2) The χ^2 is minimized by changing $\boldsymbol{f}$ and $(\sin^2 2\theta, \Delta m^2)$, which is denoted as $\chi^2_{\rm min}$.

(3) The χ^2 is minimized by changing $\boldsymbol{f}$ while fixing the oscillation parameters to the given values, which is denoted as $\chi^2_{\rm true}$.

(4) Calculate $\Delta\chi^2 \equiv \chi^2_{\rm true}$- $\chi^2_{\rm min}$.

(5) Step (1)$\sim$(4) are repeated 10000 times. From the $\Delta\chi^2$ distribution, the critical $\Delta\chi^2$ $(\Delta\chi^2_{\rm crit})$ for given confidence level (CL) is calculated; the $\Delta\chi^2_{\rm crit}$ for α CL is the value where α percent of the toy data sets satisfy $\Delta\chi^2 < \Delta\chi^2_{\rm crit}$.

(6) Construct the allowed parameter region by comparing $\Delta\chi^2$ of data and $\Delta\chi^2_{\rm crit}$ for each neutrino oscillation parameters.

Figure 8.12 and 8.13 show $\Delta\chi^2_{\rm crit}$ surface for α =68 and 90%, respectively. Comparing $\Delta\chi^2$ obtained by the real data shown in Fig. 8.14, the allowed region of the neutrino oscillation parameters is obtained, as shown in Fig. 8.15. The 90% confidence interval is obtained to be

$$\begin{aligned} &2.1\times10^{-3} < \Delta m^2_{32}[\mathrm{eV}^2/\mathrm{c}^4] < 3.1\times10^{-3} \quad \text{at } \sin^2 2\theta_{23} = 1.0 \\ &0.86 < \sin^2 2\theta_{23} \qquad\qquad\qquad\qquad\quad \text{at } \Delta m^2_{32} = 2.6\times10^{-3}[\mathrm{eV}^2/\mathrm{c}^4] \end{aligned} \tag{8.19}$$

This result is consistent with the current understandings as described in Section 1.1.3.

Figure 8.16 shows the contour with and without systematic error. The contour is slightly worse when the systematic error is taken into account.

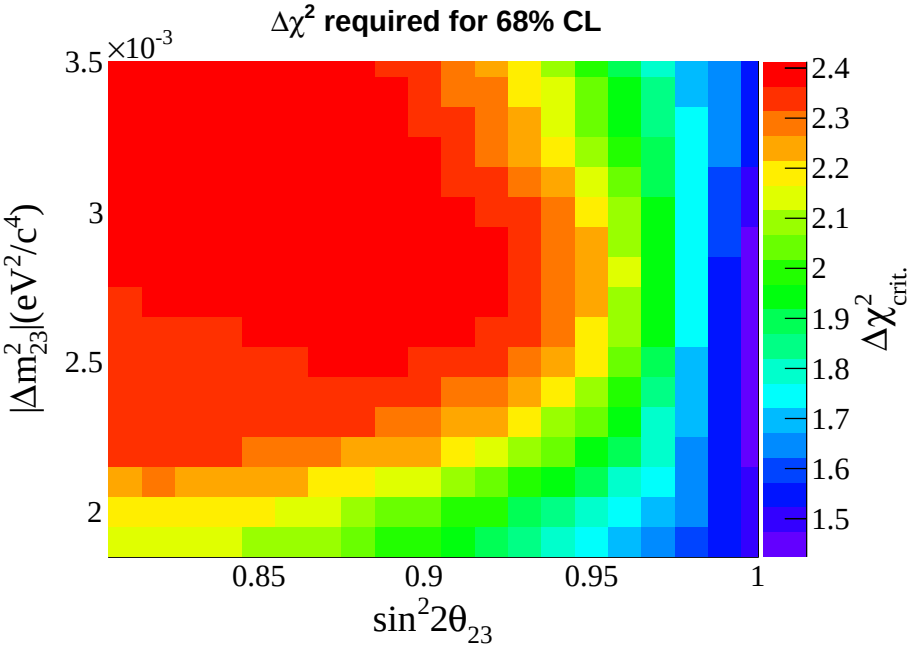

Figure 8.12: $\Delta\chi^2_{\text{crit}}$ values required for 68% CL.

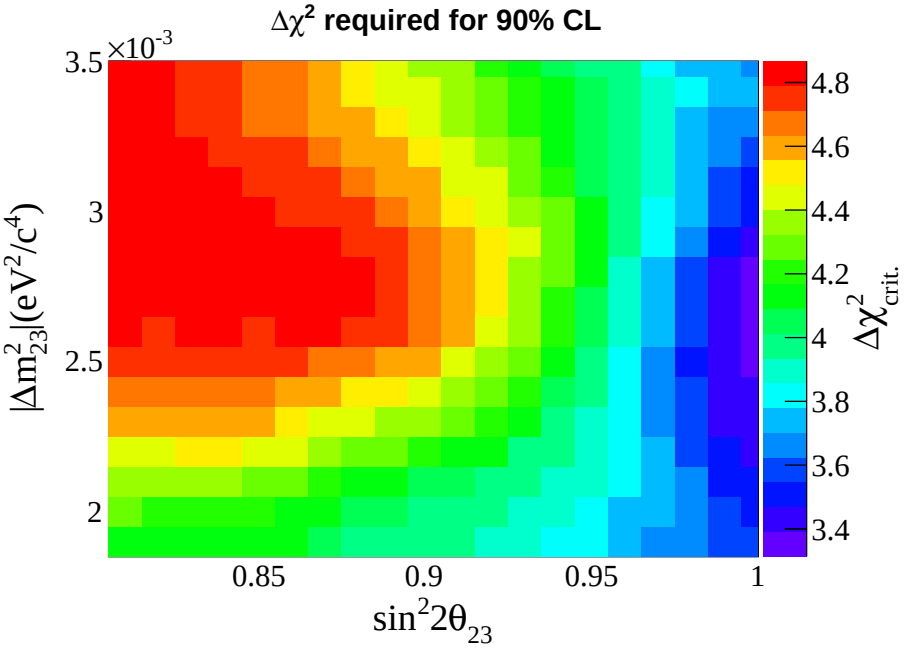

Figure 8.13: $\Delta\chi^2_{\text{crit}}$ values required for 90% CL.

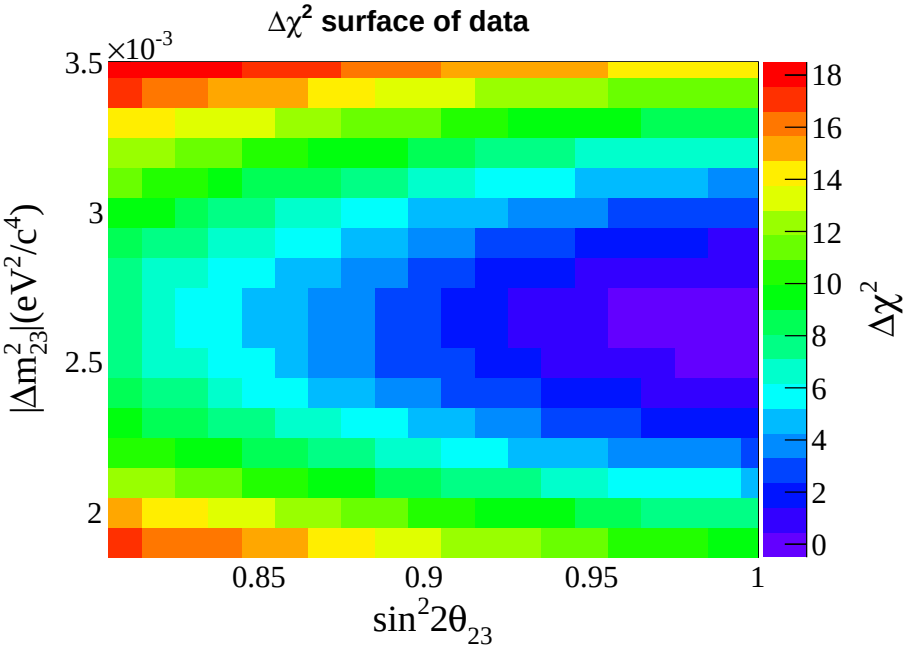

Figure 8.14: $\Delta\chi^2$ surface of data.

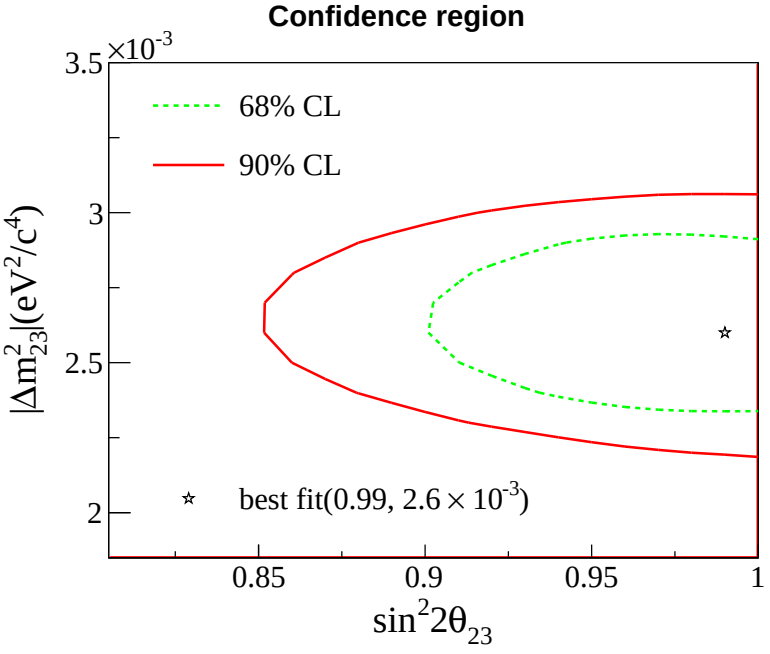

Figure 8.15: Allowed region for the neutrino oscillation parameters.

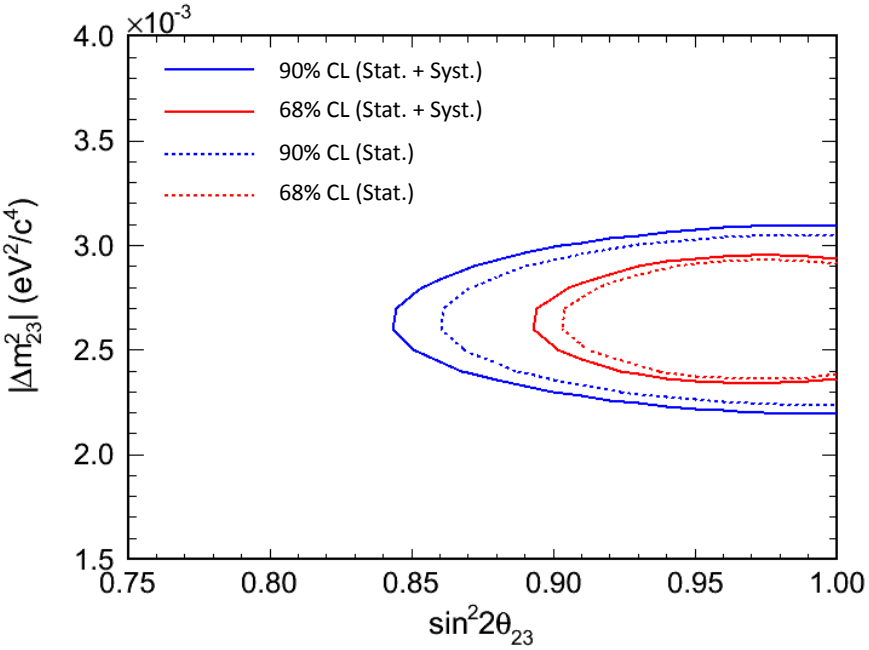

Figure 8.16: Contour for 68% (red) and 90% (blue) confidence level. Solid line shows the contours with taking into account both statistical and systematic error and dashed line shows the contours with taking into account only statistical error.

8.4 Analysis with the number of events only and with the spectrum shape only

In Section 8.3, the analysis results with the likelihood of $\mathcal{L}_{\rm norm} \cdot \mathcal{L}_{\rm shape} \cdot \mathcal{L}_{\rm syst}$ are shown. Here the analysis results with $\mathcal{L}_{\rm norm} \cdot \mathcal{L}_{\rm syst}$ and $\mathcal{L}_{\rm shape} \cdot \mathcal{L}_{\rm syst}$ are examined.

8.4.1 Best fit value of the oscillation parameters

Figure 8.17 shows the best fit value of oscillation parameters. In the case of analysis with $\mathcal{L}_{\rm norm} \cdot \mathcal{L}_{\rm syst}$, the best fit value of oscillation parameters can not be determined as a point but a line of $N_{\rm SK}^{\rm exp.} = N_{\rm SK}^{\rm obs}$. The best fit values are consistent between the analyses. Because the analysis with shape has much power than the analysis with number of events around $\sin^2 2\theta_{23} = 1.0$ as described in Section 8.4.3, the best fit value with shape only is closer to that with normalization and shape than that with normalization only.

8.4.2 Null oscillation probability

The expected number of events in SK is calculated to be 103.7 with null oscillation whereas the observed number of events is 31. The total error on the number of events including statistical error is (+16.6, -16.2), and the deviation from 103.7 events to 31 events is 4.5σ. It means that the probability of null oscillation is 3.4×10^{-6}.

The null oscillation probability is also examined by using the spectrum shape only. The χ^2 in case of the null oscillation ($\sin^2 2\theta_{23} = 0$) is obtained to be 277.2 and the χ^2 in the best fit point is obtained to be 255.9. The χ^2 difference between null oscillation and best fit is 21.3, and

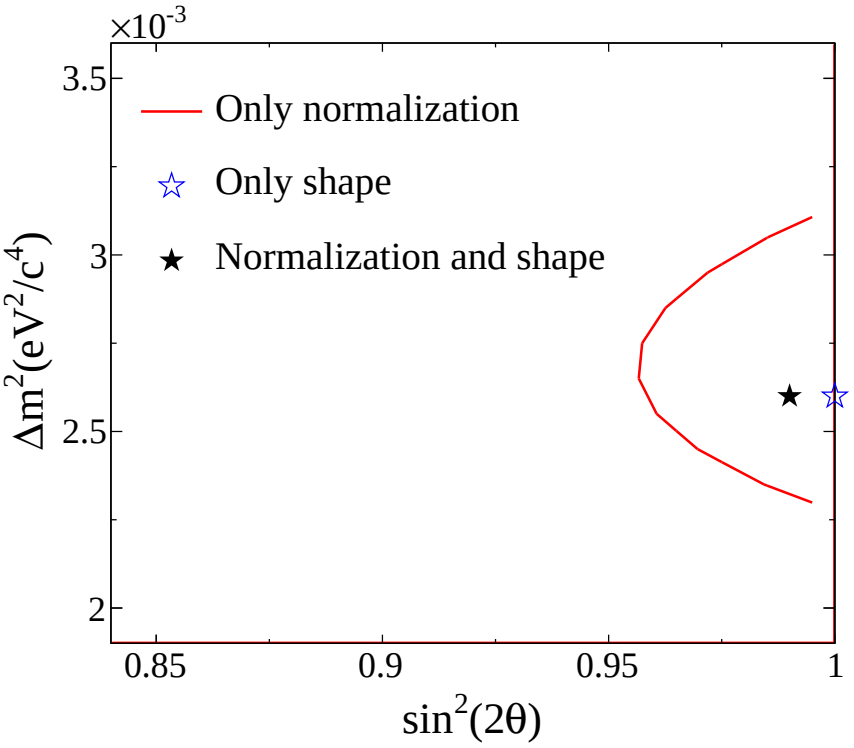

Figure 8.17: Best fit value of the oscillation parameters.

the probability that $\Delta\chi^2 > 21.3$ is calculated to be 2.4×10^{-5} assuming that $\Delta\chi^2$ obeys the χ^2 distribution of two degrees of freedom.

In all the cases, the null oscillation is strongly disfavored.

8.4.3 $\Delta\chi^2$ distribution

Figure 8.18 shows the $\Delta\chi^2$ distribution for $\chi^2 = -2\log(\mathcal{L}_{\rm norm} \cdot \mathcal{L}_{\rm syst})$ and $\chi^2 = -2\log(\mathcal{L}_{\rm shape} \cdot \mathcal{L}_{\rm syst})$. For the power to reject the null oscillation, the analysis with only normalization is more sensitive than the analysis with only shape. Around the full mixing ($\sin^2 2\theta_{23} \simeq 1$), the analysis with only shape has more sensitivity than the analysis with only normalization.

8.5 Comparison with other experiments

Figure 8.19 shows the 90% confidence level contour with that of the MINOS long baseline neutrino oscillation experiment and the SK atmospheric neutrino measurement. Even with current statistics ($N_{\rm obs.} = 31$ and it is 2% of the T2K goal), we achieve the almost same precision measurement as MINOS ($N_{\rm obs.} = 4003$) [17].

8.6 Summary and outlook

We described the oscillation analysis in ν_μ disappearance. The analysis is performed with the method of extended unbinned maximum likelihood. The likelihood is constructed from both the number of events and the neutrino energy spectrum. The best fit point is obtained at $\sin^2 2\theta_{23} = 1.0$ and $\Delta m^2_{32} = 2.4 \times 10^{-3}{\rm eV}^2/{\rm c}^4$ and represents the data well. On the other hand, observation

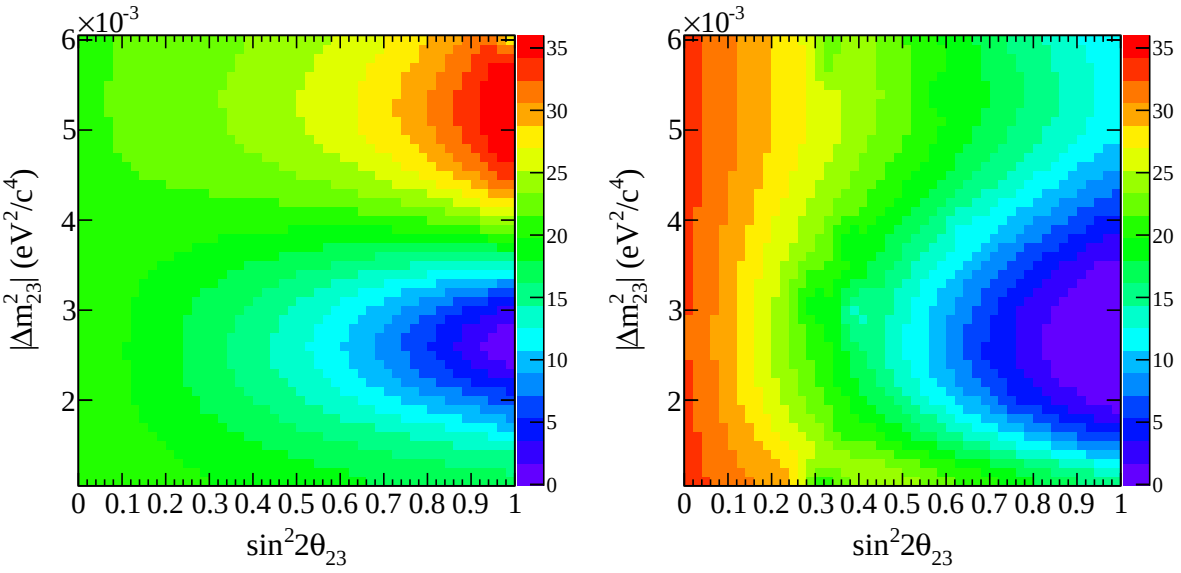

Figure 8.18: $\Delta\chi^2$ distributions as a function of oscillation parameters. The left plot is the distribution of the analysis with the spectrum shape only ($\chi^2 = -2\log[\mathcal{L}_{\text{shape}} \cdot \mathcal{L}_{\text{syst}}]$) and the right plot is the distribution of the analysis with the number of events only ($\chi^2 = -2\log[\mathcal{L}_{\text{norm}} \cdot \mathcal{L}_{\text{syst}}]$).

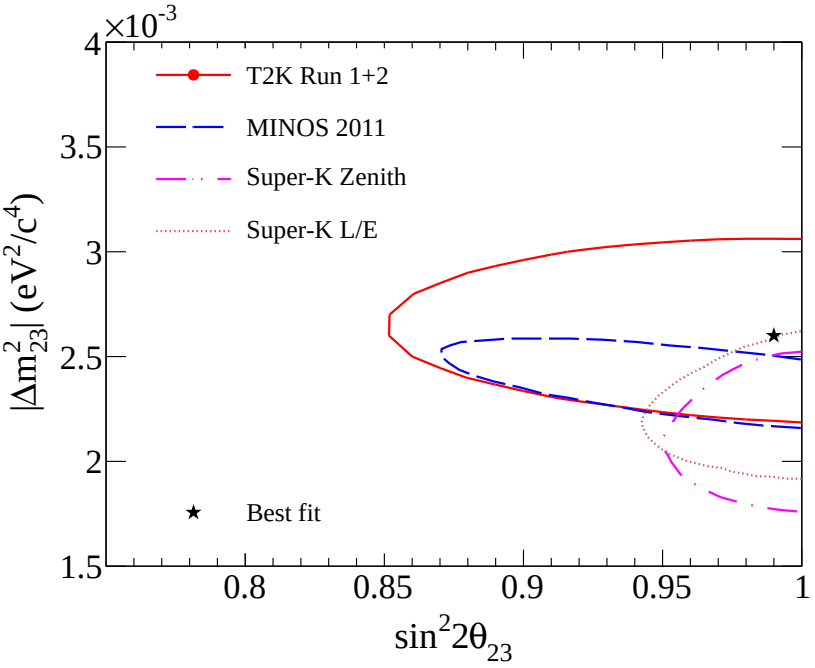

Figure 8.19: 90% confidence level contours for oscillation parameters; results are compared with those from MINOS [17] and Super-Kamiokande [18, 19]

does not agree with the null oscillation hypothesis. The hypothesis is excluded with 7.3×10^{-11}. Our 90% confidence region is obtained to be $2.1 \times 10^{-3} < \Delta m^2_{23}[\mathrm{eV}^2/\mathrm{c}^4] < 3.1 \times 10^{-3}$ at $\sin^2 2\theta_{23} = 1.0$, and $0.86 < \sin^2 2\theta_{23}$ at $\Delta m^2_{32} = 2.6 \times 10^{-3}\mathrm{eV}^2/\mathrm{c}^4$. This region is consistent with these of the other experiments.

The data used in this analysis is just 2% statistics of the T2K goal (8.0×10^{21} protons on target). With this data set, the statistical error is dominant. Figure 8.20 shows the expected allowed region with a full statistics. Here the values of the oscillation parameters are set to $(\sin^2 2\theta, \Delta m^2) = (1.0,\ 2.3 \times 10^{-3}\mathrm{eV}^2/\mathrm{c}^4)$ and only statistical error is considered. The analysis method is same as chapter 8: a maximum likelihood method is used and the likelihood is defined by the number of events and reconstructed neutrino energy shape. We really have a potential sensitivity of $\delta(\sin^2 2\theta_{23}) \sim 0.01$.

Figure 8.21 shows the possible sensitivity with current systematic error. To achieve the sensitivity of $\delta(\sin^2 2\theta_{23}) \sim 0.01$, the improvement of the systematic uncertainty is necessary. As shown in Tab. 8.3, dominant error on the expected number of events is the uncertainty of the SK efficiency and the uncertainty of FSI. As shown in Fig. 8.8, dominant error on the energy spectrum shape is the uncertainty of the SK efficiency and the uncertainty of the beam prediction.

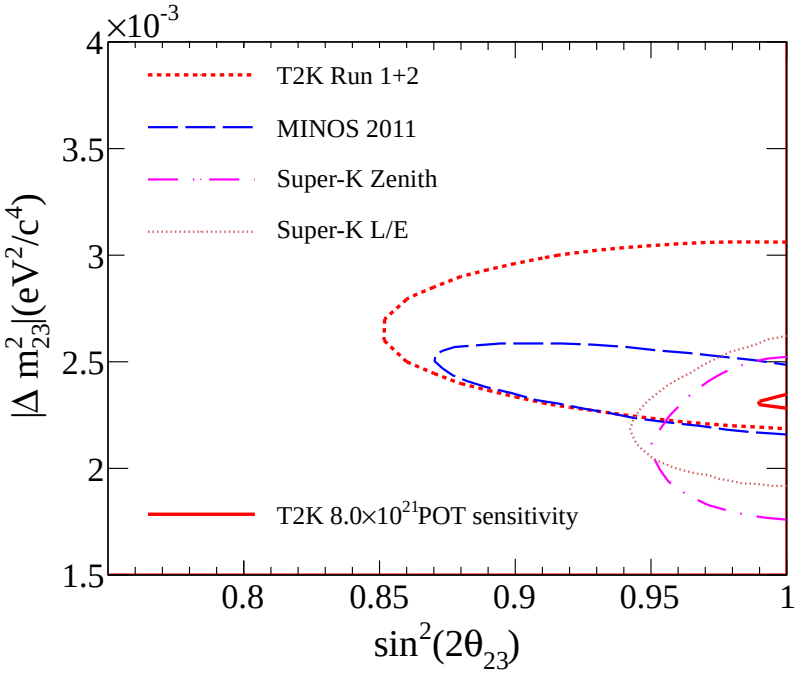

Figure 8.20: T2K sensitivity for $\sin^2 2\theta_{23}$ and Δm^2_{32} with full statistics (8.0×10^{21} protons on target). The toy data are generated with $\sin^2 2\theta_{23} = 1.0$ and $\Delta m^2_{32} = 2.3 \times 10^{-3}\mathrm{eV}^2/\mathrm{c}^4$.

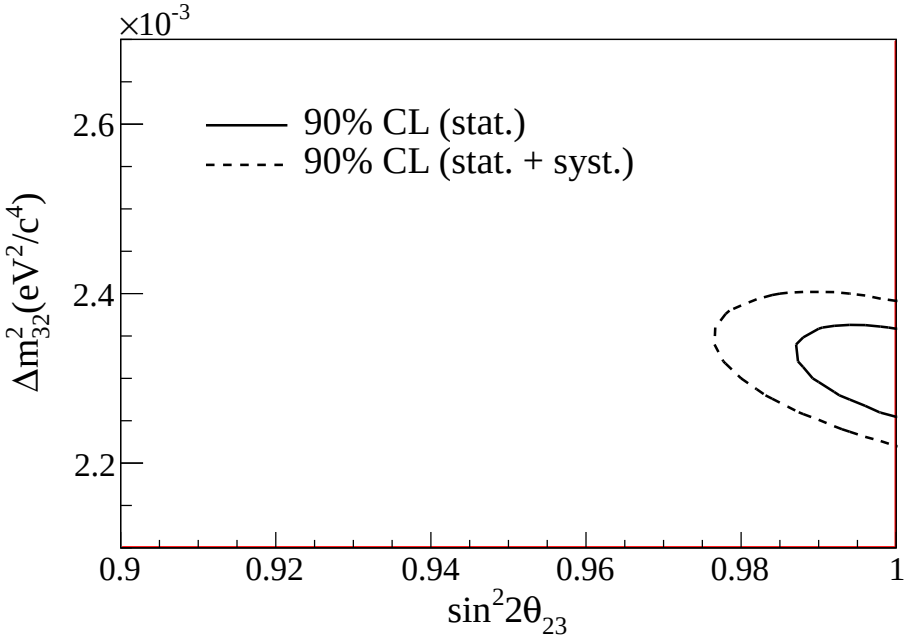

Figure 8.21: T2K sensitivity for $\sin^2 2\theta_{23}$ and Δm^2_{32} with full statistics. The toy data are generated with $\sin^2 2\theta_{23} = 1.0$ and $\Delta m^2_{32} = 2.3 \times 10^{-3}\mathrm{eV}^2/\mathrm{c}^4$. The solid line shows the result with statistical error only and the dashed line shows the result with the statistical error and current systematic error.

Chapter 9

Conclusions

T2K is a long baseline neutrino oscillation experiment. In the T2K experiment, the ν_μ beam is produced at J-PARC and is detected with SK which is 295 km away from J-PARC. T2K aims to measure ($\sin^2 2\theta_{23}$, Δm^2_{32}) via ν_μ disappearance ($\nu_\mu \to \nu_x$) and search for finite θ_{13} via ν_e appearance ($\nu_\mu \to \nu_e$). The neutrino oscillation analysis is performed by comparing observations with the expectations at Super-Kamiokande for both the neutrino energy spectrum and the number of muon neutrino events. One of the T2K features is the off-axis beam method. Thanks to this method, the signal to background ratio is increased. In the off-axis method, the neutrino beam direction is important for the precise estimation of the energy spectrum. The number of neutrino events in the near detector is also important for the precise estimation of the number of ν_μ events.

This thesis first described the measurement of the neutrino beam direction and the number of neutrino events by using the T2K on-axis near detector, INGRID. Then this thesis focused on the analysis of neutrino oscillation in ν_μ disappearance. The data used for this analysis were collected between January 2010 and March 2011, corresponding to 1.4×10^{20} protons on target.

INGRID took more than 99% of all the good beam spills and observed ∼2,180,000 neutrino event candidates. The day by day event rate normalized by protons on target is stable within the statistical error (it is 1.7% typically.). The month by month beam direction is well within ±1 mrad requirement. From these measurements, we concluded that the neutrino energy spectrum and the flux in SK are stable. The horizontal and vertical beam directions are measured to be -0.014 ± 0.025(stat.)$\pm$0.33(syst.) mrad and -0.107 ± 0.025(stat.)$\pm$0.37(syst.) mrad from the designed direction, respectively. It ensures that the beam direction uncertainty on the $\sin^2 2\theta_{23}$ measurement does not effect on achieving the precision of $\delta(\sin^2 2\theta_{23}) \sim 0.01$.

Thirty-one neutrino events were observed in SK, while the expectation without oscillation is $103.7^{+16.6}_{-16.2}$. To find the best fit value of $\sin^2 2\theta_{23}$ and Δm^2_{32}, we employ of the method of maximum likelihood. The likelihood is defined by both the neutrino energy spectrum and the number of events together with the systematic uncertainties. The best fit value is obtained to be

$$(\sin^2 2\theta_{23}, \Delta m^2_{32}) = (0.99, 2.6 \times 10^{-3}\mathrm{eV}^2/\mathrm{c}^4).$$

The probability of the null oscillation is 7×10^{-11}; the null oscillation hypothesis is strongly disfavored and we confirm neutrino oscillation. The 90% confidence region is estimated by the method based on Feldman and Cousins. It is estimated to be

$$2.1 \times 10^{-3} < \Delta m^2_{32}[\mathrm{eV}^2/\mathrm{c}^4] < 3.1 \times 10^{-3} \quad \text{at } \sin^2 2\theta_{23} = 1.0$$
$$0.86 < \sin^2 2\theta_{23} \quad \text{at } \Delta m^2_{32} = 2.6 \times 10^{-3}[\mathrm{eV}^2/\mathrm{c}^4]$$

This result is consistent with other experimental results. We measured the oscillation parameters by using off-axis neutrino beam for the first time in the world. Finally we showed we have a potential sensitivity of $\delta(\sin^2 2\theta_{23}) \sim 0.01$.

In conclusion, we have measured the neutrino oscillation in ν_μ disappearance with the first T2K physics data and showed the T2K potential sensitivity for $\sin^2 2\theta_{23}$. Some theoretical models predict the PMNS matrix as tri-bimaximal form in which θ_{23} is 45 degrees and θ_{13} is 0 degree. Now we know θ_{13} is non-zero [85, 86] and looks to be relatively large (global best fit is obtained to be $\theta_{13} \simeq 9$ degrees) [87]; it is strange that only θ_{23} remains exactly the symmetry of "full mixing" after a certain symmetry breaking. I proved that T2K can investigate this mystery with the best sensitivity in the world.

Appendix A

ν_e appearance measurement

We observed the indication of ν_e appearance [85] for the first time in the world. This appendix describes it.

A.1 Overview

Figure A.1 shows the block diagram of the analysis flow. The analysis strategy is already described in Section 1.2.5; the analysis is performed by comparing the expectation and observation in Super-Kamiokande for the number of ν_e events. To estimate the expectation precisely, it is important to measure the beam direction and the number of events in the near detector.

To perform the ν_e appearance analysis, we measure following quantities:

(1) neutrino beam direction

(2) number of events in the near detector

(3) number of events at SK

Measurement (1) and (2) are already described in Chapter 6. Measurement (3) is described in Section A.2. The ν_e appearance analysis is performed in Section A.3 and the conclusion is described in Section A.4

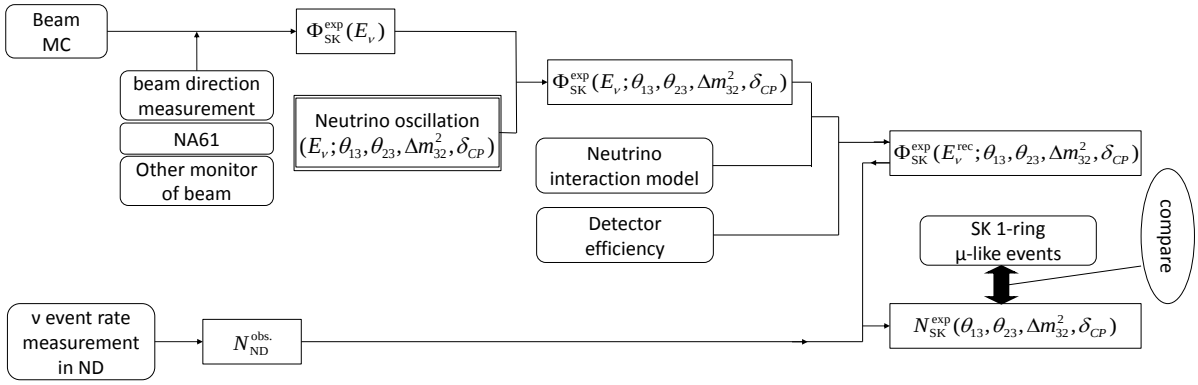

Figure A.1: Block diagram of the ν_e appearance analysis.

The analysis is based on the data set described in Section 5.2: all the RUN-I and RUN-II data sets corresponding to 1.44×20^{20} protons on target (POT).

A.2 Far detector analysis

A.2.1 Data set

After the good beam spill selections, the SK quality cut is applied as described in Section 7.1; the total POT after the SK quality cut is 1.43×10^{20}.

A.2.2 Event selection

Overview

The event selection procedure for the ν_e event is same as that for the ν_μ event up to the single ring selection; the event is extracted with hit PMTs and then FCFV single ring event is selected. After that the following selections are applied to select the ν_e event.

e-like ring

Figure A.2 shows the distribution of the PID likelihood for the observed Cherenkov ring. The e-like ring events are selected.

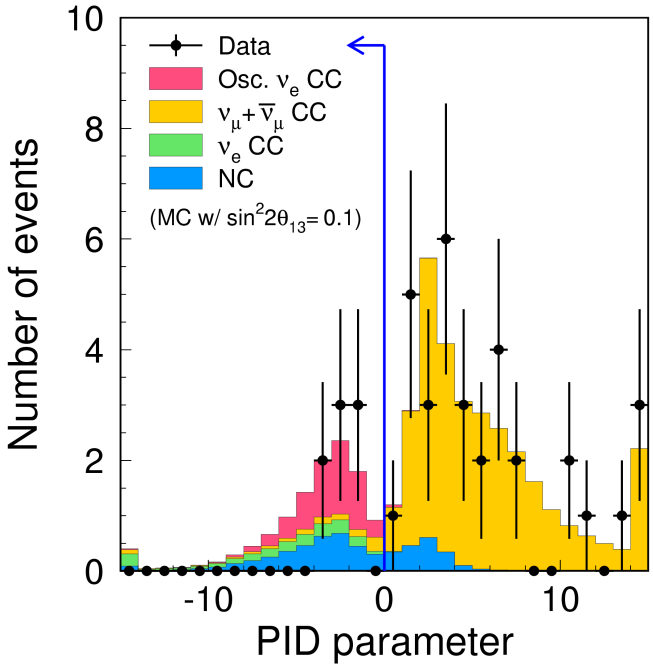

Figure A.2: PID likelihood distribution for the T2K beam data.

Visible energy > 100 MeV

To reject low energy events such as NC backgrounds and Michel electrons produced by invisible muons, the visible energy ($E_{\rm vis}$) is required to be larger than 100 MeV as shown in Fig.A.3 Given the beam energy spectrum, it is very unlikely for a CCQE event to occur in this energy range.

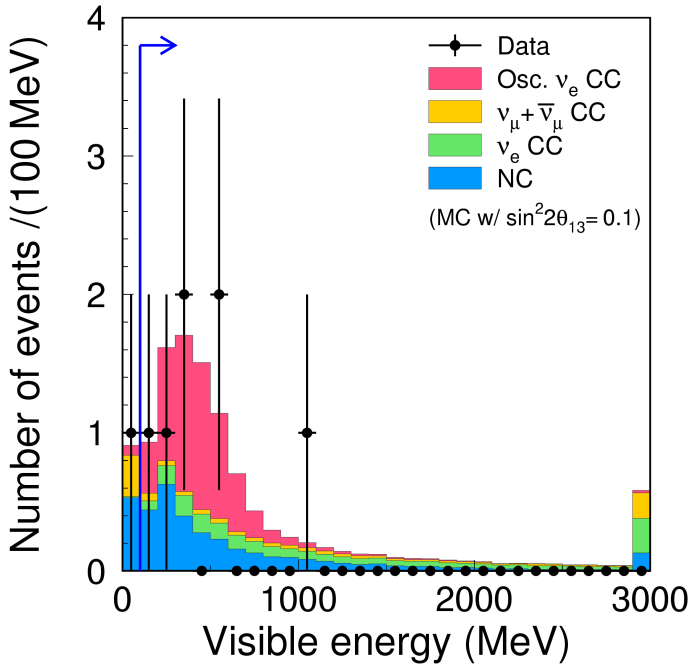

Figure A.3: Visible energy distribution for the T2K beam data.

Number of decay electrons = 0

A decay electron indicates that this event has invisible or un-identified muons or charged pions, indicating ν_μ events or CC non-QE events. Thus the number of decay electrons is required to be zero as shown in Fig.A.4.

π^0 invariant mass $<$ 105 MeV/c^2

To suppress misidentified π^0, a algorithm called POLfit (Pattern Of Light FIT) is performed. In this algorithm, the reconstruction of second ring is forced with various positions and energies. Iteratively, an optimal position and energy for a second ring is determined and an invariant mass ($M_{\rm inv}$) is computed from the first ring and the optimal second ring. Details of POLfit can be found in [88]. Events with $M_{\rm inv} > 105$ MeV/c^2 are rejected as shown in Fig.A.5.

$E_\nu^{\rm rec} < 1250$ MeV

The reconstructed neutrino energy $E_\nu^{\rm rec}$ is reconstructed by Eq. 1.32. To suppress the intrinsic beam ν_e background events, events with $E_\nu^{\rm rec} < 1250$ MeV are selected as shown in Fig.A.6.

Event selection summary

Table A.1 shows the number of selected events at each selection step. The number of selected events is six.

Figure A.7∼A.12 are event display of the final ν_e candidate events. Each display includes a reconstructed image of the second gamma found by the POLfit algorithm. From these event displays, all six events look to be clean ν_e events.

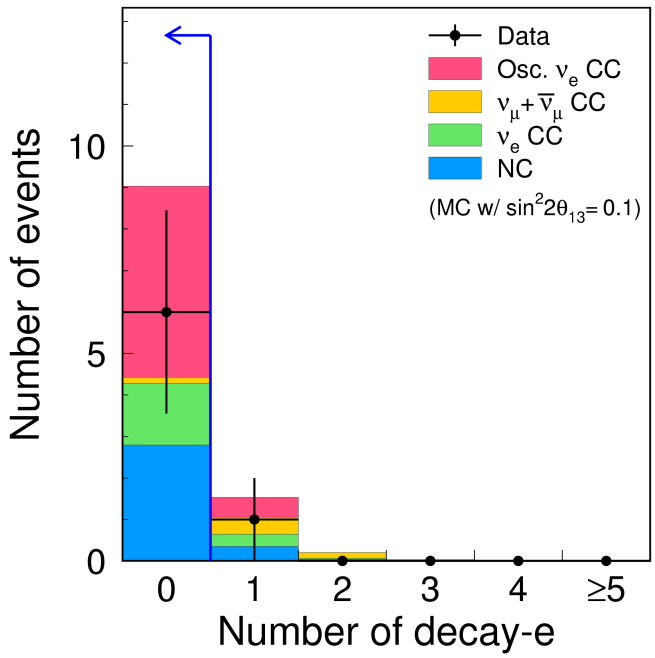

Figure A.4: Number of decay electron distribution for the T2K beam data.

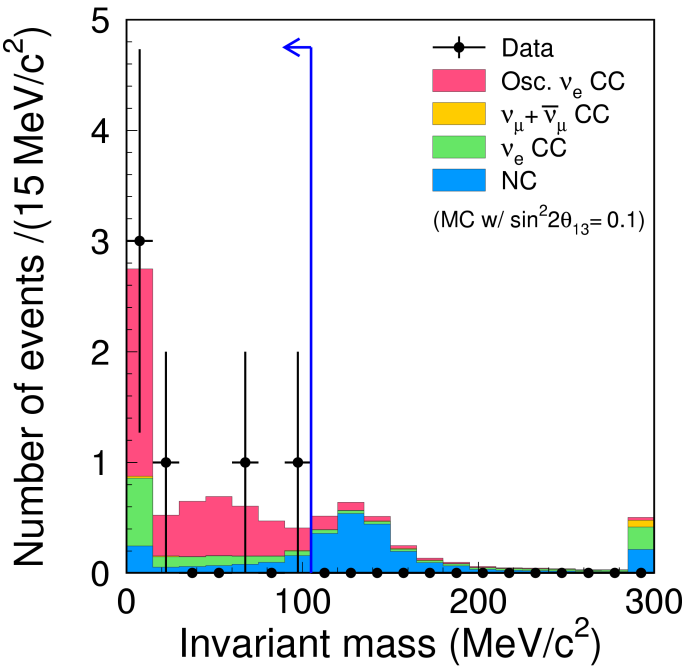

Figure A.5: Invariant mass distribution for the T2K beam data.

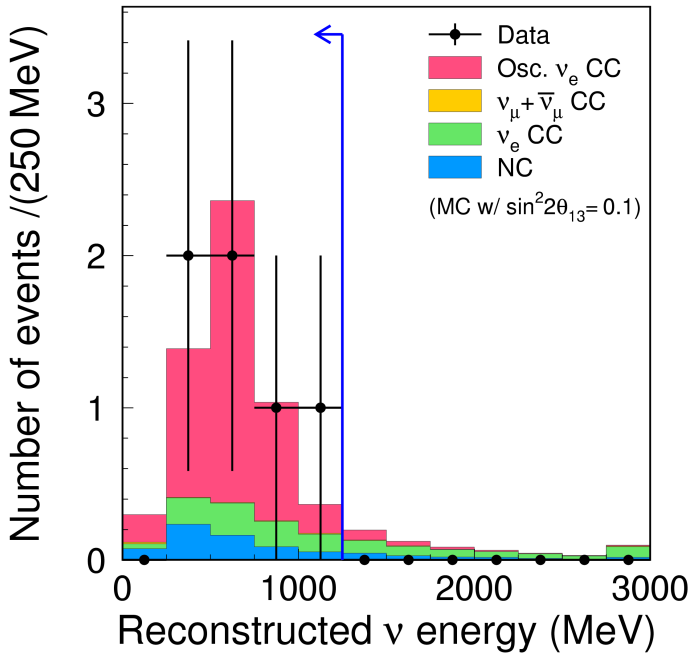

Figure A.6: Reconstructed neutrino energy distribution for the T2K beam data.

Table A.1: Number of events after each selection.

Selection	Data	BG expectation	$\nu_\mu \to \nu_e$ ($\sin^2 2\theta_{13} = 0.1$)
FCFV	88	73.6	6.0
single ring	41	38.3	5.2
e-like	8	6.6	5.2
$E_{\rm vis} > 100$MeV/c	7	5.7	5.1
# of decay electrons = 0	6	4.4	4.6
$M_{\rm inv} < 105$MeV/c^2	6	1.9	4.2
$E_\nu^{\rm rec} < 1250$ MeV	6	1.3	4.1

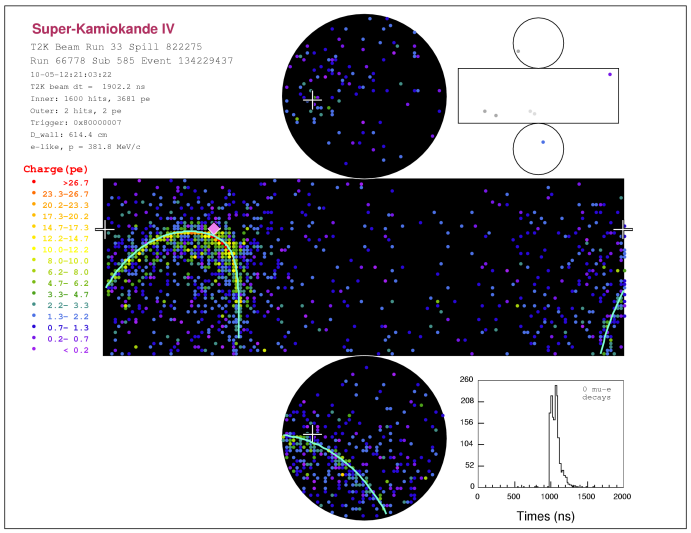

Figure A.7: An event display of a ν_e candidate event (# 1). Four white crosses represent the reconstructed vertex position; the left-right pair shows its height and the top-bottom pairs shows its horizontal position. The light-blue circle represents the fitted Cherenkov ring. The yellow circle represents the second gamma ring reconstructed by the POLfit. A pink diamond is placed on the wall in the beam direction starting from the reconstructed vertex. Reconstruction informations are D_{wall} =614.4 cm, ring-counting likelihood = -5.7, PID likelihood = -1.2, E_{vis} = 381.8 MeV, M_{inv} by POLfit = 29.9 MeV/c^2 and E_{ν}^{rec} = 485.9 MeV.

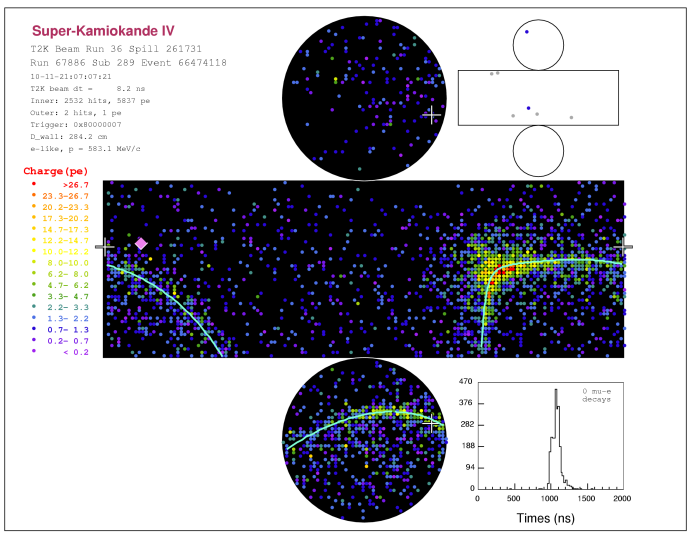

Figure A.8: An event display of a ν_e candidate event (# 2). See the caption of Fig.A.8. Reconstruction informations are D_{wall} =284.2 cm, ring-counting likelihood = -5.2, PID likelihood = -1.2, E_{vis} = 583.1 MeV, M_{inv} by POLfit = 100.4 MeV/c^2 and E_{ν}^{rec} = 842.5 MeV.

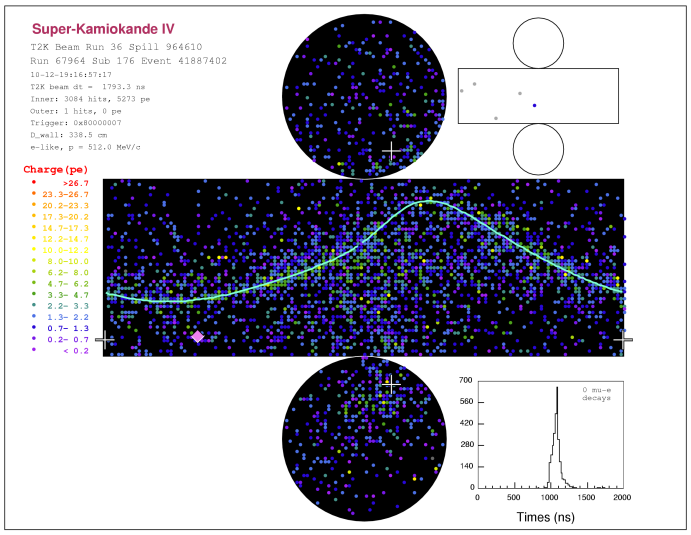

Figure A.9: An event display of a ν_e candidate event (# 3). See the caption of Fig.A.8. Reconstruction informations are D_{wall} =338.5 cm, ring-counting likelihood = -6.0, PID likelihood = -1.6, E_{vis} = 512.0 MeV, M_{inv} by POLfit = 5.1 MeV/c^2 and E_{ν}^{rec} = 722.9 MeV.

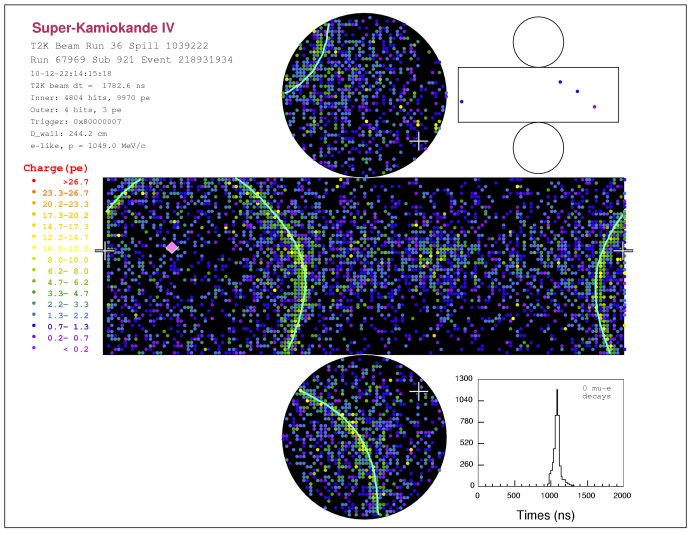

Figure A.10: An event display of a ν_e candidate event (# 4). See the caption of Fig.A.8. Reconstruction informations are D_{wall} =244.2 cm, ring-counting likelihood = -100, PID likelihood = -2.3, E_{vis} = 1049.0 MeV, M_{inv} by POLfit = 0.04 MeV/c^2 and E_{ν}^{rec} = 1120.9 MeV.

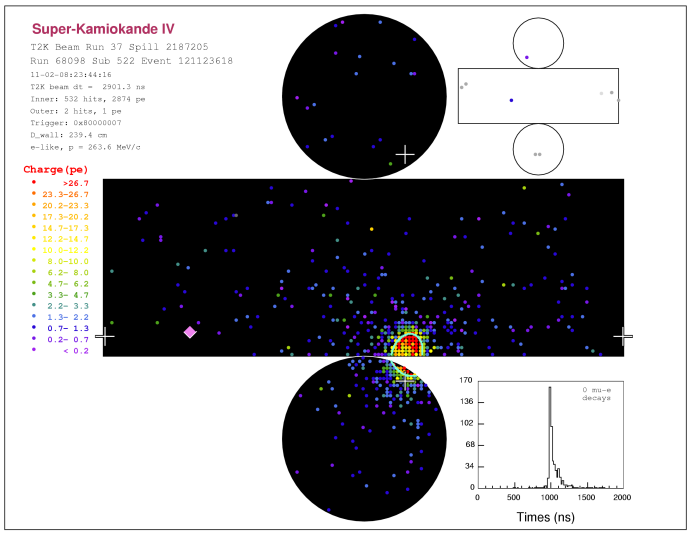

Figure A.11: An event display of a ν_e candidate event (# 5). See the caption of Fig.A.8. Reconstruction informations are D_{wall} =239.4 cm, ring-counting likelihood = -3.9, PID likelihood = -3.1, E_{vis} = 263.6 MeV, M_{inv} by POLfit = 68.9 MeV/c^2 and E_{ν}^{rec} = 580.3 MeV.

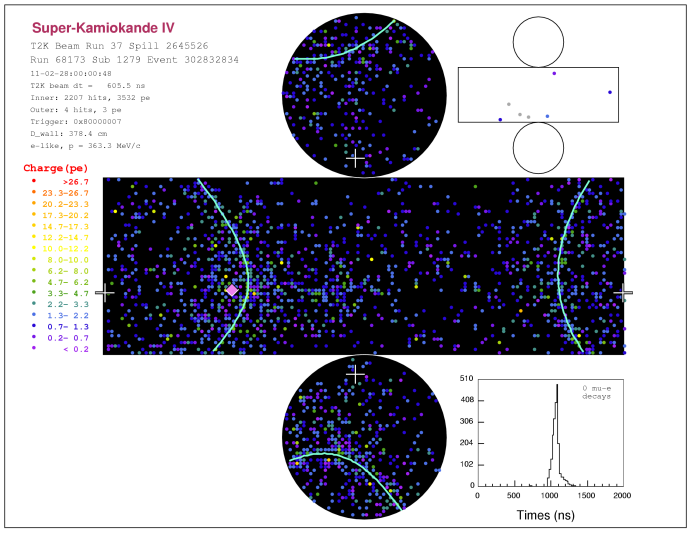

Figure A.12: An event display of a ν_e candidate event (# 6). See the caption of Fig.A.8. Reconstruction informations are D_{wall} =378.4 cm, ring-counting likelihood = -6.1, PID likelihood = -2.6, E_{vis} = 363.3 MeV, M_{inv} by POLfit = 3.4 MeV/c^2 and E_{ν}^{rec} = 419.8 MeV.

Figure A.13 shows the directional distribution of the six ν_e candidate events and the MC expectation. The agreement between the data and the MC expectation is reasonable.

Figure A.14 shows the reconstructed vertex distribution of the selected events. It seems to be clustered towards the upstream side of the SK tank with respect to the T2K beam and near to the wall. The vertex distribution is compared between the data and the MC simulation with several definitions of the position as shown in Fig. A.15. The probability to observe the vertex distribution of data is estimated by KS-test and the result is shown in Tab. A.2. The estimated probability is low, but not unreasonable. The possible unexpected background events are also examined. The estimated number of background events from the beam that leaves the dead space between ID and OD, OD, or rock and has pass all of the selection criteria is calculated to be 8.1×10^{-3}. This is much smaller than the number of expected background events (1.5). In addition, the vertex distribution of the atmospheric neutrino sample has a good agreement between real data and the MC simulation. In summary, we concluded that the observed vertex distribution of the candidate events is consistent with statistical fluctuation.

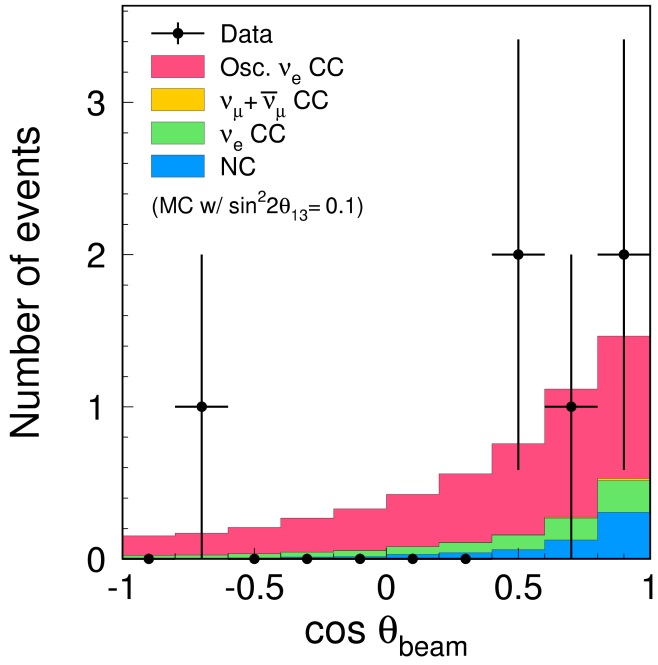

Figure A.13: Directional distribution of the e-like ring for the six ν_e candidate events. $\cos\theta_{\mathrm{beam}}$ is cosine of the opening angle between the ring direction and the beam direction.

A.3 Neutrino oscillation analysis

The analysis for neutrino oscillation with three-flavor oscillation scenario is performed. In this analysis, the oscillation probability including matte effects is calculated numerically by using the Prob3++ software [89].

For the analysis the following oscillation parameters are allowed to vary: δ_{CP}, Δm^2_{32}, θ_{13} and mass hierarchy (normal or inverted). The other oscillation parameters are assumed to be fixed. If some oscillation parameter is not specified, following "default" value is assumed:

- $\sin^2 2\theta_{12} = 0.8704$

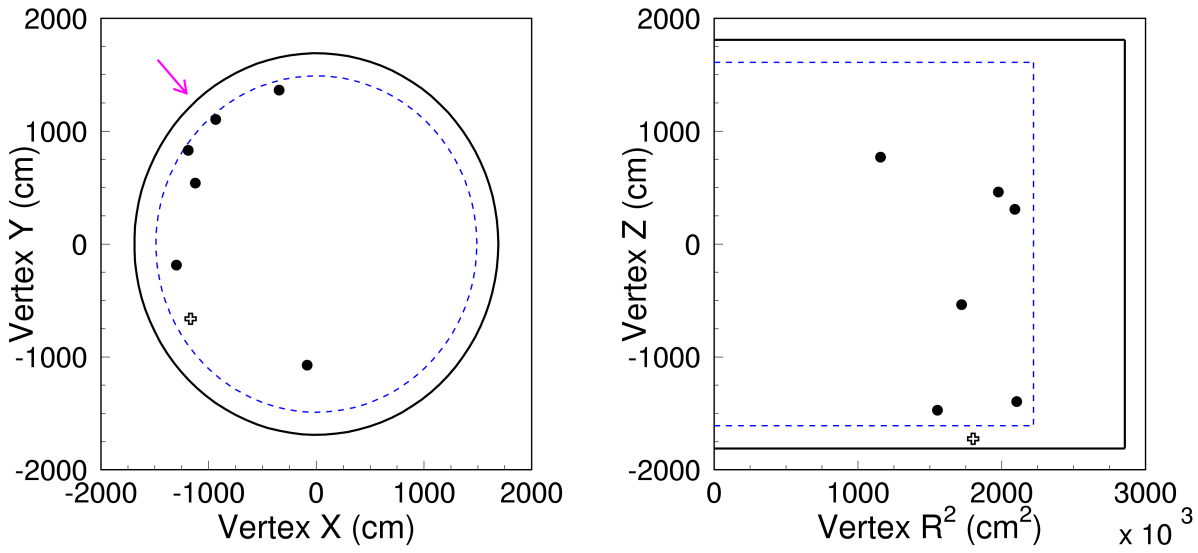

Figure A.14: Vertex distribution in x-y dimensions (left) and z-r^2 dimensions (right) for the events which satisfy all the selection criteria except the FV cut. The black circle indicates the boundary of ID, while the blue dashed circle represents the FV region. The black dots are for the events inside the FV, while the open cross is for that outside the FV. The pink arrow shows the beam direction.

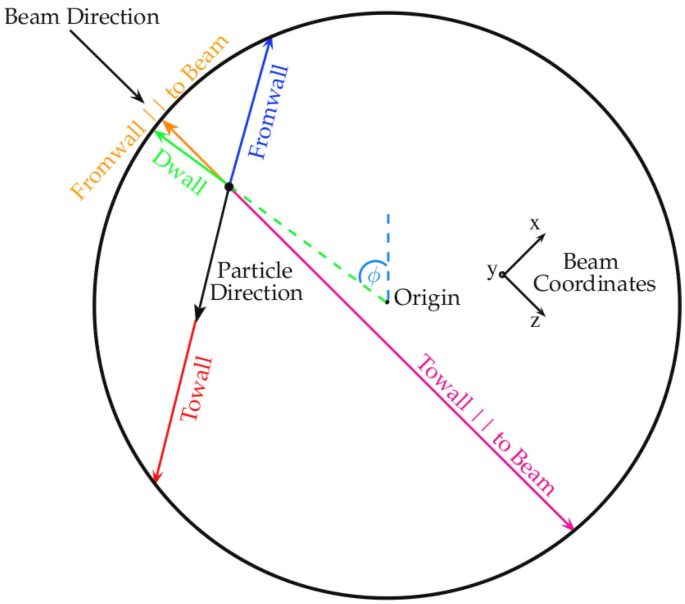

Figure A.15: Definition of parameters for checking of the vertex distribution. This is the top-side view of the SK tank.

Table A.2: Probability to observe the each distribution of the real data estimated with the MC simulation by using the method of KS-test.

Distribution	7 FC Events	6 FCFV Events
Towall||toBeam	5.1%	1.1%
Fromwall||toBeam	1.4%	0.14%
Towall	7.2%	1.9%
Fromwall	22.8%	5.8%
Dwall	22.6%	3.7%
ϕ	28.5%	11.0%

- $\sin^2 2\theta_{23} = 1.0$
- $\Delta m^2_{21} = 7.6 \times 10^{-5}\mathrm{eV}^2/\mathrm{c}^4$
- $\Delta m^2_{32} = 2.4 \times 10^{-3}\mathrm{eV}^2/\mathrm{c}^4$
- $\delta_{CP} = 0$
- Earth matter density around beam = 3.2 g/cm^3
- Beam length = 295 km

A.3.1 Expected number of events

Expected number of events in SK ($N^{\mathrm{exp.}}_{\mathrm{SK}}$) is obtained by using the number of events in the near detector ($N^{\mathrm{obs}}_{\mathrm{ND}}$);

$$N^{\mathrm{exp}}_{\mathrm{SK}}(\sin^2 2\theta_{13}, \Delta m^2_{32}, \delta_{CP}) = N^{\mathrm{obs}}_{\mathrm{ND}} \cdot \left[\frac{N^{\mathrm{MC}}_{\mathrm{SK}}}{N^{\mathrm{MC}}_{\mathrm{ND}}}\right](\sin^2 2\theta_{13}, \Delta m^2_{32}, \delta_{CP}) \cdot \frac{M_{\mathrm{SK}}}{M_{\mathrm{ND}}} \cdot \frac{\mathrm{POT}_{\mathrm{SK}}}{\mathrm{POT}_{\mathrm{ND}}} \quad \text{(A.1)}$$

M_{SK} : fiducial mass of SK, which is 22.5 kton
M_{ND} : fiducial mass of ND280, which is 1.58 kton
$\mathrm{POT}_{\mathrm{SK}}$: number of protons on target for SK, which is 1.43×10^{20}
$\mathrm{POT}_{\mathrm{ND}}$: number of protons on target for ND280, which is 2.88×10^{19}

The $[N^{\mathrm{MC}}_{\mathrm{SK}}/N^{\mathrm{MC}}_{\mathrm{ND}}\ ](\sin^2 2\theta_{13},\ \Delta m^2_{32},\ \delta_{CP})$ is expressed as

$$\left[\frac{N^{\mathrm{MC}}_{\mathrm{SK}}}{N^{\mathrm{MC}}_{\mathrm{ND}}}\right](\sin^2 2\theta_{13}, \Delta m^2_{32}, \delta_{CP}) = \frac{N^{\mathrm{MC}}_{\mathrm{SK}}(\sin^2 2\theta_{13}, \Delta m^2_{32}, \delta_{CP})}{N^{\mathrm{MC}}_{\mathrm{ND}}} \quad \text{(A.2)}$$

$$N^{\mathrm{MC}}_{\mathrm{SK}}(\sin^2 2\theta_{13}, \Delta m^2_{32}, \delta_{CP}) \quad \text{(A.3)}$$
$$= \int dE_\nu \cdot \Phi_{\mathrm{SK}}(E_\nu) \cdot P(E_\nu; \sin^2 2\theta_{13}, \Delta m^2_{32}, \delta_{CP}) \cdot \sum_I \sigma^I_{\mathrm{SK}}(E_\nu) \cdot \epsilon^I_{\mathrm{SK}}(E_\nu)$$

$$N^{\mathrm{MC}}_{\mathrm{ND}} \quad \text{(A.4)}$$
$$= \int dE_\nu \cdot \Phi_{\mathrm{ND}}(E_\nu) \cdot \sum_I \sigma^I_{\mathrm{ND}}(E_\nu) \cdot \epsilon^I_{\mathrm{ND}}(E_\nu)$$

$\Phi_{\rm SK}(\Phi_{\rm ND})$	: expected energy spectrum in SK (ND)
P	: oscillation probability in ν_e disappearance as described in Eq. 1.10
$\sigma^I_{\rm SK}(\sigma_{\rm ND})$	: neutrino cross-section of the target material of SK (ND) for each interaction mode (I)
$\epsilon^I_{\rm SK}(\epsilon_{\rm ND})$	: efficiency in SK (ND) for each interaction mode (I)

The CCQE, CC1π production, CC coherent π production, CC other interactions, NC $1\pi^0$ production, NC coherent π production and NC other interactions are considered as the possible interaction modes. The $\Phi_{\rm SK}$ is estimated with the same method as the ν_μ disappearance analysis case and is shown in Fig. 4.1.

In a similar way, the number of background events (ν_μ, $\bar{\nu}_\mu$ and intrinsic beam ν_e events) are calculated. Then $N^{\rm exp.}_{\rm SK}$ is calculated as sum of the signal (ν_e events) and background events.

Figure A.16 shows $N^{\rm exp.}_{\rm SK}$ as a function of (Δm^2_{32}, $\sin^2 2\theta_{13}$) and (δ_{CP}, $\sin^2 2\theta_{13}$). The $N^{\rm exp.}_{\rm SK}$ is 1.49 in the case of $\sin^2 2\theta_{13}$ =0 and is 5.49 in the case of $\sin^2 2\theta_{13}$ =0.1. The contributions from the signal events and background events are shown in Tab. A.3.

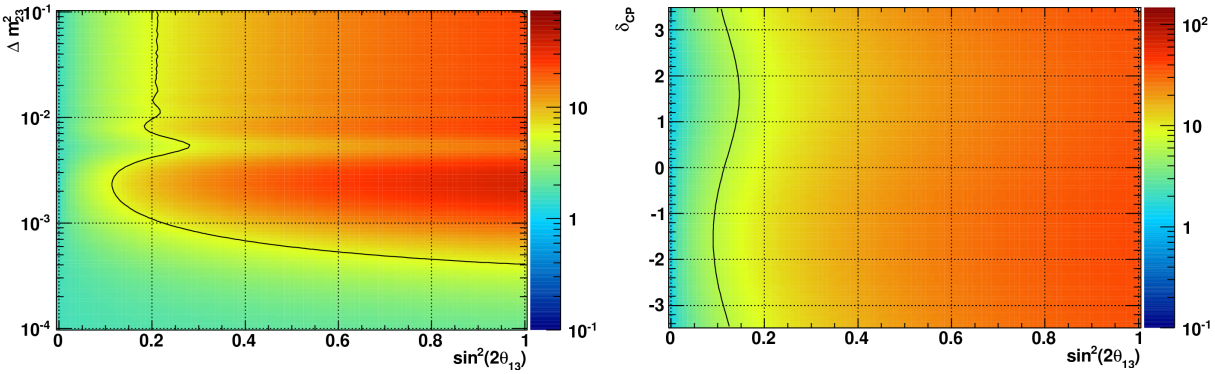

Figure A.16: Expected number of events as a function of Δm^2_{32} and $\sin^2 2\theta_{13}$ (left), and δ_{CP} and $\sin^2 2\theta_{13}$ (right). Contour lines show where the number of events equals 16.

Table A.3: Contributions from each neutrino flavor and interaction mode in the case of $\sin^2 2\theta_{13}$ =0 and $\sin^2 2\theta_{13}$ =0.1. Here $\Delta m^2_{23} = 2.4 \times 10^{-3}{\rm eV}^2/{\rm c}^4$ and $\delta_{CP} = 0$.

	$\sin^2 2\theta_{13} = 0$	$\sin^2 2\theta_{13} = 0.1$
Beam total (background)	1.40	1.34
beam $\nu_\mu + \bar{\nu}_\mu$ CC	0.03	0.03
beam ν_e CC	0.76	0.70
all NC	0.61	0.61
Signal $\nu_\mu \to \nu_e$	0.09	4.11
Total	1.49	5.45

A.3.2 Uncertainties of the number of events

The uncertainties come from the beam MC prediction, the neutrino interaction cross-section, the SK efficiency and the ND280 measurement.

Beam MC prediction

The uncertainty of the beam MC prediction on $[N_{\mathrm{SK}}^{\mathrm{MC}}/N_{\mathrm{ND}}^{\mathrm{MC}}]$ is estimated by propagating the uncertainties of the NA61 measurement and uncertainties of actual experimental condition such as the beam direction.

The error size is shown in Fig A.17. The error size is $\pm 8.5\%$ in the both case of $\sin^2 2\theta_{13} = 0$ and $\sin^2 2\theta_{13} = 0.1$.

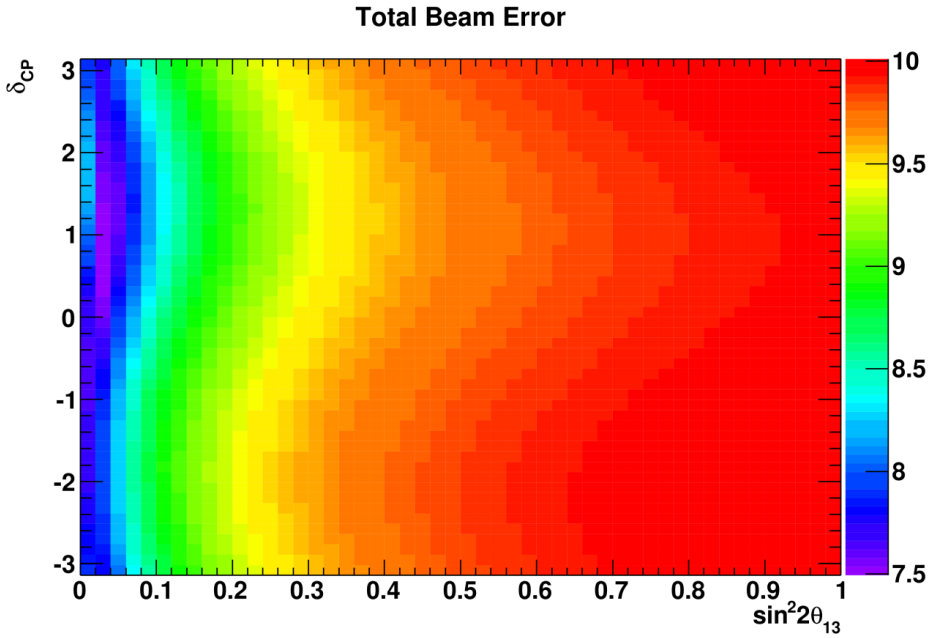

Figure A.17: Estimated fractional error size of $[N_{\mathrm{SK}}^{\mathrm{MC}}/N_{\mathrm{ND}}^{\mathrm{MC}}]$ as a function of δ_{CP} and $\sin^2 2\theta_{13}$.

Neutrino interaction cross-section

The uncertainty of the cross-sections is estimated by comparison with recent measurements from the SciBooNE [76], MiniBooNE [77, 78], and K2K [79, 80] experiments, comparisons with the GENIE [81] and NuWro [82] neutrino interaction generators and recent theoretical work [83]. The error of the cross-section for interaction other than CCQE is estimated as the error on the ratio of that cross-section to the CCQE cross-section. For CCQE interaction, the systematic error of the absolute cross-section is not considered since the absolute normalization is determined by the number of events in the near detector. However, the systematic error due to the different nuclear targets in the near detector and far detector is considered as the CCQE energy dependent error. Because this CCQE energy dependent error is the relative uncertainty between interaction targets, the error is considered only for the SK expectation.

The error size of each interaction is summarized in Tab. A.4 and Fig. A.18.

SK efficiency

The systematic errors related to the SK detector uncertainty are estimated with cosmic-ray muons, electrons from muon decays, and atmospheric neutrino events. The estimated error size is shown in Tab. A.5. In addition to the detector uncertainty, the uncertainty related to the final state interaction (FSI) is estimated by using the external pion scattering data [84] and shown in Fig. A.19.

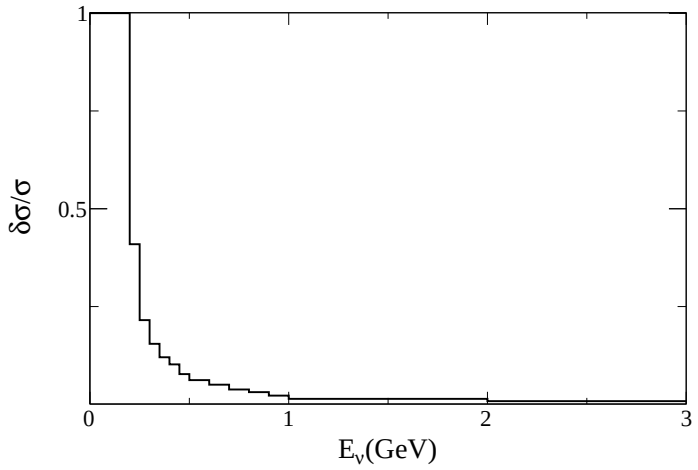

Figure A.18: Energy dependent error on CCQE cross-section error. The error size at 0.5 GeV is ±7% and that above 3 GeV is zero.

Table A.4: Systematic errors for neutrino cross sections.

CC QE	energy-dependent (±7% at 500 MeV)
CC 1π	$\pm 30\%$ ($E_\nu < 2$GeV) $\sim \pm 25\%$ ($E_\nu > 2$GeV)
CC coherent π	100%
CC other	$\pm 30\%$ ($E_\nu < 2$GeV) $\sim \pm 25\%$ ($E_\nu > 2$GeV)
NC $1\pi^0$	$\pm 30\%$ ($E_\nu < 1$GeV) $\sim \pm 20\%$ ($E_\nu > 1$GeV)
NC coherent	30%
NC other	30%
$\sigma_{\nu_e}/\sigma_{\nu_\mu}$	6%

Table A.5: Summary of the systematic error on the number of events.

Source	Signal	Background		
		Total	ν_μ (43.6%) + $\bar{\nu}_\mu$ (4.3%)	ν_e (52.1%)
POLfit mass cut	5.1	8.7	15.2	9.6
Ring-counting	3.9	8.4	15.2	8.4
PID (e)	3.8	8.1	14.5	8.3
PID (μ)	N/A	1.0	2.0	N/A
π^0 efficiency	N/A	5.9	12.8	N/A
Reduction	1.0			
FV	1.0			
Energy scale	0.3	0.5	< 0.1	1.0
Decay-electron	0.1	0.3	0.4	0.2
Total	7.6	15.8		

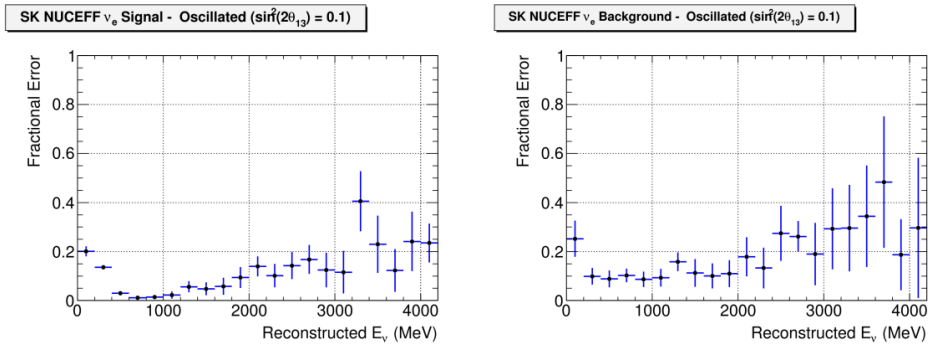

Figure A.19: Systematic error due to final state interaction for ν_e signal (left) and background (right).

ND measurement

The uncertainty of the number of events at ND280 is described in Section 6.4. The systematic error is $^{+4.2}_{-3.6}$ (detector) ± 3.7 (phys.) = $^{+5.6}_{-5.2}$% and the statistical error is 2.7%.

A.3.3 Analysis method

The goals of the analysis are getting the confidence region of oscillation parameters, especially $\sin^2 2\theta_{13}$. We employ the method based on Feldman and Cousins [71]. The actual procedure is as follows:

(1) 10000 toy MC data sets is generated for given oscillation parameters and the probability density function (PDF) for $N_{\mathrm{SK}}^{\mathrm{exp.}}$ ($\mathcal{L}_{N_{\mathrm{SK}}^{\mathrm{exp}}}$) is obtained. The systematic uncertainties are included in toy MC simulation.

(2) The PDF for $N_{\mathrm{SK}}^{\mathrm{obs}}$ ($\mathcal{L}_{N_{\mathrm{SK}}^{\mathrm{obs}}}$) is calculated as

$$\mathcal{L}_{N_{\mathrm{SK}}^{\mathrm{obs}}}(N) = \int_0^\infty dN' \cdot \mathrm{Poisson}(N, N') \cdot \mathcal{L}_{N_{\mathrm{SK}}^{\mathrm{exp}}}(N') \tag{A.5}$$

where $\mathrm{Poisson}(N, N')$ is the Poisson probability of observing N events given an expected mean of N'.

(3) Repeats (1)$\sim$(2) at several oscillation parameter and get $\mathcal{L}_{N_{\mathrm{SK}}^{\mathrm{obs}}}$

Figure A.20 shows example of $\mathcal{L}_{N_{\mathrm{SK}}^{\mathrm{exp}}}$ and $\mathcal{L}_{N_{\mathrm{SK}}^{\mathrm{obs}}}$.

A.3.4 Analysis result

Probability of $\sin^2 2\theta_{13} = 0$

Figure A.21 shows the $\mathcal{L}_{N_{\mathrm{SK}}^{\mathrm{obs}}}$ at $\sin^2 2\theta_{13} = 0$, Δm^2_{32} =2.4 $\times$ $10^{-3}\mathrm{eV}^2/\mathrm{c}^4$ and $\delta_{CP} = 0$. The exclusion level of $\sin^2 2\theta_{13} = 0$ is equal to the integral from zero to five (observed number is six). The integral gives 99.34% and it corresponds to a one-sided 2.5σ CL. The zero θ_{13} is excluded with 99.34%.

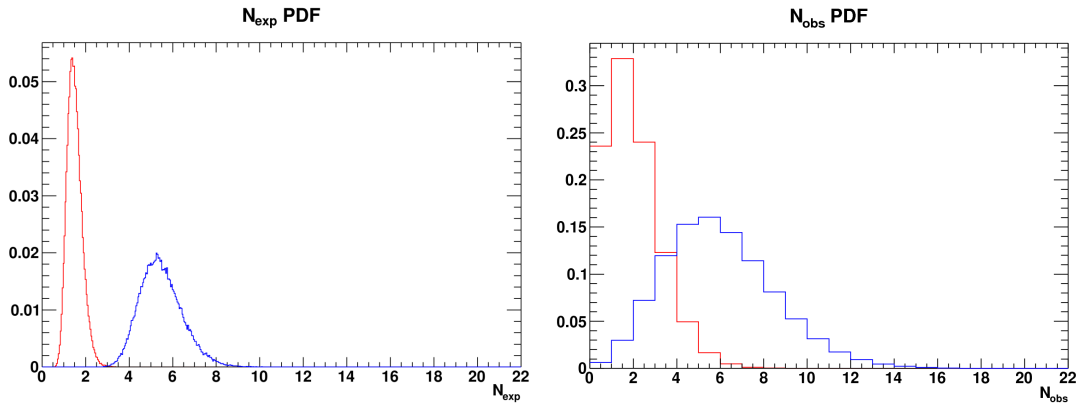

Figure A.20: $\mathcal{L}_{N_{\rm SK}^{\rm exp}}$ (left) and $\mathcal{L}_{N_{\rm SK}^{\rm obs}}$ (right). The red histogram shows PDF at $\sin^2 2\theta_{13} = 0$, Δm^2_{32} =2.4 $\times$ 10^{-3}eV^2/c^4 and $\delta_{CP} = 0$ and the blue histogram shows PDF at $\sin^2 2\theta_{13} = 0.1$, Δm^2_{32} =2.4 $\times$ 10^{-3}eV^2/c^4 and $\delta_{CP} = 0$.

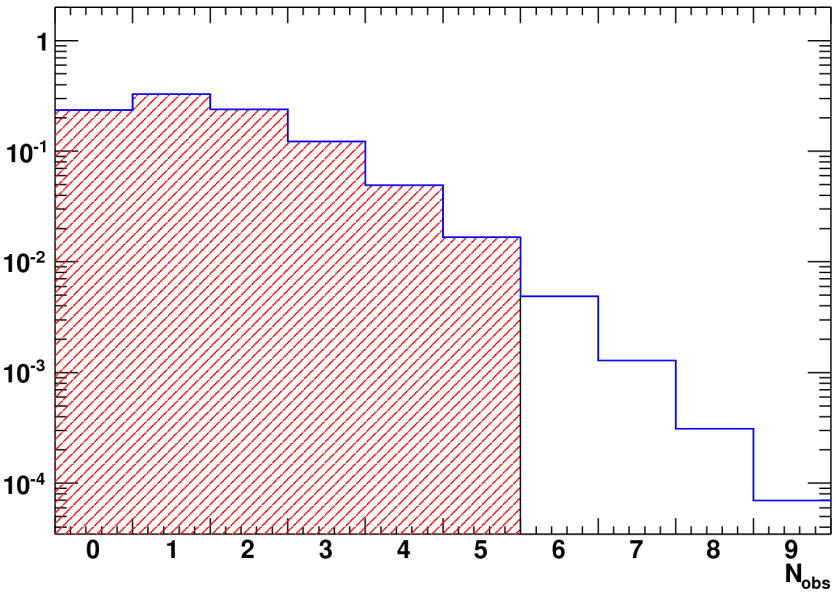

Figure A.21: $\mathcal{L}_{N_{\rm SK}^{\rm obs}}$ at $\sin^2 2\theta_{13} = 0$, Δm^2_{32} =2.4 $\times$ 10^{-3}eV^2/c^4 and $\delta_{CP} = 0$. The region from 0 to 5 observed events is integrated (hatched region) to get 99.34%.

Confidence region

Figure A.22 shows the 90% CL allowed region as a function of oscillation parameters. The confidence interval at $\Delta m^2_{23} = 2.4 \times 10{-}3\mathrm{eV}^2/\mathrm{c}^4$ and $\delta_{CP} = 0$ is $0.03 < \sin^2 2\theta_{13} < 0.28$ for a normal hierarchy and $0.04 < \sin^2 2\theta_{13} < 0.34$ for a inverted hierarchy. This is consistent with the upper limit set by the MINOS [90] and CHOOZ [15] experiment before now. Figure A.23 shows the allowed regions, with and without systematic errors. Though the upper limit contours slightly get worse by the systematic error, statistical errors are greater than systematic errors with the current POT.

A.4 Conclusion

We observed six candidates of ν_e events in Super-Kamiokande with the T2K RUN-I and RUN-II data set (1.43×10^{20} POT). The oscillation analysis is performed by comparing the observation and expectation of the three-flavor neutrino oscillation for the number of ν_e events. The probability of the $\sin^2 2\theta_{13} = 0$ hypothesis is 7×10^{-3}; the zero θ_{13} is disfavored with 2.5σ CL. The confidence interval is $0.03(0.04) < \sin^2 2\theta_{13} < 0.28(0.34)$ for $\sin^2 2\theta_{23} = 1.0$, $|\Delta m^2_{32}| = 2.4 \times 10^{-3}\mathrm{eV}^2/\mathrm{c}^4$, $\delta_{CP} = 0$ and for normal (inverted) neutrino mass hierarchy. This result is consistent with past experiments.

Thus we catch the indication of the non-zero θ_{13}. Next step is to firmly establish the non-zero θ_{13} with more data.

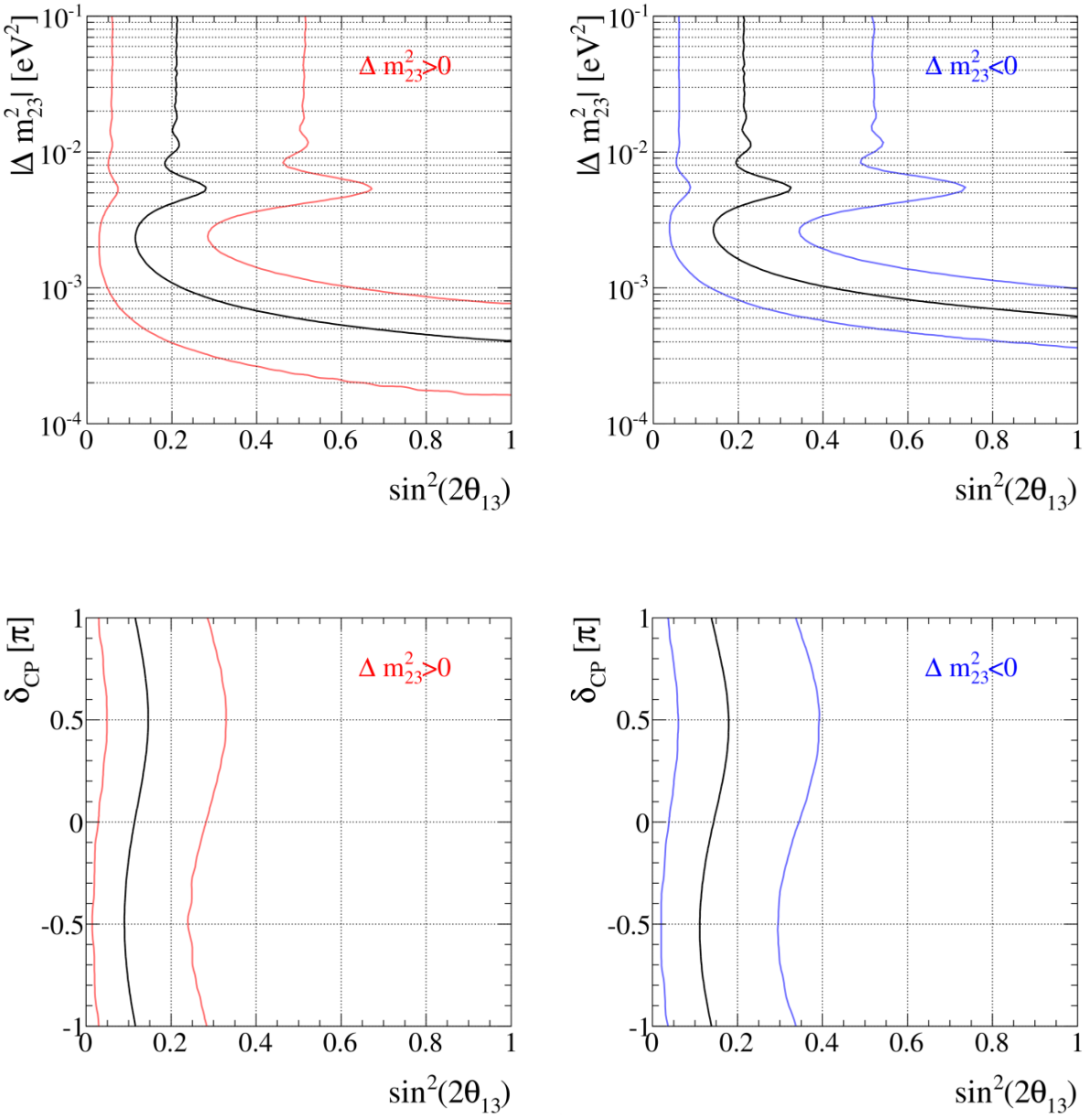

Figure A.22: Allowed region at 90% CL. The are between two red (blue) lines shows the allowed region and the black line shows the best fit parameters. Figures show contours in (Δm^2_{32},$\sin^2 2\theta_{13}$) region for normal (top left) and inverted (top right) hierarchy, and contours in (δ_{CP}, $\sin^2 2\theta_{13}$) region for normal (bottom left) and inverted (bottom right) hierarchy.

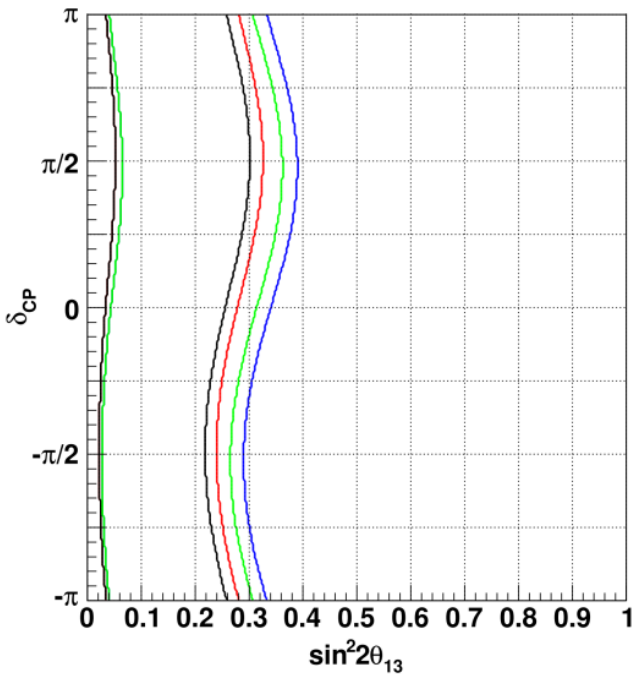

Figure A.23: Overlay plot of the 90% CL allowed region, with and without systematic errors.

List of Tables

List of Figures

Bibliography

[1] W. Pauli, Letter to L. Meitner and her colleagues dated 4 December 1930 (1930).

[2] C.L. Cowan et al., Science 124 (1956) 103.

[3] G. Danby et al., Phys. Rev. Lett. 9 (1962) 36.

[4] DONUT Collaboration, K. Kodama et al., Phys.Rev.Lett. 20 (1968) 1205.

[5] C. Weinheimer et al., Phys. Lett. B 460 (1999) 219.

[6] V.M. Lobashev et al., Phys. Lett. B 460 (1999) 227.

[7] K. Assamagan et al., Phys. Rev. D 53 (1996) 6065.

[8] R. Barate et al., Eur. Phys. J. C2 (1998) 395.

[9] The Super-Kamiokande Collaboration, Phys. Rev. Lett 81 (1998) 1562.

[10] M. Kobayashi and T. Maskawa, Prog. Theor. Phys. 49 (1973) 652.

[11] M. Z.Maki and . S.Sakata, Prog. Theor. Phys. 28 (1962) 870.

[12] B. Pontecorvo, Sov. Phys. JETP 26 (1968) 984.

[13] (SNO Collaboration), B. Aharmim et al., Phys. Rev. C 81 (2010) 055504.

[14] Y.A. et al. (Super-Kamiokande Collaboration), Phys. Rev. D 71, 112005 (2005).

[15] M. Apollonio et al., Eur. Phys. J. C27 (2003) 331.

[16] (Particle Data Group), K. Nakamura et al., J. Phys. G 37 (2010) 075021.

[17] (MINOS Collaboration), P. Adamson et al., Phys. Rev. Lett. 106 (2011) 181801.

[18] (Super-Kamiokande Collaboration), Y. Ashie et al., Phys. Rev. Lett. 93 (2004) 101801.

[19] (Super-Kamiokande Collaboration), K. Abe et al., submitted to Phys. Rev. Lett. (2011).

[20] K.T. McDonald, hep-ex/0111033 (2001).

[21] . T2K-ND280, Technical Design Report (2006).

[22] (T2K Collaboration), . K.Abe et al., Nucl. Instrum. Meth. A 659 (2011) 106.

[23] S. van der Meer, CERN-61-07 (1961).

[24] K. Matsuoka et al., Nucl. Instr. and Meth. A 623 (2010) 385.

[25] (UA1 Collaboration), M. Luque et al., Nucl. Instr. and Meth. 176 (1980) 175.

[26] L. Trung, PhD thesis, Stony Brook University (2009).

[27] N. Abgrall, Nucl. Instr. and Meth. A (2011).

[28] T. Linder and . the T2K-FGD group, J. Phys. Conf. Ser. 136 (2008) 042035.

[29] M. Ziembicki, Acta Phys. Polon. B 41 (2010) 1579.

[30] J.P.R. Y. Giomataris, P. Rebourgeard and G. Charpak, Nucl. Instr. and Meth. A 376 (1996) 29.

[31] Y. Fukuda et al., Nucl. Instr. Meth. A 501 501 (2003) 418.

[32] Y. Itow et al., (KEK-REPORT-2001-4) hep-ex/0106019 (2001).

[33] A. Pla-Dalman, A. Bross and V. Rykalin, FELMILAB-CONF-03-318-E .

[34] M. Otani et al., Nucl. Instr. Meth. A 623 (2010) 368.

[35] H. Kawamuko, T. Nakaya and M. Yokoyama, PoS PD07 043 (2007).

[36] K.K., H. Photonics, [Online]: `http://www.hahahatsu.com` .

[37] M. Yokoyama et al., Nucl. Instr. Meth. A 622 (2010) 567.

[38] P.R. L. Bellantoni, D0 note 4845 .

[39] A. Vacheret et al., in: Nucler Science Symposium Conference Record, NSS'07, IEEE, volume 3 (2007) pp. 1984.

[40] The miximum integrated acquisition system (midas), developed at psi and triumph, `https://midas.psi.ch`.

[41] M. Thorpe et al., Proceedings of the 17th IEEE Conference .

[42] Geant - detector description and simulation tool, application software group, computing and networks division, cern, geneva, 1993.

[43] G. Battistoni et al., the fluka code: Description and benchmarking (2011).

[44] J. A. Fasso, A. Ferrari and P. Sala, fluka: a multi-particle transport code.

[45] N. Abgrall, CERN preprint CERN-SPSC-2010-025. SPSC-SR-066 (2010).

[46] P.R. Feynman, Phys. Rev. Lett. 23 (1969) 1415.

[47] F.F. Chen, P.C. Leavitt and D.A. Stoyanova, Nucl. Phys. B 61 (1973) 62.

[48] C. Zeitnitz and T. Gabriel, (2011).

[49] Y. Hayato, Nucl. Phys. Proc. Suppl. 112 (2002) 171.

[50] Y. Hayato, Acta Phys. Polon B 40 (2009) 2477.

[51] R. Smith and E. Moniz, Nucl. Phys. 43 (1972) 605.

[52] E. Moniz et al., Phys. Rev. Lett. 26 (1971) 445.

[53] K. Abe et al., Phys. Rev. Lett. 56 (1986) 1107.

[54] C.H. Albright et al., Phys. Rev. D 14 (1976) 1780.

[55] D. Rein and L. Sehgal, Ann. Phys. 133 (1981) 79.

[56] D. Rein, Z. Phys. C 35 (1987) 43.

[57] D. Rein and L. Sehgal, Nucl. Phys. B223 (1983) 29 .

[58] D. Rein and L. Sehgal, Phys.Lett. B657 (2007) 207 .

[59] S. Adler, Phys.Rev. 135 (1964) B963.

[60] S. Adler, Ann. Phys. 50 (1968) 89.

[61] M. Gluck et al., Eur.Phys.J. C5 (1998) 461.

[62] A. Bodek and U. Yang, AIP Conf. Proc. 670 (2003) 110.

[63] P. Musset and J.P. Vialle, Phys. Rep. 39 (1984) 1.

[64] J.E. Kim et al., Rev. Mod. Phys. 53 (1981) 211.

[65] L. Salcedo et al., Nucl. Phys. A 484 (1988) 557.

[66] D. Ashery et al., Phys. Rev. C 23 (1981) 2173.

[67] R. Brun, F. Carminati and S. Giani, CERN-W5013.

[68] M. Hasegawa, Ph.D thesis, Kyoto University (2005).

[69] (T2K Collaboration), A. Vacheret et al., Nucl. Instr. Meth. A 623 (2010) 201.

[70] C. Giganti, PhD thesis, L'Universite Paris-Sud (2010).

[71] M. Gluck, E. Reya and A. Vogt, Eur. Phys. J. C 5 (1998) 461.

[72] J. Kameda, PhD thesis, University of Tokyo (2002).

[73] C. Ishihara, PhD thesis, University of Tokyo (2010).

[74] . Davies and E. Roy, Academic Press, San Diego (1997).

[75] `http:://wwwasdoc.web.cern.ch/wwwasdoc/minuit/minmain.html` .

[76] (SciBooNE Collaboration), J. Alcaraz-Aunion and J. Walding, AIP Conf. Proc. 1189 (2009) 145.

[77] (MiniBooNE Collaboration), A.A. Aguilar-Arevalo et al., Phys.Rev. D81 (2010) 092005.

[78] A.A.A. et al. (MiniBooNE Collaboration), Phys.Rev.Lett. 103, 081801 (2009).

[79] (K2K Collaboration), R. Gran et al., Phys. Rev. D 74 (2006) 052002.

[80] (K2K Collaboration), A. Rodriguez et al., Phys. Rev. D 78 (2008) 032003.

[81] C. Andrepoulos et al., Nucl. Instrum. Meth. 614 (2010) 87.

[82] C. Juszczak et al., Acta Phys. Polon. 840 (2009) 2507.

[83] C. Juszczak et al., Phys. Rev. C 82 (2010) 045502.

[84] T.S.H. Lee and R.P. Redwine, Annu. Rev. Nucl. 52 (2002) 23.

[85] (T2K Collaboration), K. Abe et al., Phys. Rev. Lett. 107 (2011) 041801.

[86] Y. Abe et al., arXiv:1112.6353 (2011).

[87] G. Fogli et al., arXiv:1106.6028v2 (2011).

[88] T. Barszczak, PhD Thesis, University of California, Irvine (2005).

[89] V. Barger, K. Whisnant and R.J.N. Phillips, Phys. Rev. D 22, 1636 (1980).

[90] (MINOS Collaboration), P. Adamson et al., Phys. Rev. D 82 (2010) 051102.